

DISS. ETH NO. 23628

MULTISCALE INVESTIGATION AND NUMERICAL  
MODELING OF IMBIBITION, DRAINAGE AND DRYING OF  
A MACROPOROUS MEDIUM

A thesis submitted to attain the degree of  
DOCTOR OF SCIENCES of ETH ZURICH  
(Dr. sc. ETH Zurich)

presented by

SREEYUTH LAL

M.Sc. in Nuclear Engineering,  
ETH Zurich - EPF Lausanne  
born on 21.11.1988  
citizen of Republic of India

accepted on the recommendation of

Prof. Dr. Jan Carmeliet, examiner  
Prof. Dr. Gilles Pijaudier-Cabot, co-examiner  
Dr. Marc Prat, co-examiner  
Dr. Lily Poulikakos, co-examiner  
Dr. Dominique Derome, co-examiner

2016



*to my family, friends, friends and family*



*In me I trust.  
All others should bring data.*



## ABSTRACT

---

This thesis proposes an integrated multiscale methodology to study wetting and drying in macroporous media exposed to environmental loads. The motivation behind this work arises from the fact that the durability of many porous materials exposed to the environment is significantly influenced by the residence time of water in them under typical environmental conditions. In this thesis, multiscale experimental investigations and numerical modeling of fluid transport are performed for a highly complex, macroporous material, namely porous asphalt (PA), with the aim to determine the most important environmental conditions and material characteristics that determine the residence time of water in PA.

At the smallest scale, neutron radiography experiments of imbibition, drainage and drying in PA, using a custom-built mini wind tunnel, are coupled with three-dimensional pore space characterization using X-ray microcomputed tomography to understand the physics of air and water transport in PA. The interaction of airflow with PA is further investigated using two techniques. At the smaller scale, computational fluid dynamics (CFD) simulations of airflow in a real PA geometry are performed to identify the influence of air entrainment on convective vapor removal from the internal pore space of PA. In addition, full-scale wind tunnel experiments are coupled with particle imaging velocimetry to characterize the air boundary layer above the air-PA interface and to identify the organized, turbulent flow structures in the boundary layer.

Since gravity-driven drainage and drying are found to be the most important factors determining the residence time of water in PA, pore network model (PNM) simulations of drainage in PA and subsequent drying of the residual liquid are performed. Gravity-driven drainage is simulated using a modified invasion percolation algorithm that includes the effect of gravity while drying is simulated using a cluster-based approach. An insight into the evolution of capillary pressure with saturation for macroporous media during gravity-driven drainage is obtained. It is also observed that a higher hydrophobicity in the pore network, simulated by increasing the number of pores that do not retain water after drainage, leads to shorter constant drying rate periods (CDRP) at the beginning of the drying simulations. To model the experimental observation of no CDRP at the beginning of drying in PA, a further improvement in the pore network is required in order to capture the high hydrophobicity and complex connectivity in PA as they are responsible for the low hydraulic connectivity and high vapor diffusion resistance during drying in PA. Finally, the PNM simulations are coupled to a heat-air-moisture continuum approach to show that the macroscopic drying behavior of a complex macroporous medium can be

modeled with such a coupling approach, subject to more realistic pore networks. Such a continuum approach to drying is extremely computationally efficient and can be used to easily understand the influence of dynamic environmental loads on the drying process of a macroporous medium.



## RESUMÉ

---

Cette thèse propose une méthodologie multi-échelle intégrée pour étudier le mouillage et le séchage de matériaux macroporeux exposés à des charges environnementales. La motivation derrière ce travail provient du fait que la durée de vie d'un grand nombre de matériaux poreux exposés à l'environnement est fortement influencée par le temps de séjour de l'eau sous conditions ambiantes typiques. Dans cette thèse, des recherches expérimentales multi-échelles et des modélisations numériques du transport des fluides sont effectuées pour un matériau macroporeux très complexe, à savoir le revêtement bitumineux drainant (RBD), dans le but de déterminer les conditions environnementales et les caractéristiques du matériau qui déterminent le temps de séjour de l'eau dans le RBD.

À la plus petite échelle, des expériences utilisant la radiographie à neutrons pour documenter l'imbibition, le drainage et le séchage d'éprouvettes de RBD placées dans une mini-soufflerie faite sur mesure, sont couplées à une caractérisation tridimensionnelle du système poreux obtenue par microtomographie à rayons X pour comprendre le transport de l'air et de l'eau dans le matériau. L'interaction du flux d'air avec le RBD est en outre étudiée en utilisant deux techniques. À petite échelle, des simulations de flux d'air dans une géométrie réelle de RBD sont effectuées par dynamique computationnelle des fluides pour identifier l'influence de l'entraînement de l'air sur l'élimination par convection de la vapeur d'eau des pores de RBD. En outre, des expériences en soufflerie à grande échelle utilisent la vélocimétrie par imagerie de particules afin de caractériser la couche limite d'air au-dessus de l'interface air-RBD et d'identifier les structures d'écoulement turbulent organisé dans la couche limite.

Étant donné que le drainage par gravité et le séchage se trouvent être les facteurs les plus importants déterminant le temps de séjour de l'eau dans le RBD, des simulations par modèle de réseau de pores (MRP) du drainage dans le RBD et du séchage subséquent du liquide résiduel sont effectués. Le drainage par gravité est simulé en utilisant un algorithme modifié d'invasion par percolation qui inclut l'effet de la gravité. Quant au séchage, il est simulé en utilisant une approche fondée sur la méthode des grappes. L'évolution de la pression capillaire avec le degré de saturation du matériau macroporeux pendant le drainage par gravité est bien obtenue. On observe également qu'un caractère hydrophobe plus élevé dans le réseau de pores, simulé en augmentant le nombre de pores qui ne retiennent pas l'eau après le drainage, mène à de plus courtes périodes constantes du taux de séchage (PCTS) au début de la simulation de séchage. Pour modéliser l'absence de PCTS au début du séchage, tel que observé expérimentalement, une amélioration du modèle part

réseau de pores serait nécessaire afin de capturer la forte hydrophobie et la connectivité complexe du RBD, responsables de la basse connectivité hydraulique et de la résistance à la diffusion de vapeur élevée notées pendant le séchage du RBD. Enfin, la simulation par MRP couplée à un modèle en milieux continus du transport de la chaleur, de l'air et de l'eau modéliseraient adéquatement le comportement macroscopique du séchage d'un milieu macroporeux complexe, sous réserve de l'obtention de réseaux de pores plus réalistes. Une telle approche de modèle en milieux continus pour le séchage est extrêmement efficace informatiquement et peut être facilement utilisée pour comprendre l'influence des charges environnementales sur le processus de séchage d'un matériau macroporeux.

## ACKNOWLEDGMENTS

---

*Cowards die many times before their deaths; The valiant never taste of death but once.* Julius Caesar's immortal words have driven me whenever I am faced with moments of doubt. But often, Newton's first law kicked in and my internal drive had to be supported by unbalanced external forces to ensure that the ball kept rolling, no matter what. My foremost gratitude goes to my promoter, Prof. Dr. Jan Carmeliet, for giving me the opportunity to pursue a challenging research topic that called for multiple skill sets. His support, advice, nudges and pushes formed an integral part of my PhD life, along with his nostalgic recollection of his time in the Belgian army. I would particularly like to thank Dr. Dominique Derome for her overarching role in my research and for always ensuring that I got the best possible infrastructure for learning, collaborating and propagating my research. I would also like to thank Jan and Dominique explicitly for giving me the independence to pursue my research in the directions that appeared promising to me.

My special thanks goes to Prof. Dr. Manfred Partl and Dr. Lily Poulidakos for their help in material preparation and also for introducing me to the world of porous asphalt.

I would also like to thank Prof. Dr. Gilles Pijaudier-Cabot for agreeing to be on my PhD defense committee and Prof. Dr. Robert Flatt for chairing it and also for breaking the wonderful news that every PhD student hopes for.

I can't thank enough Dr. Thijs Defraeye for always being available for insightful discussions on both the experimental and modeling works done in this thesis. In particular, I am truly thankful for his constant emphasis on sticking to a plan.

My early PhD days were made significantly more fruitful by the patience and understanding of Prof. Dr. Peter Moonen, who explained complex fluid dynamics concepts in the clearest of manners. I would also like to express my gratitude to Dr. Francesco Lucci for his patient discussions on CFD modeling and for his enthusiasm towards my research. A special thanks goes to Dr. Aytac Kubilay and Dr. Andrea Radu for sharing their expertise in numerical modeling with me.

My gratitude also goes out to Dr. Marc Prat for making my research visit to IMFT Toulouse an extremely productive one, albeit one laced with cooked-up stories of after-work activities. I would also like to thank Prof. Dr. Jeff Gostick, who, along with Marc, helped me dive deep into the world of pore network modeling.

I owe special thanks to Martina Koch for her prompt and cheerful administrative assistance and to Karin Schneider for helping me with the doctoral examination procedures.

I would like to acknowledge the technical assistance of Roger Vonbank and Beat Margelisch. My gratitude also goes out to Stephan Carl for offering his assistance whenever

it was needed the most. I would also like to thank Dr. Iwan Jerjen and Dr. Mathieu Plamondon for their help with the CT scans and Guylaine Desmarais for her assistance during the neutron imaging experiments.

My days as a PhD student would have been unthinkable without the tremendous company of my colleagues. Without their active participation in the ever-expanding 1 pm lunch group or in the multitude of social events (especially our Movie Nights!) that will forever be etched in my memory, life would have been that much less worth living. Dr. Karol Kulasinski, Dr. Behrooz Ferdowsi, Dr. Marcel Vonlanthen, Georgios Mavromatidis, Boran Morvaj, Marc Hohmann, Dr. Alessandra Patera, Marcelo Parada, Laure Lemrich, Omid Dorostkar, Lento Manickathan, Kevin Prawiranto, Christian Kanesan, Giovanni Langella, Soyoun Son, Jaebong Lee, Dr. Jonas Allegrini, Dr. Kristina Orehounig, Christoph Waibel, Somil Miglani, Chi Zhang, Mingyang Chen, Gianluca Mussetti, Etienne Jeoffroy, Dr. Biruk Hailesilassie, Dr. Andrea Radu: a big thank you! I also take this opportunity to acknowledge the people behind this L<sup>A</sup>T<sub>E</sub>X template: Marcel, Georgios and Karol. I would also like to thank Lento for introducing me, one step at a time, to the beautiful world of L<sup>A</sup>T<sub>E</sub>X.

When I needed a break from the rigors of scientific pursuit, I found a welcoming hand in ETH Model United Nations, an organization that I had the privilege to be a part of for 3 years and lead for 1.5 years. All ETH MUN members: you have played a big role in my student life and I will be forever indebted to you!

Words cannot express my gratitude towards ETH Zurich, the university I have been privileged to call mine for almost 6 years, starting from my Masters degree. I promise to repay the faith that was showed to me.

Finally, but very importantly, I would like to thank my family, especially my parents, Suman Lal and Mary Lal, for their constant support and unshakable faith in me. Acha, Amma, Jithu, Nisha: I am what I am because of you!

To everyone who is reading this, I have a message: Don't believe in messages. Do your research and think with cold-blooded, ruthless logic. And before you realize it, the world will be a better place.

Sreeyuth Lal  
June 2016

## JOURNAL PUBLICATIONS AND CONFERENCE TALKS

---

The following publications are included in parts or in an extended version in this thesis:

1. **S. Lal**, P. Moonen, L. D. Poulikakos, M. N. Partl, D. Derome and J. Carmeliet (2016). Turbulent airflow above a full-scale macroporous material: Boundary layer characterization and conditional statistical analysis, *Experimental Thermal and Fluid Science*, 74:390-403. (Contribution of S. Lal = 90%).
2. **S. Lal**, L. D. Poulikakos, M. S. Gilani, I. Jerjen, P. Vontobel, M. N. Partl, J. Carmeliet and D. Derome (2014). Investigation of water uptake in porous asphalt concrete using neutron radiography, *Transport in Porous Media*, 105: 431-450. (Contribution of S. Lal = 50%).
3. **S. Lal**, L. D. Poulikakos, I. Jerjen, P. Vontobel, M. N. Partl, D. Derome and J. Carmeliet. Investigation of gravity-driven drainage and forced convective drying in macroporous media using neutron radiography, in preparation. (Contribution of S. Lal = 50%).
4. **S. Lal**, L. D. Poulikakos, P. Vontobel, M. N. Partl, D. Derome and J. Carmeliet. An experimental investigation of wetting and drying in a macroporous medium, in preparation. (Contribution of S. Lal = 50%).
5. **S. Lal**, CFD modeling of convective vapor transport in a real macroporous medium, in preparation. (Contribution of S. Lal = 50%).
6. **S. Lal**, M. Prat, J. Gostick, L. D. Poulikakos, M. N. Partl, D. Derome and J. Carmeliet. Pore network modeling of drying of a macroporous medium, in preparation. (Contribution of S. Lal = 50%).

The following conferences were attended as part of the research carried out in this thesis:

1. **S. Lal**, F. Lucci, T. Defraeye, L. Poulikakos, M. Partl, D. Derome and J. Carmeliet (2015), Convective drying of a macroporous medium: a comparison of original porous asphalt geometry with randomized Kelvin cells, APS 68th Annual Division of Fluid Dynamics Meeting, Nov 22-24, Boston, USA. *Abstract and presentation*.

2. **S. Lal**, L. D. Poulikakos, M. N. Partl, D. Derome and J. Carmeliet (2014), Investigation of water transport and drying in porous asphalt with neutron radiography, 10th World Conference on Neutron Radiography, October 5-10, Grindelwald, Switzerland. *Abstract and presentation.*
3. **S. Lal**, L. D. Poulikakos, M. N. Partl, D. Derome and J. Carmeliet (2014), Investigation of water uptake, drainage and convective drying in porous asphalt with neutron radiography, Interpore-6th International Conference on Porous Media, May 27-30, Milwaukee, USA. *Abstract and presentation.*

## NOMENCLATURE

---

This list of symbols is not exhaustive. Symbols that only appear locally in the text, or are self-explanatory, are not included.

### ROMAN SYMBOLS

SYMBOL	DEFINITION	UNIT
$Bo$	Bond number	-
$c$	mass fraction	-
$c_p$	specific heat	J/(kgK)
$Ca$	capillary number	-
$d$	diameter or distance	m
$D$	diameter	m
$D_M$	molecular diffusion coefficient	m <sup>2</sup> /s
$e$	evaporation flux density	kg/(m <sup>2</sup> /s)
$F$	evaporation flux	kg/s
$g$	gravitational acceleration	m <sup>2</sup> /s
$g_{nw}$	non-wetting phase diffusive conductance	m <sup>3</sup> /(Pa.s)
$g_w$	wetting phase hydraulic conductance	m <sup>3</sup> /(Pa.s)
$G$	shape factor	-
$h_m$	convective mass transfer coefficient	m/s
$H$	hyperbolic hole	-
$I$	beam intensity	neutrons/(cm <sup>2</sup> s)
$J$	scalar flux	m/s
$k$	turbulent kinetic energy	m <sup>2</sup> /s <sup>2</sup>
$k_r$	relative permeability	-
$K$	permeability	m <sup>2</sup>
$\mathbf{K}$	permeability tensor	s
$K_s$	saturated permeability	m <sup>2</sup>

$K_v$	water vapor permeability	s
$l$	length	m
$L_v$	vaporization heat of water	J/(kg)
$m$	mass	kg
$m_{loss}$	normalized moisture loss	-
$\dot{m}_{dry}$	drying rate	kg/s
$M$	molar mass	kg/mol
$n$	Van Genuchten parameter	-
$N_c$	number of corners	-
$p_c$	capillary pressure	Pa
$P$	pressure	Pa
$q$	fluid flux	m/s
$q_f$	flux due to moving front	m <sup>2</sup>
$q_h$	heat flux	J/(sm <sup>2</sup> )
$q_v$	water vapor flux	kg/(m <sup>2</sup> s)
$r_0$	element radius	m
$r_t$	tube radius	m
$R$	universal gas constant	J/(mol K)
Re	Reynolds number	-
Re $_{\theta}$	Reynolds number based on momentum thickness	-
Re $_b$	Reynolds number based on channel length	-
Re $_{bc}$	Reynolds number based on channel height	-
$R_v$	specific gas constant of water vapor	J/(mol K)
$s$	degree of saturation	-
$S$	saturation	-
Sc $_t$	turbulent Schmidt number	-
$SF$	shape factor	-
Sh	Sherwood number	-
$S_u$	skewness of $u$	-
$S_v$	skewness of $v$	-
$S_w$	total water saturation	-
$t$	time	s



$T$	temperature	K
$u$	fluid velocity in streamwise direction	m/s
$u'$	fluctuating part of streamwise component of velocity vector	m/s
$u_*$	friction velocity	m/s
$U$	mean wind speed	m/s
$U_\infty$	free-stream wind speed	m/s
$U^+$	dimensionless mean wind speed	-
$v$	fluid velocity in wall-normal direction	m/s
$v'$	fluctuating part of wall-normal component of velocity vector	m/s
$w$	moisture content	kg/m <sup>3</sup>
$w_{cap}$	capillary moisture content	kg/m <sup>3</sup>
$w_{PM}$	moisture content in porous medium	kg/m <sup>3</sup>
$w_s$	solid matrix content	kg/m <sup>3</sup>
$y^+$	dimensionless wall-normal distance	-

GREEK SYMBOLS

SYMBOL	DEFINITION	UNIT
$\alpha$	shape parameter of Weibull distribution	mm
$\alpha_c$	corner half-angle	°
$\alpha_{VG}$	Van Genuchten parameter	-
$\beta$	scale parameter of Weibull distribution	-
$\chi$	dimensionless arc menisci curvature	-
$\delta$	boundary layer thickness	mm
$\delta^*$	displacement thickness	mm
$\varepsilon$	volume porosity	-
$\varepsilon$	turbulent dissipation (only chap.6)	m <sup>2</sup> /s <sup>3</sup>
$\Sigma$	neutron beam attenuation coefficient	m <sup>-1</sup>
$\phi$	relative humidity	-

$\gamma$	surface tension	N/m
$\eta$	film thickness cut-off factor	-
$\lambda$	thermal conductivity	W/(m K)
$\mu$	dynamic viscosity	kg/(m s)
$\mu_{dry}$	water vapor resistance	-
$\nu$	kinematic viscosity	m <sup>2</sup> /s
$\nu_t$	turbulent viscosity	m <sup>2</sup> /s
$\theta$	contact angle	°
$\theta$	momentum thickness (only chap. 5)	mm
$\theta_c$	critical contact angle for film flow	°
$\rho$	density	kg/m <sup>3</sup>
$\tau$	mass thickness	kg/m <sup>2</sup>
$\tau_t$	tortuosity	-
$\tau_w$	wall shear stress	N/m <sup>2</sup>

---

## SUBSCRIPTS

SYMBOL	DEFINITION
$\infty$	external environment
$b$	bulk
$cl$	cluster
$eff$	effective
$e$	equilibrium
$f$	film
$g$	gas
$i$	inlet
$l$	liquid
$nw$	non-wetting phase
$r$	receding
$s$	saturated
$s$	solid (only ch. 7)

$t$	time
$v$	vapor
$w$	wetting phase

---

## SUPERSCRIPTS

---

SYMBOL	DEFINITION
$s$	snap-off
$t$	threshold

---



## LIST OF ACRONYMS

---

AM	arc meniscus
CDRP	constant drying rate period
CFD	computational fluid dynamics
CHTC	convective heat transfer coefficient
CMTC	convective mass transfer coefficient
DDRP	decreasing drying rate period
DOS	degree of saturation
IP	invasion percolation
MB	Maximal Ball algorithm
MCD	moisture content distribution
MS-P	Mayer and Stowe-Princen
NR	neutron radiography
PA	porous asphalt
PIV	particle imaging velocimetry
PNM	pore network modeling
PSD	pore size distribution
REV	representative elementary volume
ROI	region of interest
TP	transition period
TSD	throat size distribution



# CONTENTS

---

ACKNOWLEDGMENTS	xi
NOMENCLATURE	xv
LIST OF ACRONYMS	xxi
List of Figures	xxxix
List of Tables	xxxix
1 INTRODUCTION	1
1.1 Motivation	1
1.2 Objectives and methodology	3
1.3 Outline of the dissertation	5
2 STATE OF THE ART	7
2.1 Introduction	7
2.2 Transport properties in porous media	7
2.3 Investigations of flow mechanisms in porous media	11
2.3.1 Imbibition	11
2.3.1.1 Capillary-driven imbibition	11
2.3.1.2 Gravity-driven imbibition	15
2.3.2 Drainage and drying in porous media	18
2.3.2.1 Gravity-driven drainage	18
2.3.2.2 Forced convective drying	20
2.3.2.3 Thermal drying	25
2.3.3 Turbulent airflow above porous media	26
2.4 Numerical modeling of multiphase flow in porous media	31
2.4.1 Modeling multiphase flow with pore network modeling	31
2.4.1.1 Modeling drainage with pore network modeling	33
2.4.1.2 Modeling drying with pore network modeling	34
2.5 Composition and characterization of porous asphalt	40
2.6 Needs for further research	44
3 EXPERIMENTAL INVESTIGATION OF IMBIBITION IN PA	47
3.1 Introduction	47
3.2 Water uptake experiment	47
3.2.1 Material characterization	48
3.2.1.1 Preparation	48
3.2.1.2 Cumulative porosity distribution from X-ray microcomputed tomography	51

3.2.2	Experimental setup and procedure . . . . .	52
3.2.2.1	Neutron beamline specifications . . . . .	52
3.2.2.2	Remote-controlled ascending platform . . . . .	52
3.2.2.3	Determination of water content from neutron beam attenuation . . . . .	52
3.2.2.4	Neutron radiography image corrections . . . . .	54
3.2.2.5	Results and discussion . . . . .	55
3.2.2.6	Analysis of moisture content distribution and degree of saturation . . . . .	55
3.2.2.7	Distinguishing saturated and unsaturated flow . . . . .	59
3.2.2.8	Simulation of preferential liquid flow path . . . . .	63
3.2.3	Conclusions . . . . .	67
3.3	Droplet wetting experiment . . . . .	67
3.3.1	Material characterization . . . . .	67
3.3.1.1	Preparation . . . . .	67
3.3.1.2	Pore size distribution . . . . .	68
3.3.2	Experimental setup and procedure . . . . .	72
3.3.2.1	Neutron beamline specifications . . . . .	72
3.3.2.2	Mini wind tunnel with rain simulator . . . . .	72
3.3.2.3	Procedure . . . . .	73
3.3.3	Results and discussion . . . . .	73
3.3.4	Conclusions . . . . .	79
3.4	Synthesis . . . . .	79
4	EXPERIMENTAL INVESTIGATION OF DRAINAGE AND DRYING IN PA . . . . .	81
4.1	Introduction . . . . .	81
4.2	Design of mini wind tunnel . . . . .	81
4.3	Gravity-driven drainage and forced convective drying . . . . .	83
4.3.1	Material characterization . . . . .	83
4.3.1.1	Preparation . . . . .	83
4.3.1.2	Cumulative porosity distribution from X-ray microcomputed tomography . . . . .	84
4.3.2	Experimental setup and procedure . . . . .	84
4.3.2.1	Neutron beamline specifications . . . . .	84
4.3.2.2	Mini wind tunnel with remote drainage . . . . .	86
4.3.2.3	Procedure . . . . .	86
4.3.3	Results and discussion . . . . .	88
4.3.3.1	General observations . . . . .	88
4.3.3.2	Analysis of water flow during a sudden drop in moisture content . . . . .	92



4.3.3.3	Analysis of water flow during redistribution of water between two pores . . . . .	96
4.3.4	Conclusions . . . . .	101
4.4	Forced convective drying and thermal drying . . . . .	102
4.4.1	Material characterization . . . . .	102
4.4.2	Experimental setup and procedure . . . . .	103
4.4.2.1	Mind wind tunnel with rain, wind and solar radiation simulators . . . . .	103
4.4.2.2	Procedure . . . . .	103
4.4.3	Results and discussion . . . . .	104
4.4.3.1	Overview . . . . .	105
4.4.3.2	Influence of initial moisture distribution on drying . . . . .	106
4.4.3.3	Influence of pore sizes on drying . . . . .	109
4.4.3.4	Influence of wind speed on drying . . . . .	111
4.4.4	Conclusions . . . . .	113
4.5	Influence of gravity-driven drainage on total moisture loss . . . . .	114
4.6	Synthesis . . . . .	116
5	EXPERIMENTAL INVESTIGATION OF AIRFLOW ABOVE PA . . . . .	117
5.1	Introduction . . . . .	117
5.2	Material characterization . . . . .	117
5.3	Experimental setup and procedure . . . . .	120
5.4	Results and discussion . . . . .	122
5.4.1	Uncertainty in the estimation of statistical quantities . . . . .	122
5.4.2	Mean and turbulent statistics . . . . .	122
5.4.3	Conditional sampling of turbulence parameters . . . . .	131
5.5	Conclusions . . . . .	136
5.6	Synthesis . . . . .	137
6	CFD MODELING OF AIRFLOW AND VAPOR TRANSPORT IN PA . . . . .	139
6.1	Introduction . . . . .	139
6.2	Materials and methods . . . . .	139
6.2.1	Numerical model and computational domain . . . . .	139
6.2.2	Governing equations . . . . .	143
6.2.3	Numerical simulation . . . . .	145
6.3	Results and discussion . . . . .	145
6.3.1	CFD validation with convective scalar transfer from a flat plate . . . . .	145
6.3.2	CFD simulation of convective scalar transport from PA . . . . .	146
6.3.2.1	Integrated scalar flux at the air-material interface . . . . .	146
6.3.2.2	Air flow-field and scalar distribution in PA . . . . .	150
6.3.2.3	Convective and diffusive fluxes along the air-material interface . . . . .	151

6.3.2.4	Visualization of air flow-field and scalar distribution in pores near the air-material interface . . . . .	154
6.3.2.5	Effect of air entrainment into the pore space on scalar convection . . . . .	155
6.4	Conclusions . . . . .	158
6.5	Synthesis . . . . .	159
7	PORE NETWORK MODELING OF DRAINAGE AND DRYING IN PA . . . . .	161
7.1	Introduction . . . . .	161
7.2	Fundamentals of pore network modeling with corner films . . . . .	161
7.3	Drainage and drying algorithms with governing equations . . . . .	164
7.3.1	Modeling gravity-driven drainage with invasion percolation . . . . .	164
7.3.2	Modeling drying of residual liquid after drainage with a cluster-based algorithm . . . . .	167
7.4	Pore network extraction from porous asphalt specimens . . . . .	172
7.5	Results and discussion . . . . .	177
7.5.1	Gravity-driven drainage and snap-off . . . . .	177
7.5.2	Drying of residual liquid and experimental validation . . . . .	181
7.6	Sensitivity analysis . . . . .	187
7.7	Upscaling to continuum modeling . . . . .	192
7.7.1	Introduction . . . . .	192
7.7.2	Governing equations . . . . .	193
7.7.3	Numerical model and input parameters . . . . .	194
7.7.4	Results and discussion . . . . .	197
7.8	Conclusions . . . . .	199
8	CONCLUSIONS AND PERSPECTIVES . . . . .	201
8.1	Main conclusions . . . . .	201
8.2	Contributions to research fields . . . . .	204
8.3	Future perspectives . . . . .	205
A	APPENDIX A . . . . .	207
	BIBLIOGRAPHY . . . . .	211
	CURRICULUM VITAE . . . . .	227

## LIST OF FIGURES

---

Figure 2.1	Evolution of saturation and relative permeability during primary and secondary drainage . . . . .	10
Figure 2.2	Water droplets on marble . . . . .	13
Figure 2.3	Moisture retention of Toray with and without hydrophobic agent	14
Figure 2.4	Schematic of a stable and unstable gravity-driven imbibition . . .	16
Figure 2.5	Drying and wetting curves of sands with different hydrophobicity	17
Figure 2.6	Photographs of oil saturation in the upper and lower blocks of a micromodel . . . . .	21
Figure 2.7	Temporal and spatial distribution of segmented saturation degree of aged PA . . . . .	21
Figure 2.8	Drying regimes in porous media . . . . .	22
Figure 2.9	Time evolution of droplet inside a porous medium . . . . .	23
Figure 2.10	3D visualization of water in PA . . . . .	24
Figure 2.11	Temperature distributions underneath the surface of different types of building materials . . . . .	27
Figure 2.12	Streamwise velocity contour maps of water flow over porous media	29
Figure 2.13	Illustration of airflow patterns over a porous layer . . . . .	30
Figure 2.14	Schematic of representation of the void space in a porous material as pore network . . . . .	31
Figure 2.15	Liquid and gas patterns during drying in a capillary-dominated porous medium . . . . .	35
Figure 2.16	Drying rate as a function of Bond number . . . . .	37
Figure 2.17	Percolation front and drying rate in packings of different bead sizes	38
Figure 2.18	Effects of Sherwood number on the drying rate . . . . .	39
Figure 2.19	Schematic representation of snap-off in a pore . . . . .	40
Figure 2.20	Microstructure of porous asphalt concrete . . . . .	41
Figure 2.21	Evolution of complex moduli of dry and wet PA11 cores . . . . .	42
Figure 2.22	Pore network model of pavements and permeability calculations .	43
Figure 3.1	Specimens used in the uptake experiment . . . . .	50
Figure 3.2	Schematic representation of water uptake experiment setup . . .	53
Figure 3.3	Temporal and spatial variations of the moisture content distribution in VD4-1 during water uptake . . . . .	56
Figure 3.4	Temporal and spatial variations of the moisture content distribution in VD4-2 during water uptake . . . . .	57

Figure 3.5	Temporal and spatial variations of the degree of saturation in VD4-2 during water uptake . . . . .	58
Figure 3.6	Temporal and spatial variations of the degree of saturation in VD4-1 during water uptake . . . . .	59
Figure 3.7	Region of interest chosen for detailed analysis of water uptake in PA	61
Figure 3.8	Analysis of mechanism of water uptake in PA . . . . .	62
Figure 3.9	Liquid flow path analysis of left region of interest in VD4-1 during water uptake . . . . .	65
Figure 3.10	Liquid flow path analysis of right region of interest in VD4-1 during water uptake . . . . .	66
Figure 3.11	Schematic depiction of the specimen used in droplet wetting experiments . . . . .	69
Figure 3.12	Histograms of the pore diameter distribution of the three specimens in the droplet wetting experiments . . . . .	70
Figure 3.13	Segmentation of the pore space connected to the top surface of specimens used in the droplet wetting experiment . . . . .	71
Figure 3.14	Schematic representation of wind tunnel with droplet generator for the droplet wetting experiments . . . . .	74
Figure 3.15	Temporal evolution of moisture profiles in PA during the droplet wetting experiments . . . . .	75
Figure 3.16	Temporal evolution of the degree of saturation in PA during the droplet wetting experiments . . . . .	76
Figure 3.17	Temporal evolution of the degree of saturation in PA11 during droplet wetting . . . . .	77
Figure 3.18	Analysis of gravity imbibition in PA11 during droplet wetting . .	78
Figure 4.1	Photograph and schematic with major dimensions of the mini wind tunnel designed and developed in this study . . . . .	82
Figure 4.2	Description of specimens used in drainage-drying experiments . .	85
Figure 4.3	Schematic representation of the wind tunnel test section with remote-controlled drainage of water . . . . .	87
Figure 4.4	Temporal evolution of average moisture content during drainage-drying experiments . . . . .	89
Figure 4.5	Temporal evolution of moisture profiles during drainage-drying experiments . . . . .	90
Figure 4.6	Temporal evolution of the contribution of different regions of interest towards drainage and drying . . . . .	91
Figure 4.7	Temporal evolution of moisture content distribution in PA8(A) during drying . . . . .	93

Figure 4.8	Temporal evolution of degree of saturation during sudden moisture drop in PA8(A) . . . . .	95
Figure 4.9	The postulated path of water during the sudden drop in moisture content in PA8(A) . . . . .	96
Figure 4.10	Temporal evolution of moisture content distribution in PA8(C) during drying . . . . .	98
Figure 4.11	Temporal evolution of degree of saturation in a region of interest of PA8(C) during liquid redistribution . . . . .	99
Figure 4.12	Temporal evolution of degree of saturation in a region of interest of PA8(C) during liquid redistribution . . . . .	100
Figure 4.13	Overview of the temporal evolution of average moisture loss during the forced convective and thermal drying experiments . . . . .	105
Figure 4.14	Influence of the initial moisture content (type of wetting) on the drying process of PA . . . . .	107
Figure 4.15	Temporal evolution of degree of saturation in PA when wetted by pouring and droplets . . . . .	108
Figure 4.16	Influence of pore sizes on the drying process of PA specimens wetted by pouring . . . . .	110
Figure 4.17	Thresholded images of moisture content distribution during the drying of PA specimens of different pore sizes . . . . .	111
Figure 4.18	Influence of wind speed on the drying process of PA specimens . . . . .	112
Figure 4.19	Influence of gravity-driven drainage on total moisture loss in PA . . . . .	115
Figure 5.1	Photographs and porosity profiles of the specimens used in wind tunnel experiments . . . . .	119
Figure 5.2	Description of the wind tunnel experimental setup . . . . .	121
Figure 5.3	Vertical profiles of mean streamwise velocity above foam and PA . . . . .	123
Figure 5.4	Vertical profiles of mean streamwise velocity, scaled by friction velocity, above foam and PA . . . . .	124
Figure 5.5	Schematic explanation of displacement and momentum thickness . . . . .	126
Figure 5.6	Skewness profiles of streamwise and spanwise velocity components . . . . .	127
Figure 5.7	Profiles of Reynolds stress components without scaling . . . . .	129
Figure 5.8	Profiles of Reynolds stress components in inner scaling . . . . .	129
Figure 5.9	Profiles of Reynolds stress components in outer scaling . . . . .	130
Figure 5.10	Schematic and graphical representations of sweeps and ejections . . . . .	132
Figure 5.11	Q-H analysis on foam board with inner velocity scaling . . . . .	133
Figure 5.12	Q-H analysis on PA8 with inner velocity scaling . . . . .	134
Figure 5.13	Q-H analysis on PA11 with inner velocity scaling . . . . .	134
Figure 5.14	Comparison of ejection and sweep events between foam, PA8 and PA11 . . . . .	135

Figure 6.1	Computational domain and boundary conditions in the CFD simulations . . . . .	141
Figure 6.2	Computational grid of the near-wall region in the CFD simulations	142
Figure 6.3	Comparison of CFD results and analytical expression of convective scalar transfer from a flat plate in a rectangular channel . . . . .	147
Figure 6.4	Integrated convective and diffusive scalar flux for different wind speeds and scalar source levels . . . . .	149
Figure 6.5	Scalar distribution in PA at different wind speeds when scalar source level is at half-depth . . . . .	151
Figure 6.6	Scalar distribution in PA at different wind speeds when scalar source level is at full-depth . . . . .	152
Figure 6.7	Convective and diffusive interface-normal fluxes at the air-material interface as a function of the distance from the leading edge . . .	153
Figure 6.8	Scalar distribution and streamlines of the air flow-field in a cavity pore at the air-PA interface . . . . .	156
Figure 6.9	Scalar distribution and streamlines of the air flow-field in a connected pore at the air-PA interface . . . . .	157
Figure 6.10	Interface-normal scalar fluxes at air-PA interface as a function of the distance from the leading edge . . . . .	158
Figure 7.1	Schematic representation of part of an irregular pore space with a regular pore shape . . . . .	162
Figure 7.2	Schematic representation of arc menisci in an equilateral triangle during two-phase flow . . . . .	163
Figure 7.3	Flowchart of the drying algorithm developed in this study . . . . .	171
Figure 7.4	Schematic of extraction of pore network using the Maximal Ball algorithm . . . . .	173
Figure 7.5	Histograms of pore and throat size distributions of PA11 cubes .	173
Figure 7.6	Cumulative probability plots of pore and throat size distributions fitted with 2-parameter Weibull distribution . . . . .	175
Figure 7.7	Air and water relative permeability as a function of saturation during drainage in PA . . . . .	179
Figure 7.8	Capillary pressure as a function of saturation during drainage in PA	180
Figure 7.9	Experimental and pore network modeling results of normalized moisture loss as a function of time during drying . . . . .	182
Figure 7.10	Comparison of drying rate curves of experiments and pore network model simulations . . . . .	183
Figure 7.11	Checkerboard pattern of drying as simulated by the pore network model . . . . .	186

Figure 7.12	Influence of randomness in the pore network on capillary pressure drying curves . . . . .	188
Figure 7.13	Checkerboard pattern of drainage in the pore network with and without the effect of gravity . . . . .	189
Figure 7.14	Effect of corner films on the simulated drying process using pore network modeling . . . . .	190
Figure 7.15	Influence of increasing the number of dry elements on the drying rate, as simulated using pore network modeling . . . . .	191
Figure 7.16	Computational domain of the continuum simulations . . . . .	195
Figure 7.17	Input parameters to the continuum model . . . . .	195
Figure 7.18	Comparison of experimental, pore network modeling and continuum modeling drying curves of PA . . . . .	198
Figure A.1	Sensitivity study of displacement thickness . . . . .	208
Figure A.2	Sensitivity study of momentum thickness . . . . .	208
Figure A.3	Sensitivity study of shape factor . . . . .	209

## LIST OF TABLES

---

Table 2.1	Commonly used correlations of permeability. . . . .	8
Table 3.1	Material specifications of PA specimens used in the water uptake experiment . . . . .	49
Table 4.1	List of experiments with different wetting and drying conditions .	104
Table 5.1	Aggregate size distributions of the specimens used in wind tunnel experiments . . . . .	118
Table 5.2	Boundary layer parameters calculated in the wind tunnel experiments	125
Table 6.1	Total interface-normal scalar flux measured at different wind speeds and source levels . . . . .	148
Table 7.1	Material and thermodynamic properties used in the continuum modeling simulations . . . . .	196





## INTRODUCTION

---

### 1.1 MOTIVATION

A comprehensive understanding of fluid transport in porous media is of great commercial, environmental and scientific interest. A variety of commercial activities like, to name a few, enhanced oil recovery from seabed reservoirs, drying of paper pulp, water management in polymer electrolyte membrane fuel cells, cooling by porous heat exchangers etc. are directly dependent on the accurate prediction of transport properties in porous media. The durability of several porous materials used in the built environment such as concrete, sandstone, limestone, brick, asphalt etc. is highly dependent on the residence time of water within these materials as water is their main agent of degradation. An accurate modeling of water transport in soil, the most widely occurring natural porous medium, is important for groundwater management and agriculture. Other important porous media flows from an ecological perspective are mobilization of methane in gas hydrates and the storage of CO<sub>2</sub>, nuclear and other hazardous waste in the Earth's subsurface. From a scientific point of view, transport in porous media is a challenging area to understand due to the co-occurrence of many physical, thermal, chemical and biological processes.

In this study, due to the lack of a standard definition in building physics, materials that have pore sizes smaller than 0.1 mm are termed as microporous media while those with pore sizes greater than 0.1 mm are termed as macroporous media. A large amount of experimental, analytical and numerical research has gone into the investigation of transport phenomena in microporous media. Liquid flow in microporous media is primarily driven by capillary forces in the small pores, although other factors such as pressure and thermal gradients, wettability, pore surface roughness etc. can also be driving factors. However, in macroporous media, due to the presence of large pores in the range of millimeters, gravity becomes the most important driving force for liquid transport. Additionally, in large pores, gaseous transport can be enhanced e.g. by convection, and consequently, continuum-scale transport properties such as permeability and capillary pressure curves cannot be calculated in a straightforward manner without assessing the influence of the enhanced vapor diffusion. At the same time, the large pores hinder liquid redistribution within the material. Moreover, pore space characteristics such as pore size distribution, tortuosity, connectivity etc. can influence both the rate of evaporation of the liquid within the material and the subsequent vapor diffusion, although the degree of their influences may be different in microporous and macroporous media.

Most of the research to date has concentrated on microporous media as many porous materials of commercial and natural importance are microporous structures. However, many types of rocks, soils and building materials are macroporous structures and, hence, transport behavior in macroporous media deserves more attention. For instance, in macroporous media, the relative importance of the different liquid and gaseous transport phenomena such as gravity-driven drainage, capillary flow, gaseous diffusion, evaporation and forced convection is expected to be significantly different than what is seen in microporous media. Understanding the individual role of each of these phenomena is key to identifying the factors that influence the residence time of water in such materials.

This study focuses on the investigation of imbibition, drainage and drying in porous asphalt (PA), a macroporous material with a wide range of pore sizes ranging from microns to millimeters. In a strict sense, PA is partly microporous. However, the presence of large pores is what makes PA unique as compared to other porous materials, and therefore, it is classified as a macroporous material in this study. PA is used as the surface layer of roads to allow the seepage of water and thereby prevent aquaplaning and splash-spray effects during and after rain events. PA has a porosity of approximately 20% and is a composite material made from fine and coarse mineral aggregates, a bituminous binder and air voids. Due to its high permeability, a large area of the internal structure of PA is exposed to water after a rain event. After drainage by gravity, a certain amount of water is retained within the structure mainly due to the adhesion of water to bitumen or aggregate, especially at the sharp edges, and the accumulation of water at dead-end pores. Due to the complex and tortuous nature of the pore systems in PA, this retained water can take a very long time to completely exit the specimen even in the presence of wind and solar radiation. This retention of water for a long duration leads to an accelerated deterioration of the material since water is an agent that leads to the loss of adhesion at the bitumen-aggregate interface, a phenomenon called stripping. Therefore, in order to design longer lasting PA pavements, it is imperative to obtain a comprehensive understanding of the residence time of water in PA under typical environmental loadings. Towards this end, the following broad questions have to be addressed: how does water enter and redistribute within PA, how environmental factors influence the removal of moisture from PA and to what extent, what are the time scales of the various liquid and gaseous transport phenomena in PA and how are they influenced by the pore space characteristics of PA. From a modeling perspective, the most important question addressed in this study is whether multiphase transport in PA can be modeled using simplified domains such as pore networks or continuum models and what are the material characteristics that influence the accuracy of such models. By attempting to answer these questions, this study is the first integrated experimental and modeling study on the environmental loading of a macroporous material towards identifying the residence time of water, the main deterioration agent of most porous materials.

By contributing new insights to the transport of air and water in porous media, this work will be directly relevant for testing and designing durable porous building materials that are continuously exposed to the environment. The larger motivation behind this study is to demonstrate how various experimental and modeling techniques, at different material scales, can be combined to obtain a holistic understanding of the various transport phenomena in a highly complex porous media.

This study is within the framework of a Swiss National Science Foundation (SNF) project “Wetting and drying of porous asphalt pavement: a multiscale approach”. The global goal of this project is to develop an integrated multiscale methodology, based on numerical models with experimental validation, to accurately capture the main physics of wetting and drying of PA at the material scale. Such an integrated methodology is intended to be applicable, through a multiscale approach, in road engineering at the pavement scale and in the development and assessment of pavement solutions. Two doctoral students are funded by the project. While this author’s research focuses on the multiscale characterization of PA and on the experimental and numerical investigation of wetting and drying in PA, another student, Soyoun Son, focuses on modeling diverse two-phase flow mechanisms at the pore scale using Lattice Boltzmann Method (LBM).

## 1.2 OBJECTIVES AND METHODOLOGY

With the overall aim of identifying the most important parameters influencing the residence time of water in a macroporous medium exposed to the environment, the specific objectives of this thesis are to firstly identify the specific imbibition, drainage and drying mechanisms in PA using multiscale experiments and simulations, and thereafter to model the observed drainage and drying behaviors of PA at different scales. The boundary conditions and assumptions used in the modeling of drainage and drying in PA are obtained from the results of the experiments and simulations carried out at the first stage.

A typical imbibition process of a porous material exposed to environmental loadings consists of wetting by rain and/or absorption from a wet source in contact with the material. A typical drainage and drying cycle consists of drainage and redistribution driven by gravity and capillary forces, and drying driven mainly by wind and solar radiation. The occurrence of each of these mechanisms in PA is experimentally investigated by subjecting PA to various environmental loadings in laboratory conditions. Neutron radiography (NR) imaging is used to visualize the spatial and temporal distributions of water in PA during these experiments. The three-dimensional pore space of all the PA specimens used in these experiments is characterized by high-resolution X-ray microcomputed tomography (X-ray  $\mu$ -CT). Various pore space characteristics such as pore diameter distribution, connectivity and tortuosity are identified from the 3D images. By carefully combining the moisture content distribution obtained from NR images with the 3D structure of the specimens

obtained from X-ray  $\mu$ -CT images, a deeper understanding of the physics of moisture flow in PA is obtained. The expected outcomes from these experiments are firstly, a macroscopic understanding of which pore space characteristic influences which aspect of the various imbibition, drainage and drying mechanisms and secondly, identifying the key assumptions to be used when multiphase flow in PA is modeled at a later stage.

Consequently, from the NR experiments, a macroscopic picture of the influence of wind speed on drying in PA is obtained. However, further investigations are required to conclusively establish the role of wind. It is known that wind flow above a wet macroporous material can accelerate the drying of the material in two ways. Firstly, the air boundary layer above the air-material interface carries away the evaporated water vapor and thereby enhances the vapor-air diffusion rate at the interface. Secondly, air entrainment into the material through the large pores at the interface may enhance the drying process within the material. To investigate the first phenomenon i.e. boundary layer above the air-PA interface, wind tunnel experiments are carried out on large slabs of PA. Particle imaging velocimetry (PIV) is used to visualize the wind boundary layer as well as the turbulent structures that are active just above the air-PA interface at different wind speeds. To investigate the second phenomenon i.e. possible air entrainment into PA, single-phase computational fluid dynamics (CFD) simulations of airflow above a real PA geometry are performed. Through these simulations, the transport of water vapor within PA during the drying process is investigated at different wind speeds and also without wind. Such an investigation enables a clear identification of the role of wind on the drying process in PA. From a modeling perspective, the CFD simulations will provide information about boundary layer modeling at the air-material interface for a realistic simulation of forced convective drying of PA, by throwing light on the sensitivity of the boundary layer to air entrainment into the specimen.

Having obtained a clear picture of the transport mechanisms that are critical to predict the residence time of water in PA, the next step is to model the drainage and drying behaviors of a fully saturated PA using pore network models, in which the pore space of PA, obtained from X-ray  $\mu$ -CT scans, is converted to an idealized geometry in which the large voids, the pores, are connected to each other by constrictions, the throats. Multiphase flow is modeled in this synthetic geometry to determine macroscale transport properties such as relative permeability curves and capillary pressure curves. The influence of various factors such as gravity and solid matrix wettability on flow in macroporous media is also investigated using pore network models. Finally, macroscale transport properties determined from pore networks are used as inputs for modeling the drying of PA with a continuum approach and the implications of representing a macroporous medium as a continuum are discussed.

In summary, the following outputs are expected at the end of this comprehensive study on PA: (i) a comprehensive understanding of the pore space of a macroporous material, (ii)

identification of the major imbibition, drainage and drying mechanisms in a macroporous material as well as the environmental factors and material properties influencing them, and (iii) modeling of the drainage and drying of a macroporous material exposed to the environment using simplified approaches.

### 1.3 OUTLINE OF THE DISSERTATION

The dissertation is composed of eight chapters. The state of the art is presented in *Chapter 2*, which starts with a discussion of studies investigating the physics of air and water flow in macroporous media. Thereafter, the state of the art of the various modeling approaches used to model heat and mass transfer in macroporous media at different material scales are discussed. An overview of the experimental studies performed specifically on PA is also given. *Chapter 2* concludes by identifying the knowledge gaps in understanding the transport processes that are relevant to macroporous media exposed to the environment.

The next two chapters, *Chapters 3 and 4*, describe the experimental investigations to study the imbibition and drying-cum-drainage processes in PA respectively, using neutron radiography. Specifically, *Chapter 3* focuses on imbibition in PA through capillary uptake and droplet wetting while *Chapter 4* focuses on gravity-driven drainage, forced convective drying and thermal drying in PA. The preparation and characterization of the PA specimens used in the experiments are explained in the description of the respective experiments.

In *Chapter 5*, wind tunnel experiments on airflow above different types of full-scale PA slabs are presented. The important boundary layer parameters near the air-PA interface are calculated and the turbulent structures in the region are analyzed. *Chapter 6* describes the CFD simulations that are performed to analyze the influence of airflow in transporting water vapor generated from evaporation within PA through comparison with cases of pure diffusive transport. In particular, the extent and influence of air entrainment into the material on the overall convection process is analyzed.

Finally, the insights gained from *Chapters 3-6* are used to model multiphase flow in PA using pore network modeling (PNM), which is described in *Chapter 7*. The extraction of pore networks from X-ray  $\mu$ -CT scans is described in detail. Experiments of drying of PA specimens under controlled conditions, performed to assess the capabilities of the PNM drying model and the accuracy of its results, are also presented in *Chapter 7*. *Chapter 7* concludes by describing the results of a continuum approach of modeling drying in PA, the inputs for which are taken from the PNM simulations and their validation experiments. Finally, *Chapter 8* summarizes the main conclusions of this dissertation and lists the important contributions of this work and elaborate future perspectives for research in the areas covered in this thesis.



## STATE OF THE ART

---

### 2.1 INTRODUCTION

The multiscale approach applied in this thesis, and introduced in Chapter 1, consists of investigating transport mechanisms in porous media at the microscale and macroscale, followed by upscaling to a continuum scale using transport properties calculated with pore network modeling. In accordance with the scope of the investigation, this chapter first presents, in Section 2.2, an overview of the most commonly used parameters for quantifying transport in porous media. Thereafter, in Section 2.3, recent investigations that analyze (i) imbibition, (ii) drainage and drying and (iii) airflow above porous media are presented. Wherever applicable, studies specific to porous asphalt are also presented. In Section 2.4, an overview of the various pore network modeling approaches to simulate multiphase flow in porous media, specifically drainage and drying, are presented, followed by a brief review of continuum approaches to model coupled heat and moisture transport in porous materials. Additionally, as the macroporous medium used in this study is porous asphalt, the composition of PA and its hydraulic and mechanical properties are presented in Section 2.5. Finally, in Section 2.6, the existing gaps in understanding multiphase flow in macroporous media in general, and in porous asphalt in particular, are highlighted from both experimental and modeling perspectives.

### 2.2 TRANSPORT PROPERTIES IN POROUS MEDIA

Transport of fluid through connected pores in porous materials is a complex phenomenon influenced by a variety of physical factors and material properties. In principle, flow properties should be accurately predicted by solving heat and mass transport equations based on the actual geometry of the pore space. However, this approach is impractical in most of the cases due to the complexity of a real pore space and the limitations of computational resources. A common way to overcome this difficulty is to consider a porous medium as a macroscopic continuum and determine, mostly via experiments, the volume-averaged transport properties at this scale.

Table 2.1.: Commonly used correlations of permeability  $K$  based on mean pore diameter  $d$  and total volume porosity  $\varepsilon$ 

Correlation	Permeability	Major assumptions
Carman-Kozeny	$K = \frac{d^2}{180} \left( \frac{\varepsilon^2}{(1-\varepsilon)^2} \right)$	Laminar flow (Reynolds number $\approx 1$ )
Brinkman	$K = \frac{d^2}{72} \left( 3 + \frac{3}{1-\varepsilon} - 3\sqrt{\frac{8}{1-\varepsilon} - \varepsilon} \right)$	Densely-packed porous medium
Happel	$K = \frac{d^2}{18} \left( \frac{3-4.5\gamma+4.5\gamma^5-3\gamma^6}{\gamma^3(3+2\gamma^5)} \right)$	Densely-packed porous medium

Permeability, as a continuum scale transport property, is a measure of the ease with which a fluid can pass through a porous medium. The flow inside a porous medium can be described by the Navier-Stokes equation:

$$\frac{d}{dt}(\rho u) + \nabla \cdot (\rho u u) = -\nabla P + \mu \nabla^2 u, \quad (2.1)$$

where  $\rho$  is the fluid density,  $u$  is the velocity,  $P$  is the liquid pressure and  $\mu$  is the dynamic viscosity of the fluid. For stationary, creeping and incompressible flow, the Navier-Stokes equation simplifies to the Stokes equation, which is homogenized to Darcy's law:

$$\langle q \rangle = -\frac{\mathbf{K} \cdot \nabla \langle P \rangle}{\mu}, \quad (2.2)$$

where  $\langle q \rangle$  and  $\langle P \rangle$  are volumetric averages of fluid flux and pressure respectively and  $K$  is the permeability tensor. For a one dimensional case with a pressure gradient only in the z-direction, permeability,  $K$ , is simply defined as:

$$K = u \frac{\mu \Delta z}{\Delta P}. \quad (2.3)$$

Since the exact permeability of most porous media is difficult to determine experimentally or numerically, many empirical correlations have been developed for calculating permeability, the most common of which (Li and Logan 2001) are: the Carman-Kozeny equation (Rogak and Flagan 1990), Brinkman equation (Brinkman 1949) and Happel equation (Happel and Brenner 1983). These equations, along with their major assumptions, are given in (Table 2.1), where  $d$  is the mean pore diameter and  $\varepsilon$  is the total volume porosity of the porous material.

In porous media with two-phase flow, assuming the two phases are flowing macroscopically independent of each other, the relative permeability of each phase is given by:



$$q_w = - \left( \frac{k_{r,w} K}{\mu_w} \right) \frac{dP_w}{dz}, \quad (2.4)$$

$$q_{nw} = - \left( \frac{k_{r,nw} K}{\mu_{nw}} \right) \frac{dP_{nw}}{dz}, \quad (2.5)$$

where  $q$  is the fluid flux,  $k_r$  is the relative permeability and the subscripts  $w$  and  $nw$  indicate the wetting and non-wetting phase respectively. Relative permeability is the ratio of the effective permeability of a phase at a particular two-phase configuration to the absolute permeability of the phase when the system is fully saturated with that particular phase. Despite the wide use of relative permeabilities for characterizing two-phase flow in porous media, this approach has certain disadvantages. As stated before, there is the implicit assumption that the two phases flow independently of each other. In other words, there is no interaction between the two fluids. Although there have been some studies that investigated this fluid-fluid interaction (Adler and Brenner 1988; Gunstensen and Rothman 1993; Olson and Rothman 1997), there is no widely-accepted relative permeability relation that takes into account the same. However, since relative permeability macroscopically represents the permeability of each phase in a wide range of porous media, it is used in this study as well to characterize flow in porous asphalt.

There is an extensive amount of literature on experiments to determine relative permeabilities during two phase and three phase flows in porous media. However, the discussion in this section is limited to the calculation of relative permeabilities during fast gravity-driven drainage in porous media. The method suggested by Watson (1966) is often used to calculate the relative permeability of a wetting phase in a fast gravity-driven drainage experiment:

$$k_{r,w} = \frac{\mu_w}{K \left( \rho_w g - \frac{dP_w}{dz} + \frac{dP_{n,w}}{dz} \right)} u_w. \quad (2.6)$$

However, the actual determination of relative permeabilities during fast drainage experiments presents several challenges due to the difficulty of accurately determining flow velocities and, in case of using imaging experiments for this determination, the low time resolution of images during the drainage stage (DiCarlo et al. 2000; Sahni et al. 1998). For instance, Dehghanpour et al. (2010) measured the spatial and temporal evolution of water saturation degree during gravity drainage along an 80 cm long sand pack of  $D_{50} = 0.25$  mm and average porosity of 0.3. Two dimensional CT scans were obtained with a time resolution of 6 seconds and used to determine water saturation. Their results are shown in Fig. 2.1. It can be seen from Fig. 2.1(a) that even though the water front traverses a distance of 40 cm from the top within 30 minutes, the next 20 cm is traversed across a duration of 4 days. More recently, Kianinejad et al. (2014) carried out similar

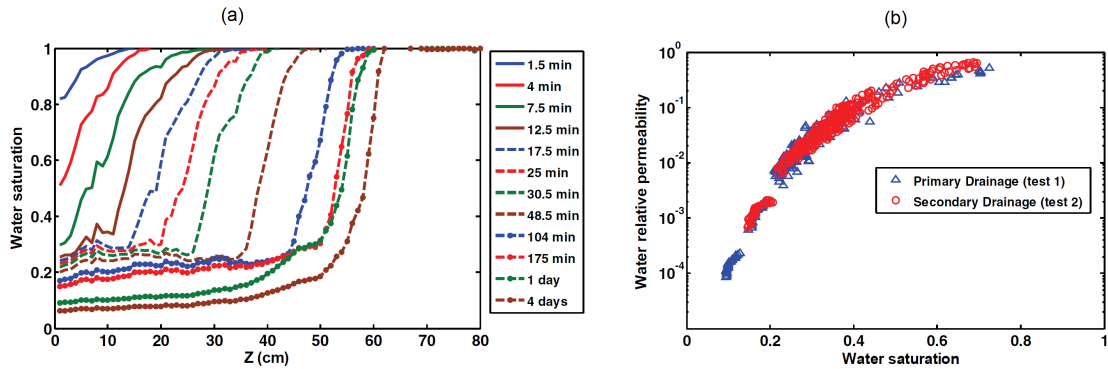


Figure 2.1.: (a) Spatial and temporal evolution of water saturation during air/water primary drainage from a sand pack of  $D_{50} = 0.25$  mm, average porosity = 0.3 and (b) relative permeability of water as a function of saturation during the same experiment i.e. dry initial condition (primary drainage), as well as during wet initial condition (secondary drainage) (Dehghanpour et al. 2010)

experiments on the same experimental setup used by Dehghanpour et al. (2010) with a similar time resolution. Indeed, the foremost challenge to acquiring a 3D visualization of a fast drainage process is the often inadequate time resolution of current 3D imaging techniques. Moreover, although relative permeability curves may accurately represent the ease of fluid flow during drainage in most porous media as shown in Fig. 2.1(b), an open question is whether these curves are also applicable to macroporous media due to the influence of gravity, especially for a fluid like water. For instance, DiCarlo et al. (2000) noted that water saturation was almost constant in space far from the air front during gravity drainage from a sand pack of  $125 \mu\text{m}$  particles. However, in case of macroporous media, there could be strong heterogeneity in liquid distribution during drainage, resulting in disconnected clusters of wetting fluid which would yield a low relative permeability. An additional complexity is to determine the size of a representative elementary volume (REV) for macroporous media. For instance, even though a material like porous asphalt has many pores with sizes larger than 5 mm, the thickness of a typical PA layer, in the direction of gravity, is usually 30 mm. Due to this relatively high pore size to specimen thickness ratio, flow behavior in a smaller region of PA may not be representative of the entire PA layer, which would then make continuum modeling meaningless. Thus, determining relative permeabilities during two-phase flow in macroporous media is an open research question.

## 2.3 INVESTIGATIONS OF FLOW MECHANISMS IN POROUS MEDIA

A variety of fluid flow mechanisms can be observed in porous media exposed to the environment. These mechanisms are mainly influenced by the characteristics of the pore systems, the material and liquid physical properties, and environmental loadings such as air temperature and relative humidity, wind, solar radiation and rain. In this section, the most relevant flow mechanisms in porous media exposed to the environment, namely, water imbibition, water drainage, drying and air flow, are discussed, and the state-of-the-art of investigations analyzing the influence of material characteristics and environmental loadings on these mechanisms is presented.

### 2.3.1 *Imbibition*

Imbibition is the process in which a wetting phase partially or completely displaces a non-wetting phase in a porous medium. In other words, during imbibition, the invading phase is the wetting phase and the defending phase is the non-wetting phase. Due to the dependence of imbibition on several material and fluid properties, the microscopic picture of imbibition in porous media is much more complicated than that of drainage (Oren et al. 1998; Patzek 2001). The two main types of imbibition in porous media are capillary-driven imbibition and gravity-driven imbibition.

#### 2.3.1.1 *Capillary-driven imbibition*

Capillary-driven imbibition is a ubiquitous natural transport phenomenon observed in a wide range of porous materials exposed to the environment. Bell and Cameron (1906) carried out one of the first studies on capillary-driven imbibition and observed a square-root dependency of time for absorption of water into tubes. Lucas (1918) and Washburn (1921) formulated the now widely-used equation which relates the imbibition height or the uptaken mass with the square root of elapsed time. However, the Lucas-Washburn equation in its original form, developed for parallel cylindrical tubes, is applicable only to homogeneous microporous media. For more complex porous media, the dynamics of spontaneous capillary imbibition has been investigated as part of material characterization by several studies lately (Cai and Yu 2011; Cai et al. 2014; Makhanov et al. 2014; Marmur 2003; Mirzaei-Paiaman et al. 2011; Schmid and Geiger 2012). However, in terms of the complexity of the pore space and the range of pore sizes, the porous media used in these studies are very different from PA.

The critical capillary pressure for capillary imbibition in a cylindrical tube is given by the Young-Laplace equation:

$$p_c = \frac{2\gamma \cos \theta}{r_t}, \quad (2.7)$$

where  $p_c$  is the capillary pressure,  $\gamma$  is the surface tension of the wetting fluid,  $\theta$  is the contact angle between the wetting fluid and tube surface and  $r_t$  is the tube radius. However, this equation is valid only for saturated flow i.e. either a wetting or a non-wetting fluid occupies the tube cross-section at a given time. This type of imbibition has also been called as piston-type imbibition. Another type of capillary imbibition that can occur in non-circular capillaries, where the wetting phase fills edges or corners, is snap-off imbibition (Mahmud and Nguyen 2006), where wetting fluid films advance far ahead of the main displacement and ultimately snap off when the films become thick enough, thereby trapping the non-wetting fluid between them. The threshold capillary pressure in case of corner flow is much lower than that of piston-type imbibition (Hughes and Blunt 2000) and is given by:

$$p_c = \frac{2\gamma}{r_t} (\cos \theta - \sin \theta \tan \alpha_c), \quad (2.8)$$

where  $\alpha_c$  is the corner half-angle in case of a regular polygonal pore shape.

Capillary-driven imbibition of water in porous media is strongly influenced by material properties such as porosity, pore size distribution, pore shape, pore space connectivity and tortuosity, roughness of the solid matrix and wettability of the pore walls. From Eqs. (2.7) and (2.8), it can be seen that a larger pore radius results in easier capillary imbibition due to its lower entry pressures. Additionally, frictional forces become less influential as pore sizes become larger. Similarly, a lower tortuosity and higher average porosity also favors capillary imbibition. The relation between pore size, tortuosity, porosity and permeability of the medium can be expressed in terms of the effective pore radius,  $r_{ae}$  (Leverett 1941):

$$r_{ae} = 2\sqrt{\frac{2\tau_t K}{\varepsilon}}, \quad (2.9)$$

where  $\tau_t$  is the tortuosity. From the definition of effective pore radius, it can be clearly seen that the permeability of a medium undergoing capillary imbibition is directly proportional to pore size and average porosity and inversely proportional to tortuosity.

The influence of another material property, surface roughness, on capillary imbibition in non-circular capillary tubes was first studied by Lenormand and Zarcone (1984). They observed that, at low flow rates, liquid flow along the surface roughness and pore corners in glass-etched square capillary tubes was significant enough to influence the formation of liquid clusters in the network. In fact, at extremely low flow rates i.e. at  $Ca < 10^{-9}$  (where  $Ca = \mu u_c / \gamma$  is the capillary number of the network and is a characteristic velocity in the network), flow due to roughness was the most important transport process. The surface

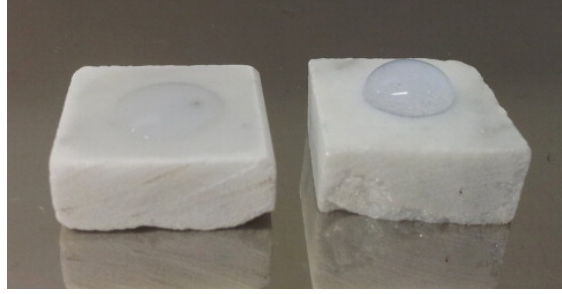


Figure 2.2.: The behavior of water droplets placed on an untreated marble stone (left) and a stone treated with 10 vol-% Capstone FS-63 for 24 h. The picture is taken after a contact time of  $\approx 5$  min (Kronlund et al. 2015)

roughness of their capillary tubes was  $10\ \mu\text{m}$  and  $100\ \mu\text{m}$ . Geistlinger et al. (2015) studied the trapping of non-wetting phase between the wetting phase during capillary imbibition for  $10^{-7} < Ca < 5 \times 10^{-5}$ . They used porous media of different surface roughness. They observed that surface roughness plays an important role in determining the pattern of capillary trapping, especially at low flow rates. In the context of porous media such as asphalt and soil, capillary trapping can be a relevant phenomenon, since wetting during a rain event leads to discrete infiltration paths where air entrapment is likely to occur, and thus can significantly influence the drying behavior of these media.

The wettability of the porous structure can also significantly influence its permeability. Kronlund et al. (2015) investigated capillary absorption of water into hydrophobically treated and untreated marble stones. The untreated marble stone absorbed a water droplet in 2 minutes while the treated stone hardly absorbed any water even after 5 minutes, as can be seen in Fig. 2.2. In a next set of experiments, Kronlund et al. (2015) changed just the top surface of the marbles to hydrophilic through ultraviolet radiation treatment. This was found to significantly improve the absorption rate of water into the samples, even though the hydrophobicity of only a thin layer of the sample was changed. Furthermore, they also observed that the diffusion rate of water vapor through hydrophobic pores is higher than the diffusion rate through hydrophilic pores. Gostick et al. (2009) studied the capillary uptake of water in Toray, a widely-used material in fuel cells. They observed that the capillary pressure required for injecting the same amount of water into the material was significantly higher in case of a sample treated with PTFE, a hydrophobic agent, than in an untreated material. This observation, as shown in Fig. 2.3, is obviously due to the higher resistance from the hydrophobic pores in the treated material.

For a material like porous asphalt, the discussion in this section is very relevant since the material properties of a freshly-made PA, which is composed primarily of hydrophobic bitumen and hydrophilic aggregates, can drastically change with aging, which in turn is

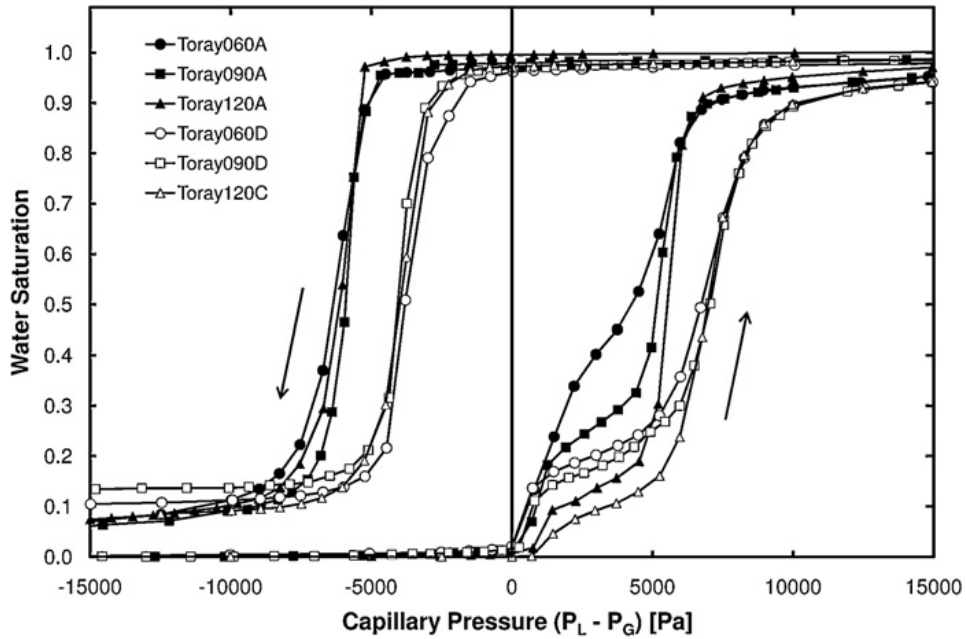


Figure 2.3.: Primary injection and primary withdrawal curves for Toray materials of different thickness with (white markers) and without (black markers) PTFE, a hydrophobic agent. The addition of hydrophobic agent increases the capillary pressure (Gostick et al. 2009)

dependent on a variety of factors like vehicular load, environmental loads (mainly UV) etc. Therefore, parameters such as wettability, pore size distribution, roughness and porosity, and consequently the capillary imbibition behavior of PA, are expected to change with the level of aging.

### 2.3.1.2 Gravity-driven imbibition

Gravity-driven imbibition is yet another ubiquitous phenomenon in geophysics. Early studies of gravity-driven imbibition in porous media were undertaken due to their relevance in oil recovery from fractured reservoirs (Du Prey 1978; Bech et al. 1991). Over time, gravity-driven multiphase flow in porous media became a topic of wide interest due to its importance in soil physics. Although surface roughness has shown some influence on gravity imbibition at near-zero matric potentials (Tokunaga and Wan 1997), the main factors influencing gravity imbibition are pore size, porosity and wettability. However, since the influence of these parameters on gravity imbibition is similar to their influence on capillary imbibition, a further discussion on this influence is avoided in this section. Instead, the focus in this section is on the stability, i.e. the uniformity of the wetting front during gravity imbibition since, in the case of macroporous media, the presence of large pores often lead to instabilities in the gravity imbibition process. This is in contrast to the capillary imbibition process in macroporous media, which is expected to be in the stable region. The stability of the wetting front is an important criterion to analyze the deviation of the imbibition behavior in PA from that in microporous structures.

A schematic of stable and unstable gravity imbibition is given in Fig. 2.4. The Saffman-Taylor criterion (Saffman and Taylor 1958) says that, for gravity-driven displacements, the front is unstable when the flux,  $q_f$ , is less than the saturated permeability,  $g_s$ , of the porous medium:

$$q_f < K_s, \quad (2.10)$$

Here,  $K_s = K\rho_w g/\mu_w$  is the saturated (absolute) permeability expressed as a flux. In case of macroporous media, this criterion is easily satisfied due to the high conductivity of the media as a consequence of the large pores. When a stable wetting front breaks up into many discrete flow paths after becoming unstable, preferential flow paths are created. Gravity-driven preferential flow paths are relevant in areas such as transport of radionuclides in soil (Bundt et al. 2000) and oil recovery through water and gas flooding (Lake 1989). However, observations from (Yoon et al. 2008), who used magnetic resonance imaging (MRI) to investigate water flow through five layers of natural quartz sand fractions, the coarsest of which (Accusand Grade 12/20) had minimum and maximum particle diameters of 0.85 and 1.7 mm respectively, indicate that pore size is not the only criterion to influence stability as even at this large grain size, the effect of gravity on preferential flow was not significant

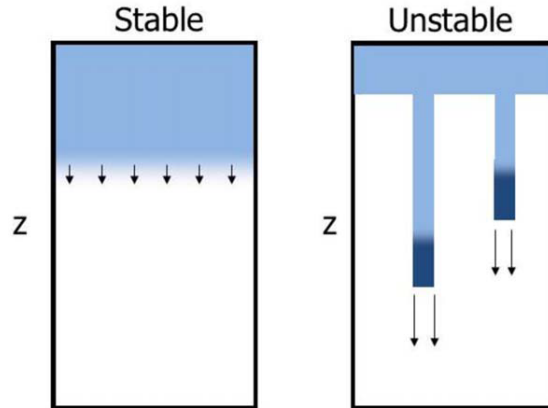


Figure 2.4.: Schematic of a stable (left) and unstable (right) gravity-driven imbibition. (DiCarlo 2013)

and the flow was more or less stable. Indeed, in case of a porous medium like soil, it has been observed that when soil has a sufficient initial water content (Bauters et al. 2000), or if it is sufficiently sandy (with a wide pore size distribution) (Diment and Watson 1985), or if the liquid flux is sufficiently low (Hendrickx and Yao 1996), gravity imbibition is completely stable even if  $q_f < K_s$ . This shows that the Saffman-Taylor stability criterion is a necessary but not the only criterion to predict gravity-driven instability (DiCarlo 2010). Therefore, it is imperative that the stability behavior of gravity-driven flow in a medium is verified experimentally.

Unstable flow was first recorded in field experiments in soil (Parlange and Hill 1976). They concluded that the most unstable wavelength of the water front is larger for fine-textured soils than for coarse-textured soils and is also directly proportional to the initial moisture content. Preferential flow paths of water in soil were clearly observed in later field experiments (Glass et al. 1988; Starr et al. 1978). Incidentally, Glass et al. (1988) was the first to use light transmission to non-destructively image preferential flow in porous media. Similar to the discussion in the previous section, a few studies investigated the influence of hydrophobicity on gravity-driven flows. Bauters et al. (1998) and Ritsema et al. (1996) found that increased hydrophobicity in the soils increased the occurrence of instability. In fact, many soil samples exhibited preferential flow only when they were made fully or partially hydrophobic. Bauters et al. (1998) reported the drying and wetting behaviors of partially hydrophobic soil subjected to gravity-driven imbibition, as shown in Fig. 2.5. The maximum particle size was 0.15 mm. During drying, air entry pressure, which is the maximum pressure potential at which soil begins to desaturate and is determined by the largest pores in the soil, decreased from -7 cm for the hydrophilic sand to -20 cm for all



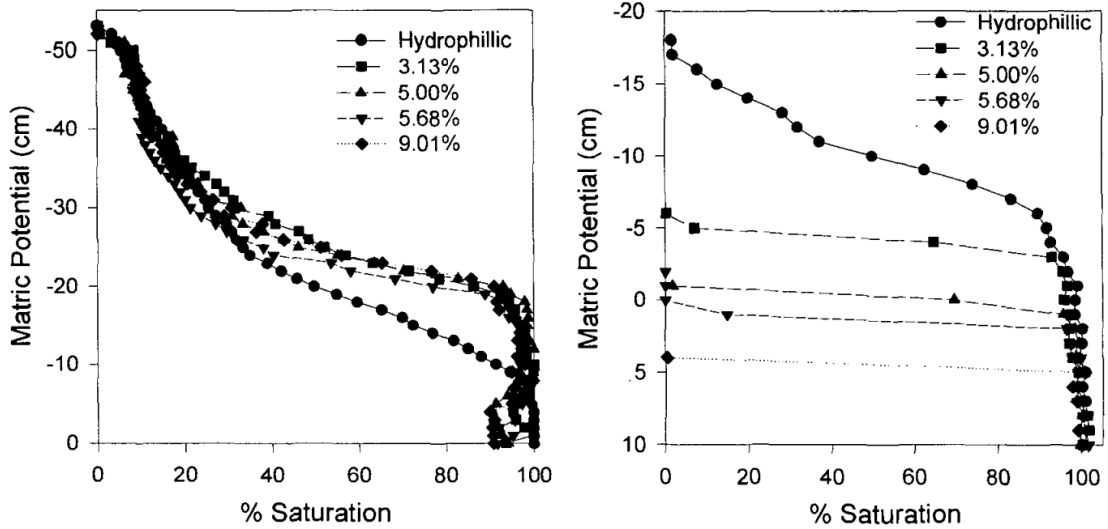


Figure 2.5.: Averaged drying curves (left) and averaged wetting curves (right) of identical sands of maximum particle size 0.15 mm but with different degrees of hydrophobicity. The higher air entry pressure and the lower water entry pressure of hydrophillic sand is clearly evident. (Bauters et al. 1998)

the partially hydrophobic sands. During wetting, water entry pressures increased with increasing hydrophobicity. It is to be noted that in Fig. 2.5, the air entry pressure is defined in terms of the matric potential (capillary pressure).

The discussion so far in this section and the previous one has centered on capillary imbibition and gravity imbibition in porous media through an advancing water front. However, in many industrial and environmental conditions, imbibition also takes place via discrete droplets of wetting fluid. Examples of such discrete capillary and gravity imbibition are inkjet printing and wetting of asphalt and soil by rain respectively. While there has been extensive research on capillary imbibition of discrete droplets in microporous media (Clarke et al. 2002; Denesuk et al. 1993; D’Onofrio et al. 2010; Hapgood et al. 2002; Hilpert and Miller 2001; Hyvaluoma et al. 2006; Jazia et al. 2011; Pack et al. 2015; Reis et al. 2006; Reis Jr et al. 2004; Taghilou and Rahimian 2014; Yiotis et al. 2015), combined capillary and gravity imbibition of discrete droplets in macroporous media has got far less attention, despite the fact that macroporous media may have a wide range of pore sizes that can bring both the forces into play. Specifically, the liquid uptake dynamics in macroporous media is expected to be significantly different to what occurs in microporous media. In fact, the preferential flow paths of droplets deposited on a macroporous substrate are expected to be greatly influenced by gravity. Apart from (Prazak et al. 1992), who investigated droplet penetration into a porous medium made up of 3 mm diameter glass

beads and observed oscillations of macroscopic parameters such as permeability due to strong inhomogeneity in the flow at the microscopic level due to gravity-driven instability, to the best of our knowledge, there is no study of gravitational penetration of droplets in macroporous media.

### 2.3.2 *Drainage and drying in porous media*

Drainage and drying are processes in which a non-wetting phase partially or completely displaces a wetting phase in a porous medium. In other words, during drainage and drying, the invading phase is the non-wetting phase and the defending phase is the wetting phase. A distinct characteristic of drainage and drying processes when compared to imbibition is their lower dependency on material properties but higher dependency on external conditions. For a porous material exposed to environment, the three major drainage and drying mechanisms are gravity-driven drainage, forced convective drying and thermal drying.

#### 2.3.2.1 *Gravity-driven drainage*

Gravity-driven drainage is an important source of moisture loss (or redistribution) in many porous media. Gravity drainage is also the main oil extraction mechanism from fractured reservoirs (Moghaddam and Rasaei 2015). Gravity drainage in porous media is dependent largely on the pore size distribution of the material and to a lesser extent on the wettability of the material and connectivity of the pore space, all of which ultimately determine the contribution of gravity-driven drainage to the total moisture loss from the entire material. Most of the early gravity-driven drainage experiments in porous media were driven by the role of such drainage in oil extraction. Terwilliger et al. (1951) developed a method to determine the performance of a linear homogenous gravity drainage system by separately measuring fluid and rock characteristics in the laboratory. They calculated the time evolution of saturation distribution by keeping the time step very small while  $(\partial f_g / \partial S_g)$  was changed rapidly, where  $f_g$  is the gas flow rate fraction and  $S_g$  is the gas saturation. Their model was validated with experiments on an unconsolidated sand column which was filled with sand of maximum diameter 0.074 mm and was 13 feet long in the direction of gravity. Column drainage experiments continued to be carried out with a variety of sand particles such as Day and Luthin (1956) [OSO Flaco fine sand], Liakopoulos (1964) [Del Monte fine sand], Watson (1967) [Botany sand] and Prill et al. (1965) [Fresno medium sand]. In the experiments of Yang and K. Yanful (2002), it was observed that while the coarse sand ( $D_{10} = 0.9$  mm) lost water by both drainage and evaporation, the fine sand

( $D_{10} = 0.16$  mm) did not exhibit any drainage. This competition between capillary forces and gravity at the pore scale is represented by the dimensionless Bond number,  $Bo$ :

$$Bo = \frac{\Delta\rho g d^2}{\gamma}, \quad (2.11)$$

where  $\Delta\rho$  is the density difference between the two fluids and  $d$  is the pore diameter. If  $Bo \gg 1$ , gravity dominates and acts as a stabilizing force for drainage by reducing height differences induced by viscous instability or capillary fluctuations, hence flattening the front (Chau and Or 2006). For an air-water system at room temperature, for the condition to be satisfied, it follows that the pore diameters should be at least 2.7 mm. Although there are some studies on cases in which capillary, viscous and gravity effects are all prominent (Méheust et al. 2002; Or 2008; Grattoni et al. 2001), only a few experiments in which gravity drainage is dominant are reported in literature.

One such study was carried out by Prazak et al. (1992). In their experiments, droplets of water were deposited in a porous media of glass beads of 3 mm diameter, and the time-dependent outflow rate of water from the medium was then monitored. The initial moisture content of the medium was changed to see its effect on the outflow rate. The type of inflow was also changed from one point to multiple points distributed over the inflow surface. The outflow from an initially dry medium showed a pronounced time evolution in contrast to the outflow from the initially wet medium. The pattern of outflow when the inflow was distributed across the surface was completely different from those of single-point inflow in that for the former case, a period of high initial discharge is followed by a period of consistently low discharge. These observations were explained by predicting the clustering behavior, due to capillary forces, of the wetting phase inside the medium after visualizing the clustering behavior in a similar experiment with two-dimensional glass micromodels.

Other researchers have also used micromodels to visualize gravity drainage in porous media. Mashayekhizadeh et al. (2011) performed oil drainage experiments on a micromodel with a fracture apertures of 1 mm, pore width of 1 mm and throat width of 350  $\mu\text{m}$ . Two identical blocks of the micromodel were stacked on top of each other with a small gap in between them to simulate the effect of a fracture. They determined the drainage flow rate versus time using the derivative of a fitted curve for recovery factor,  $R$ , where  $R = 1 - S$ , and  $S$  is the saturation. Additionally, they also tracked the gas-oil front during drainage which lasted for 400 minutes. The front movement in the upper and lower parts of the micromodel during the first 160 minutes, measured at 20 minute intervals, as well as the final front position after 400 minutes, is given in the right column of Fig. 2.6 while the left column shows the photograph of the oil distribution in the upper and lower parts after 400 minutes of drainage. The formation of a liquid bridge in the aperture at the bottom of the upper block increased the drainage from the upper block due to capillary continuity,

an observation which was analyzed in more detail in a later study Mashayekhizadeh et al. (2012). Capillary continuity increases the height of a liquid cluster and therefore makes the gravity drainage processes stronger due to a higher static pressure. The influence of capillary continuity on free fall gravity drainage (FFGD) in unconsolidated macromodels was studied by Zendehboudi and Chatzis (2011). They used three types of glass beads as porous media, with mean diameters of 0.5, 0.7 and 1.1 mm. They proposed an empirical correlation to predict the saturation level as a function of Bond number,  $Bo$ :

$$R = 1 - S = \begin{cases} (1 + 0.0111 \ln(Bo)) \cdot \left(\frac{L_{eff}}{L}\right)^{1.11} + \frac{\varepsilon_f}{\varepsilon_e}, & L_{eff} > 0 \\ \frac{\varepsilon_f}{\varepsilon_e}, & L_{eff} \leq 0 \end{cases} \quad (2.12)$$

where  $L$  is the height of the network,  $L_{eff} = L - h_c$  where  $h_c$  is the capillary threshold height i.e. the height of the liquid column at which air can enter the pore,  $\varepsilon_f$  is the fracture porosity and  $\varepsilon_e$  is the effective porosity of the medium. In case of gravity drainage in macroporous media, the influence of capillary continuity is an open question, especially its influence on the drainage of residual liquid in smaller pores after the first phase of fast drainage from larger pores is completed.

There are only a few experiments reported on gravity drainage in porous asphalt. Tan et al. (2004) studied the influence of PA road geometry and slope on drainage properties of PA. Poulidakos et al. (2013a) performed gravity drainage experiments on aged and new PA11 specimens, which were fully saturated at the beginning of the experiments. PA11 specimens have a maximum aggregate size of 11 mm. The spatial and time evolutions of moisture content distribution in the specimens was visualized with neutron radiography, as shown in Fig. 2.7. In this figure, moisture loss from a fully wet, aged PA specimen is clearly visualized since those pores that went from above to below 30% degree of saturation in one time interval are marked in black, while those pores which remain wet are in grey. The white regions indicate the presence of impermeable aggregates. The importance of gravity drainage in PA11 specimens was clearly evident from the experiments as the specimens lost moisture in a top-down gradient. During the latter part of the experiment, most of the moisture loss is from the bottom as the top part already lost most of its initial moisture content due to the high static pressure head. However, the specimen size of  $28 \times 47 \times 10 \text{ mm}^3$  was too small to draw any general conclusions.

### 2.3.2.2 *Forced convective drying*

Although gravity-driven drainage is expected to be the most important water loss mechanism in PA, the contribution of forced convective drying near the top surface to the overall moisture loss will be non-negligible. Drying of water from porous media is a coupled heat

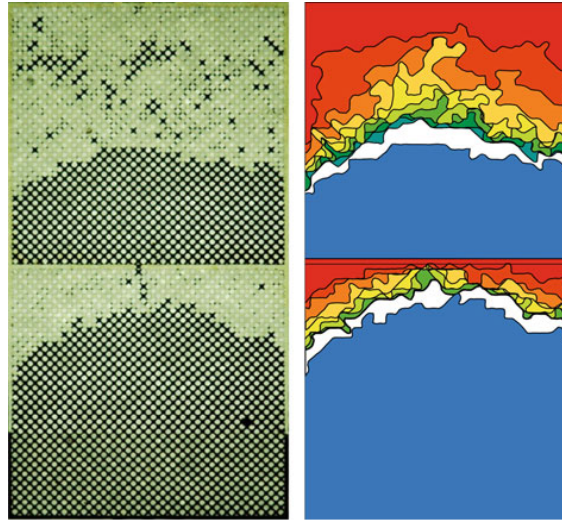


Figure 2.6.: Photographs of oil saturation in the upper and lower blocks of a micromodel, with a gap of 1 mm separating the two blocks, at the end of drainage (left) and superimposed successive images of gas–oil fronts in micromodel at 20 min time intervals (right). Due to capillary continuity effect in the upper block, the drainage from the upper block is faster than that from the lower block. (Mashayekhizadeh et al. 2011)

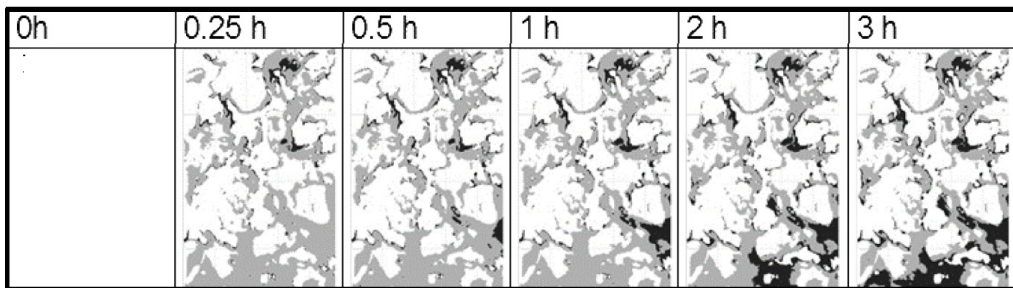


Figure 2.7.: Temporal and spatial distribution of segmented saturation degree of aged PA. The grey background shows all the pores with an initial saturation degree above 30%, while black represents pores that went from above to below 30% saturation degree in one time interval. Moisture loss displays a top-down gradient due to the influence of gravity. (Poulikakos et al. 2013a)

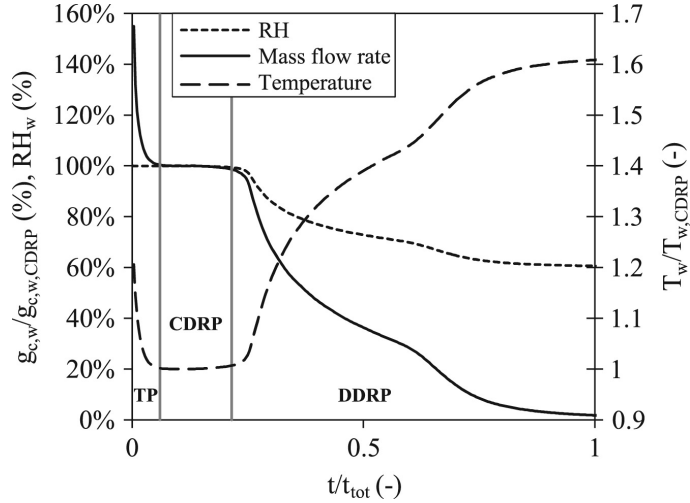


Figure 2.8.: Typical drying rate  $g_{v,w}$ , surface temperature  $T_w$  and relative humidity at the surface  $RH_w$  of a porous material during drying, as a function of dimensionless time  $t/t_{tot}$ . The different drying periods are indicated. For  $g_{v,w}$  and  $T_w$ , scaling is performed using the values during the CDRP (temperatures are in °C). The time is scaled with the total simulation time  $t_{tot}$ . (Defraeye et al. 2012)

and mass transfer process driven mainly by atmospheric conditions as well as the hydraulic conductance and vapor diffusivity of the material. Early experimental investigations of heat transfer (Amiri et al. 1995; Vafai et al. 1985) and mass transfer (Geller and Hunt 1993; Genuchten and Wierenga 1977) in microporous media gave many insights into the transport phenomena present at both Darcy and larger scales. A typical drying process in a porous material is depicted in Fig. 2.8, where after an initial transition period (TP), the material experiences a constant drying rate period (CDRP) in which temperature, relative humidity (RH) and mass flow rate at the air-material interface remain constant, followed by a decreasing drying rate period (DDRP) in which the relative humidity and mass flow rate goes down while the temperature goes up. During the CDRP, there is a constant supply of liquid from the interior of a material to its drying surface, as can be seen by the constant RH levels at the surface in Fig. 2.8. During this period, the outgoing vapor flux is equal to the incoming liquid flux at the surface. However, this condition is sustained only until there is hydraulic connectivity of the liquid within the porous medium, where after the DDRP begins. Since hydraulic connectivity of liquid within a macroporous material is expected to be very weak, it has to be investigated if the typical drying rate curve shown in Fig. 2.8 is applicable to macroporous media.

Forced convective heat and mass transfer has also been studied for different porosity scales, ranging from microporous media (James et al. 2010) to highly porous macroporous

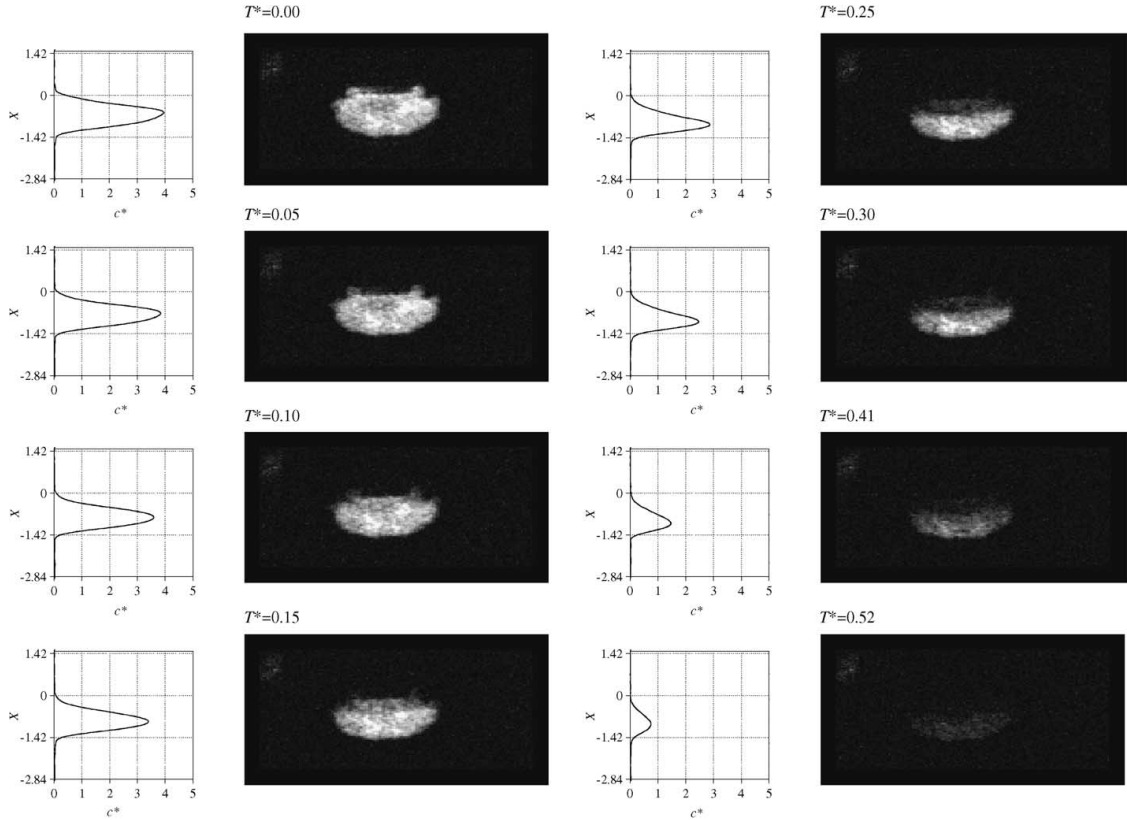


Figure 2.9.: Time evolution of the concentration profiles of liquid and images of the shape of the droplet inside a porous substrate of  $120 \mu\text{m}$  glass beads subjected to airflow at a rate of  $10 \text{ ml/min}$  (Reis et al. 2006)

media (Calmidi and Mahajan 2000) to variable-porosity media (Vafai 1984). In case of a porous medium with pore sizes  $< 1 \text{ mm}$  undergoing drying in typical natural air flow conditions (mean wind speed  $< 4 \text{ m/s}$ ), Haghghi et al. (2013) concluded that considering only diffusion from individual pores across a constant boundary layer accounts for most of the evaporation predicted by the full advection-diffusion equation. However, the relative contributions of diffusion and advection to the total moisture loss from a porous medium that is dominated by pore sizes larger than  $1 \text{ mm}$  have not been explored yet.

More recently, efforts have been made to combine the investigations on wetting and drying in porous media. Reis et al. (2003) was the first to investigate droplet penetration into porous media and subsequent drying by forced convection. The porous media in their study were sand particles of  $180 \mu\text{m}$  and glass beads of  $50, 120$  and  $400 \mu\text{m}$ . For sand particles, they found that capillary diffusion of water to the top surface played an

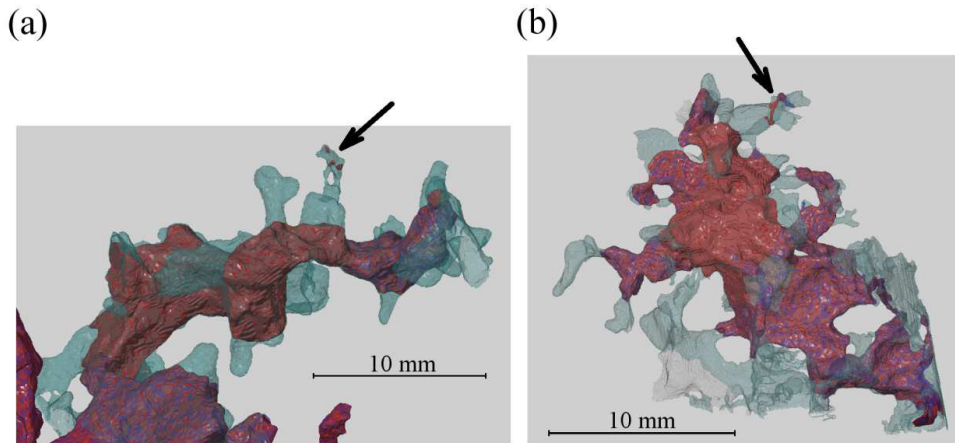


Figure 2.10.: Porous asphalt pores filled with air (transparent green) and with water at time 11.41 h (red) and 15.27 h (blue). (a) Site of first sudden water loss, (b) site of second sudden water loss. The arrows indicate the location of the water islands. (Jerjen et al. 2015)

important role in the evaporation process. Shahidzadeh-Bonn et al. (2006) studied droplet wetting and subsequent evaporation from a porous surface but their focus was restricted to finding a correlation between the droplet radius on the surface and elapsed time. In other words, their observations were restricted to the surface of the porous material. Reis et al. (2006) investigated droplet penetration into porous media and subsequent drying by forced convection at different airflow speeds. They embedded a single diethyl-malonate (DEM) droplet of 2.3 mm diameter into a porous substrate consisting of 120  $\mu\text{m}$  glass beads. Time evolutions of one-dimensional moisture concentration profiles and moisture content distribution within the porous substrate were then monitored for different airflow speeds. In Fig. 2.9, the time evolution of moisture profiles at an airflow of 10 ml/min is given. They concluded that although liquid expectedly evaporated faster at higher airflow speeds, the vapor diffusion resistance of the porous medium was very high. However, it needs to be investigated if the resistance to vapor diffusion is strong in the case of macroporous media where significant momentum transfer from air penetration into the medium can be expected.

Poulikakos et al. (2013b) was the first to carry out investigations of forced convective drying in porous asphalt. They investigated the drying behaviors of new and aged PA11 specimens in a micro wind tunnel at a wind speed of 2.4 m/s. Drainage was completely blocked. From two-dimensional neutron radiography images of the drying process, they postulated that drying was relatively faster as long as water was distributed within the specimen in a well-connected configuration. Even after 8 hours of convective drying, the



specimens were still wet. Jerjen et al. (2015) investigated water evaporation rate from a 30 mm diameter PA8 core of height 67 mm, using X-ray micro computed tomography (X-ray  $\mu$ -CT). 26 three-dimensional X-ray  $\mu$ -CT scans were obtained over a duration of 57 hours. Their study was the first instance of three-dimensional visualization of moisture distribution in PA. They observed sudden drops of the total water content in PA due to accelerated moisture loss at two sites, as shown in Fig. 2.10. According to them, water islands at these two sites prevented the evaporation of water in the pore below them and once those islands dried, evaporation accelerated locally. The complex drying mechanism of PA was effectively brought out by their experiments.

### 2.3.2.3 *Thermal drying*

Thermal drying of porous media is of considerable importance in materials exposed to the environment as well as in the preserved food industry. In general, thermal drying can be induced either by direct solar radiation or by blowing hot air on top of a porous material. A good review of the various applications of both these types of drying and the different modeling approaches to take them into account is given by Belessiotis and Delyannis (2011). From the point of view of natural drying of porous materials exposed to the environment, mainly the drying from direct solar radiation is important. On one hand, solar radiation can accelerate drying by providing the latent heat required for evaporation while on the other, thermal gradients induced by solar radiation can facilitate redistribution of water from the pores to the surface. An interesting phenomenon is that a positive thermal gradient enhances vapor transport and opposes liquid transport. Philip and De Vries (1957) pioneered the study of moisture flow in porous media under the influence of thermal gradients. Since then, various experimental and numerical studies (Grifoll et al. 2005; Huinink et al. 2002; Plourde and Prat 2003; Surasani et al. 2008; Wang et al. 2011) have been carried out to better understand the coupling between heat and mass transfer at the liquid-gas interface through temperature-dependent equilibrium vapor pressure, surface tension and phase change enthalpy (Surasani et al. 2008).

In an experimental study conducted near Tokyo, Japan, Asaeda and Ca (2000) investigated the evolution of temperature in different types of building materials and in the soil beneath them, as shown in Fig. 2.11. They observed that when the air temperature was 35 °C at noon, the surface temperature of porous asphalt was close to 50 °C due to the high solar radiation absorption of PA. They recorded a positive temperature gradient of approximately 7 °C between the PA surface and a depth of 6 cm. At midnight, a negative gradient of 5 °C was recorded since considerable heat was stored in the material. At the two other observation times, 06:00 and 18:00, the gradients were not so pronounced. It is worth mentioning that these measurements were observed on a typical hot summer day. A similar investigation that explored the thermal behavior of PA on a hot summer was

carried out by Stempihar et al. (2012). Both these studies, however, focused on the effect of PA on the urban heat island effect and were as such not interested in the temperature gradients in PA during or immediately after a large event.

It is to be noted that during and immediately after a large rain event, which is when the drying of PA assumes significance, the temperature gradients in PA will be far less pronounced due to absence of solar radiation and the temperature of the rain water. However, solar radiation may play a role afterwards if the region receives significant solar radiation. Moreover, in macroporous media with pore sizes large enough for gravity to dominate over capillary force, it remains to be seen how a positive or a negative temperature gradient influences the liquid redistribution and drying processes. Yet another open question is whether thermal gradients develop due to evaporative cooling in a wet PA layer undergoing drying, even in the absence of any external heat source, in which case it needs to be investigated if such gradients would be large enough to influence the drying process.

### 2.3.3 *Turbulent airflow above porous media*

Turbulent airflow over porous media can be observed in a variety of materials ranging from those that are exposed to airflow in the atmosphere, such as bricks, concrete, soil, rocks, asphalt etc., to those that are subjected to forced airflow in industrial drying processes, such as fruits, paper pulp, wood etc. On comparing the convective drying behaviors of microporous and macroporous media, it can be seen that while drying of microporous media is accelerated by the enhanced air-water vapor mixing near the air-material interface due to turbulence induced by the porosity at the air-material interface, drying in macroporous media has the additional contribution from air penetration into the macro-pores connected to the surface. The first phenomena, i.e. turbulence in the near-wall region of rough surfaces, has been experimentally and numerically investigated by considering a combined free flow-porous media domain (Agelinchaab et al. 2006; Arthur et al. 2009; Liu et al. 2013; Narasimhan et al. 2014; Prinos et al. 2003). The second phenomenon, i.e. fluid penetration into macro-porous media, has been studied using refractive-index matching techniques (Northrup et al. 1991; Saleh et al. 1992). A different but related effect is flow-through drying (Iida et al. 2014; Mahadevan et al. 2006) in which a gas phase injected into a wet porous medium immiscibly displaces the liquid, followed by the evaporation of the liquid into the gas phase. A macroporous material, due to the considerable air penetration into its internal structure, is expected to display a complex drying process resulting from the interaction of all the aforementioned mechanisms. Nevertheless, it can be asserted that the air boundary layer near the air-porous asphalt interface will play an important role in the overall drying process.

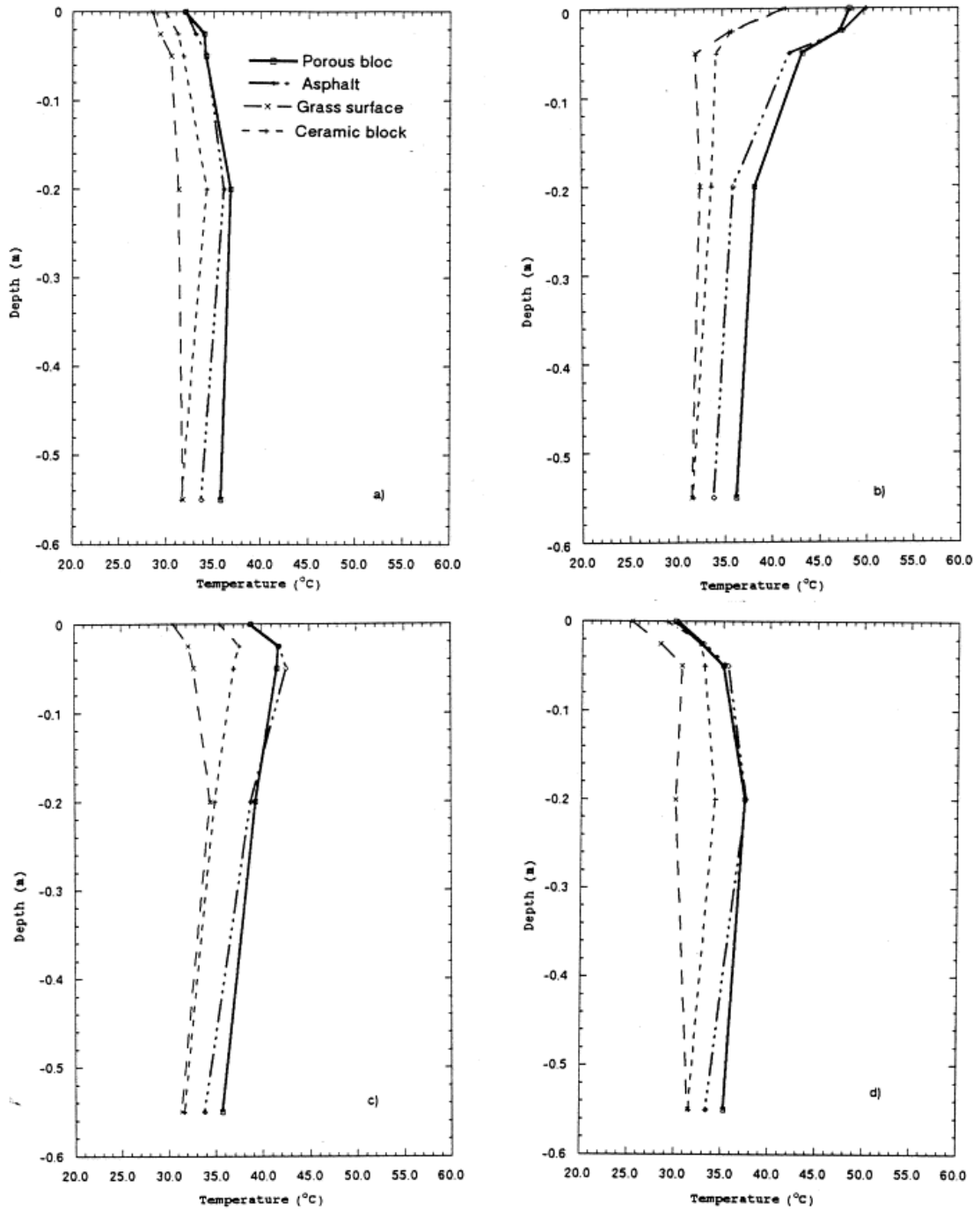


Figure 2.11.: Vertical temperature distributions underneath the surface of different types of building materials exposed to the environment, at various times of the day: (a) 06:00 h; (b) 12:00 h; (c) 18:00 h; (d) 00:00 h. It is to be noted that 'Porous bloc' is the material closest to porous asphalt. (Asaeda and Ca 2000)

Boundary layers over porous surfaces tend to be more turbulent than those above impermeable rough surfaces (Zippe and Graf 1983). Therefore, analyzing the turbulent boundary layer above PA is relevant in the context of studying convective drying of PA by wind. Turbulent wind boundary layers over rough surfaces have been extensively studied in the past (Raupach et al. 1991; Schlichting and Gersten 2000; Townsend 1976). From these studies, it was found that the structure of the turbulent boundary layer primarily depends on the air speed and surface roughness. However, turbulence structures in the near-wall region and the effects of porous structures on turbulence are still not well understood (Iida et al. 2014). Recent studies towards this end have been carried out by Iida et al. (2014), Suga et al. (2013), and Suga and Kuwata (2014). Iida et al. (2014) carried out water flow experiments using Particle Image Velocimetry (PIV) on two types of porous media, type A and type B, with similar porosity (0.8) and absolute permeability ( $\approx 0.4 \text{ mm}^2$ ) and different mean pore diameters (8 and 12 mm). The Reynolds number based on the hydraulic diameter of the channel was 3600. From the PIV images, particularly Fig. 2.12(c), it was observed that a larger streamwise permeability of the porous media leads to larger streamwise mean velocities of water inside the porous media while a larger mean pore diameter, and a higher absolute permeability value, leads to a higher level of turbulence near the water-porous media interface.

Suga et al. (2013) conducted airflow experiments above different porous media after mounting a square rib in the fully developed channel flow. They used both solid and porous rib for the experiments. The porous media were three types of foamed ceramics of similar porosities (0.8) but with different mean pore diameters of 1.7, 2.8 and 3.8 mm and different permeabilities with values, normalized by the rib height, of  $0.89 \times 10^{-4}$ ,  $1.47 \times 10^{-4}$  and  $3.87 \times 10^{-4}$ . At all tested wind speeds and with both types of ribs, they observed significant air penetration into the porous media, as can be seen in Fig. 2.13, where airflow patterns as deduced from experiments and visualized with PIV are shown for the different cases. However, these studies considered either simplified porous media (using ribs or tubes) or restricted the fluid flow region to narrow channels, for analyzing the effect of those flows on the heat and/or momentum transfers in catalyst surfaces, heat exchangers and fuel cells. Full-scale investigations of airflow above large porous media such as soil and asphalt have not yet been published, to the best of our knowledge, despite the application of wind tunnels to study phenomena such as soil erosion (Gabriels et al. 1997; Gillette 1978). It should be noted that although the general velocity field near large structures can be captured by scaled-down wind tunnel experiment using Reynolds analogy, several flow characteristics are not proportional to the size of the model and thus cannot be extrapolated directly from such experiments (Liu et al. 2014). Although Poulidakos et al. (2013b) carried out smoke tests on PA at a mean wind speed of 1.2 m/s and observed some penetration of smoke into the internal structure of PA, their specimen size of  $28 \times 47 \times 10 \text{ mm}^3$  was again too small to draw general conclusions.

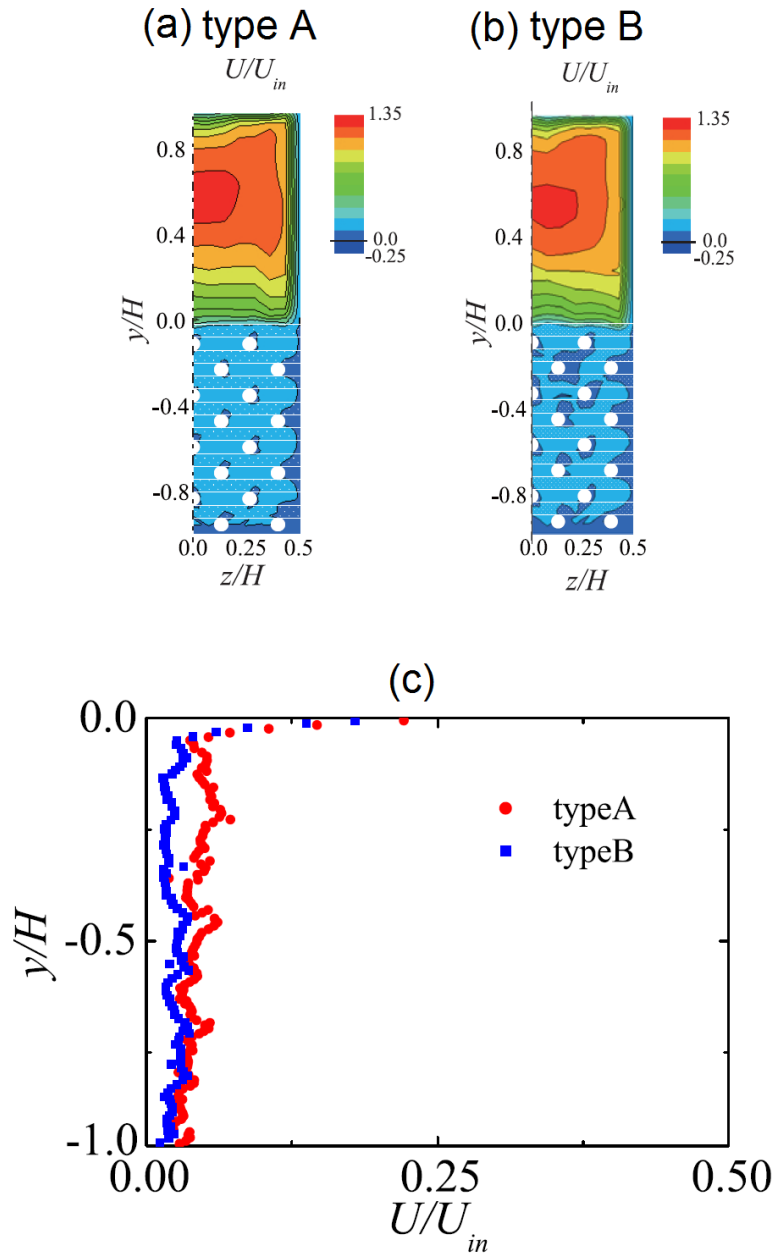


Figure 2.12.: Streamwise velocity contour maps of water flow over two types of porous media, (a) type A and (b) type B, having mean pore diameters of 8 and 12 mm respectively, and (c) streamwise mean velocities inside the two types of porous media. (Iida et al. 2014)

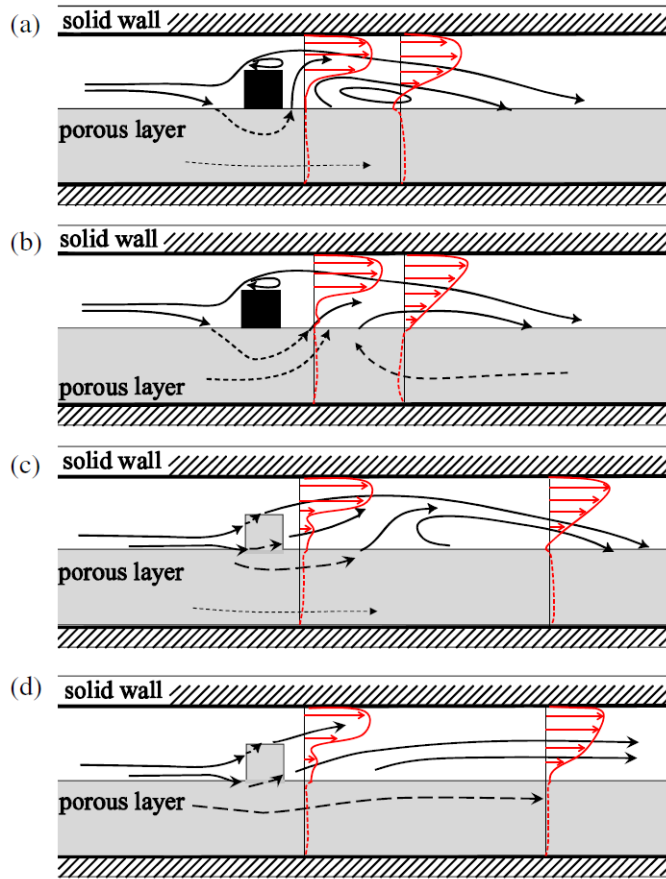


Figure 2.13.: Illustration of airflow patterns, as deduced from experiments, over a porous layer after mounting a rib in the upstream section; (a) solid rib flow, (b) solid rib flow at higher porous layer permeability or higher  $Re_b$ , (c) porous rib flow and (d) porous rib flow at porous layer permeability. (Suga et al. 2013)

## 2.4 NUMERICAL MODELING OF MULTIPHASE FLOW IN POROUS MEDIA

Multiphase flow at the pore scale has been modeled using various approaches such as pore network models, Lattice-Boltzmann simulations, mesh-based computational fluid dynamics simulations with fluid-fluid interface tracking and mesh-free, particle-based Lagrangian methods. In this research (see Chapter 7), pore network models are used to study multiphase flow in porous asphalt, mainly due to its computational efficiency when dealing with a highly complex pore space like PA. Specifically, pore network modeling is used to model drainage from a fully-saturated PA specimen, followed by evaporative drying. Therefore, in this section, the state-of-the-art of pore network models used to simulate two-phase drainage and drying in porous media is presented.

2.4.1 *Modeling multiphase flow with pore network modeling*

Pore network models (PNM) are based on the representation of the void space in a material as a network of wide pores connected to each other by narrow throats, a schematic of which is shown in Fig. 2.14. The main geometric characteristics of a pore network are the shapes of its pores and throats, the diameters of the pores and throats and the connectivity of the pores. The diameters and coordination number often follow a distribution law to take into account the wide range of values of these parameters in a typical pore space. A sensitivity study of various simulation parameters, among them the simplified pore shape assumed for simulations, on the modeling of drying using pore networks is given by Prat (2007), where it is found that pore shape has an influence on the drying rate when film flows are considered. In Fig. 2.14, the irregular topology of the real pore space is converted to a regular pore space, as is often done in many studies. This approach is justified as several essential properties are independent of the exact topology or orientation of the pore space (Stauffer and Aharony 1992).

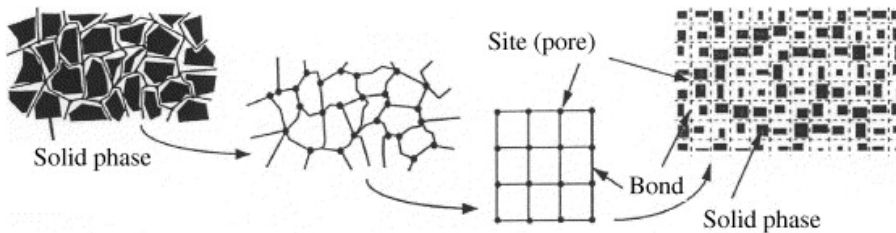


Figure 2.14.: Schematic of representation of the void space in a porous material as a network of sites (pores) connected to each other by bonds (throats). (Prat 2002)

Multiphase flow in porous media was first represented using pore networks by Fatt (1956). Since then, several researchers have used PNM to study various flow mechanisms such as drainage (Blunt et al. 1992; Lenormand 1988; Sahni et al. 1998), imbibition (Joekar Niasar et al. 2009; Hughes and Blunt 2000; Patzek 2001), drying (Laurindo and Prat 1998; Prat 2002; Yiotis et al. 2015), as well as for practical applications such as modeling of solute transport in soil (Vogel 2000) and fluid transport in the gas diffusion layer of fuel cells (Gostick et al. 2007). In PNM, essentially pore-scale equations are solved in the given domain of pores and throats. Some researchers have used PNM at the REV scale to calculate basic parameters such as relative permeability and capillary pressure as a function of saturation (Daian and Saliba 1991; Nowicki et al. 1992). However, the discussion in this section will be on the application of PNM to the next scale i.e. product scale or material scale (Prat 1993). PNM at the product scale can be classified into two major streams: quasi-static PNM and dynamic PNM. Quasi-static PNM simulates the equilibrium states during flow processes; for instance, step changes in global pressure differences are applied during drainage to go from one equilibrium state to another. Information on the flow between the equilibrium states is not obtained. On the other hand, in dynamic PNM, the transient behavior of liquid at the pore scale is studied by determining the local viscous, capillary and gravitational forces. However, dynamic PNMs are extremely computationally intensive, thereby negating to an extent the advantage of using PNM in the first place. Besides, quasi-static PNM has been used to successfully predict capillary pressure and relative permeability as a function of saturation during drainage and imbibition (Blunt et al. 2002; Carmeliet et al. 1999; Oren et al. 1998; Vandersteen et al. 2003). Therefore, quasi-static PNM is also used in this study to determine transport properties of PA during drainage and drying.

To have a representative pore network model capable of accurately predicting transport properties, it is essential to translate the information from the complex pore space topology to a pore network accurately. For this purpose, imaging techniques such as X-ray microtomography (Al-Raoush and Willson 2005; Knackstedt et al. 2013; Wildenschild et al. 2002), laser confocal microscopy (Fredrich et al. 1993; Montoto 1995), serial sectioning imaging (Vogel 1997) etc. are often used. Pore network extraction algorithms such as the maximal ball algorithm (Dong and Blunt 2009) or the medial axis-based algorithm (Lindquist and Lee 1996) are often used to convert the 3D pore space to a pore network. The conversion can be done in two ways: either by statistically capturing the size distributions and connectivity of the pores and throats and thereafter applying it to a structured pore network (Gostick et al. 2007), or by capturing the exact topology of the pores and throats, including the orientation, position and connectivity (Joekar Niasar et al. 2009).



### 2.4.1.1 *Modeling drainage with pore network modeling*

Drainage in PNM is often simulated as a percolation problem. Percolation phenomenon in a porous medium refers to the properties that emerge at the onset of macroscopic fluid connectivity within the medium. This application of percolation theory to simulate drainage is known as invasion percolation (IP), with air as the invading phase and water as the defending phase. During IP, the invading phase must be connected to the inlet to continue the invasion while the defending fluid must be connected to the outlet to continue to be displaced. In the IP algorithm, the key parameter that determines the ranking of the throats to be invaded is the throat entry capillary pressure at quasi-equilibrium. The early models of IP (Chandler and Koplik 1982; Lenormand 1988; Wilkinson and Willemsen 1983) were used to simulate slow drainage in porous media, usually capillary displacement of water by air. Over the years, the original IP model (Wilkinson and Willemsen 1983) has been modified to include several additional features. Meakin et al. (1992) included the effect of gravity in the classical IP algorithm. In a system with large clusters of liquid, which leads to a high hydrostatic pressure in some pores, capillary forces can be dominant at the shorter length scales while gravity can be dominant at the longer length scales (Meakin et al. 2000). Meakin et al. (1992) observed that for gravity-destabilized drainage, the displacement pattern pointed to a fractal invasion percolation structure at short length scales ( $\ll \xi$ ), while at the longer length scales ( $\gg \xi$ ), the pattern was a directed percolation, where  $\xi \sim |Bo|^{-\eta}$  is the critical length scale,  $\eta = \nu/(\nu + 1)$  and  $\nu$  is the ordinary percolation correlation length exponent.

To make PNM in general and the invasion percolation algorithms better reflect the flow patterns in real porous media, pore network geometries have evolved in terms of complexity. An important characteristic of real porous media is their angular corners of pores and throats, which allow the retention of wetting fluid at the corners, in the form of arc menisci (AMs), and non-wetting fluid at the center, after the bulk drainage process is completed. In such a scenario, the invasion of air into saturated throats takes place at a lower threshold capillary pressure as compared to the threshold capillary pressure of a simple circular pore, which is given by eq. (2.7). The most commonly used method for calculating entry pressures of angular throats is the Mayor, Stowe and Princen (MS-P) method (Mason and Morrow 1984), which relies on equating the curvature of the AMs to the curvature of the invading interface. Oren et al. (1998) performed a generalization of the MS-P method and expressed the threshold entry pressure,  $p_c^t$ , as:

$$p_c^t = \frac{\gamma}{r_0} \cos \theta_r \left( 1 + 2\sqrt{\pi G} \right) F_d(\theta_r, G), \quad (2.13)$$

where  $\theta_r$  is the receding contact angle,  $r_0$  is the inscribed circle radius of the pore and  $F_d$  and  $G$  are parameters dependent on pore shape and the contact angle between the wetting fluid and the solid. In the presence of AMs, drainage and imbibition in porous

media proceeds through several mechanisms such as snap-off, piston-type displacement, cooperative pore-body filling etc. (Patzek 2001). A detailed description of the formulae and criteria for all relevant mechanisms in this study are given in Chapter 7.

#### 2.4.1.2 *Modeling drying with pore network modeling*

Compared to the application of PNM in modeling imbibition and drainage in porous media, the application of PNM for drying in porous media has only received attention lately. PNM was used to simulate drying at the material scale for the first time by Prat (1993). His model combined the principles of invasion percolation with a discrete computation of diffusive vapor transport in the medium. Moreover, Prat (1993) was the first to use pore networks to investigate liquid patterns during the drying process and assess its influence on the drying rates. Prat (1993) applied invasion percolation to drying by drawing an analogy between the drying and drainage processes as both are characterized by the movement of menisci through the porous medium and the progressive invasion of the non-wetting fluid. This analogy was first drawn by Shaw (1987) who experimentally observed the similarity of drying invasion fronts to drainage invasion fronts. Subsequent studies reinforced this analogy (Prat and Bouleux 1999; Tsimpanogiannis and Yortsos 1999), specifically by observing that viscous effects stabilize invasion. The key difference, however, between the IP algorithms of drainage and drying is the treatment of disconnected liquid clusters. Owing to the incompressibility of the wetting fluid, throats in a disconnected cluster cannot be invaded during drainage since no path exists anymore to the outside, although the cluster itself can move. On the contrary, during drying, wet throats can be invaded and this should be incorporated into the IP algorithm for a realistic simulation of slow drying, as shown by the validation of this model with experiments on etched networks by Laurindo and Prat (1998). However, when viscous effects in the gas and liquid phase are considered, the drying behavior departs from IP (Prat and Bouleux 1999).

Since Prat (1993), increasingly sophisticated IP algorithms have been proposed to take into account gravity effects (Prat 1995), thermal effects (Huinink et al. 2002), viscous effects (Yiotis et al. 2001) and the presence of an external mass transfer boundary layer (Yiotis et al. 2007). A common feature of most of the earlier studies, however, is the absence of consideration of films during the drying process. The presence of films in pore and throat corners can greatly increase the hydraulic connectivity and therefore increase the mass transfer and evaporation rates. Yiotis et al. (2004) was the first to consider the effect of films when modeling isothermal drying using pore networks. They divided the pore space into three kinds of pores: gas-filled pores (in the dry region), liquid-filled pores (in the liquid region) and film pores with gas at the center and liquid as films in the corner (in the film region), a schematic of which was presented in a later paper (Yiotis et al. 2015) and is reproduced in Fig. 2.15. They accounted for viscous effects in the

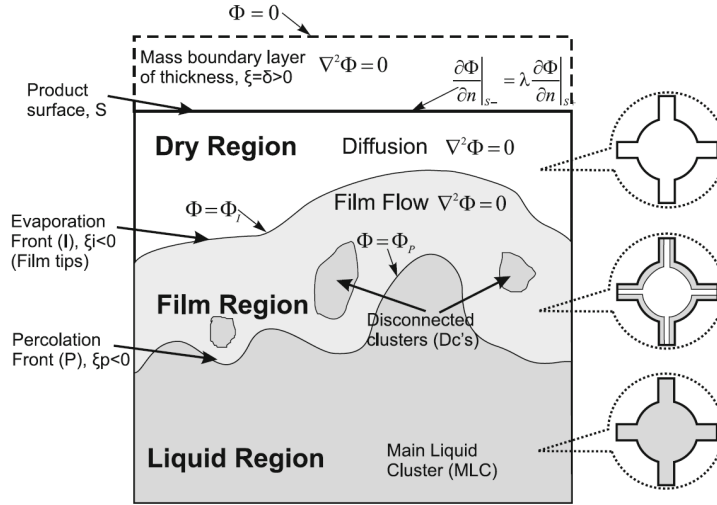


Figure 2.15.: Liquid and gas patterns during drying in a capillary-dominated porous medium. (Yiotis et al. 2015)

liquid and film pores and mass transfer in the gaseous phase was assumed to be purely by diffusion. The most important effect of films is that in their presence, the gas phase remained saturated, thereby blocking the evaporation in such pores. A further observation was the capillary transport of water towards the open surface, where large concentration gradients existed. As expected, the spread of films increased with a decrease in capillary number. In the same study, an extension of their approach to non-isothermal conditions showed that if film flow dominates, temperature effects are secondary. However, their approach had several assumptions, most important of which were: transport effects near the open surface were lumped into an effective diffusivity parameter, heterogeneity in diffusive conductance among the pores as a result of their different radii was neglected and the possibility of inter-cluster communication was also neglected by postulating that all films at the clusters have the same initial film radius. The effect of gravity was also not considered in their model.

In a later study, Yiotis et al. (2012a) developed analytical solutions for drying in porous media, incorporating the effects of corner flow, mass transfer within and above the surface

of the medium and gravity. For gravity-opposed drying (evaporation from top surface), the drying rate,  $\dot{S}$ , was calculated to be:

$$\dot{S} = -\frac{D_M r_0^2 c_e (1 + \text{Ca}_f) N_y N_z}{\text{Ca}_f} \frac{d\Theta}{d\xi} \Big|_{S+}, \quad (2.14a)$$

$$\Theta = \frac{\sigma^3 - 3\text{Bo}_x I + \text{Ca}_f \zeta}{1 + \text{Ca}_f}, \quad (2.14b)$$

$$I = \int_0^\xi \sigma^4 d\xi, \quad (2.14c)$$

where  $D_M$  is the apparent molecular diffusion coefficient,  $N$  denotes the network size,  $r_0$  is the capillary size,  $c_e$  is the equilibrium mass concentration,  $\zeta = c/c_e$  is the dimensionless concentration, is the dimensionless film thickness,  $\sigma$  is the dimensionless film length,  $\Theta$  is a scalar variable that captures mass transport through both the film and dry regions,  $\text{Ca}_f$  is the dimensionless capillary number, and  $\text{Bo}_x$  is the dimensionless Bond number. The application of the Laplacian equation,  $\nabla^2 \Theta = 0$ , in the film and dry regions yields a linear system of equations whose solution determines the fluid mass in these regions. In a follow-up paper, Yiotis et al. (2012b) built upon the theoretical considerations of their earlier paper, but additionally considered the dependence of  $\beta$ , the dimensionless resistance to flow and  $C^*$ , the dimensionless film area, on film thickness  $\sigma$ , and introduced a new parameter  $\text{Ca}_f^* \equiv C^* \text{Ca}_f / \beta$ , to calculate the extent of the film region in the porous media at a given time as:

$$\int_{\sigma=p}^1 \frac{3\sigma_f d\sigma_f}{\frac{\text{Ca}_f^* \beta \text{Sh}}{C^*(1-\text{Sh}\xi_i)} + 3\text{Bo}\sigma^4} = \xi_i - \xi_p, \quad (2.15)$$

where  $\text{Sh}$  is the Sherwood number (ratio of external mass transfer to internal diffusion) and the subscripts  $i$  and  $p$  indicate the evaporation and percolation front positions respectively. Their equations provided a direct relationship between the drying rates and position of the film tips. The drying curves obtained from their simulations, shown in Fig. 2.16, shows that the constant drying rate period (CDRP) is shorter for larger values of  $\text{Bo}$ , i.e. when the influence of gravity gets stronger.

As shown in Fig. 2.17(a), Yiotis et al. (2012b) determined the extent of the film region in the porous domain as a function of the position of the percolation front during an isothermal experiment and compared it with the solution of eq. (2.15). Packings of bead sizes 100-160  $\mu\text{m}$ , 150-200  $\mu\text{m}$ , 200-250  $\mu\text{m}$ , 300-315  $\mu\text{m}$  and 400-500  $\mu\text{m}$  were used in their experiments. As bead sizes increased, the influence of gravity increased, and therefore the growth of the film region as the percolation front moves away from the surface became less

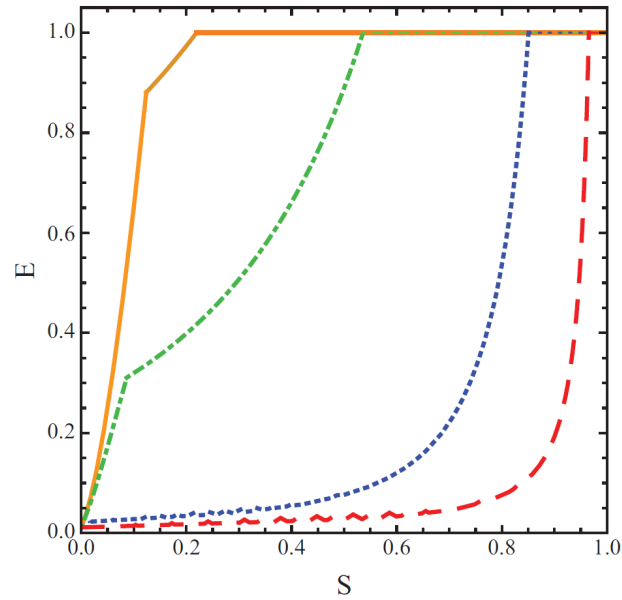


Figure 2.16.: Dimensionless drying rate as a function of the liquid saturation for different values of the bond number;  $Bo_x = -0.1$  (red-dashed line);  $Bo_x = -0.01$  (blue-dotted line);  $Bo_x = -0.001$  (green-dot-dashed line);  $Bo_x = -0.0001$  (orange continuous line). The smaller the effect of gravity, the longer the CDRP. (Yiotis et al. 2012a)

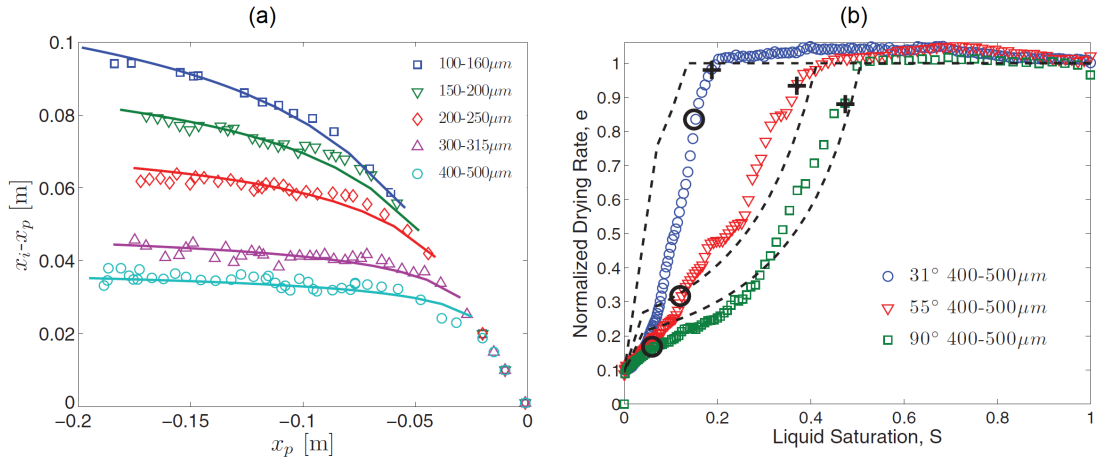


Figure 2.17.: (a) Experimental results of the extent of film region  $x_i - x_p$  as a function of the percolation front  $x_p$  for packings of different bead sizes. The theoretical curves obtained from the solution of eq. (2.15) are shown as continuous lines. The film extent generally increases as the front recedes, but the trend becomes less prominent as bead sizes increase. (b) Drying rate as a function of liquid saturation for the same bead packings but at different inclination levels. As inclination increases, the effect of gravity increases. (Yiotis et al. 2012b)

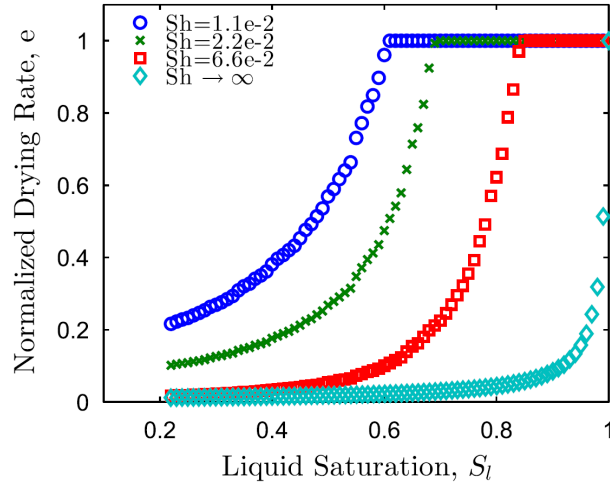


Figure 2.18.: Effects of Sherwood number on the drying curves of a  $150 \times 30 \times 30$  pore network. As Sherwood number increases, the constant drying rate period becomes progressively shorter and consequently, the decreasing drying rate period sets in earlier. (Yiotis et al. 2015)

pronounced due to earlier film detachment from the percolation inlet surface. Additionally, the drying rate as a function of liquid saturation was calculated for a packing of 400-500  $\mu\text{m}$  beads at different inclination angles,  $31^\circ$ ,  $55^\circ$  and  $90^\circ$ , as shown in fig. 2.17(b). As the inclination angle increased, which implied that the influence of gravity increased, the constant drying rate period (CDRP) became shorter as a result of the smaller film regions and the decreasing drying rate period (DDRP) set in earlier. In a recent study, Yiotis et al. (2015) introduced a drying model that improved upon the 1D model of Yiotis et al. (2012a) with a 3D model that also captured the gradual desaturation of the surface due to disorder in the underlying percolation front. Their simulations showed that as the Bond number increased, i.e. as the influence of gravity increased, the film thickness profiles and therefore, the capillary pressure gradients in the system, became more complex, which lead to shorter film regions and shorter CDRPs. They also investigated the effect of increasing Sherwood number, namely thinner boundary layer near the evaporating surface, on the drying rate of the porous medium. As shown in Fig. 2.18, as Sherwood number increases, the higher evaporative flux at the evaporation front induces higher capillary pressure gradients in the film region, which again leads to a shorter CDRP, analogous to the effect of gravity on drying, as observed from Fig. 2.16.

For modeling convective drying in a macroporous medium using a continuum approach, the above discussion has a very important implication. Since gravity plays an important role in macroporous media, the drying phase could completely skip the CDRP and directly



Figure 2.19.: Schematic representation of snap-off in a pore. (Rossen 2000)

enter the DDRP. In this case, the internal diffusion in the medium will determine the overall drying rate and as such, accurately modeling the convective boundary conditions will be less critical than an adequate material characterization in terms of liquid and vapor transport (Defraeye et al. 2012). This implies that constant heat and mass transfer coefficients can be applied to the evaporating surface to account for the exchange with the environment, instead of treating the heat and mass transfer as a conjugate problem. Another point to note is that in the drying models of Yiotis, the possibility of snap-off, which is the collapse of arc menisci in very small pores (shown schematically in Fig. 2.19) and is an important pore-filling mechanism, is not accounted for. Snap-off results in refilling of water in pores that are already invaded by air and can therefore affect macroscopic vapor transport by rendering those pores impermeable to vapor flow.

## 2.5 COMPOSITION AND CHARACTERIZATION OF POROUS ASPHALT

Porous asphalt is a special road material that is used as the surface layer of road pavements in many countries due to its excellent drainage properties. In combination with a well-designed impervious asphalt concrete layer, which acts as a structural support for the upper PA layer, PA has proven to be an efficient tool in water-management strategies of many cities (Cahill et al. 2004). The acoustical absorption property of PA leads to a significant absorption of both engine and tire noises (Meiarashi et al. 1996). The good hygric and acoustic properties are used to promote PA as an environment-friendly road material.

PA typically has a porosity of around 20% and is a composite material made from fine and coarse mineral aggregates, a bituminous binder and air voids. Typically, aggregates make up 94% by mass of the composition of PA while bitumen has a mass content of 6%. Despite the low mass content of bitumen, it holds together the aggregates in PA. During the production process, hot bitumen is mixed together with a mixture of heated fine and coarse aggregates in a mixer where a thin mastic forms around the aggregates. In some cases, fibers are also added to PA to allow thick binder films for the sake of improved



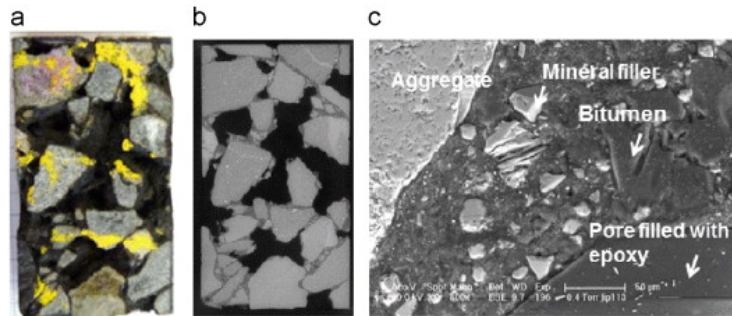


Figure 2.20.: Microstructure of porous asphalt concrete consisting of coarse and fine mineral aggregates, bitumen and air voids: (a) photograph of 47 mm×28 mm specimen, (b) X-ray  $\mu$ -CT slice of the same specimen, where voids are black, aggregates light gray and bitumen darker gray, and (c) ESEM micrograph, the voids are filled with epoxy resin (scale bar 50  $\mu$ m). (Poulikakos et al. 2013b)

mechanical behavior and reduced binder drain-down effects. The microstructure analysis of PA presented in Fig. 2.20 shows the components in a typical PA internal structure. A more detailed investigation of the microstructure of PA is given in Poulikakos and Partl (2010).

In a freshly prepared PA specimen, the bituminous binder covers most of the aggregates and shields the aggregates from water as a result of its low permeability. However, due to the high porosity of PA, a large area of the microstructure of PA is exposed to the deteriorative effects of oxidation by air and degradation by water. This leads to rapid aging of the bitumen binder, damage of the bitumen-aggregate bond and structural distress of the compounds (Poulikakos and Partl 2012). Poulikakos and Partl (2012) conducted coaxial shear tests of dry and water submerged cylindrical field cores of PA of diameter 150 mm and height 60 mm. They observed that the complex moduli of elasticity of the cores, a measure of their fatigue behavior, were considerably lower when the cores were submerged in water, as shown in Fig. 2.21. This clearly showed the reduced strength of PA when exposed to moisture. Other studies have macroscopically investigated various material properties of PA that are relevant to wetting and drying such as permeability, density and porosity (Arambula et al. 2010; Bäckström and Bergström 2000; Perraton and Carter 2005; Praticò and Moro 2007).

In comparison to the extensive literature of standardized tests on PA, there are only a few studies that investigate the prediction of transport properties of PA using analytical and numerical methods. Gruber et al. (2012) investigated the effect of structural anisotropy of PA on its hydraulic conductivity. They used a finite volume solver to simulate fluid

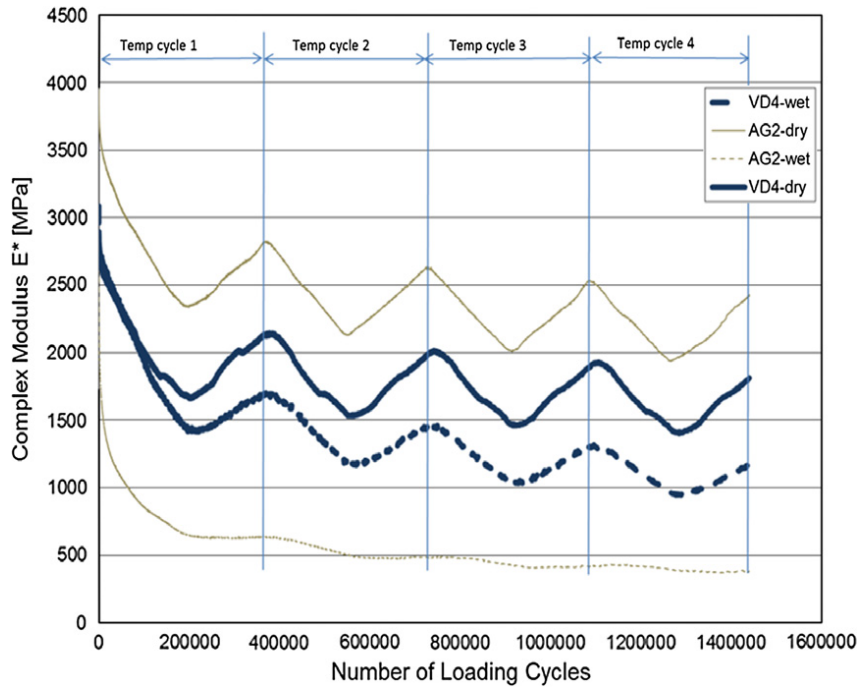


Figure 2.21.: Evolution of complex moduli of two PA11 cores, VG4 and AG2, subjected to coaxial shear tests during dry and wet test conditions. The reduced fatigue strength of wet PA specimens is clearly evident from the figure. (Poulikakos and Partl 2012)

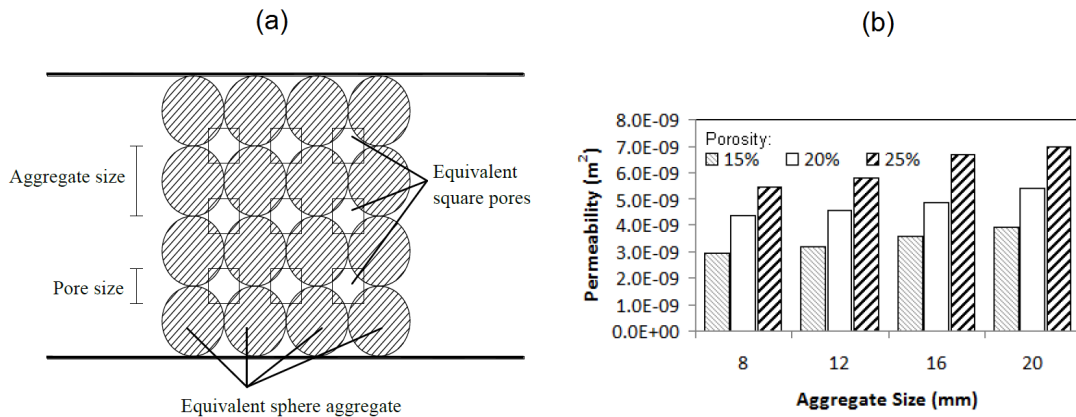


Figure 2.22.: (a) Simplified representation of the porous layer structure used in pore network simulations of drainage in a permeable pavement and (b) influence of porosity and aggregate size on permeability values calculated using pore network models. (Zhang et al. 2013)

flow in a real PA geometry as obtained from X-ray  $\mu$ -CT scans and postulated that the absolute permeability of PA varied by a factor of two depending on the flow direction. Furthermore, they approximated PA as a Darcy model of porous medium and calculated the Forchheimer coefficient of PA. While the original Darcy model is applicable when the flow rate is low enough and pressure drop due to inertial losses is negligible, the addition of the Forchheimer coefficient to the Darcy model accounts for inertial losses at high flow rates, which is a possibility in PA due to its large pore sizes. The calculated permeabilities of two PA11 specimens in their study was  $6.083 \times 10^{-11} \text{ m}^2$  and  $3.137 \times 10^{-9} \text{ m}^2$  while their Forchheimer coefficients were  $1.4569 \times 10^6 \text{ m}^{-1}$  and  $5.5039 \times 10^6 \text{ m}^{-1}$ . They postulated that this approximation of PA as a Darcy model was valid only for specific flow rates and will underestimate the pressure drop at greater flow rates. The anisotropic nature of permeability of porous pavements in general was investigated in further detail by Masad et al. (2007).

Zhang et al. (2013) published the first application of pore network models to the investigation of drainage properties of porous pavements. Porous mixtures with three porosity values (15%, 20% and 25%) and four aggregate sizes (8, 12, 16 and 20 mm) were used in their study. They developed a cubic pore network model with two characteristic length variables to define the network, namely the edge length of each drainage channel and the distance between the centers of two successive parallel channels. However, the distance between the channel centers was a constant that was equal to the nominal aggregate size of the single-sized aggregates that they considered for their simulations. All the simulations

were performed for 100 mm thick porous layers. They used  $k-\varepsilon$  turbulence model to simulate water flow within the network for different aggregate sizes, and calculated the permeability for each case. A schematic representation of their pore network and the calculated permeabilities at different nominal aggregate size is given in Fig. 2.22. The order of magnitude of permeabilities was similar to those calculated by Gruber et al. (2012). However, similar to previous modeling efforts on permeable pavements, only single-phase, saturated flow was taken into account for determining the transport properties. Finally, it is also noted that a detailed investigation into the pore-scale physics of fluid flow in permeable pavements, experimental or numerical, is missing in literature.

## 2.6 NEEDS FOR FURTHER RESEARCH

The current understanding of fluid flow in macroporous media in general, and in porous asphalt in particular, is still very limited. Gravity is the defining feature that determines flow behavior in macroporous media, especially during imbibition and drainage. Experimental studies so far have clearly established the instability and complexity of pore-scale mechanisms such as capillary imbibition, gravity imbibition and gravity drainage in macroporous media. However, even with the advent of advanced non-destructive imaging techniques, pore-scale visualizations of fluid flow in macroporous media is still non-existent. A remarkable research gap is the absence of studies investigating the effect of gravity on unsaturated flow in complex macroporous media. Moreover, a large majority of flow experiments are done on simplified porous media that does not capture the complexity of flow mechanisms in real porous media. A similar scenario can be seen in studies on convective drying of macroporous media, in which case the additional momentum exchange induced by air penetration into the system should be taken into account. Recent advancements on this front have been the visualization of air penetration into highly permeable porous media and the analysis of its effect on the boundary layer above the surface. However, full-scale airflow investigations on real, complex macroporous media is missing in literature. Moreover, experimental observations of flow mechanisms in PA is also necessary to provide realistic assumptions for modeling.

Pore network modeling has steadily advanced to become one of the most efficient computational tools to simulate quasi-static multiphase flow in porous media. Invasion percolation algorithms have become the de facto method for modeling drainage, as long as viscous effects can be neglected. Recent studies have improved the efficiency of IP algorithms by accounting for, among other things, more complicated pore shapes and the effect of gravity. The use of pore networks for modeling drying has also reached an advanced stage, with dry and film regions above the percolation front being explicitly taken into account for calculating the evaporative flux at the material surface, and validated with analytical solutions. However, the applicability of pore network modeling to predict

the transport properties of a highly complex materials such as porous asphalt is still an open question, especially since pore networks do not take into account the tortuosity of the pore space, the heterogeneity in the wettability (solely due to the lack of sufficient knowledge about the same) and the roughness of the solid matrix. Nevertheless, if pore network modeling can indeed be used to determine macroscopic transport properties of PA, the results can be used as inputs to an upscaled continuum model to efficiently predict the performance of the material in typical atmospheric conditions. This can be a powerful tool for road engineers engaged in designing more durable pavements. Therefore, a multiscale approach from experimental investigations and pore network modeling to continuum modeling is designed in this study to first understand and consequently predict the wetting and drying processes in PA.



## EXPERIMENTAL INVESTIGATION OF IMBIBITION IN POROUS ASPHALT

---

### 3.1 INTRODUCTION

This chapter presents the experimental investigations to study the spatial and temporal distributions of moisture in porous asphalt specimens subjected to capillary imbibition and gravity imbibition. The experiments are carried out at the thermal neutron radiography station (NEUTRA) of the Swiss Spallation Neutron Source (SINQ) facility of the Paul Scherrer Institute, in Villigen, Switzerland. Capillary imbibition is studied with a water uptake experiment on PA while gravity imbibition is studied with droplet wetting of PA. For each experiment, a description of the PA specimens used in the experiments is first provided, followed by a description of the experimental setup and the procedure. The most important observations from the experiment are then analyzed in detail. In case of the capillary imbibition (water uptake) experiment, complementary simulations are carried out to obtain a better understanding of the experimental observations, which is also described in detail.

### 3.2 WATER UPTAKE EXPERIMENT

*This section is based on the paper Lal et al. (2014)*

The objective of this experiment is to understand the phenomenon of capillary imbibition in porous asphalt by combining neutron radiography and microtomography imaging techniques. To investigate this behavior, PA specimens are placed in contact with a free pool of water and the water uptake in different specimens is documented. Since water uptake is from the bottom surface of the specimens, capillary force is the only driving force. By combining neutron radiography images with the pore structure information obtained from X-ray  $\mu$ -CT scans, an attempt is made to distinguish between saturated and unsaturated flows within the PA structure. Additionally, using finite volume numerical simulations, the influence of tortuosity and pore connectivity on the rate of capillary imbibition is investigated.

### 3.2.1 *Material characterization*

#### 3.2.1.1 *Preparation*

A detailed description of the microstructure of PA was given in Section 2.5 in Chapter 2 and is not repeated here. In this experiment, the type of PA used is PA11, which has a nominal maximum aggregate size of 11 mm. Two different types of PA11 specimens with known in-situ performance (Poulikakos et al. 2006) are used for comparison purposes. These mixtures were used in the Swiss cantons of Aargau (referred to as AG1) and Vaud (referred to as VD4). VD4 is part of a large piece that was harvested from a road after 7 years of service. AG1 was freshly made in the laboratory using the mix design specifications of the road that had been monitored for 5 years. The compositions of these two materials differ firstly in the aggregate gradation, with VD4 having a slightly higher proportion of aggregates in the 8-11.2 mm range than in the 5.6-8 mm range as compared to AG1, and secondly in the type and content of the bituminous binder (Tab. 3.1). VD4 contains polymer-modified bitumen (PmB), with styrene butadiene styrene (SBS) co-polymer. AG1 has 55/70 penetration-graded straight run bitumen with Trinidad natural asphalt with NAF 501 additive; a fine grained granular product, consisting of 83.3 mass-% Trinidad Epuré and 16.7 mass-% cellulose fibers (<http://www.trinidad-lake-asphalt.de/english/Produkte-NAF-501.php>). Using the sessile drop method, the static contact angle of a drop of water was found to be more than  $99.2^\circ$  for the PmB binder and  $105.6^\circ$  for the 55/70 binder (Poulikakos and Partl 2012) i.e. both binders can be categorized as hydrophobic. The mineral aggregate of AG1 is siliceous lime aggregate from the Balmholz quarry with high pressure and abrasion resistance as well as good water resistance. Mineralogical data indicates 30-45% quartz by mass ([www.balmholz.ch](http://www.balmholz.ch)). The mineral aggregates used in VD4 are from the Famsa quarry, a hard sand aggregate from the sedimentary rock category with 20-30% quartz ([www.famsa.ch](http://www.famsa.ch)). Three specimens are used in this study, one from the AG1 pavement (named AG1) and two specimens from the VD4 pavement (named VD4-1 and VD4-2). The specimens have been chosen to study the effect of both spatial inhomogeneity (two specimens from the same material) as well as different chemical and physical properties (specimens from laboratory-made and in-situ materials) on the water uptake process. All three specimens selected have the dimensions of  $45 \times 25 \times 10 \text{ mm}^3$  (Fig. 3.1). In the neutron experiment, as expected due to its hydrophobic solid matrix, AG1 did not exhibit any significant water uptake. Therefore, only the results for VD4-1 and VD4-2 are presented here.



Table 3.1.: Material specifications of PA specimens used in the water uptake experiment.

	<b>AG1<sup>a</sup></b>	<b>VD4<sup>b</sup></b>
EN 13108-7 designation	PA11	PA11
Voids [% by vol]	21	22.8
Sieve size (mm)	Percent passing	
16	100	100
11.2	98	95
8	60	49
5.6	16	20
4	13	15
2.8	12	13
2	11	11
1	8	7
0.5	7	6
0.09	4.8	4.8
Penetration Graded Binder type	Bit.55/70+TrinidadNAF 501	PmB <sup>c</sup> Styrelf <sup>®</sup> 13/80
Binder [weight-% of total mixture]	4.8	4.8
Penetration at 25°C [0.1mm]	18	50
Softening point [°C]	72.2	56.6
Aggregate type	Siliceous limestone	Quartz sandstone
Los Angeles abrasion test (LA)	13-18	<18
Polished Stone Value test (PSV)	53	>50

<sup>a</sup>Laboratory produced specimen.

<sup>b</sup>Field core.

<sup>c</sup>Polymer modified bitumen.

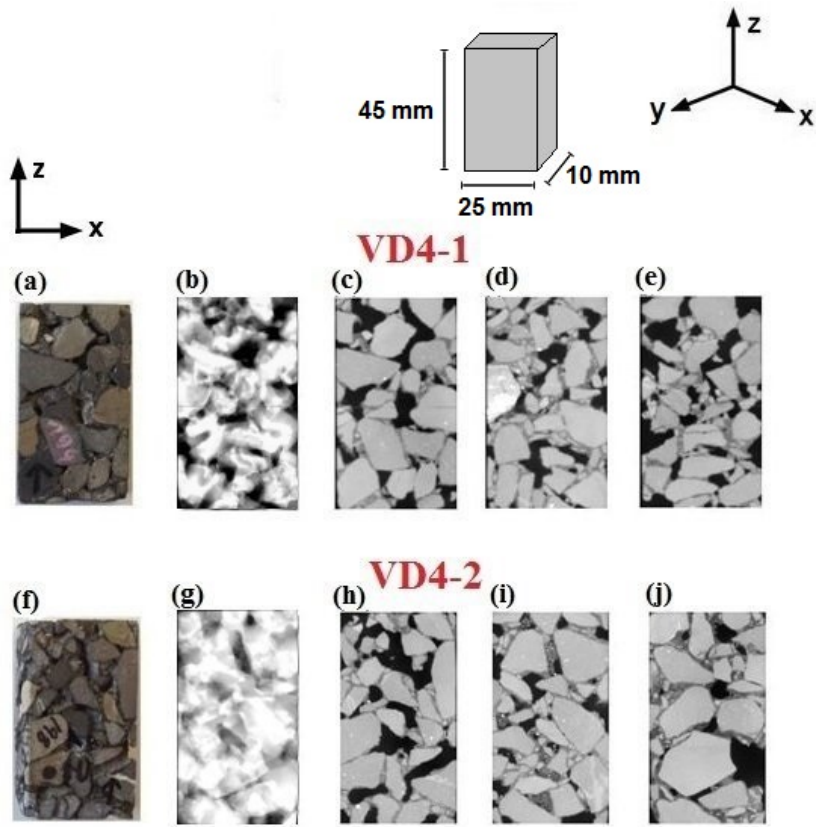


Figure 3.1.: Visible light photographs (a,f), 2D cumulative porosity distribution images (b,g) in which the porosity ranges from 0 (white) to 1 (black) and X-ray  $\mu$ -CT slices at the front (c,h), middle (d,i) and rear (e,j) slices of VD4-1 and VD4-2.

### 3.2.1.2 Cumulative porosity distribution from X-ray microcomputed tomography

The pore structures of the three specimens are imaged with the X-ray micro-computed tomography (X-ray  $\mu$ -CT) setup of Empa. The setup consists of an X-ray source (X-ray tube 'XT9225-TEP', Viscom), an XYZ linear stage (composed of three linear stages 'LS-270', Micos) for positioning the specimen, a rotation table ('UPR-160 F air', Micos) and an X-ray detector ('XRD 1621 CN3ES', Perkin-Elmer). The X-ray tube was operated at 220 kV and 0.1 mA and the emitted X-ray spectrum was hardened with a 0.5 mm thick Cu filter. The focal spot size was below the nominal spatial resolution of 55  $\mu$ m, which was calculated from the detector pixel size (0.4 mm,  $2 \times 2$  binned), the distance between the source and the object (158 mm), and the distance between the source and the detector (1146 mm). The three-dimensional distribution image of the attenuation coefficient was reconstructed by means of a Feldkamp algorithm from 720 projection images (1024  $\times$  800 pixel, 3.6 s exposure) recorded from different viewing angles distributed evenly over  $2\pi$  (Feldkamp et al. 1984).

In Fig. 3.1, the visible light photographs (a,f), the two dimensional cumulative porosity distributions (CPD) obtained from reconstructions of 3D X-ray  $\mu$ -CT scans (b,g) and the X-ray  $\mu$ -CT slices at the front, middle and rear slices of VD4-1 (c,d,e) and VD4-2 (h,i,j) are shown. The procedure to obtain the CPD from X-ray  $\mu$ -CT images is as follows: All the 2D X-ray  $\mu$ -CT images are binarized using an automatic threshold as calculated by the open-access image processing software Fiji (Schindelin et al. 2012). This process converts each pixel in an image to either a pore (pixel value=1) or a solid i.e. binder/aggregate (pixel value=0). The final CPD image is then obtained by adding all the images along the direction perpendicular to the image plane and then dividing the resulting image by the total number of images. The absence of porosity, i.e. an aggregate that crosses the entire thickness of the specimen, results in pixels with a value of 0 (white). All the other pixels have values ranging between 0 and 1, where 1 (black) represents pixels where pores cross the entire thickness of the specimen.

The CPD was calculated from X-ray  $\mu$ -CT images with two restrictions: voids smaller than 150  $\mu$ m were not detected due to resolution limitation, and the specimen is not a representative elementary volume (REV) of the material as its thickness of  $\approx 10$  mm and the largest aggregate size (11 mm) are of similar dimensions. An ideal REV should have dimensions which are larger than at least 3 times the aggregate size, but the available neutron beam does not have the energy to go through such a thick specimen. Hence, the porosity distribution calculated from the specimen is not representative of the porosity of PA in the pavement scale, but is useful for the analysis of neutron radiography images.

### 3.2.2 *Experimental setup and procedure*

#### 3.2.2.1 *Neutron beamline specifications*

The experiments are performed at the NEUTRA beam line and the neutron beam is in the thermal spectrum i.e. neutrons with a most probable energy of 0.025 eV and a speed of 2200 m/s. Neutrons in the thermal energy spectrum have a high interaction with water, making the NEUTRA beamline suitable for tracking the flow of water inside porous materials. The features of this facility include high collimation ratio, low gamma background and large beam diameter. A detailed description of the entire setup is given by Lehmann et al. (2001). The detector used is a scintillator-CCD camera-system, with a field-of-view of  $152 \times 152 \text{ mm}^2$ . The camera used is Andor iKon-L with  $2048 \times 2048$  pixels with a region of interest setting of  $1505 \times 1505$  pixels, providing a field of view of  $152 \times 152 \text{ mm}^2$ . The exposure time in the experiments is 12 s per radiograph with an attained spatial resolution of  $100 \text{ }\mu\text{m}$  per pixel. The neutron chamber had a temperature of  $22 \text{ }^\circ\text{C}$  and 30% relative humidity during the experiments. Radiographs are acquired initially every 12 s for the first 100 images and thereafter every 2 minutes for the duration of the experiments which lasted a minimum of three hours.

#### 3.2.2.2 *Remote-controlled ascending platform*

To image the PA specimens during the water uptake process, a custom-made setup is fabricated. The setup consists of a specimen-holder resting on a precision balance of  $\pm 0.1 \text{ mg}$  accuracy, and a remote-controlled ascending platform to raise the water container towards the specimen holder. The entire setup is placed in the neutron beamline during the experiments. Figure 3.2 shows a schematic of the experimental setup and a neutron radiograph of the same.

#### 3.2.2.3 *Determination of water content from neutron beam attenuation*

Neutron radiography (NR) is based on the different attenuation levels undergone by a neutron beam as it traverses different objects, the attenuation being particularly high by hydrogen, the main component of water.

The Beer-Lambert law for the attenuation of radiation passing through matter can be written as:

$$I = I_0 e^{-\left(\frac{\Sigma}{\rho}\right)\rho d}, \quad (3.1)$$

where  $I$  is the final beam intensity after the beam traverses a distance of  $d$  in the specimen,  $I_0$  is the incident beam intensity,  $\rho$  is the mass density of the specimen,  $\Sigma$  is the attenuation

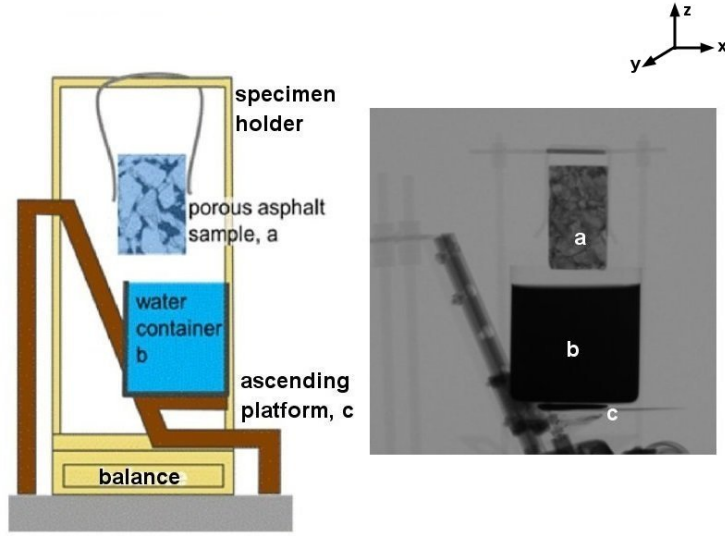


Figure 3.2.: Schematic representation of the experimental setup (left) and corresponding neutron radiograph image (right) showing: (a) PA specimen, (b) water container and (c) ascending platform.

coefficient for neutron, and the term  $(\Sigma / \rho)$  is the mass attenuation coefficient. From eq. (3.1), we can calculate the mass thickness,  $\tau(x, z)$  (Hassanein et al. 2005), i.e. the product of the specimen density and the specimen thickness at each pixel, as:

$$\tau(x, z) = \rho(x, z)d(x, z) = -\frac{\rho(x, z)}{\Sigma} \ln \frac{I(x, z)}{I_0(x, z)}, \quad (3.2)$$

where  $(x, z)$  denotes the coordinates of a pixel.

In this study, the parameter of interest is the water content in each pixel at any time step, in terms of mass per unit volume. As water moves through the material, any change of gray value of a pixel is attributed to the change in the moisture content. Thus, the moisture content distribution (MCD),  $w_t(x, z)$ , can be calculated as:

$$w_t(x, z) = \frac{\tau(x, z)_t - \tau(x, z)_i}{d_y}, \quad (3.3)$$

where  $d_y$  is the constant specimen thickness in the direction of the beam (y-direction),  $\tau(x, z)_i$  and  $\tau(x, z)_t$  are the initial mass thickness (of the dry specimen) and the mass thickness after a time  $t$  respectively, for a given pixel. In terms of the beam intensities, eq. (3.3) can be rewritten as:

$$w_t(x, z) = -\frac{\rho(x, z)}{\Sigma d_y} \ln \frac{I(x, z)_t}{I(x, z)_i} = -\frac{\rho(x, z)}{\Sigma d_y} [\ln I(x, z)_t - \ln I(x, z)_i], \quad (3.4)$$

where  $I(x, y)_i$  and  $I(x, y)_t$  are the initial beam intensity (of the dry specimen) and the beam intensity after a time  $t$  respectively, for a given pixel, as recorded by the detector. Since there is no deformation of PA during the experiments, no image registration is required and the moisture content at each pixel can be calculated by simply subtracting the logarithms of the dry image and wet images.

#### 3.2.2.4 Neutron radiography image corrections

To ensure an accurate quantitative determination of water content from the radiographs, the NR images have to be corrected for different types of artifacts. The corrections performed on the NR images in this experiment, in the order of their application, are as follows:

1. Dark current correction: corrects the false signal from thermally generated electrons in the charge-coupled device of the CCD camera.
2. Black body correction: corrects the false signal from the neutrons which are scattered from the experimental setup or the environment to the detector.
3. Spectral effect correction: accounts for the shift in the mean neutron beam energy to higher energies after traversing a strongly attenuating specimen.
4. Intensity correction: scales the measured radiographs to remove the effects of the inhomogeneity of the neutron source.
5. Flat field correction: accounts for the spatial inhomogeneity of the neutron beam intensity or detector sensitivity.

When all the above corrections, except the spectral effect correction, are applied to the radiographs, eq. (3.4) transforms to:

$$w_t(x, z) = -\frac{\rho(x, z)}{\Sigma z_s} \ln \frac{\{I(t)/IF\}/I(x, z)_{FF}}{\{I(i)/IF\}/I(x, z)_{FF}}, \quad (3.5a)$$

$$I(t) = I(x, z)_t - I(x, z)_{DC} - I(x, z)_{BB}, \quad (3.5b)$$

$$I(i) = I(x, z)_i - I(x, z)_{DC} - I(x, z)_{BB}, \quad (3.5c)$$

where the subscripts  $DC$ ,  $BB$  and  $FF$  refers to the dark current, black body and flat-field correction reference images respectively, while  $IF$  is the Intensity Factor which is purely a

function of the beam quality. Equations (3.1) - (3.7) are derived based on the assumption that the incident neutron beam is monochromatic. In reality, the energy distribution of the NEUTRA beam is similar to a Maxwell spectrum at 23.8 meV (Hassanein et al. 2005). The spectral effect correction takes this factor into account and eq. (3.1) can then be rewritten as:

$$\frac{I}{I_0} = \frac{\int_0^{+\infty} P(E) \cdot \varepsilon(E) \cdot e^{-\left(\Sigma(E)/\rho\right)\rho d} dE}{\int_0^{+\infty} P(E) \cdot \varepsilon(E) dE}, \quad (3.6)$$

where  $E$  is the energy of the incident neutrons,  $\varepsilon(E)$  is a parameter to account for the energy sensitivity of the detector and  $P(E)$  is the Maxwell-Boltzmann probability density function which represents particle speeds (energy) in gases. The corrections are performed with the Quantitative Neutron Imaging (QNI) method (Hassanein et al. 2005).

### 3.2.2.5 Results and discussion

### 3.2.2.6 Analysis of moisture content distribution and degree of saturation

The uptake and distribution of water in the PA specimens is first tracked in terms of the moisture content distribution (MCD), as defined by eq. (3.3), with units of  $\text{kg}/\text{m}^3$ , where the dry image at time  $t = 0$  is subtracted from the wet image at a given time step. Figures 3.3 and 3.4 show the spatial and temporal evolution of MCD of the two VD4 specimens, at five selected time steps. The time steps are chosen with the aim of documenting the main event of water uptake. The selected time steps also make it possible to focus on the initial stages of uptake, where the uptake rate is expected to be higher. In Figs. 3.3 and 3.4, the top row of images (a-e) are contour plots of MCD. In order to focus more effectively on the movement of water within the specimens, a second series of images (referred to as binarized images) is shown in the bottom row (f-j), where the first wet image in the upper row of images is subtracted from the wet images at the remaining time steps. In these images, pixels have a binary representation, white or black, where a black pixel represents a value that has crossed a threshold of  $30 \text{ kg}/\text{m}^3$  when subtracted by the first wet image, while a white pixel represents a value that does not change (e.g. absence of porosity) or which is below the threshold. This threshold has been selected through trial and error to achieve a clear visualization of the water front, thereby indicating the areas in the specimen which undergo significant water uptake.

It is also to be noted that the level of submergence of the bottom part of the specimens in water varies during the experiment with VD4-1. Also, between the two specimens, depending on their pore structure, different levels of ascension are necessary to initiate uptake. The exact level of submergence can be visualized by the gray pixels at the base of the specimens in the top row of images, and the white pixels at the base of the specimens

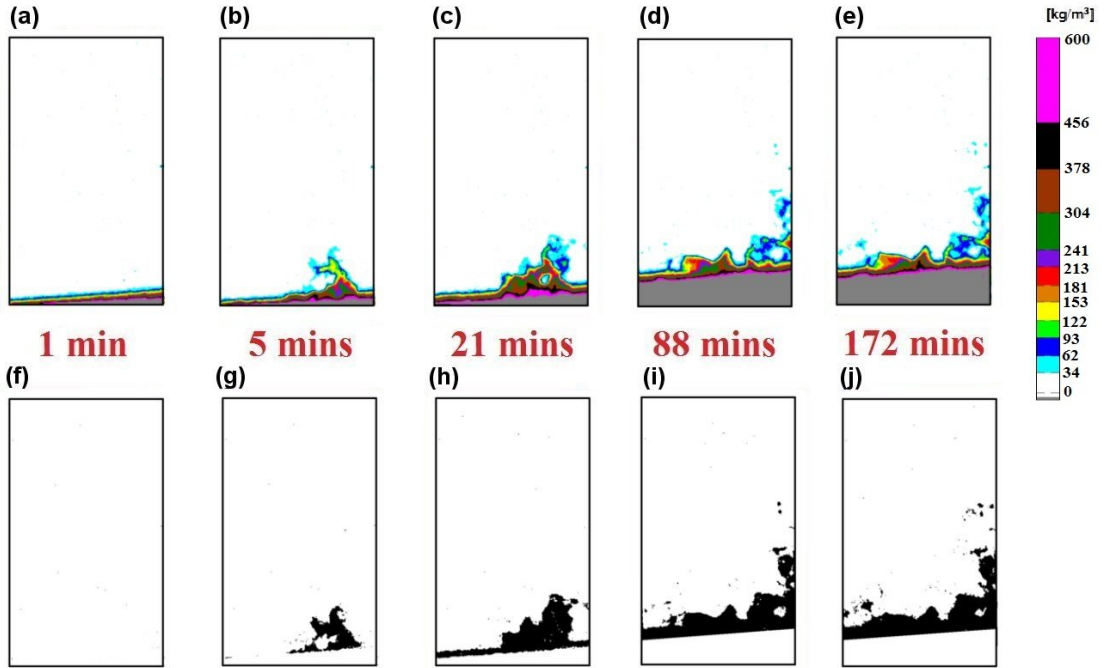


Figure 3.3.: (a-e) Temporal and spatial variations of the moisture content distribution (MCD) inside specimen VD4-1 at five time steps, (f-j) MCD segmented at  $30 \text{ kg/m}^3$  wet threshold, after subtraction from the wet image at  $t = 1 \text{ min}$ .

in the bottom row of images. No analysis in these parts is done since they are submerged under water. Additionally, the white patches in between the wet areas indicate the areas of 0% porosity i.e. the areas where a single aggregate crosses the entire width of the specimen, as also visible in Figs. 3.1(b) and 3.1(g) and Figs. 3.4(e) and 3.4(j).

A few general observations can be made from Figs. 3.3 and 3.4. Firstly, it is seen that water travels a significant distance inside both VD specimens, with the higher uptake being in VD4-2. Furthermore, in both specimens, there is not much difference in MCD between the penultimate and final time steps. This implies that much before the final time step, all the paths which could potentially be followed by uptaken water have been filled and additional uptake of water had stopped. The exact time at which water uptake stops is influenced by a variety of factors like gravity, dead-end pores, the presence of pores with sharply diverging diameters etc. In VD4-1, the uptake initially begins on the right side of the specimen while in VD4-2, there is no clear preference. This aspect is investigated further later in a later section. In VD4-2, at the last two time steps, the emergence of a water island can be seen at the top part of the specimen. It can be further observed that, in VD4-2, there are high moisture content regions (yellow, green and red)



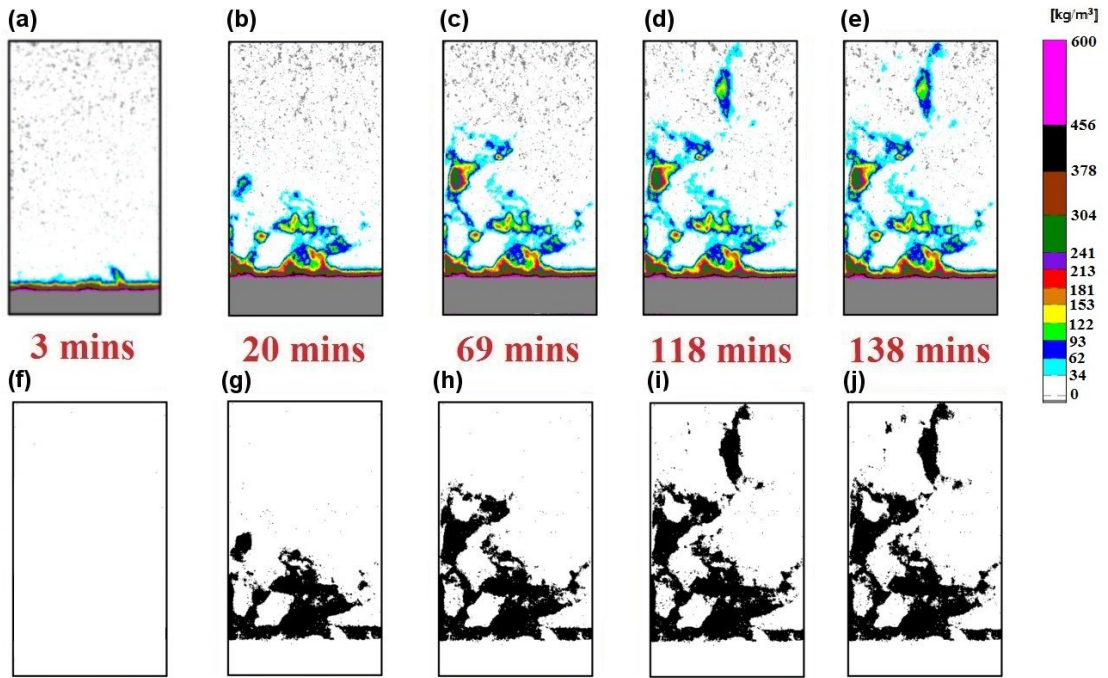


Figure 3.4.: (a-e) Temporal and spatial variations of the moisture content distribution (MCD) inside specimen VD4-2 at five time steps, (f-j) MCD segmented at 30 kg/m<sup>3</sup> wet threshold, after subtraction from the wet image at  $t = 3\text{ mins}$ .

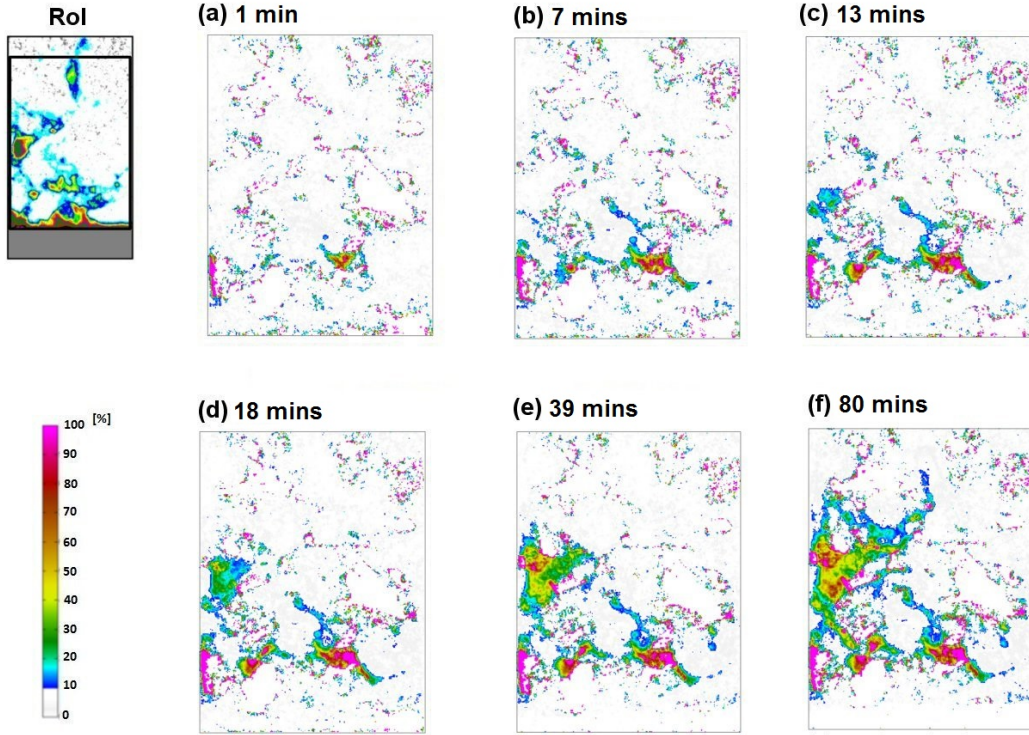


Figure 3.5.: Temporal and spatial variations of the degree of saturation inside a selected ROI of specimen VD4-2 at different times during the uptake experiment.

surrounded by low moisture content regions (dark and light blue), where the low moisture content regions could be aggregate-dominated cross-sections which are surrounded by high moisture content pore-dominated cross-sections.

A more detailed analysis of water propagation is now studied in terms of another parameter, the degree of saturation (DoS),  $s_t(x, z)$ , defined as:

$$s_t(x, z) = \frac{w_t(x, z)}{\rho_w \cdot \varepsilon(x, z)}, \quad (3.7)$$

where  $\varepsilon(x, z)$  is the two dimensional porosity distribution as shown in Figs. 3.1,  $w_t(x, z)$  is the MCD calculated with eq.(3.3) and  $\rho_w$  is the density of water. Unlike the MCD analysis, the DoS analysis makes it possible to clearly identify those pores that are water saturated. The transformation of MCD to DoS analysis is done for a Region of Interest (ROI) smaller than the specimen, as shown in Figs. 3.5 and 3.6 for specimens VD4-2 and VD4-1 respectively. The dimensions of the ROIs chosen for specimens VD4-2 and VD4-1 are  $35 \times 25 \text{ mm}^2$  and  $9 \times 25 \text{ mm}^2$  respectively. The DoS analysis is performed over an

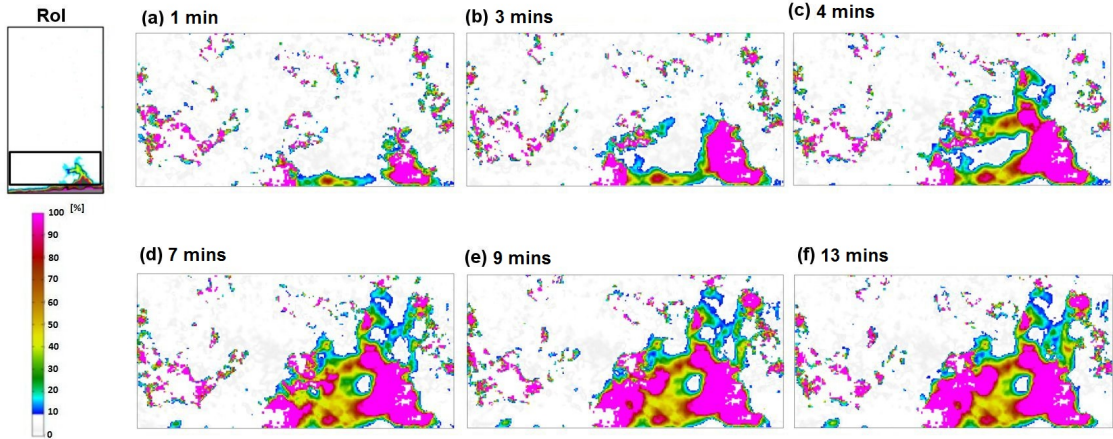


Figure 3.6.: Temporal and spatial variations of the degree of saturation inside a selected ROI of specimen VD4-1 at different times during the uptake experiment.

interval of time i.e. 80 minutes and 13 minutes after the dry image is taken, for specimens VD4-2 and VD4-1 respectively. Like in the MCD images of figs. 3.3 and 3.4, the large patches of white pixels in Figs. 3.5 and 3.6 indicate aggregates that run through the specimen, i.e. indicating areas of zero porosity.

From Figs. 3.5 and 3.6, it can be observed that the patterns of water uptake are different in the two specimens. In VD4-2, the number of pores where saturated flow occurs is not large, as can be inferred from the low number of pink pixels at all time steps. However, as confirmed from Figs. 3.3 and 3.4, water travels much further in VD4-2 than it does in VD4-1, thereby indicating the occurrence of unsaturated flows in VD4-2 i.e. flow by not completely filling the pores with water. Compared to VD4-2, VD4-1 has a larger number of saturated pores, where saturated flow could be certainly active. In VD4-1, this number increases rapidly in the initial stages of water uptake (1 min, 3 mins, 4 mins). Towards the later stages (7 mins, 9 mins, 13 mins), there is hardly any growth of this number.

### 3.2.2.7 Distinguishing saturated and unsaturated flow

The focus now shifts to understanding the mechanisms by which water uptake takes place in porous asphalt more thoroughly. It is reiterated that saturated flow implies water flow through the pores while completely filling the pore cross-section while unsaturated flow implies the movement of water along the pore corners i.e. in a pore with unsaturated flow, the central region of the pore cross-section is air-filled while the edges of the cross-section are water-filled. This next step of distinguishing between saturated and unsaturated flow is pursued using the VD4-1 results. For this purpose, two datasets are considered together:

the data from the three dimensional X-ray  $\mu$ -CT scans and the two dimensional degree of saturation images. Since 3D data is being compared with 2D data, the region of interest has to be restricted to that part of the DoS images where the saturated and unsaturated regions can be clearly distinguished. Moreover, the pore sizes as seen in the corresponding CT scans should be large enough to be able to neglect errors arising from the unavoidable imperfect overlapping of X-ray  $\mu$ -CT and NR images. Hence, a smaller ROI is chosen within the ROI selected for Fig. 3.6. This ROI, which is shown in Fig. 3.7(a), satisfies the above two conditions i.e. a clear pattern of uptake and large pore sizes. The dimensions of the ROI are also marked in Fig. 3.7(a). To visualize the pore structure within this ROI, the evolution of the specimen cross-section along the  $z$  direction has to be studied using X-ray  $\mu$ -CT scans. This concept is illustrated in Fig. 3.7(b) where the  $x - y$  plane at a certain  $z$  value is shown. These slices are of dimensions  $25 \times 10 \text{ mm}^2$ . Figure 3.8 depicts the results of the approach described above. In Fig. 3.8(a), the evolution of the specimen cross-section within the ROI along the  $z$  direction can be visualized with a series of X-ray  $\mu$ -CT images at different heights. In Fig. 3.8(b), the DoS distributions of the same ROI are shown at different time steps. These time steps are the same as used in Fig. 3.6. Positions along the  $x$  direction are marked on all the figures. Additionally, the  $z$  values of the DoS distribution in Fig. 3.8(b), at which the corresponding X-ray  $\mu$ -CT scans in the  $x - y$  plane are shown in Fig. 3.8(a), can be matched by the color code given for each  $z$  value in Fig. 3.8(a) and its location in Fig. 3.8(b).

In Fig. 3.8(a), it can be observed that there are five large pores at the bottom of the specimen ( $z = 0.53 \text{ mm}$ ), named pores A, B, C, D and E, through which water can enter. Uptake of water initiates at the three positions marked P, Q and R in Figs. 3.8(a) and 3.8(b). The uptake at position P is due to pore B, the uptake at position Q is due to pores C and D while the uptake at position R is mainly due to pore D and the connection between pores D and E. The uptake at position P stops midway along the  $z$ -direction, whereas the uptake at position R is the strongest and appears to be saturated flow. At position Q, the uptake is mostly unsaturated and it also stops very early. With time, uptake seems to be active only at position R. The water uptaken at R even flows laterally and fills up the pores above the points at which the uptake from positions P and Q stopped. This means that, as expected, the uptake in PA is essentially a 3D process.

From Figs. 3.8(a) and 3.8(b), a few conclusions can be drawn. Firstly, pore A does not play a significant role in water uptake. This could be due to the fact that it is a pore which is highly connected to the lateral boundaries or open to the surroundings, thereby incapable of any capillary uptake in saturated conditions. This is probably also true for pore E. Pore C, though similar in topology to pores A and E, does exhibit some uptake at its left corner. Similarly, pore B also shows some uptake, but only at its right corner. Therefore, in these pores, unsaturated film flow is expected to be the dominant mode of uptake. Going up the specimen along the  $z$  direction, pore B gradually changes to a

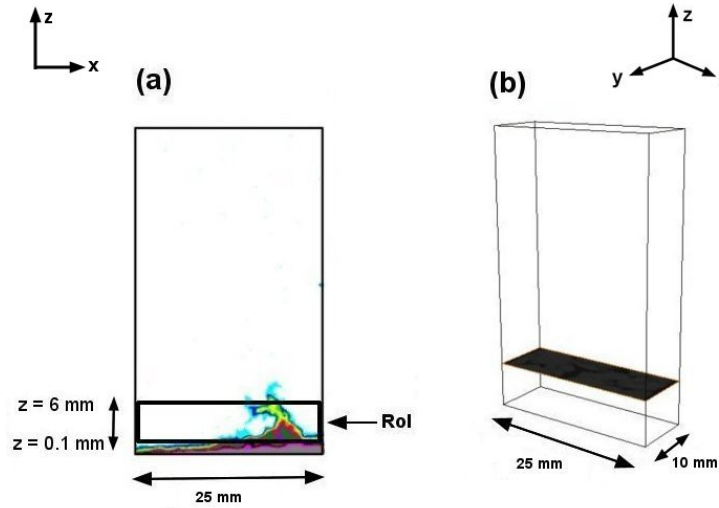


Figure 3.7.: For the analysis of the mechanism of water uptake, (a) a region of interest (ROI) is chosen from VD4-1 in which there is a clear pattern of uptake and (b) the three dimensional structure of the selected ROIs is visualized with slices along the  $z$  direction.

region with many binders-aggregate interfaces. This region is expected to be porous with very small holes, thereby allowing saturated flow through them. Due to this phenomenon, in combination with the film flow in the left corner of pore C, a pink region can be seen between  $x = 10 \text{ mm}$  and  $x = 15 \text{ mm}$  from  $t = 7 \text{ mins}$  onwards, around  $z = 1.96 \text{ mm}$ . Meanwhile, water uptake in pore D starts with film flow on its right side. Going up the specimen, pore D, which is initially not completely closed, reduces in size and splits into two well-defined pores F and G, which are not connected to the surroundings. These two pores most likely display saturated flow as can be seen in the large pink region between  $x = 15 \text{ mm}$  and  $x = 20 \text{ mm}$  from time  $t = 4 \text{ mins}$  onwards. The large yellow region around  $x = 15 \text{ mm}$  at this same time step is due to very little uptake in pore C, which is open to the surroundings.

At  $z = 2.81 \text{ mm}$ , it can be seen that all the three pores (C, F, G) merge into a larger pore, but only for a short distance. At  $z = 3.92 \text{ mm}$ , the merged pores breakup into two new pores, pores H and I. This merging and breakup seems to hinder the further saturated flow through the pores F and G. From the DoS distribution at  $t = 7 \text{ mins}$ , it can be inferred that the new pores H and I now display film flow at their corners, but definitely not saturated flow, because of the large yellow-colored region between  $x = 15 \text{ mm}$  and  $x = 20 \text{ mm}$ . The presence of many small pores between  $x = 10 \text{ mm}$  and  $x = 15 \text{ mm}$  and around  $x = 20 \text{ mm}$  lead afterwards to fully saturated flows in these

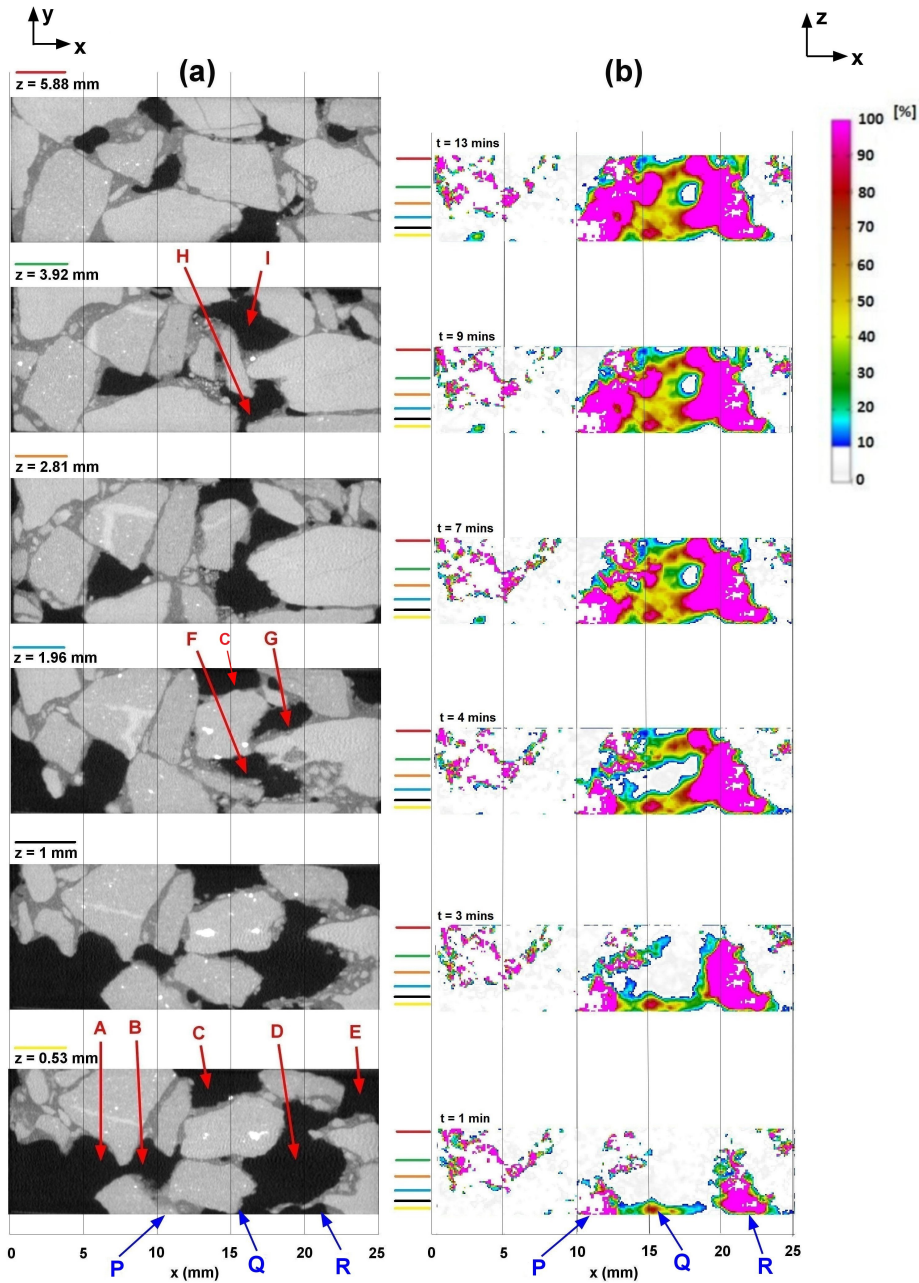


Figure 3.8.: Analysis of mechanism of water uptake in a region of interest (ROI) of VD4-1. (a) X-ray  $\mu$ -CT slices along the  $z$  direction of the selected ROI and (b) degree of saturation (DoS) distribution of the ROI at different time steps. Large pores in the microstructure (A-I) and the positions at which water uptake is initialized (X-Z) are marked. The microstructure of the specimen at a certain  $z$ -value in (a) can be visualized by matching it with the section indicator of the same color in (b).

regions, as can be concluded from the large pink-colored regions at these areas at  $t = 9$  and  $t = 13$  mins. These pores are either completely within the binder or in some cases surrounded partially by aggregate. Thus, these pores are generally smaller than the pores which are surrounded by large aggregates. As water further moves upwards with time, the region around  $x = 20$  mm still has a significant amount of saturated flow due to the presence of many pores in the solid matrix, whose presence only increases along the specimen height. But saturated flow in the region around  $x = 15$  mm reduces drastically since most of the pores in the binder which were present at  $z = 3.92$  mm are now replaced with impervious aggregate.

From this analysis, it is clear that there is a combination of saturated flow and unsaturated film flow in the pores of porous asphalt despite the fact that the binder in the material is hydrophobic. This observation points to a complex interaction of water with the various components of porous asphalt, an aspect which needs to be further investigated in the future. It is also important to note that, in an ideal pore surface, the binder covers all aggregates, leading to a hydrophobic surface throughout the pore system. However, in a real PA, not all surfaces are necessarily covered with binder as shown in previous microstructural investigations (Poulikakos and Partl 2010). This is especially the case for the VD4 specimens as they were in the field for seven years and thereby exposed to water, climate and traffic. Therefore, some of the binder from the aggregate surfaces could have been removed by stripping. This could very well be the reason why no uptake is observed in the laboratory-prepared fresh AG1 specimen, where proper binder coating of the aggregates and no binder degradation is ensured.

#### 3.2.2.8 *Simulation of preferential liquid flow path*

From the previous figures presented in this study, it is seen that water uptake in porous asphalt follows certain preferential paths. In other words, there is no occurrence of uniform waterfront as seen in isotropic microporous materials. Factors like tortuosity, pore accessibility, pore connectivity and pore size play important roles in determining this preferential path. In case of VD4-1, which was in situ for 7 years, many physical and chemical factors will also play a role as part of the solid matrix changes from hydrophobic to hydrophilic due to stripping. In the following analysis, we limit our study to the influence of tortuosity and pore connectivity in determining the direction of the preferential path in VD4-1. For this purpose, the bottom part of the X-ray  $\mu$ -CT scan of VD4-1 is divided into two ROIs, the right ROI (henceforth called RROI) and the left ROI (henceforth called LROI), as shown in Figs. 3.9 and 3.10. From Fig. 3.6, it is clear that during the initial time steps, the RROI has a higher water uptake than LROI, i.e. water travels more easily in the RROI. This characteristic makes the chosen ROIs ideal for the preferential flow analysis.

The software Avizo Fire 8.0 is used for the analysis presented in this section. First, a three dimensional volume of the specimen is rendered from the X-ray  $\mu$ -CT images. Then this volume is segmented with an automatic threshold into pores and non-pores (binders or aggregates). A fully saturated permeability simulation (i.e. absolute permeability) is then performed on this segmented three-dimensional volume. Absolute permeability is computed with a simplified Navier-Stokes equation system, with the following major assumptions:

- the fluid is incompressible and Newtonian,
- the flow is steady-state and in the laminar regime.

A finite volume method with a staggered-grid arrangement is used to solve the Navier-Stokes equations. The permeability experiment is simulated with a pressure difference of 30 kPa between the inlet and outlet, and the main direction of fluid flow is specified to be the  $z$ -direction (along the height of the specimen). The results from the simulations are presented in Figs. 3.9 (for LROI) and 3.10 (for RROI), along with an illustration of the selected ROIs.

Figures 3.9(a) and 3.10(a) are the binary porosity maps of the respective regions of interest. The black pixels represent regions with zero porosity while the grey pixels have a non-zero porosity value. The segmented volume combined with the streamlines of the simulated fluid flow can be seen in Figs. 3.9(b) and 3.10(b). These figures provide a more graphical description of the simulated flow within the material structure. In Figs. 3.9(c) and 3.10(c), for the sake of clarity, the predicted fluid paths are shown without displaying the three-dimensional material structure. In Fig. 3.9(c), it can be clearly seen that there is one major path taken by the fluid, but that this path is highly tortuous. Also, there are many paths which lead to dead ends. These dead-end pores, where the velocity of fluid falls to zero, are marked in Fig. 3.9(c). From Fig. 3.9(a), it can be seen that, in the LROI, there are two clusters of non-porous pixels, one each on the left and right sides. It is on the left cluster that most of the dead-end pore networks are present. Because of the presence of these clusters, the water has to flow upwards between them, which results in the highly tortuous path. Hence, water cannot travel upwards easily in the LROI. On the contrary, it can be seen in Fig. 3.10(c) that there are multiple paths available for water to travel in the RROI, most of which are relatively less tortuous. Also, in Fig. 3.10(a), no big cluster of non-porous pixels is present. Hence, the presence of relatively less tortuous paths with higher pore connectivity could be one of the most important reasons why water travels upward more easily in the RROI, as compared to the LROI.



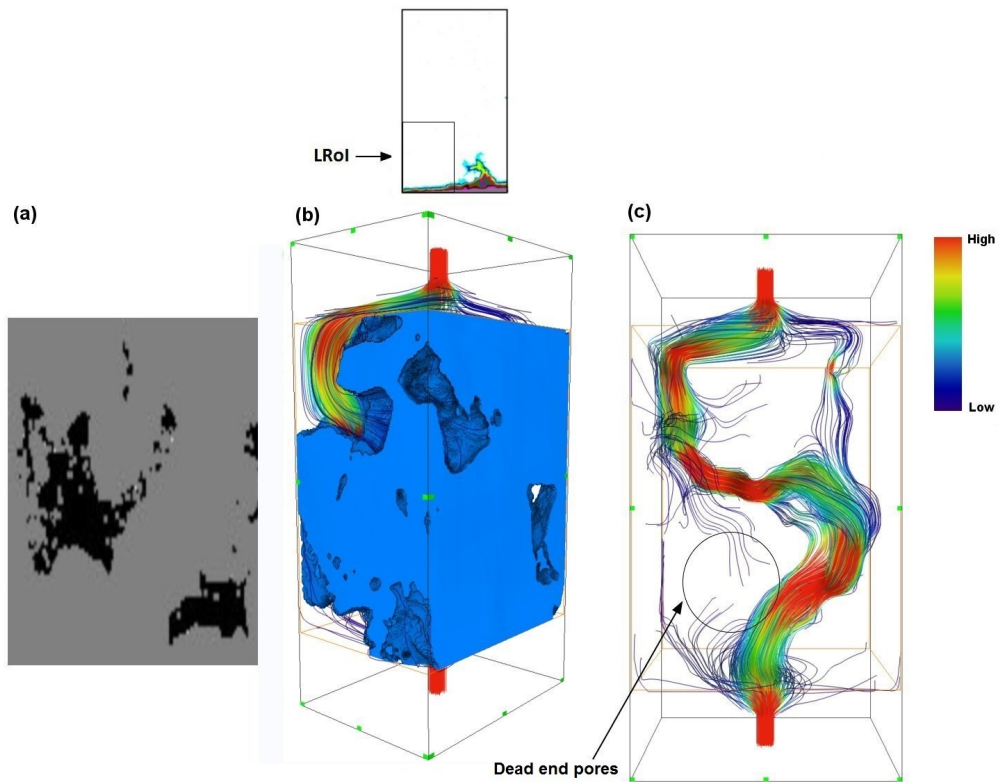


Figure 3.9.: Liquid flow path analysis of left region of interest (LROI) (Specimen VD4-1). (a) Binary porosity map, (b) 3D binary segmentation with a simulated fluid flow in the  $z$  direction and (c) streamlines of the simulated fluid flow through the pore network, where the color map indicates the velocity of water.

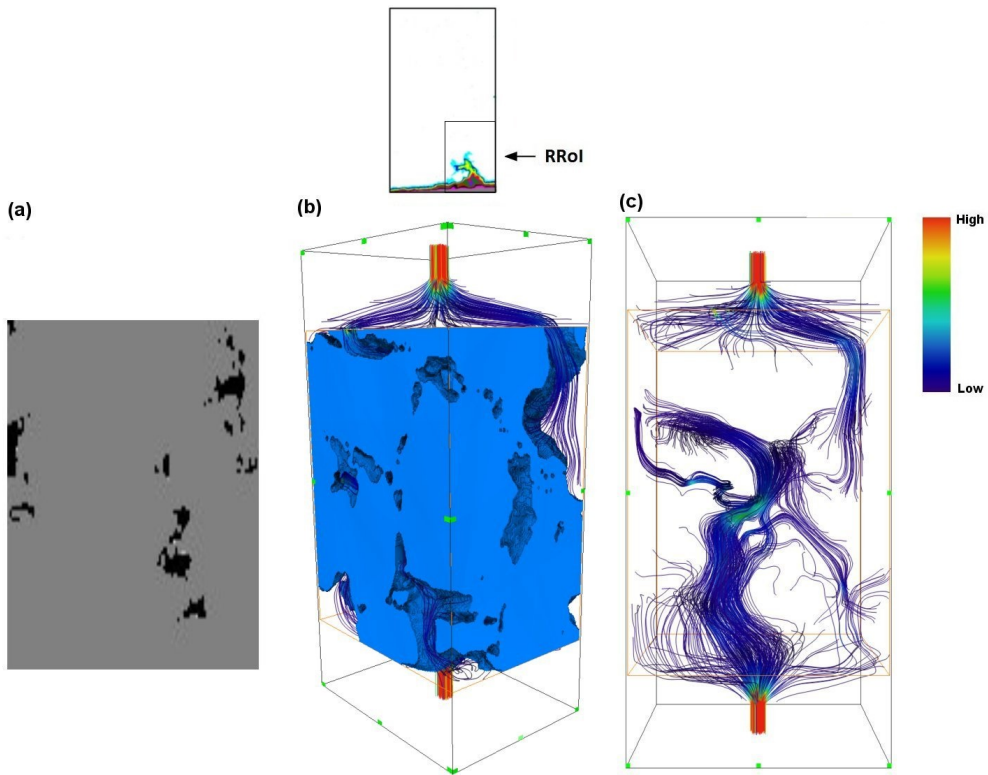


Figure 3.10.: Liquid flow path analysis of right region of interest (RROI) (Specimen VD4-1). (a) Binary porosity map, (b) 3D binary segmentation with a simulated fluid flow in the  $z$  direction and (c) streamlines of the simulated fluid flow through the pore network, where the color map indicates the velocity of water.

### 3.2.3 Conclusions

Water uptake in porous asphalt is studied using neutron radiography (NR) on three different PA specimens. While the laboratory-prepared fresh PA specimens hardly showed any uptake, considerable uptake is seen in the aged specimens taken from the road. Moisture content distribution plots of the aged PA specimens are derived from the NR images, from which the paths followed by water became clearly visible. By combining neutron radiography and X-ray  $\mu$ -CT techniques, saturation degree distributions are plotted, from which the regions where saturated flow was certainly active could be identified. In order to clearly distinguish between saturated flow and unsaturated flow in the other regions, the three dimensional micro-structure of the specimen is combined with its two dimensional saturation degree distributions. It is observed that uptake begins mainly as unsaturated film flow in the large pores which have narrow cross-sections open to the surroundings. As this uptaken water travels further into the material, a combination of saturated flow and unsaturated film flow is observed. Saturated flow is active mostly in the small pores which are completely or partially surrounded by binder. Thus, a succession of both unsaturated and saturated flows in aged PA is observed despite the fact that the bitumen binder in PA is hydrophobic. This is due to the presence of the hydrophilic aggregates now exposed to water, thanks to the stripping of binder from aggregate surfaces due to years of mechanical and environmental loads. Moreover, by simulating an absolute permeability experiment, the roles played by tortuosity and connectivity of the pore system in determining the speed and direction of water uptake is determined. It is found that the region with relatively less tortuous and more connected paths showed faster uptake during the experiments.

## 3.3 DROPLET WETTING EXPERIMENT

The objective of this second NEUTRA experiment is to understand the phenomenon of gravity imbibition in porous asphalt through droplet wetting of PA, a process that mimics the wetting of PA by rainfall. Specifically, the aim is to study the wetting process, which is studied with neutron radiography, with the pore space characteristics of different types of PA, which are studied with X-ray  $\mu$ -CT.

### 3.3.1 Material characterization

#### 3.3.1.1 Preparation

Three types of porous asphalt specimens are used in this study: PA4, PA8 and PA11, whose maximum aggregate sizes (as measured from sieve analysis) are 4, 8 and 11 mm respectively. The mix for the PA8 and PA11 specimens are procured from a local mixing

plant. They conform to Swiss standards and contain 6 mass-% polymer modified bitumen, PmB-E 45/80-65, and 0.2 mass-% cellulose fibers. The PA4 specimens are from an artificial mixture fabricated using only the 2/4 mm fraction minerals, 1 mass-% mineral filler and 7 mass-% straight run bitumen with penetration grade 70/100. As a first step, specimens with dimensions  $180 \times 500 \times 50 \text{ mm}^3$  and an approximate mass of 18 kg are compacted at  $155^\circ\text{C}$  in the laboratory using a rolling compactor. From these large specimens, the bottom 20 mm is cut away and thereafter smaller specimens of dimensions  $180 \times 10 \times 30 \text{ mm}^3$  are cut for the experiments. In this study, one PA4, two PA8 and two PA11 specimens are used. They are named PA4(1), PA8(1), PA8(2), PA11(1) and PA11(2). The top surfaces of these specimens are rough, replicating road pavement conditions. All surfaces except the top one are covered with an aluminium tape. Therefore, gravity-driven drainage is completely blocked and consequently, the only mechanism through which water can exit the specimen is evaporation from the top surface. This is similar to the in situ state after a large rain event, when a fully saturated base below PA makes gravity-driven drainage ineffective and the only form of moisture loss is drying.

### 3.3.1.2 Pore size distribution

The pore structure of the specimens are investigated with an X-ray  $\mu$ -CT setup. The technical specifications of the X-ray  $\mu$ -CT setup are already described in the discussion of the water uptake experiment (Section 3.2.1.2) and are not repeated here. The spatial resolution of the final 3D X-ray  $\mu$ -CT dataset for this experiment is  $103.7 \mu\text{m}$ . Figure 3.11 provides a macroscopic view of specimens PA4(1), PA8(1) and PA11(2). The X-ray  $\mu$ -CT slice ( $x - y$  plane) at the center of the width of the three specimens, i.e. at  $z = 6 \text{ mm}$ , is given in Figs. 3.11(a-c). Figures 3.11(d-f) presents the three dimensional porosity of the specimens as two-dimensional cumulative porosity distributions (CPD). The procedure to calculate 2D CPD from 3D binary scans was previously described in Section 3.2.1.2. It is noted again that, in the CPD figures, each pixel represents the volume porosity at that location. The blackest regions represent the presence of an aggregate which runs along the entire specimen thickness i.e. the porosity is 0, while the whitest regions represent the presence of a void which runs along the entire specimen thickness, i.e. the porosity is 1 or 100%. Intermediate grey values represent porosities between 0 and 100% along the specimen thickness. For separating the void and solid regions of the specimen, the default thresholding algorithm (Huang and Wang 1995) of Fiji/ImageJ is used. Additionally, from the 3D binary stack, the overall porosity volume fractions of the three specimens are calculated using the plugin BoneJ (Doube et al. 2010) of Fiji/ImageJ. The porosity volume fractions are 32.7%, 20.4% and 20.2% for PA4(1), PA8(1) and PA11(2) respectively. The high porosity of PA4(1) is due to the fact that it is an artificial PA mix. Indeed, the porosities of the other two PA specimens, whose mix conforms to Swiss standards, are

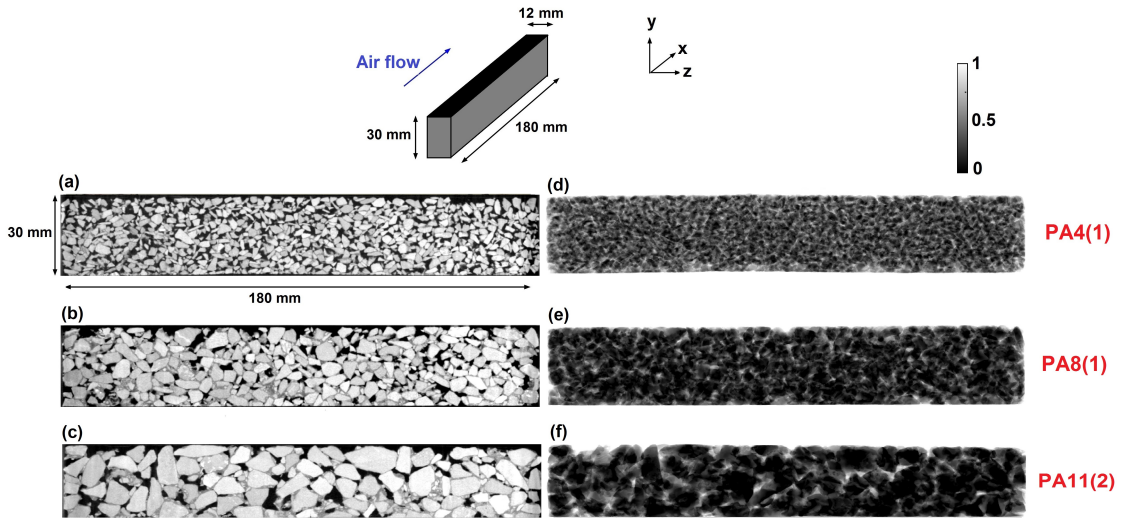


Figure 3.11.: Schematic depiction of the specimens used in droplet wetting experiments (top). X-ray  $\mu$ -CT slices at  $z = 6 \text{ mm}$  of (a) PA4(1), (b) PA8(1) and (c) PA11(2) specimens, and 2D cumulative porosity distribution images in which the porosity ranges from 0 (black) to 1 (white), of (d) PA4(1), (e) PA8(1) and (f) PA11(2) specimens.

around the expected value of 20%. The specimen thickness of 12 mm is not a representative thickness of an actual PA pavement, but the available neutron beam does not have the required energy to go through thicker specimens. However, the specimen dimensions in the other two directions ( $x$ ,  $y$ ) are good representations of an actual pavement since a representative dimension should be 2.5 to 3 times larger than the maximum aggregate size (4, 8 and 11 mm in the current specimens). Nevertheless, using a specimen of another size should not change the qualitative nature of the conclusions drawn from this study.

To obtain a comprehensive understanding of the pore space of the specimens under investigation, a twin-pronged approach is adopted. On the one hand, the pore space is represented as a simplified network of pores connected to each other by throats and the histogram of the pore sizes are analyzed while, on the other, the width as well as the connectivity of the real pore space is visualized using Avizo Fire 8.0. For the former approach, the pore network is extracted from the X-ray  $\mu$ -CT images using the modified Maximal Ball algorithm of Dong and Blunt (2009), which is explained in detail in Chapter 7. In Fig. 3.12, the pore diameter distributions of PA4(1), PA8(1) and PA11(2) as calculated with the MB algorithm is presented. The increase of pore diameters from PA4(1) to PA8(1) to PA11(2) is clearly evident from Fig. 3.12, as the maximum pore diameter increases from 0.8 mm to 7 mm to 10 mm across the three specimens.

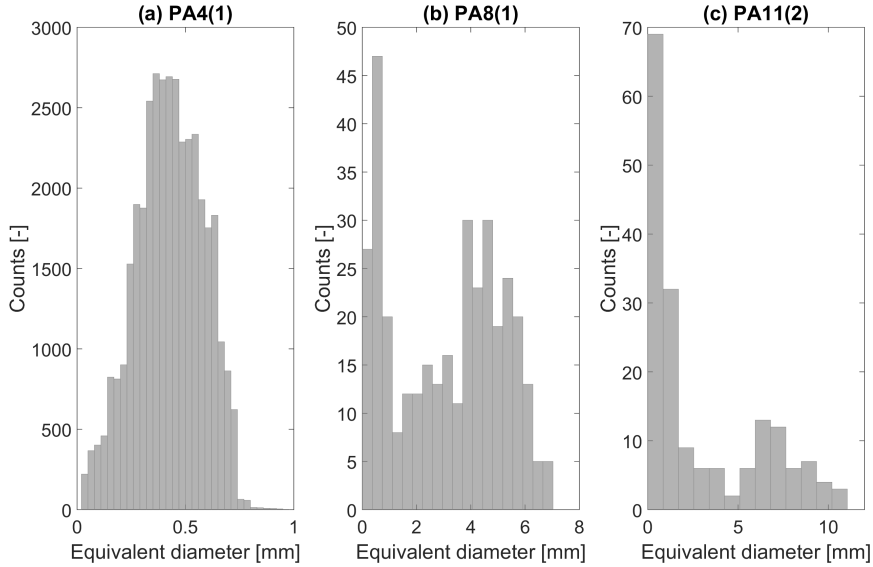


Figure 3.12.: Histograms of the pore diameter distribution of the three specimens in the droplet wetting experiments as calculated with the Maximal Ball algorithm.

Figure 3.13 shows the results of the volume rendering of the pore space of the three specimens with Avizo Fire 8.0. From the X-ray  $\mu$ -CT image stack, the pore space is first segmented with Avizo using interactive thresholding, which was possible due to the distinct peaks in the image intensity map. From the resulting 3D binary image, only the pore space connected to the top surface of the material is segmented since this pore space contains the pores into which water can potentially enter. During segmentation, pore space voxels are assumed to be connected if they shared at least one common face. Thereafter, the pore space is converted to a surface consisting of triangles. Finally, the 'surface thickness' module of Avizo is applied to the generated surface. This module computes the surface-normal distance from each triangle to the opposite edge. Thus, the surface thickness is analogous to the diameter of a perfect sphere and is therefore an ideal parameter to characterize the width of a pore space. From Fig. 3.13, it can be seen that PA4(1) and PA11(2) have a well-connected pore space though the same cannot be said of PA8(1). However, we note that PA4(1) shows this high connectivity due to its high porosity resulting from the uniform aggregate sizes. Overall, it can be said that the pore space of PA11(2) is the most suitable for water entry since it is both well-connected and large enough to counter the resistance by capillary forces.

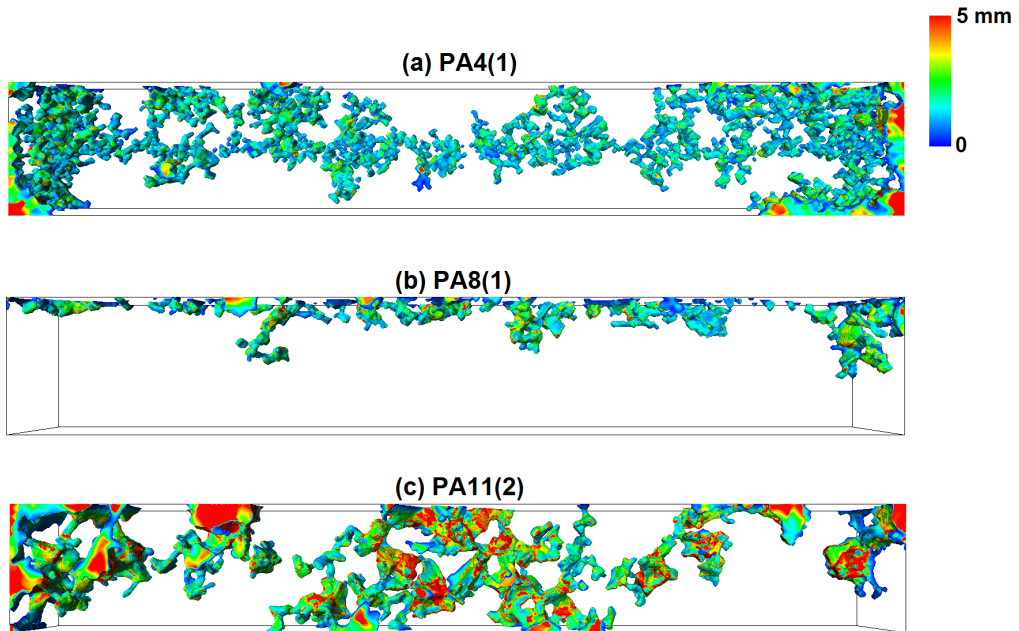


Figure 3.13.: Segmentation of the pore space connected to the top surface of (a) PA4(1), (b) PA8(1) and (c) PA11(2), followed by the conversion of the pore space to a surface consisting of triangles where, at each vertex, the distance along the vertex normal to the normal's intersection with the closest triangle of the same surface is calculated and is indicated by color.

### 3.3.2 *Experimental setup and procedure*

#### 3.3.2.1 *Neutron beamline specifications*

The experiments in this study are also performed at the NEUtron Transmission Radiography beam line of the Paul Scherrer Institute (PSI) in Villigen, Switzerland. The imaging detector consists of a 100  $\mu\text{m}$  thick  $^6\text{Li}$  doped zinc sulfide scintillator screen and a CCD camera. The camera is an Andor iKon-L camera with  $2048 \times 2048$  pixels with a region of interest setting of  $1601 \times 1031$  pixels, providing a field of view of  $262 \times 169$   $\text{mm}^2$ . The exposure time in the experiments was 23 s per radiograph with an attained spatial resolution of 163.6  $\mu\text{m}$  per pixel. The neutron chamber had a temperature of approximately 26  $^\circ\text{C}$  and 40% relative humidity during the imbibition experiments. The processing of neutron radiographs is the same as described above in section 3.2.2.4.

#### 3.3.2.2 *Mini wind tunnel with rain simulator*

A custom-made mini wind tunnel fitted with a rain simulator is used for the droplet wetting experiments, the schematic of which is shown in Fig. 3.14(a). The droplet wetting experiments are one part of an experiment that aims to study wetting, forced convective drying and thermal drying, and therefore a wind tunnel is used as the base setup to which additional components are added. For a description of the entire experimental setup that includes forced convective drying and thermal drying, the reader is referred to Section 4.4.2.1. The test section of the wind tunnel, where the PA specimen is placed during the experiments, is 50 mm high and 105 mm wide. A part of the sidewalls of the test section was made of pure aluminium to minimize neutron absorption and scattering in the region of interest. The wind tunnel is fitted with temperature and relative humidity sensors to gather information about the environmental conditions of the experiment.

Gravity imbibition is studied with a rainfall simulator that generates water droplets with an approximate diameter of 2.1 mm. Although droplets in an actual rain event can have a wide range of diameters ranging from 0.1 to 6 mm, a droplet diameter of 2.1 mm is a common droplet size in moderate to large rain events at various locations (Best 1950; Kubilay et al. 2014) and is easy to generate for experimental purposes. Outlets of twelve 10 mL syringes, mounted on a New Era programmable 12-channel syringe pump (<http://www.syringepump.com/NE-16001800.php#cc>), are connected to the top of the wind tunnel test section via twelve Idex 1531-PEEK Tubing (<http://tinyurl.com/jd9ebvz>), which have an inner diameter of 0.25 mm. The syringe inner diameter has been chosen according to the calculations of De Gennes et al. (2013), who showed that given the tubing inner radius,  $R_i$ , the radius of a droplet discharged from the tubing is calculated as:



$$R = \left( \frac{3}{2f_d} Ca^2 R_i \right)^{1/3}, \quad (3.8)$$

where  $f_d$  is the fraction of the original droplet weight which breaks off from the tube (typically 0.6) and  $Ca$  is the capillary number, which is equal to 2 mm for water-air interface. This setup facilitates the wetting of porous asphalt specimens placed in the wind tunnel by generating twelve 2.1 mm diameter droplets at twelve equispaced locations (13 mm separation) that are spread across the length of the specimens, as shown schematically in Fig. 3.14(b). The drop impact velocity at the point of contact is approximately 1 m/s.

### 3.3.2.3 Procedure

A dry specimen, that is covered with aluminium tape on all sides except at its the top surface, is first placed in the test section of the mini wind tunnel. Thereafter, the neutron beam is activated and then the multi-syringe pump is switched on to start the droplet wetting process, which lasts for a total duration of 5 minutes. The average flow rate for each syringe during the wetting is 0.0007 ml/sec. This procedure allows the entire droplet wetting process to be captured by neutron radiography. Neutron radiographs are acquired every 30 seconds.

### 3.3.3 Results and discussion

Imbibition in macroporous media is largely dependent on the pore size distribution and connectivity of the pore space as well as the wettability of the solid matrix, and to a lesser extent on the surface roughness of the solid matrix. The wettability of the different specimens in this study is expected to be similar due to their similar chemical composition. However, it should be noted that a fresh specimen with bitumen covering most of the aggregate surfaces is expected to be hydrophobic as contact angles with water will be in the range of 100-110° (Poulikakos and Partl 2012). The most important variation among the specimens used in this study is the pore size distribution. Therefore, in this section, the effect of pore size distribution on moisture penetration into the porous structure is investigated. In Fig. 3.15, the temporal evolution of moisture content in the specimen along the specimen depth is plotted for all the five specimens used in this study. Profiles are shown for every 30 seconds during the first 25 minutes of each experiment. Each point in Fig. 3.15 represents the average moisture content of all the pixels at that particular height. It can be clearly observed, from Figs. 3.15(a-f), that moisture penetrates the PA4 and PA8 specimens only up to a depth of 5 mm from the top. However, in the two PA11 specimens, moisture penetrates down through the entire specimen, as can be seen in Figs. 3.15(g-h). Even though the pore sizes of PA8(1) are larger than those of PA4(1), as can

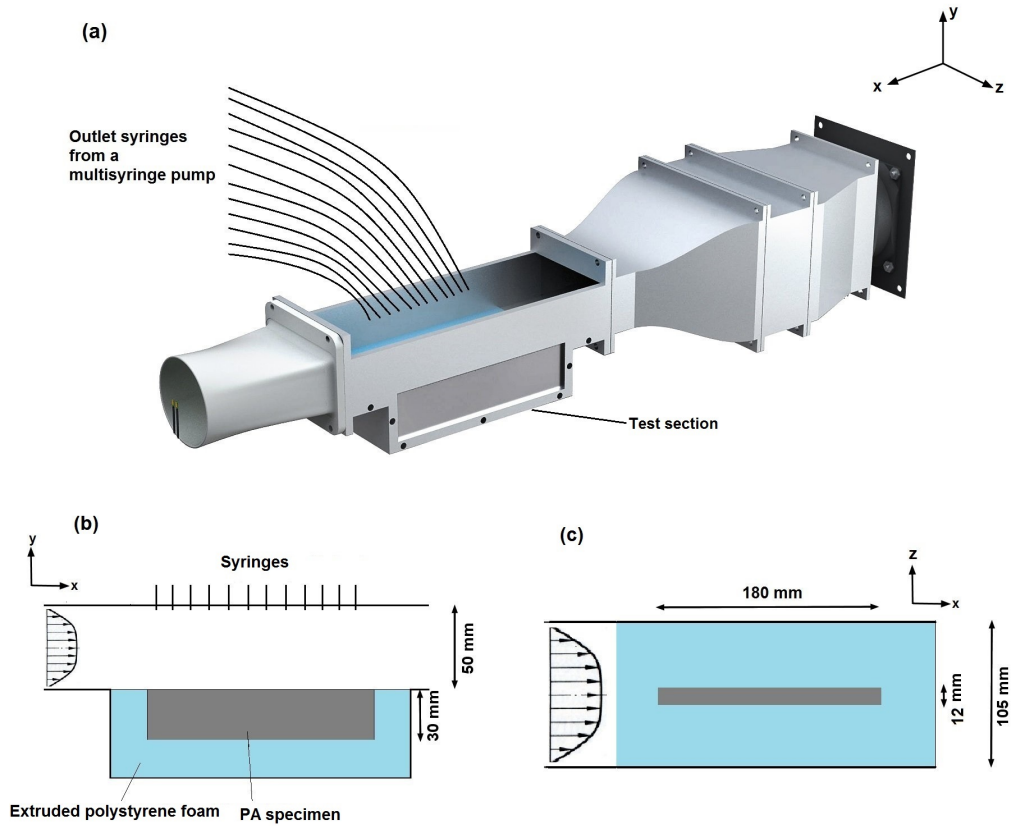


Figure 3.14.: (a) Schematic representation of the experimental setup consisting of a mini wind tunnel and a multi-syringe pump (not shown) which acts as a droplet generator. The outlets of the droplet generator are positioned directly above the test section of the wind tunnel where the specimens are placed during the experiments. (b) Side-view of the test section with a PA specimen inside and (c) top view of the test section.

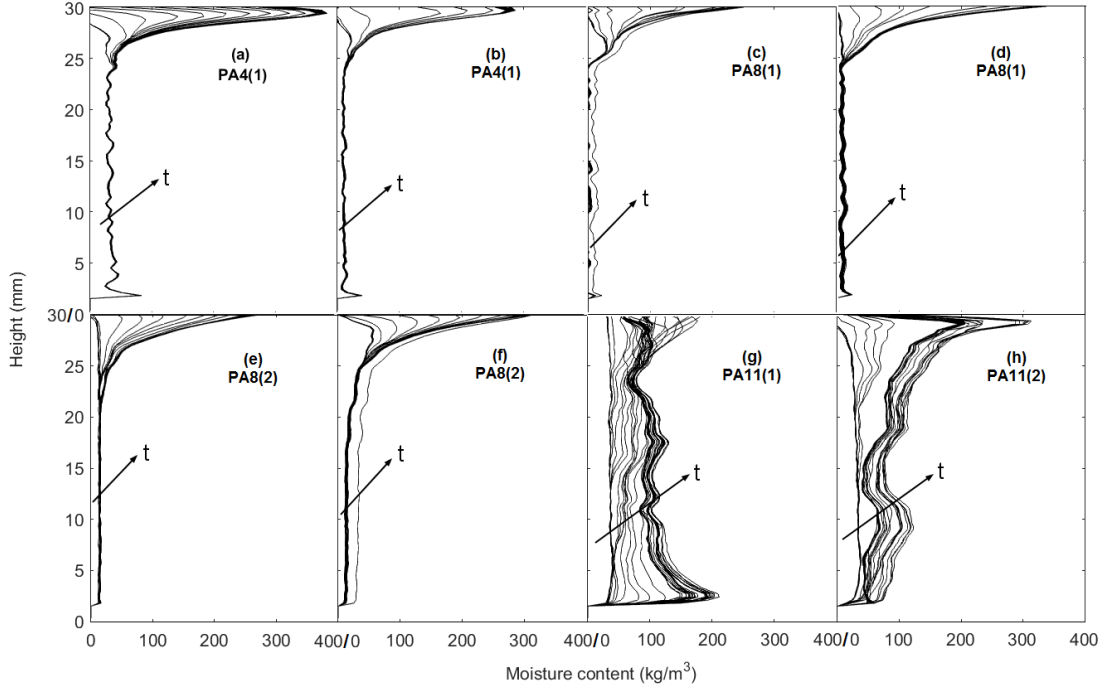


Figure 3.15.: Temporal evolution of moisture profiles during the droplet wetting experiments. PA4 and PA8 specimens are subjected to droplet wetting twice, for repeatability. Profiles are shown for every 30 seconds in the first 25 minutes of the experiment.

be seen from Fig. 3.13, this difference is not large enough to change the wetting behavior significantly. However, in case of PA11, the larger pore sizes result in a completely different wetting pattern due to the strong influence of gravity. Specifically, the presence of pores of diameters ranging from 6 to 11 mm in PA11, as read from Fig. 3.12(d), and the resulting low capillary pressure in them, enables the static pressure head of water in these pores to easily overcome the resistance from the capillary force and thereby leads to a high water penetration. However, we note that these findings are applicable only for wetting by discrete droplets and not when water is poured over the specimens, in which case water shows significant penetration across all the specimens (see Section 4.4.3).

In Fig. 3.16, the temporal and spatial evolution of the degree of saturation (DoS) of the specimens, as defined by eq. (3.7), is plotted for the entire wetting duration of 5 minutes and a few minutes thereafter. For better visualization, a smaller region of interest (ROI) of  $30 \times 30 \text{ mm}^2$  is chosen from the center of the specimens for the DoS analysis. The penetration of water into the internal structure of PA11(1) can be clearly seen in Fig.

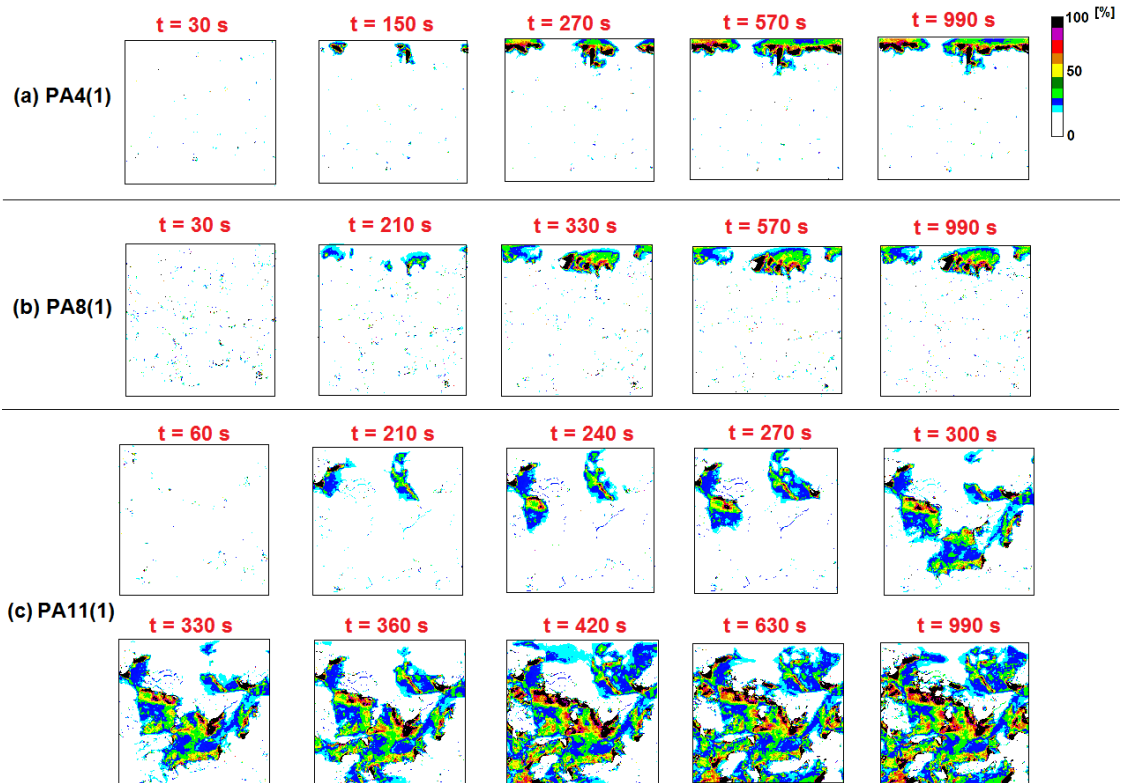


Figure 3.16.: Temporal evolution of the degree of saturation during the droplet wetting of (a) PA4(1), (b) PA8(1) and (c) PA11(1). For clear visualization, a smaller region of interest (ROI) of  $30 \times 30 \text{ mm}^2$  is chosen from the center of the specimens. Since only PA11(2) shows significant water penetration, additional time steps are added to the analysis of this specimen.

3.16(c). In PA4(1) and PA8(1), water droplets remain at the top surface of the specimens and coalesce to form discrete wet patches while in PA11(1), droplets start penetrating into the specimen from the first droplet fall and travel the entire specimen depth by  $t = 330$  s. The fact that it took more than 5 minutes for water to penetrate the entire depth of PA11(1) despite its large pores gives a further indication of the tortuous nature of the pore network of PA.

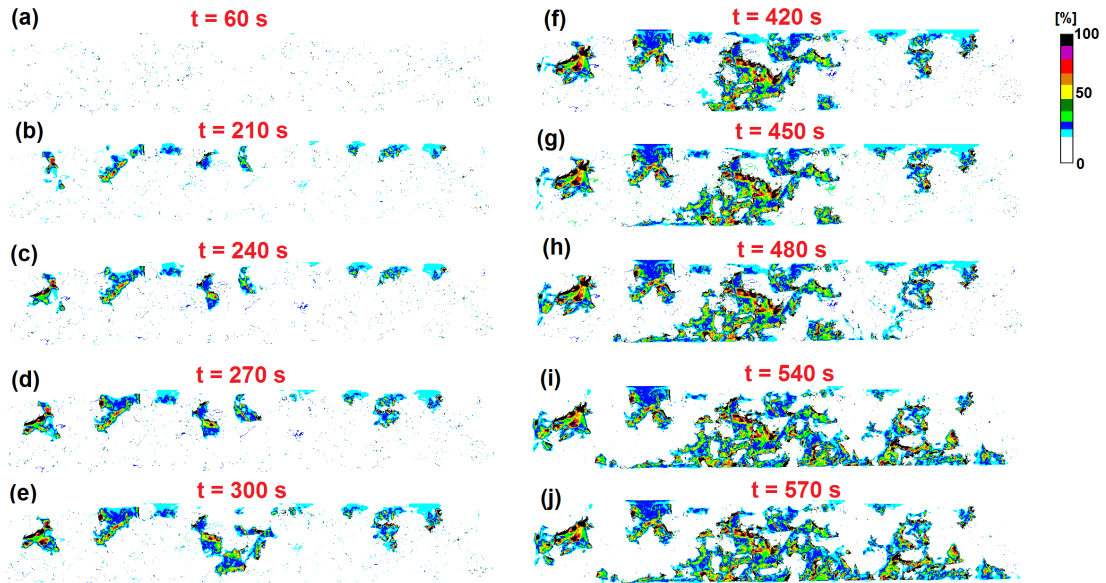


Figure 3.17.: Temporal evolution of the degree of saturation in the entire PA11(1) specimen during droplet wetting

As a result of the significant imbibition of water into the internal pore space of PA11(1), the temporal evolution of the degree of saturation in the entire PA11(1) specimen is analyzed in Fig. 3.17. As already observed from Fig. 3.16, water droplets initially accumulate at the upper region of the specimen until  $t = 300$  s, at which point water is seen to penetrate the entire depth of the specimen (in the middle region). In the next time steps thereafter, there is a co-occurrence of two phenomena: water in the middle region spreads laterally and water starts to move from top to bottom at the right region of the specimen. This co-occurrence ensures that water is spread across almost the entire specimen by  $t = 570$  s. Significantly, Fig. 3.17 shows the importance of lateral redistribution of water during an imbibition process in PA, and therefore, this process is analyzed in more detail.

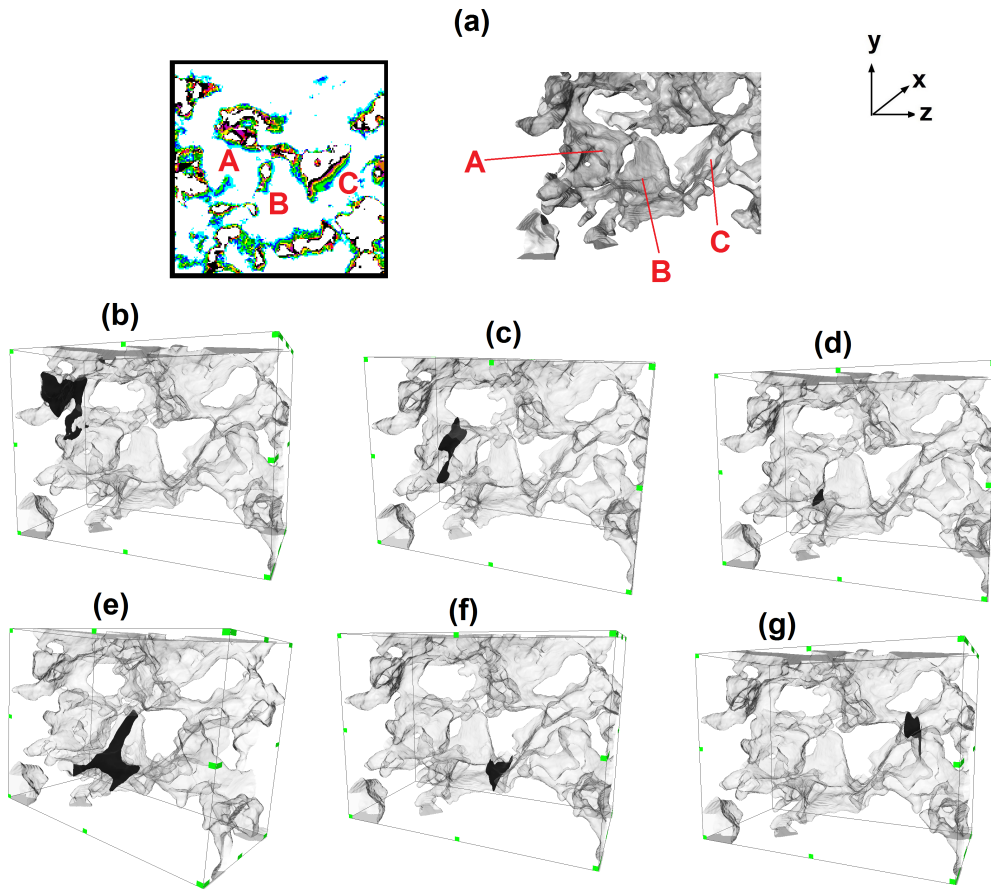


Figure 3.18.: Analysis of gravity imbibition in a  $30 \times 30 \text{ mm}^2$  region of interest (ROI) (the same ROI that is used in Fig. 3.16(c)) at the center of PA11(1). Three well-defined pores, named A, B and C, as observed from neutron radiographs, are also identified from reconstructed X-ray  $\mu$ -CT images, as shown in (a), and the predicted water path along these pores is shown in (b)-(g).

From Figs. 3.16(c) and 3.17, it appears that gravity imbibition in PA11(1) is mainly due to unsaturated flow, as the degree of saturation is less than 50% at most regions. However, to obtain a definitive picture, further analysis is required. Therefore, the PA11(1)  $30 \times 30 \text{ mm}^2$  ROI of Fig. 3.16(c) is chosen for further analysis as it shows significant water imbibition. As shown in Fig. 3.18(a), three well-defined pores are identified from the neutron radiographs and these pores are named A, B and C. Figure 3.18(a) also shows a 3D reconstruction of the same pore space with Avizo Fire 8.0, and the three pores of interest are also marked in the 3D reconstruction. In Figs. 3.18(b-g), the path taken by

water between  $t = 210$  s and  $t = 310$  s in PA11(1), as shown in Fig. 3.16(c), is visualized in the actual 3D pore space. The regions in black show the intersection of the  $x - y$  plane with the pore cross-section. The intersection of the plane with all other pores except A, B and C are not shown for clarity. However, it is found that the black regions shown in the figure does not overlap significantly with the corresponding  $x - y$  plane intersection of other pores, in the  $x$  direction. In other words, the preliminary observation made from two-dimensional neutron images that unsaturated flow occurs in pores A, B and C is valid, as there are no other large pores in the direction of the neutron beam. Thus, it can be concluded that fast imbibition in PA as a result of gravity is a mix of both saturated and unsaturated flows, similar to what was observed for capillary uptake. Unsaturated flows can be especially important in the fast lateral redistribution of water, as is seen in the case of PA11(1).

### 3.3.4 Conclusions

Gravity imbibition in porous asphalt is studied using neutron radiography (NR) for three different types of PA, PA4, PA8 and PA11, with increasing pore sizes. A custom-made wind tunnel with a multi-syringe droplet generator is used for the experiments. The pore size distributions of the three specimens are extracted from X-ray  $\mu$ -CT scans using the Maximal Ball algorithm. While PA11 exhibited strong gravity imbibition, the other types of PA did not exhibit any. The presence of pores ranging from 6 to 11 mm diameter in PA11 is responsible for the strong gravity imbibition. While saturated gravity-driven flow is primarily responsible for gravity imbibition in PA11, fast lateral redistribution of water is also observed due to unsaturated flow in the pore corners. Therefore, gravity imbibition in PA, like capillary uptake, is also a mix of saturated and unsaturated flows.

## 3.4 SYNTHESIS

This chapter analyzed in detail the mechanisms of capillary imbibition and gravity imbibition in porous asphalt through a water uptake experiment and droplet wetting experiment respectively. The distinct imbibition behavior of PA due to its highly complex and macroporous structure was clearly evident in these experiments. In the next chapter, the reverse phenomena of imbibition i.e. drainage and drying in PA, are studied experimentally.





## EXPERIMENTAL INVESTIGATION OF DRAINAGE AND DRYING IN POROUS ASPHALT

---

### 4.1 INTRODUCTION

This chapter presents the experimental investigations to study the spatial and temporal distributions of moisture in porous asphalt specimens subjected to gravity-driven drainage, forced convective drying and thermal drying. The experiments are performed at NEUTRA in a custom-made mini wind tunnel. In the first set of experiments, the co-occurrence of gravity-driven drainage and forced convective drying in PA is investigated. In the second set of experiments, gravity-driven drainage is completely blocked and therefore, the only mechanism by which moisture can leave the specimen is through forced convective drying and thermal drying. The spatial and temporal distributions of moisture during both the experiments are once again tracked using neutron radiography. Finally, by comparing the two sets of experiments, the influence of gravity-driven drainage on the total moisture loss from PA specimens is isolated.

### 4.2 DESIGN OF MINI WIND TUNNEL

The experiments presented in this chapter, as well as the droplet imbibition experiment in the previous chapter, are performed using a mini wind tunnel which reproduces environmental loads such as solar radiation, wind and rain. The mini wind tunnel has undergone different levels of customization for each experiment, which is described in the discussion of the respective experiments. The purpose of this section is to describe the design of the basic components of the wind tunnel.

The mini wind tunnel is an open-circuit type wind tunnel i.e. airflow is not confined within a closed loop. The main components of the mini wind tunnel are (i) the axial fan, (ii) inlet diffuser, (iii) settling chamber, (iv) contraction, (v) entry section, (vi) test section and (vii) outlet. The axial fan produces a static pressure rise which generates turbulent, swirling airflow. The airflow generated by the fan first passes through the inlet diffuser, which is a gradually expanding passage in which the flow speed decreases and static pressure increases. This reduction in speed is performed to reduce the pressure loss in the settling chamber, where components are located that have a large resistance to airflow. Thereby, the power required to drive the wind tunnel is reduced. The settling chamber

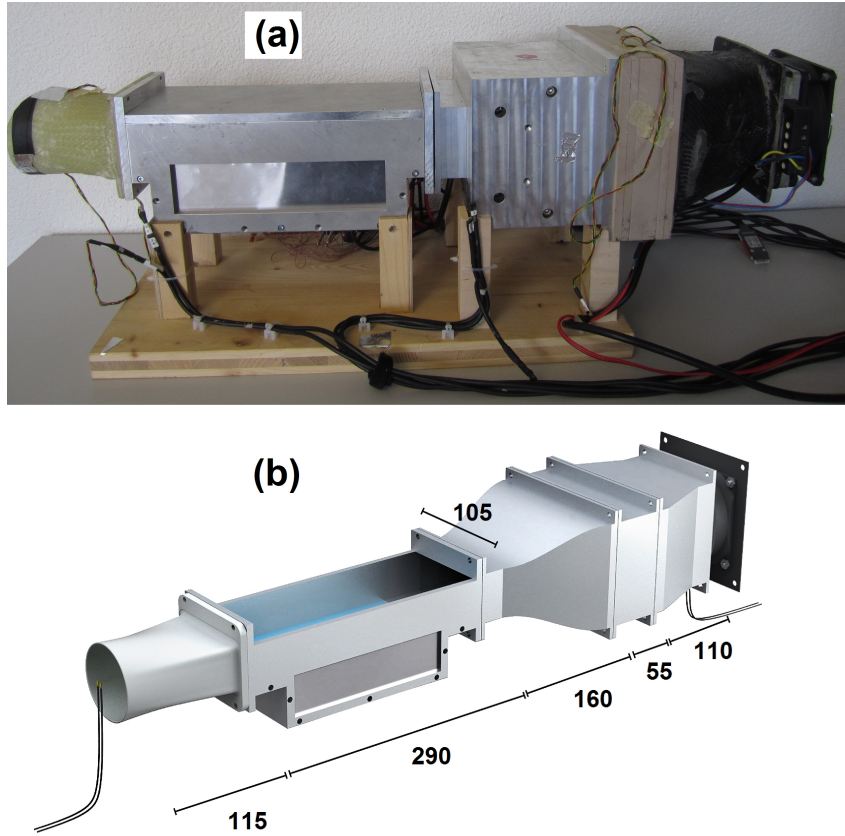


Figure 4.1.: (a) Photograph and (b) schematic with major dimensions of the mini wind tunnel designed and developed in this study. All dimensions are in mm.

has the largest cross-section in the wind tunnel and holds two components: a honeycomb and a screen. These components reduce lateral and streamwise velocity fluctuations, and therefore, reduce turbulence. Airflow then passes through the contraction, which accelerates the flow from the settling chamber to the entry section, and also reduces velocity fluctuations. The test section is the component where the material under investigation is placed during the experiments. The overall aim of wind tunnel design is to produce as low-turbulent, uniform airflow as possible in the test section to have well-defined flow conditions in the test section.

A photograph of the mini wind tunnel is given in Fig. 4.1(a) while its basic dimensions are given in Fig. 4.1(b). The key design constraint of the mini wind tunnel was making it compact enough to fit in the sample stage of the NEUTRA beamline. The most important design parameter is the width to height ratio of the test section, which is 2.1 for the mini

wind tunnel, which is within acceptable limits (Bell and Mehta 1989). The dimensions of all other components are based on the dimensions of the test section. The lateral edges of the test section are made of pure aluminium to minimize neutron attenuation when the mini wind tunnel is placed in a neutron beam. Other key parameters which determine the quality of airflow in the test section is the contraction ratio (ratio of inlet cross-section to outlet cross-section) and the length to inlet height ratio of the contraction. These two parameters are 2 and 0.92 respectively for the mini wind tunnel. A two-dimensional curvature is given for the contraction, as can be seen in Fig. 4.1(b). The honeycomb-screen combination is designed according to the recommendations of Kulkarni et al. (2011), with a honeycomb cell size of 0.005 m. The inlet diffuser has an expansion ratio of 1.5.

### 4.3 GRAVITY-DRIVEN DRAINAGE AND FORCED CONVECTIVE DRYING

The objectives of this study are twofold: to estimate the overall moisture loss from fully saturated PA specimens due to the co-occurrence of gravity-driven drainage and forced convective drying, and to understand the mechanisms by which water leaves the specimen and is redistributed within the specimen due to capillary effect and gravity. As shown in the previous chapter, by combining neutron radiography images with pore structure information obtained from X-ray microcomputed tomography scans, a clear distinction is made between saturated and unsaturated flows within the PA structure. In addition, by reconstructing the real 3D PA geometry from X-ray  $\mu$ -CT scans, the flow path of water within the specimen during certain events is visualized.

#### 4.3.1 *Material characterization*

##### 4.3.1.1 *Preparation*

The two porous asphalt materials used in this study, PA8 and PA11, are obtained directly from a local mixing plant. They satisfy Swiss standards and contain 6 mass-% polymer modified bitumen, PmB-E 45/80-65, and 0.2 mass-% cellulose fibers. PA8 has a maximum aggregate size of 8 mm whereas PA11 has a maximum aggregate size of 11 mm. Specimens with dimensions  $180 \times 500 \times 50 \text{ mm}^3$  and an approximate mass of 18 kg are compacted at  $155 \text{ }^\circ\text{C}$  in the laboratory using a rolling compactor. Thereafter, the bottom 20 mm is cut away and the final specimens are cut to dimensions of  $180 \times 10 \times 30 \text{ mm}^3$ . The top surface of the specimen is rough, replicating field conditions. In this study, three PA8 and three PA11 specimens are investigated. The specimens are named PA8(A), PA8(B), PA8(C), PA11(A), PA11(B) and PA11(C). During the experiments, specimens PA8(A) and PA11(A) are taped at the bottom  $x - z$  plane (Fig. 4.2) with an aluminium tape to constrain gravity-driven drainage. This configuration closely replicates in situ conditions

as the interface to the next asphalt layer is sealed and as a result, the drainage occurs sideways. All the other four specimens are open on all sides during the experiment.

#### 4.3.1.2 *Cumulative porosity distribution from X-ray microcomputed tomography*

The X-ray  $\mu$ -CT setup used to obtain the three dimensional pore space data is already described in detail in the previous chapter (Section 3.2.1.2) and is not repeated here. The specimens are mounted together at a distance of 503.2 mm from the X-ray source and a distance of 467 mm from the detector. From a pixel size of 200  $\mu\text{m}$  and a geometrical magnification of  $\sim 1.9$ , a spatial resolution of 103.7  $\mu\text{m}$  is obtained in the final 3D dataset. The chosen tube parameters are an acceleration voltage of 200 kV and a nominal current of 100  $\mu\text{A}$ . In order to reduce artefacts, the X-ray spectrum is hardened by means of a 1 mm Cu filter. For each scan, a region of interest of  $1000 \times 2000$  pixels is chosen given the elongated geometry of the objects. 720 radiographic images are recorded with a total integration time of 10 s per image from different viewing angles distributed over  $360^\circ$  in  $0.5^\circ$  steps. The X-ray detector is calibrated before the start of the measurement and no additional dark and flat field corrections are necessary. After ring and beam hardening artefact corrections, the three-dimensional spatial distribution of the attenuation coefficient is calculated by an in-house Feldkamp code (Feldkamp et al. 1984). For overlapping of the X-ray  $\mu$ -CT images with the neutron radiography images as described in Section 3.2, the spatial resolution of the X-ray  $\mu$ -CT images is reduced to 150  $\mu\text{m}$  by bilinear interpolation.

In Fig. 4.2, visible light photographs (a,f), X-ray  $\mu$ -CT slices at  $z = 1 \text{ mm}$  (b,g),  $z = 5 \text{ mm}$  (c,h), and  $z = 9 \text{ mm}$  (d,i), and the two dimensional cumulative porosity distributions (CPD) obtained from reconstructions of 3D X-ray  $\mu$ -CT scans (e,j), are shown for one specimen each from the PA8 and PA11 types of material. Similar to Figs. 3.1 and 3.11, in the CPD figures in Fig. 4.2, the blackest regions represent the presence of an aggregate along the entire thickness ( $z$ -direction) of the specimen i.e. the porosity is 0, and the whitest regions represent the presence of a pore space along the entire thickness of the specimen i.e. the porosity is 1. Intermediate grey values represent porosities between 0 and 1 along the specimen thickness.

### 4.3.2 *Experimental setup and procedure*

#### 4.3.2.1 *Neutron beamline specifications*

The technical specifications of the fixed components of the NEUTRA beamline have already been described in the previous chapter and are not repeated here. For this experiment, an Andor iKon-L camera is used with  $2048 \times 2048$  pixels with a region of interest setting of  $1370 \times 1010$  pixels, providing a field of view of  $206 \times 152 \text{ mm}^2$ . The exposure time in the experiments is 23 s per radiograph with an attained spatial resolution of 150  $\mu\text{m}$  per pixel.

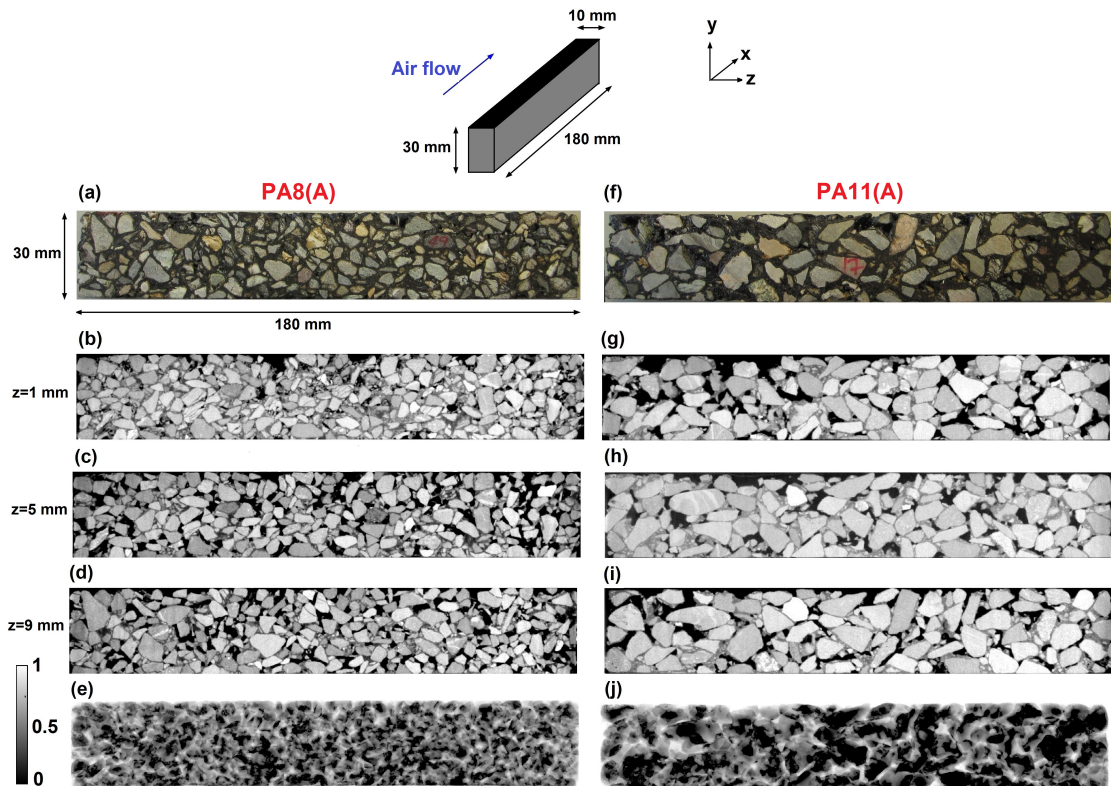


Figure 4.2.: Schematic depiction of the specimen (top). Visible light photographs (a,f), X-ray  $\mu$ -CT slices at  $z = 1$  mm (b,g),  $z = 5$  mm (c,h), and  $z = 9$  mm (d,i) and 2D cumulative porosity distribution images (e,j), in which the porosity ranges from 0 (black) to 1 (white), of PA8(A) and PA11(A) specimens.

The moisture content resolution is expected to be around the range of  $0.01 \text{ kg/m}^3$ . The neutron chamber had a temperature of approximately  $26 \text{ }^\circ\text{C}$  and 40% relative humidity during the experiments.

#### 4.3.2.2 *Mini wind tunnel with remote drainage*

The mini wind tunnel used for this experiment was described in detail in Section 4.2. The schematic of the test section in this experiment is given in Fig. 4.3. The test section, where the PA specimen is placed during the experiments, is 50 mm high and 105 mm wide. For this experiment, the test section of the wind tunnel is designed to be drained remotely. Once drainage is activated remotely, water flows out from the test section via a tube that is connected to the base of the test section (not shown in figure). The wind tunnel is fitted with temperature and relative humidity sensors to gather information about the neutron chamber environment. During the experiments, the fan is operated at a voltage of 8 V, which translates to a mean wind speed of approximately 1.5 m/s, as measured by an anemometer. At this speed, the calculated Reynolds number at the test section, using the height of the channel as the representative length, is  $\text{Re}=6500$ , indicating turbulent flow in the channel.

#### 4.3.2.3 *Procedure*

The drainage and drying behaviors of three PA8 and three PA11 specimens from a fully saturated state are documented in this study. The specimens are first submerged in deionized water for at least 8 hours. Previous laboratory tests showed that this is a sufficient time for the specimen to be fully saturated with water. At the beginning of each experimental run, a specimen is taken out of water, its sides are wiped with a cloth to ensure that no water is dripping out any more and the mass of the specimen is recorded on a microbalance. The specimen is then placed in the test section of the mini wind tunnel and the test section is flooded with deionized water. This step ensures that all pores that emptied during the transfer of the specimens from a submerged state to the test section are refilled with water again, thereby ensuring that the specimen is fully saturated when the experiment begins. Once the neutron beam is activated and the first two images are acquired, the water in the test section is drained via a remote-controlled valve. Due to the neutron imaging procedure of acquiring an image every 30 s, the first wet image of the specimen in an experimental run is therefore the third image of that run i.e. the image at  $t = 90 \text{ s}$ . Initiating the draining procedure by remote control makes it possible to record the gravity-driven drainage in the PA specimens that occurs in the first few minutes. When the drainage process is completed, i.e. after 60 or 120 minutes, the fan in the mini wind tunnel is switched on to initiate forced convective drying of the specimen. This way, the impact of airflow on the total moisture loss from the specimen

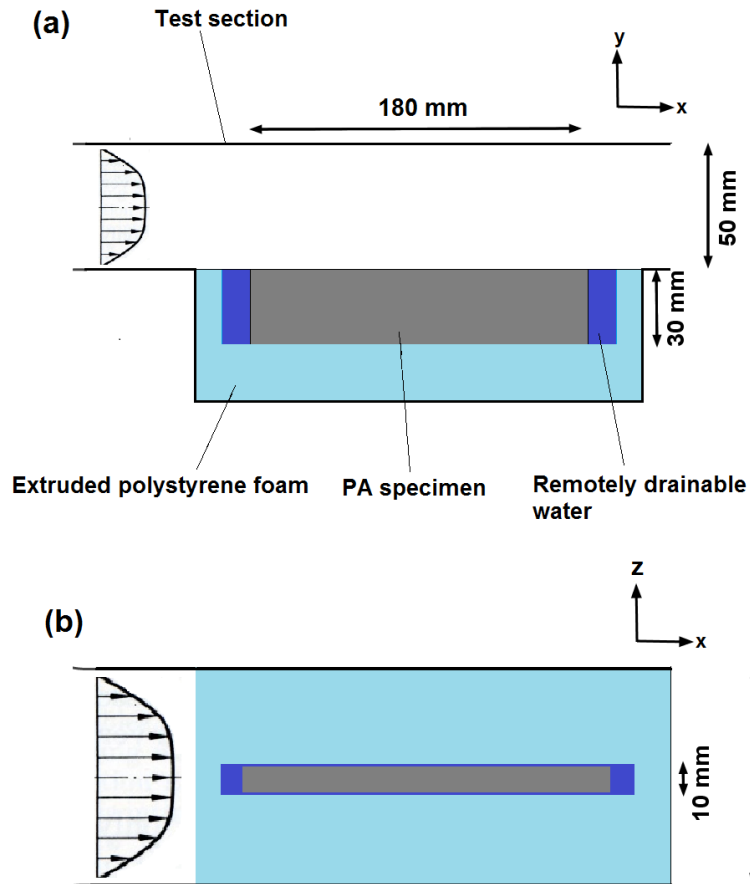


Figure 4.3.: Schematic representation of the test section of the wind tunnel with a provision for remote-controlled drainage of water. (a) Side view and (b) top view.

can be identified. The total duration of the experimental runs varied from 6 h to 11 h. At the end of each experimental run, the specimen is taken out of the test section and its mass is again recorded by weighing. The specimen is then dried inside a convection oven at 55 °C and its mass is monitored. Once fully dry, a neutron image of the dry specimen is acquired as a reference image, allowing the quantification of moisture content in wet specimens by subtracting the dry image from the wet images. The mass measurements of the specimen taken at the different stages of wetness are used as control values for the corrections of the water mass detected by neutron radiographs.

### 4.3.3 *Results and discussion*

#### 4.3.3.1 *General observations*

The post processing of neutron radiography images to account for various corrections and the subsequent derivation of specimen moisture content has already been explained in detail in the previous chapter (Sections 3.2.2.4 and 3.2.2.5) and is not repeated here. Due to the wide range of pore sizes in PA ranging from sub-microns to millimeters, a combination of different mechanisms such as gravity-driven drainage in the macropores, capillary-driven flow in the finer pores and evaporation are expected to occur simultaneously. In this discussion, moisture flow within the specimen is analyzed in detail to separate the different mechanisms from each other, and the conditions under which they occur are also investigated.

Figure Fig. 4.4 shows the temporal evolution of the average moisture content (in  $\text{kg/m}^3$ ) in all the specimens analyzed in this study. The time at which the fan is switched on for each of the specimens is indicated by an arrow on its corresponding curve. The most apparent observation from Fig. 4.4 is the higher water retention by specimens PA8(A) and PA11(A), both of which are taped at the bottom. As mentioned earlier, this condition is the closest to the real in situ situation. This high water retention occurs despite the fact that the lateral sides of the specimens are open and gravity-driven drainage can take place through the sides as well. The other specimens show a high initial moisture loss, which shows the significance of the contribution of gravity-driven drainage from the bottom side towards the overall water loss from a specimen. It can also be observed that switching on the fan does not increase the rate of moisture loss significantly in any of the specimens, which indicates that at a mean wind speed of 1.5 m/s, the enhancement of drying by forced convection is limited. As a result, the slope of the curves in Fig. 4.4 does not change after the time at which the fan is switched on. There is no significant difference between the drainage and drying behaviors of PA8 and PA11. This is due to the fact that the pore size distribution is only one of the factors influencing drainage and drying. Other factors such as pore connectivity and overall porosity are also important. However, as the available



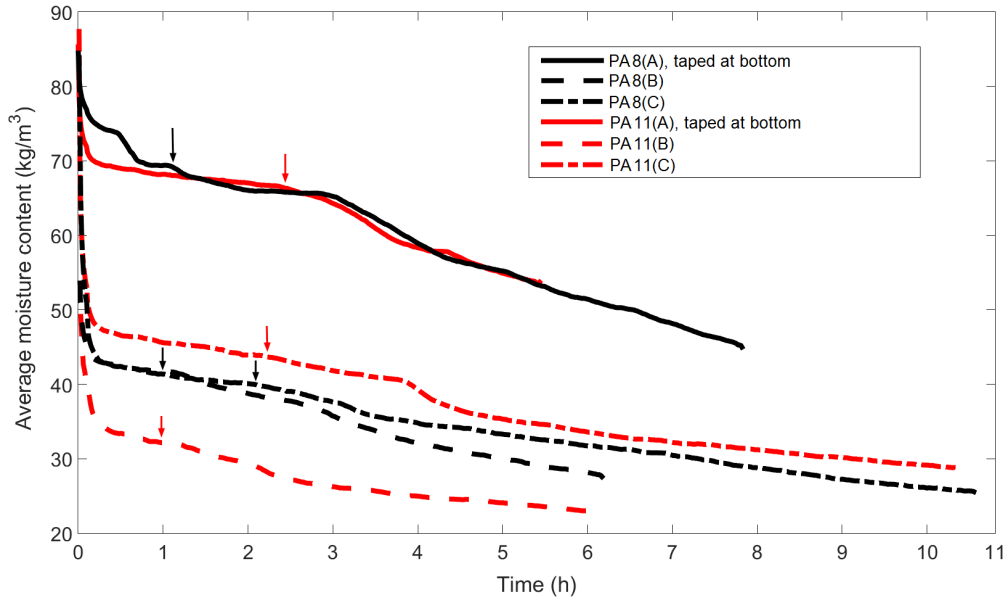


Figure 4.4.: Temporal evolution of average moisture content in the six specimens used in this study. Arrows indicate the time at which the fan is switched on.

neutron beam does not have the energy to go through very thick specimens, the specimen thickness in this study is restricted to 10 mm and, consequently, the behavior of these specimens will not be totally representative of PA at the pavement scale. Since pore sizes in PA11 are in the range of 5-10 mm, an ideal representative thickness is at least 30 mm.

Moisture content profiles along the height of the specimens are given as a function of time in Fig. 4.5. In these images, at each selected time step, the moisture content is averaged over the entire length of the specimen (180 mm) for every 0.3 mm (2 pixels) along the specimen height i.e. along the direction of gravity. The profiles are plotted for every 30 s for the first 15 mins, every 2.5 mins for the next 2 h and every 5 mins for the remaining duration of the experiment. In Fig. 4.5(b), it can be seen that PA11(B) loses a lot of moisture in the first few time steps, which explains the steep drop of the average moisture content curve of PA11(B) in Fig. 4.5. In general, at the bottom part of the specimens, there is a significantly higher moisture loss in the first few time steps, except in specimens PA11(A) and PA8(A), since they are taped. Thus, Fig. 4.5 gives a first indication of the importance of gravity-driven drainage, an aspect which will be explored in detail below. Another observation from Fig. 4.5 is that in case of the untaped specimens, the bottom part of the specimens shows a higher moisture content than the upper part even towards the end of the experiments. This higher moisture content at the

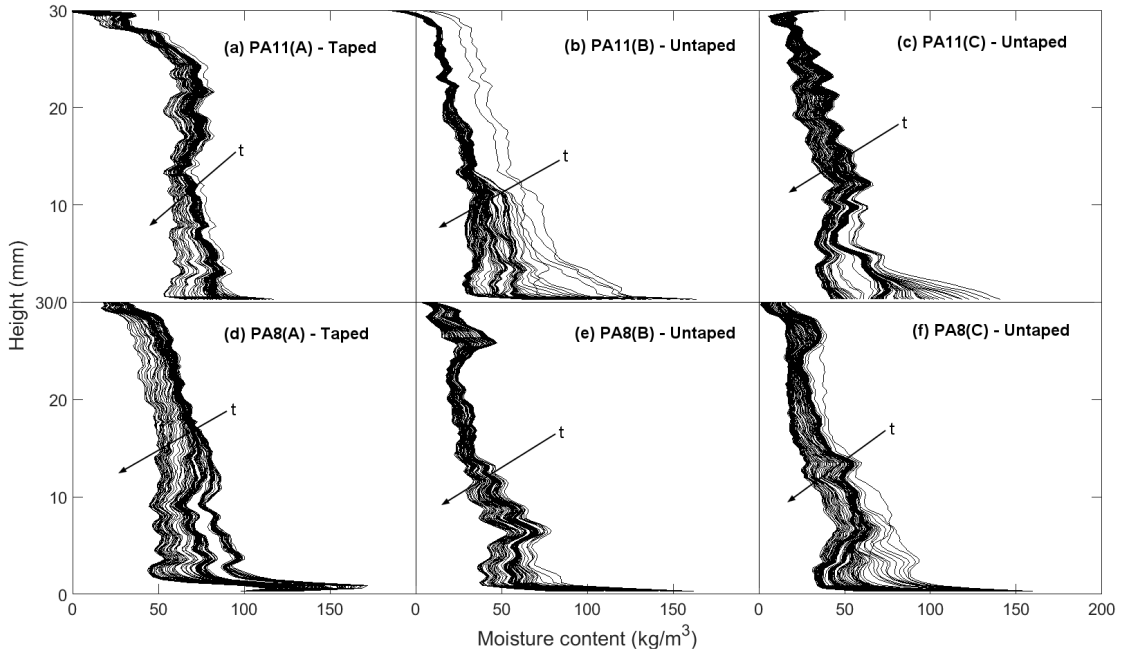


Figure 4.5.: Temporal evolution of moisture profiles during drying in the six specimens used in this study. Profiles are shown for every 30 s for the first 15 mins, every 2.5 mins for the next 2 h and every 5 mins for the remaining duration of the experiments.

bottom part is attributed to water moving from the top of the specimen to the bottom, due to gravity, and then getting trapped in some pores at the bottom part.

To analyze gravity-driven drainage as well as convective drying in more detail, the specimens are divided into different regions of interest (RoIs), as schematically depicted at the top of Fig. 4.6. The specimens are first divided vertically (along the direction of gravity) into three equal parts, namely RoIs 1, 2 and 3. RoI 1 is then divided horizontally into three equal parts, namely RoIs 4, 5 and 6, to analyze the effect of drying in sections along the direction of airflow. In Fig. 4.6(a)-(f), the moisture loss from the RoIs as a fraction of the total moisture loss from the entire specimen is shown as a function of time. These figures are derived as follows: first, the total moisture loss from the entire specimen at a particular time step is calculated by subtracting the image at that time step from the first wet image that is acquired immediately after the test section is allowed to start draining i.e. at  $t = 90$  s. Similarly, the moisture loss from all the other RoIs are calculated by restricting the image subtraction to only the respective RoIs. By dividing the moisture loss in each RoI at a particular time step with the total moisture loss in the entire specimen at the same time step, the contribution of each RoI towards the total moisture loss in the

specimen at that time step can be determined. This process is repeated for all the time steps to obtain Fig. 4.6.

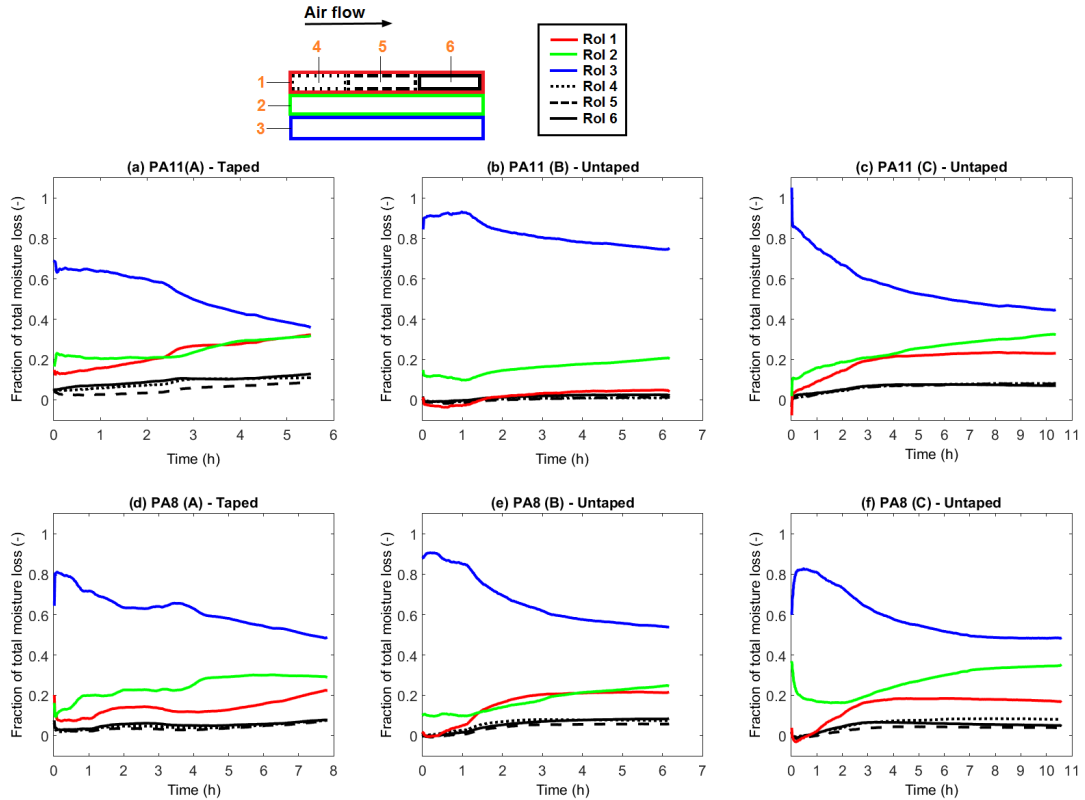


Figure 4.6.: Temporal evolution of the contribution of different regions of interest (ROIs) towards the total moisture loss in the specimen with schematic of the selected ROIs.

From Fig. 4.6, it can be seen that in all the specimens, Rol 3 is the region where most of the moisture loss occurs, although the mechanisms for this loss are different at the initial and final stages of the experiment. In the first few time steps, Rol 3 loses moisture due to water leaving the specimen from the bottom edge due to gravity. With time, the fractions of moisture loss from ROIs 1 and 2 increase due to a combination of gravity-driven drainage and evaporation, although these losses are still lower than the one from Rol 3. Towards the end of the experiments, while Rol 1 has lost most of its initial moisture content, ROIs 2 and 3 remain wet and continues to lose moisture. Time-evolution of moisture loss over the entire length of the specimens in ROIs 4, 5 and 6 do not show any particular trend. Studies of forced convective drying in microporous media have demonstrated the existence

of a three dimensional drying front which develops from the windward edge to the leeward edge and from the top surface (the surface exposed to air flow) to the bottom (Defraeye et al. 2012). However, RoI 4, the windward RoI, does not exhibit a higher rate of moisture loss when compared to RoIs 5 and 6.

#### 4.3.3.2 *Analysis of water flow during a sudden drop in moisture content*

In Fig. 4.4, it can be observed that there is a sudden drop in moisture content inside the specimen PA8(A) around  $t = 0.5 h$ . From Fig. 4.6(d), around the same time, a sudden rise in the contribution of RoI 2 towards the total moisture loss can be seen. This indicates that this sudden moisture loss occurs in the middle part of the specimen. To analyze this process in more detail, the temporal evolution of moisture content distribution (MCD) in the entire specimen is shown first, followed by focusing on a smaller region of interest where the sudden drop in moisture content takes place. The MCD plot of PA8(A) is given in Fig. 4.7(a). A second series of images are shown in Fig. 4.7(b) to highlight areas undergoing considerable moisture loss. These images are derived using a procedure similar to the one used in Fig. 4.6 i.e. the moisture loss at a particular time step is calculated by subtracting the image at that time step from the first wet image at  $t = 90 s$ . In Fig. 4.7(b), pixels have a binary representation, blue or white, where a white pixel is one whose value has crossed a moisture loss threshold of  $30 \text{ kg/m}^3$ , while a blue pixel is one whose value does not change (e.g. absence of porosity) or whose moisture loss is below the threshold. This threshold has been selected to achieve a clear visualization of the spatial distribution of water by indicating only those areas in the specimen that undergo significant moisture loss.

Since PA8(A) is covered at the bottom with a tape during the experiments, no significant difference can be seen between the MCD plots at  $t = 0.07 h$  and  $t = 1.3 h$ . Some moisture loss in the bottom corners, especially the left corner, can be visualized clearly in the thresholded image at  $t = 1.3 h$ . From this, it can be concluded that the sudden moisture loss observed in fig. 4.4 is a result of water exiting from the bottom left corner. This will be analyzed in detail in the subsequent paragraphs. Complementary to the conclusion drawn from fig. 4.6, no drying front can be seen in the windward to leeward direction at the top of the specimen. However, a strong bottom-up front of emptying pores can be clearly observed, which continues long after the fan is switched on at  $t = 1.2 h$ . At  $t = 7.8 h$ , water-filled zones can be seen in a few regions of the specimen, demonstrating that the specimen still contains a lot of water even after more than 6.5 hours of forced convective drying.

The next objective is to understand the exact mechanism by which the sudden moisture loss in the bottom left corner of PA8(A) took place. For this purpose, water redistribution

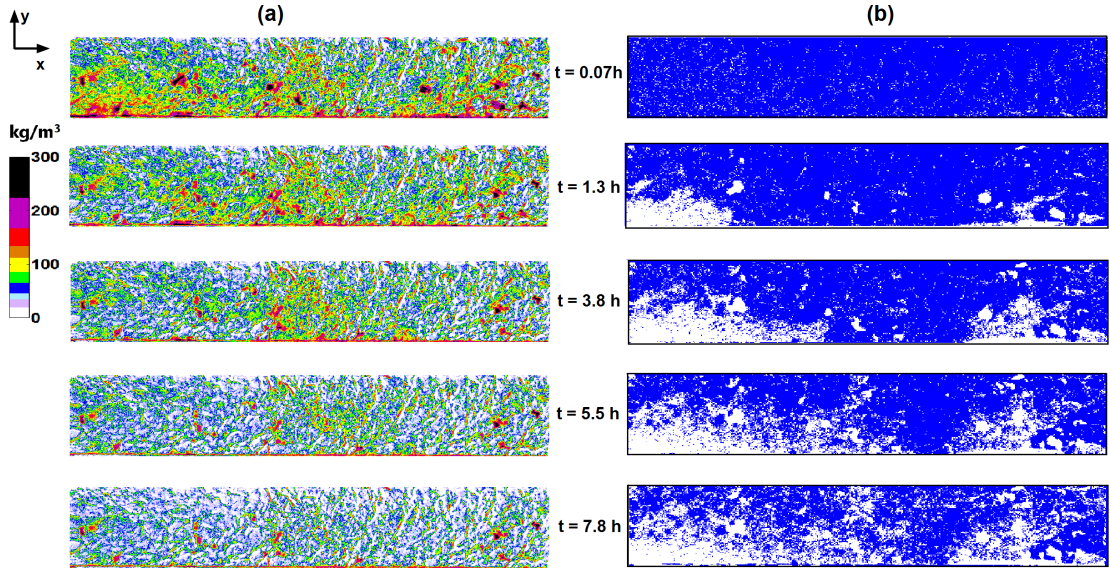


Figure 4.7.: Temporal evolution of (a) moisture content distribution and (b) the corresponding thresholded images in which white pixels represent a moisture loss of more than  $30 \text{ kg/m}^3$  as compared to the wet image at  $t = 90 \text{ s}$ . The specimen is PA8(A), which is taped at the bottom, and the fan is switched on at  $t = 1.2 \text{ h}$ .

is studied in terms of the degree of saturation (DoS),  $s_t(x, y)$ , which was defined in Chapter 3 as:

$$s_t(x, y) = \frac{w_t(x, y)}{\rho_w \cdot \varepsilon(x, y)}, \quad (4.1)$$

where  $\varepsilon(x, y)$  is the two dimensional porosity distribution as shown in Fig. 4.2,  $w_t(x, y)$  is the MCD and  $\rho_w$  is the density of water. According to Eq. (4.1), neutron radiography (NR) images should be divided by X-ray  $\mu$ -CT images to get DoS images. However, the image resolutions of the NR and microCT images are different. Therefore, as mentioned earlier, using bilinear interpolation, the resolution of microCT images is lowered to match that of NR images before division.

Figure 4.8 shows the degree of saturation images for a region of interest of  $30 \text{ mm} \times 15 \text{ mm}$  in the lower left corner of specimen PA8(A). The spatial distribution of DoS is given in Fig. 4.8(a) while the corresponding thresholded images, in which white pixels represent a reduction of more than 10% DoS compared to the wet image at  $t = 90 \text{ s}$ , are given in Fig. 4.8(b). The total duration of the sudden moisture drop event analyzed here is less

than 3 minutes and has been captured by six successive images of the RoI with a gap of 30 s between them. In Fig. 4.8(b), the movement of the water from left to right is clearly visible. From Fig. 4.8(a), it can be seen that the color of most of the pixels in the middle region of the RoI change from green (20-30%) to blue (5-20%) as we go from  $t = 33.5 \text{ mins}$  to  $t = 36 \text{ mins}$ . In the upper right corner i.e. between  $y = 10$  to  $y = 15 \text{ mm}$  and  $x = 18$  to  $x = 25 \text{ mm}$ , the reduction in DoS is much higher since the color changes from red to green. The highest reduction in DoS is at the bottom part of the RoI (which is also the bottom part of the specimen) where there is a connected region of fully saturated (black) pores at  $t = 33.5 \text{ mins}$ . This black region almost completely disappears by  $t = 36 \text{ mins}$ . Furthermore, water movement stops at  $x = 30 \text{ mm}$  because it has reached a dead end pore, as will be shown further. From these observations, there is a strong indication of a connected pore network which starts at  $x = 30 \text{ mm}$  and ends at  $x = 0$ , where it is connected to the environment. The next step is to visualize this pore network from the X-ray  $\mu$ -CT scans of the specimen.

In Fig. 4.9, the path followed by water, which is visualized in 2D in Fig. 4.8(b), is now visualized in 3D within the actual three-dimensional geometry of the RoI. The predicted water path is shown by highlighting the pore cross-section in black. The 3D image analysis software Avizo Fire 8.0 is used for this analysis. First, the three dimensional volume of the specimen is rendered from the X-ray- $\mu$ CT images. Then this volume is segmented into pores and non-pores (binders or aggregates). In the final step, all those pores which are not connected to the network under investigation are removed from the domain for the sake of clarity.

In Fig. 4.9, the movement of water occurring in the pore space starting from right to left is shown in black. Water starts moving from the two dead end pores shown in Fig. 4.9(a). From there, water continues to travel along the  $x$ -axis from  $x = 30 \text{ mm}$  towards  $x = 0$ , where it finally exits from the specimen, as shown in Fig. 4.9(e). At the plane  $x = 0$ , a large cross section of the pore network is exposed to the surrounding environment. The phenomenon seen here is analogous to the air entry point in soil hydrology, which is the water content at which air starts to penetrate the saturated porous medium (Braudeau et al. 1999). Once this water content is reached, the capillary pressure inside the specimen will be large enough to allow displacement of water by the invading air phase. This point is characterized by a sudden decline in water content, which is precisely what is seen in PA8(A) in Fig. 4.6(d). Alternatively, this moisture drop could also be a 'Haines jump' (Haines 1930). According to this theory, when a non-wetting phase (air) displaces a wetting phase (water), a situation is reached when the water meniscus can no longer increase its curvature at the narrowest pore of the air-water interface to cope up with the increasing capillary pressure. At this stage, the meniscus simply jumps to the next narrow capillary pore, thereby emptying the former pore instantaneously. Due to the favorable conditions for air entry at  $x = 0$ , and the presence of coarse pores that are connected to

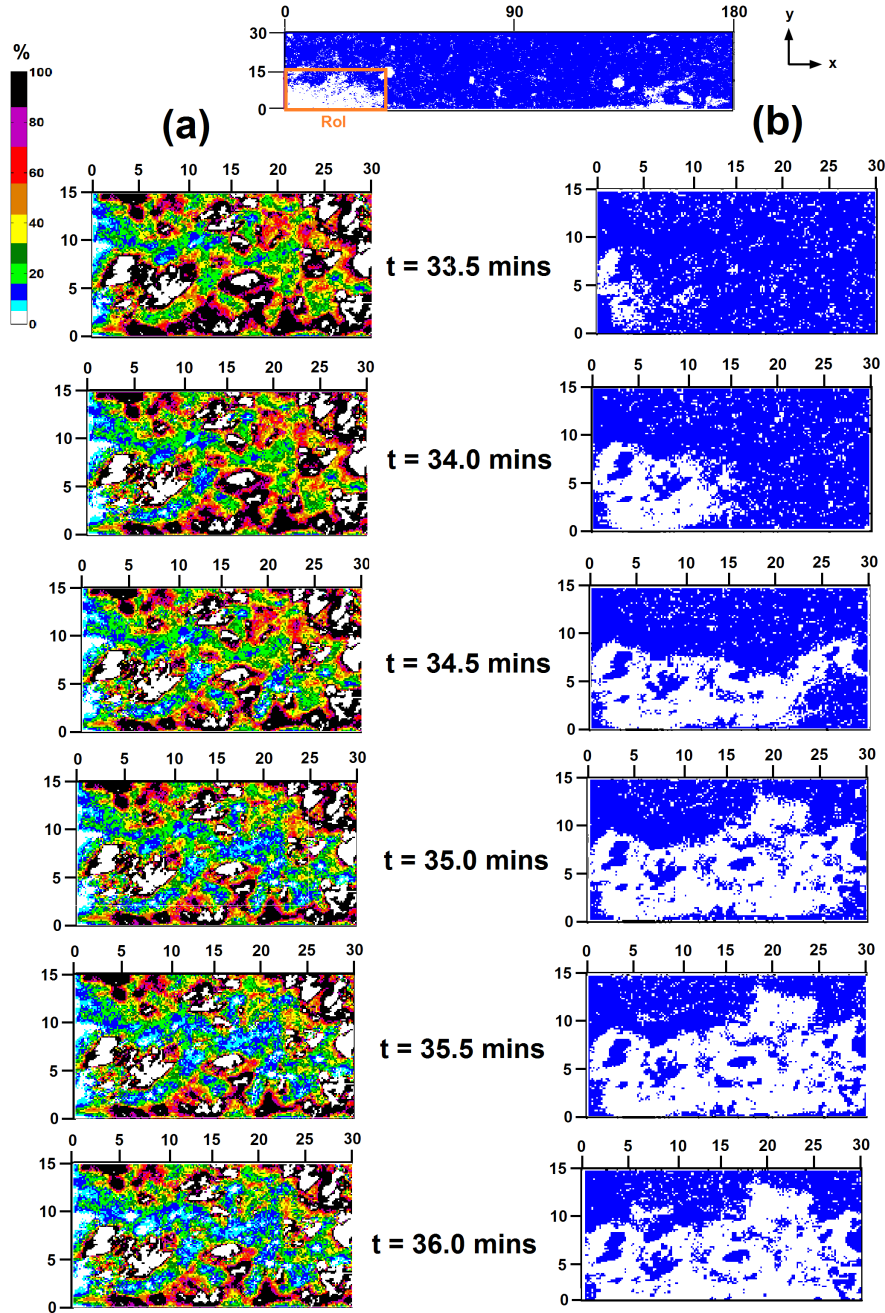


Figure 4.8.: (a) Degree of saturation images (DoS) and (b) the corresponding thresholded images (right) in which blue pixels represent a reduction of more than 10% degree of saturation as compared to the wet image at  $t = 90$  s. The figures are for a region of interest (RoI) within the specimen PA8(A) where a sudden drop in moisture content occurs. All dimensions are in mm.

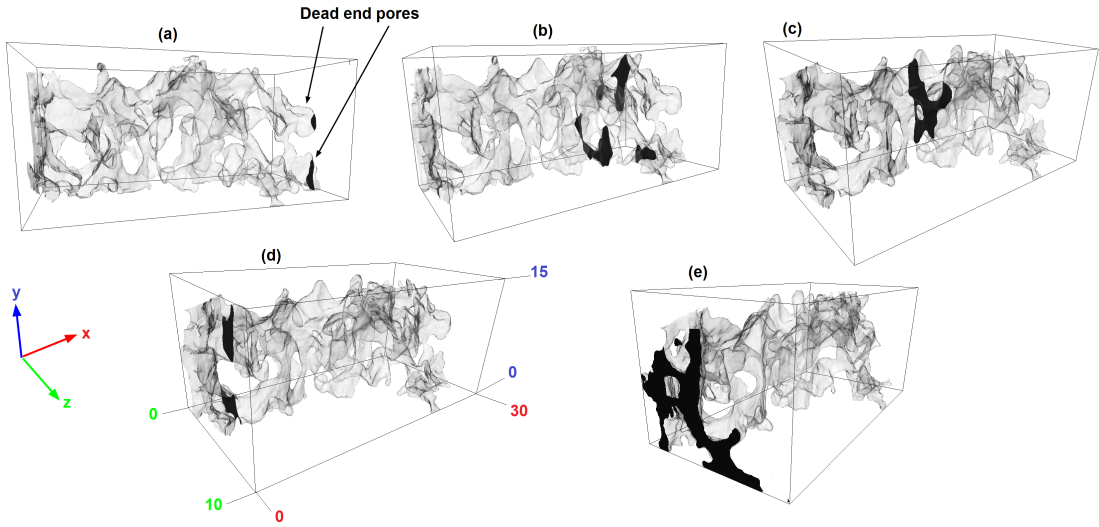


Figure 4.9.: The postulated path of water during the sudden drop in moisture content in PA8(A), between the time steps  $t = 33.5 \text{ mins}$  and  $t = 36.0 \text{ mins}$ , is shown in black. The pore geometry is obtained from 3D X-ray- $\mu$ CT scans and only the connected pores within the region of interest chosen in Fig. 4.8 are shown. The movement of water starts from the two dead-end pores shown in (a) and continues till the plane  $x = 0$ , where it exits to the surroundings. All dimensions are in mm.

the internal structure of the specimen, a sudden drop in water content was seen in the RoI. The displacement of water by air cannot go further than  $x = 30 \text{ mm}$  since at this point, the pore network reaches a dead end. It is also observed that the direction of water propagation is not always directly in the direction of gravity. Drainage in PA8(A) through side pores, i.e. pores connected to the lateral edges of RoI 3, contributes to the high total moisture loss even though the bottom was taped, as is observed in Fig. 4.6(d).

#### 4.3.3.3 Analysis of water flow during redistribution of water between two pores

Redistribution of water within the internal structure of PA, through capillary action and gravity, can have important consequences from the point of view of material durability. Redistribution of water can lead to the formation of disconnected water islands within the material, which can take a long time to drain or dry by evaporation. This leads to long periods of binder exposure to moisture, potentially affecting the mechanical properties of the binder in the long run. During the drainage/drying experiment of



PA8(C), redistribution of water within the specimen is observed, and is analyzed in detail in this section.

Figure 4.10(a) shows the spatial distribution of moisture content (in  $\text{kg}/\text{m}^3$ ) in PA8(C) while Fig. 4.10(b) shows the corresponding thresholded images where a white pixel represents a moisture loss of more than  $30 \text{ kg}/\text{m}^3$  as compared to the first wet image at  $t = 90 \text{ s}$ . In Fig. 4.10(c), an additional column presents thresholded images of a region of interest of dimensions  $90 \times 67 \text{ mm}^2$ , marked in yellow in Fig. 4.10(b), but with the important difference that the thresholding is performed for moisture gain, as opposed to moisture loss, when compared to the image at  $t = 90 \text{ s}$ . In Fig. 4.10(c), a red pixel represents a moisture gain of more than  $20 \text{ kg}/\text{m}^3$  when compared to the wet image at  $t = 90 \text{ s}$  while a white pixel represents either no moisture gain or a moisture gain below the threshold of  $20 \text{ kg}/\text{m}^3$ . In a drying/drainage experiment, the only source of moisture gain within the specimen is water that is redistributed from other regions. Indeed, at  $t = 6 \text{ h}$ , a small region where moisture gain occurs can be observed. This region will be analyzed in detail in the subsequent paragraphs. When compared to the specimen PA8(A) in Fig. 4.7(a), water retention is seen to be much lower in the specimen PA8(C) in Fig. 4.10(a). This is expected since gravity-driven drainage is not constrained by a tape at the bottom of PA8(C). This is also the reason why there is a much larger difference in the moisture content distribution between the first two time steps in Fig. 4.10(a) as compared to the ones in Fig. 4.7(a). Similar to PA8(A), a strong bottom-up water front movement can be observed in PA8(C). However, the bottom-up water front in PA8(C) is more distinctive since most of the water is exiting from the pores that are connected to the bottom plane, unlike in PA8(A) where water was blocked from exiting from the bottom side and consequently was exiting from the pores open to the lateral sides.

In a next step, the redistribution of water within PA8(C) observed in Fig. 4.10(c) is analyzed in more detail by looking at the degree of saturation images for a RoI of  $16 \times 11 \text{ mm}^2$ , as shown in Fig. 4.11. In this figure, a fully saturated region (black) which moves from the upper left corner to the lower right corner of the RoI can be clearly seen. This redistribution of water takes place over 4 h, indicating a slow process. At  $t = 4.06 \text{ h}$ , there is a quasi-stable configuration of a connected water phase stretching from a fully saturated pore in the upper left corner ( $x = 86$  to  $x = 90 \text{ mm}$  and  $y = 10$  to  $y = 14 \text{ mm}$ ), named pore M, to a fully saturated pore in the lower right corner ( $x = 92$  to  $x = 96 \text{ mm}$  and  $y = 6$  to  $y = 10 \text{ mm}$ ), named pore N, as marked in Fig. 4.11(b). These two pores are connected by a throat, throat T, which is marked in Fig. 4.11(d). At  $t = 4.06 \text{ h}$ , throat T is not completely filled. Therefore, an unsaturated capillary flow like film or corner flow could be present inside the throat. Pore N is connected to a reservoir, reservoir R, marked in Fig. 4.11(c). The trigger for the redistribution of water from pores M to N is the drainage of reservoir R, which begins at  $t = 4.06 \text{ h}$ . As the drainage of R begins, the water saturation level of N decreases, which triggers the redistribution of water from M to

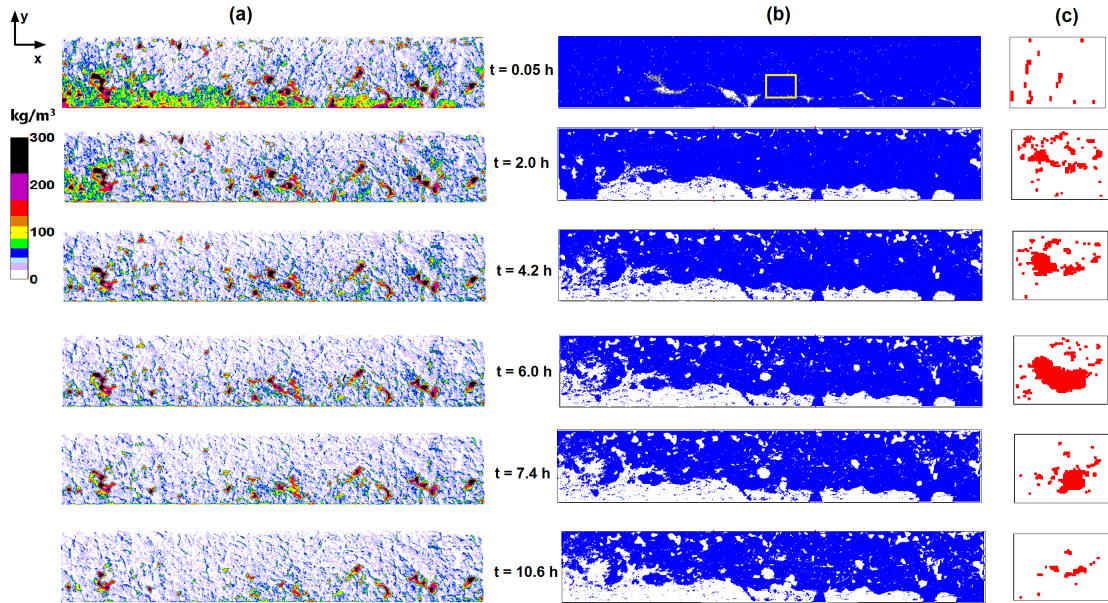


Figure 4.10.: Temporal evolution of (a) moisture content distribution, (b) the corresponding thresholded images in which blue pixels represent a moisture loss of more than  $30 \text{ kg/m}^3$  as compared to the wet image at  $t = 90 \text{ s}$  and (c) the thresholded images of a region of interest of  $90 \times 67 \text{ mm}^2$ , as shown with a yellow box in (b), in which red pixels represent a moisture gain of more than  $20 \text{ kg/m}^3$  when compared to the wet image at  $t = 90 \text{ s}$ . The specimen is PA8(C), which was untaped at the bottom, and the fan was switched on at  $t = 2 \text{ h}$ .

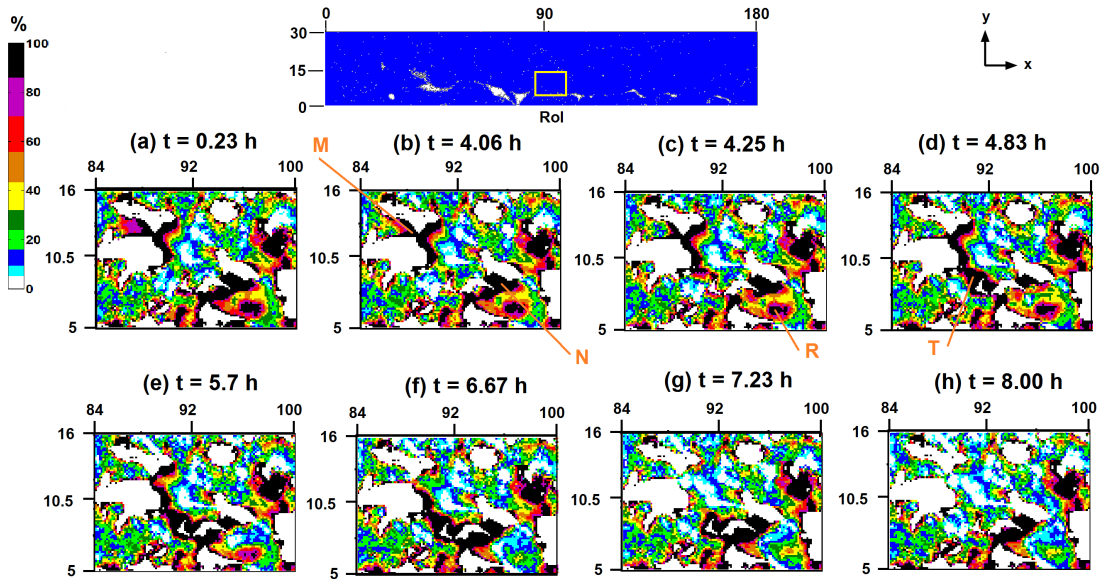


Figure 4.11.: Degree of saturation images of a region of interest within specimen PA8(C) where redistribution of water is observed. Water distribution takes place from pore A to pore B through throat T. Pore B is in turn connected to a reservoir R. All dimensions are in mm.

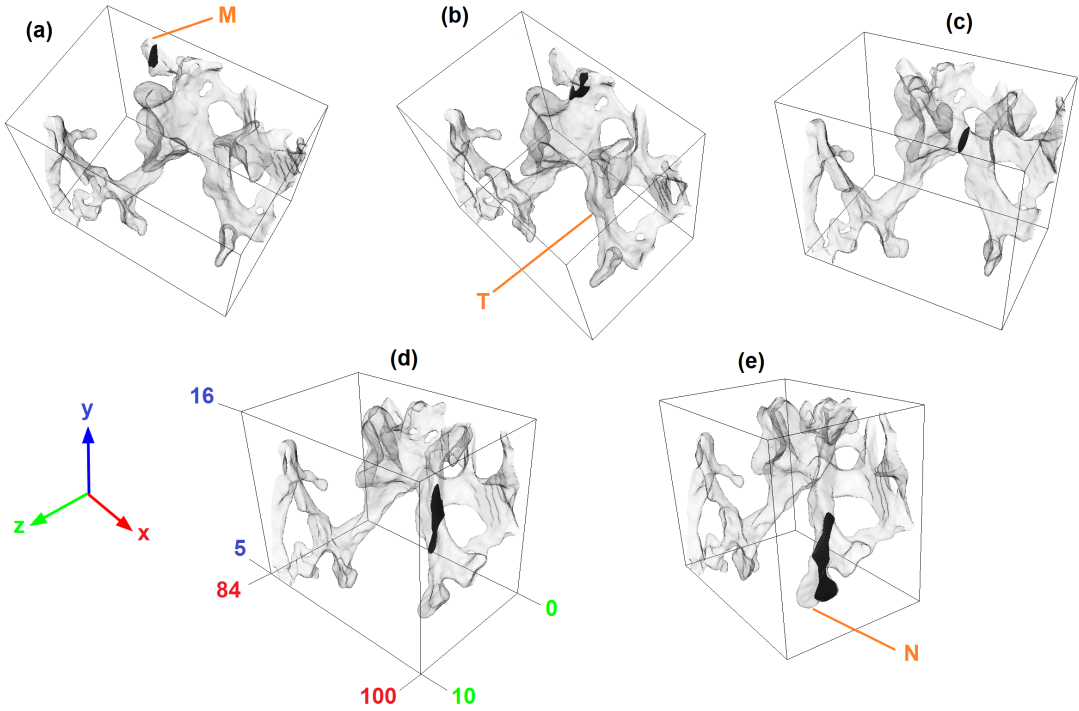


Figure 4.12.: The path of water redistribution within PA8(C), between the time steps  $t = 4.06 h$  and  $t = 8 h$ , is shown in black. The pore geometry is obtained from 3D X-ray  $\mu$ -CT scans and only the connected pores within the region of interest chosen in Fig. 4.11 are shown. Water travels from pore M to pore N through throat T. All dimensions are in mm.

N through T. During this redistribution process, T is fully saturated with water, as can be seen in Figs. 4.11(d)-(f). The redistribution of water finally ends when most of the water in R is drained by  $t = 8 h$ , as seen in Fig. 4.11(h).

In Fig. 4.12, using the methods used above for obtaining Fig. 4.9, the 3D reconstruction of the RoI analyzed in Fig. 4.11 is presented, where water redistribution was observed. The pores M and N as well as throat T, which are distinctly marked in Fig. 4.11, can be clearly visualized in Fig. 4.12. Reservoir R was not clearly distinguishable from the X-ray  $\mu$ -CT scans and hence it is not presented here. The predicted water path is shown by highlighting the pore cross-section in black. The redistribution of water from pore M to pore N through throat T is visualized in Fig. 4.12. Moreover, Fig. 4.12 also illustrates the wide range of connectivity numbers in a typical PA pore network. Connectivity (also called coordination number) is defined as the number of pores connected to a given pore,

and can be calculated from a binary image after pore segmentation. Even in such a small segment, connectivity numbers ranging from 1 to 5 can be observed. For future pore network simulations of water transport inside PA, information about connectivity numbers from such 3D visualizations will be an important input parameter.

The in-depth analysis presented in this section illustrates the complex nature of water movement in porous asphalt. On the one hand, gravity-driven drainage causes sudden drops in moisture content in one specimen while on the other hand, a slow redistribution of water within another specimen is observed. The simultaneous prevalence of gravity-driven drainage in large pores and capillary-driven movement of water in smaller pores is unique to a material like porous asphalt due to its wide range of pore sizes. Additionally, local surface roughness, wettability of the solid (bitumen or aggregate) in contact with water, tortuosity of the pore network etc. can also influence water flow inside PA. Experimental studies like the ones reported in this study can provide an insight into the relative importance of each of these parameters in determining the residence time of water inside the specimen. Moreover, a clear pattern of water flow like the redistribution between pores as observed in this study can serve as validation for multiphase flow simulations. From the results reported in this study, it is clear that gravity-driven drainage is the most important factor responsible for the overall moisture loss from a wet PA specimen.

#### 4.3.4 *Conclusions*

Drainage and forced convective drying in porous asphalt are studied using neutron radiography (NR) in a custom-made mini wind tunnel. Three specimens of two types of porous asphalt are used in the experiments, of which one type has larger aggregate sizes and consequently larger pore sizes. The specimens are fully saturated at the beginning of the experiments. Gravity-driven drainage is constrained in the vertical direction in two of the specimens to observe its effect on the overall moisture loss. By combining neutron radiography and microcomputer tomography, saturation degree distributions are obtained, from which the regions where saturated flow is active is identified. Based on the experimental results, the following important observations and conclusions are made:

1. In all specimens, the maximum water loss was through the bottom region of the specimen, thereby indicating the dominance of gravity-driven drainage over evaporation from the top surface. Consequently, a bottom-up front of emptying pores is visible in two specimens that are analyzed in more detail.
2. Even after many hours of forced convective drying, water retention occurs inside the specimens.

3. In one of the specimens in which gravity-driven drainage at the bottom was constrained, a sudden drop in moisture content is attributed to air invasion in a pore that was connected to the lateral edge. The air invasion proceeded until it is stopped by dead-end pores.
4. Water redistribution between two pores is clearly observed. The total duration of this redistribution is close to four hours. Water moved from one pore to another by saturated flow through the throat which connected the two pores.
5. Both the observed phenomena i.e. sudden drop in moisture content and water redistribution, are visualized by reconstructing the actual three dimensional pore geometry from X-ray  $\mu$ -CT scans.

#### 4.4 FORCED CONVECTIVE DRYING AND THERMAL DRYING

The influence of partially blocking gravity drainage on the overall drying process of PA was observed in the previous experiments. The next step is to study the drying process of PA after completely blocking gravity drainage, thereby allowing moisture to exit the specimen only through evaporation, a process that might be influenced by airflow and solar radiation in case of in situ PA. In reality, this represents a worst-case scenario in terms of the residence time of water in PA pavements, arising as a consequence of gravity drainage rendered ineffective due to a saturated underneath layer or highly clogged pores. Specifically, the objectives of this study are to analyze the effects of initial water distribution in the specimen, turbulent airflow above the surface and a temperature gradient opposite to the overall drying direction in PA and to correlate these effects with the pore space characteristics of the specimens.

##### 4.4.1 *Material characterization*

The experiments in this study are carried out together with the droplet wetting experiments presented in Section 3.3. Therefore, the same specimens that are used for the droplet wetting experiments are used in this experiment. However, for the sake of clarity, the important characteristics of the specimens are briefly described again. For the preparation process of the specimens, the reader is referred to Section 3.3.1.1. Three types of porous asphalt specimens are used in this study: PA4, PA8 and PA11, whose maximum aggregate sizes are 4, 8 and 11 mm respectively. Specifically, one PA4, two PA8 and two PA11 specimens are used. They are named PA4(1), PA8(1), PA8(2), PA11(1) and PA11(2). All surfaces except the top one are covered with an aluminium tape during the experiments. Therefore, gravity-driven drainage is completely blocked and consequently, the only

mechanism through which water can exit the specimen is evaporation from the top surface. The reader is referred to figs. 3.11, 3.12 and 3.13 for a detailed pore space characterization of the specimens.

#### 4.4.2 *Experimental setup and procedure*

The neutron radiography beamline specifications are exactly the same as described in Section 3.3.2.1 and is not repeated here. However, the experimental setup is slightly modified and the experimental procedures are different, and therefore they are described in detail in the next sections.

##### 4.4.2.1 *Mini wind tunnel with rain, wind and solar radiation simulators*

The custom-made mini wind tunnel that is described in Sections 3.3.2.2 and 4.3.2.2 is used for the experiments in this study. The important addition to the setup is a 300 W Osram Ultra Vitalux ultraviolet lamp that is placed above the test section during the experiments, which acts as a solar radiation simulator. The lamp has a radiated power of 13.6 W in the longwave (315-400 nm) range and 3 W in the shortwave (280-315) range. The top part of the test section is made of Plexiglas<sup>®</sup>. Plexiglas<sup>®</sup> has a visible light transmission rate of 92%, transmits most of the longer wavelengths (those near the visible region) in the UV region and transmits most of the invisible near-infrared energy in the 700-2800 nm wavelength range. During the experiments, thermocouples are mounted on the lateral edges of the specimens to monitor the rise in their temperature due to heat from the UV light. Airflow is generated during the experiments by operating the wind tunnel fan at two voltages, 5.8 V and 17 V, which translates to mean wind speeds of 1 and 3 m/s respectively, as measured by an anemometer. At these speeds, the calculated Reynolds numbers at the test section, using the height of the channel as the representative length, are  $Re=3060$  (laminar to turbulent transition) and  $Re=9190$  (fully turbulent flow).

##### 4.4.2.2 *Procedure*

Table 4.1 lists all the experiments carried out in this study. Depending on the experiment number, a dry specimen is wetted either by simply pouring water on top of it or by droplets discharged from the top of the wind tunnel test section, after having placed the dry specimen in the test section. The wetting of PA specimens in two different ways enables the study of the effect of initial moisture distribution on the drying process. The droplet wetting process lasts for 5 minutes. If the specimen is wetted by pouring, then neutron imaging captures only the drying process of the wet specimen. When the specimen is wetted by droplets, then neutron imaging captures both the wetting and drying processes

Table 4.1.: List of experiments with different wetting and drying conditions

Exp no.	Specimen	Type of wetting		Wind speed		Solar radiation
		Pouring	Droplets	Low	High	
1	PA4(1)					
2	PA4(1)					
3	PA4(1)					
4	PA8(1)					
5	PA8(1)					
6	PA8(1)					
7	PA8(1)					
8	PA8(2)					
9	PA8(2)					
10	PA11(1)					
11	PA11(2)					

in the specimen. The details of the droplet wetting process are described in Section 3.2.2.2. The effect of solar radiation is investigated for all the experiments.

The duration of each experiment is 3.5 hours. The first 30 minutes is used to investigate either the drying process under natural convection (in case of specimens that are wetted by pouring) or both the droplet wetting process and the drying process under natural convection (in case of specimens that are wetted by droplets). After the first 30 minutes, all the experiments are similar in terms of the physics investigated. If  $t_0$  is the time at which the experiment begins, the fan is turned on at  $t_0 + 0.5$  h and remains on throughout the experiment, while the lamp is switched on at  $t_0 + 2.5$  h. These times are indicated by vertical lines in all applicable figures. Therefore, three types of drying conditions are present in each experiment: natural convection ( $t_0 : t_0 + 2.5$  h), forced convection ( $t_0 + 0.5$  h :  $t_0 + 2.5$  h) and a combination of forced convection and thermal drying ( $t_0 + 2.5$  h :  $t_0 + 3.5$  h). It is to be noted that in a particular experiment, only one of the two wind speeds, i.e. 1 m/s (low) or 3 m/s (high), is used for forced convective drying. At the beginning and end of each experiment, the mass of the specimen is measured to be used as control values for the correction of the acquired neutron radiographs.

#### 4.4.3 Results and discussion

Drying is a process that is significantly influenced by external conditions, in addition to being influenced by material properties themselves. Therefore, in this section, first an overview of the results from all the drying experiments carried out in this study is presented, followed by a detailed verification of the influence of the most important factors on drying.



#### 4.4.3.1 Overview

An overview of all the drying experiments performed in this study is given in Fig. 4.13, in which the temporal evolutions of the average moisture loss from the entire specimens during the drying process are plotted. Figures 4.13(a), 4.13(b) and 4.13(c) show the drying curves of PA4, PA8 and PA11 specimens respectively. The type of wetting by which the specimen is wetted (pouring or droplets) as well as the wind speed used for forced convective drying (low or high) in each experiment is given. In Fig. 4.13, and throughout the subsequent figures of this experiment, a uniform convention is followed in all applicable figures: a solid line implies wetting by pouring while a dashed line implies wetting by droplets, and a thin line implies drying in low wind speed while a thick line implies drying in high wind speed. The times at which the fan and lamp are switched on, i.e.  $t = 0.5 h$  and  $t = 2.5 h$  respectively, are indicated by magenta dotted lines.

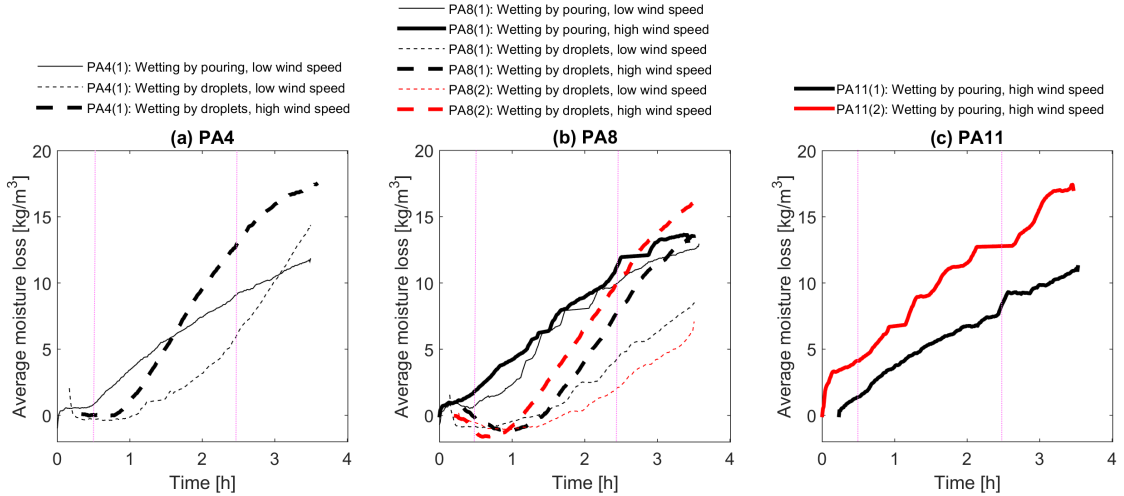


Figure 4.13.: Overview of the temporal evolution of average moisture loss during the forced convective and thermal drying experiments, where the fan is switched on at  $t = 0.5 h$  and the lamp is switched on at  $t = 2.5 h$ , as indicated by the two vertical lines.

The curves in Fig. 4.13 initially show a negative moisture loss due to moisture gain from droplets. The PA4 specimens wetted by droplets dry faster, irrespective of the wind speed, compared to a specimen wetted by pouring. The PA8 specimens that are wetted by droplets also dry faster but only at high wind speed. In all droplet-wetted PA4 and PA8 specimens, droplets coalesced to form discrete wet patches at the top surface, as seen in Fig. 3.16, explaining the faster drying rate of droplet-wetted specimens where all the moisture is accumulated at or close to the surface and a higher wind speed enhances the

drying. On the contrary, when there is penetration of water into the specimen, a higher wind speed has a smaller effect on the overall drying process. This aspect will be discussed in detail in the subsequent sections. Finally, despite an average specimen temperature rise of 6 °C due to heating up by the UV lamp, thermal drying is seen not to have a major impact on the overall drying process as the slope of the drying curve does not change after  $t = 2.5 h$ . A possible reason could be that by the time the lamp is switched on, airflow has already dried most of the water near the top surface and the influence of the heat from the lamp is limited to enhancing the drying of water in pores that are further into the material. No further analysis is done on the effect of the heating by UV lamp. In the subsequent sections, the effect of various other parameters on the drying process of PA is investigated in detail.

#### 4.4.3.2 *Influence of initial moisture distribution on drying*

From the wetting experiments presented in Section 3.3, it was clearly observed that the type of wetting influences the moisture pattern within the specimens. To study if this initial moisture pattern has an influence on the drying process, it is necessary to compare in detail the drying process of a specimen that has been wetted in both manners i.e. droplets and pouring. In Fig. 4.14, a comparison of the drying processes of PA4(1) and PA8(1) is presented in detail after they are wetted in both manners. While Figs. 4.14(a-b) shows the drying processes of PA4(1) subjected to low wind speed, Figs. 4.14(c-d) and 4.14(e-f) show the drying process of PA8(1) subjected to low and high wind speeds respectively. In Fig. 4.14, the specimens are divided into various regions of interest (ROI), as schematically shown at the top of the figure. First, the specimen is divided into two ROIs, ROI-1 and ROI-2, in the vertical direction, to analyze the difference in the moisture loss between the region exposed to the wind flow and the region which is not. ROI-1 is further divided horizontally into three additional ROIs, ROI-3, ROI-4 and ROI-5, to check if the windward ROI-3 dries faster than the other two horizontal ROIs.

As already observed in Fig. 4.13, at low wind speed, a PA8 specimen wetted by droplets does not always dry faster as compared to the case when it is wetted by pouring, as can be seen in Figs. 4.14(c-d). However, when the wind speed is high, then PA4 and PA8 specimens wetted by droplets are likely to dry significantly faster as can be seen in Figs. 4.14(a-b) and 4.14(e-f). Furthermore, it can be seen from Figs. 4.14(b), 4.14(d) and 4.14(f) that the windward ROI-3 is not always the ROI with the fastest drying rate. This is in line with the assertion that the drying behavior of PA is different from that of a conventional porous medium in which usually a clear windward-to-leeward edge drying front can be seen (Defraeye et al. 2012).

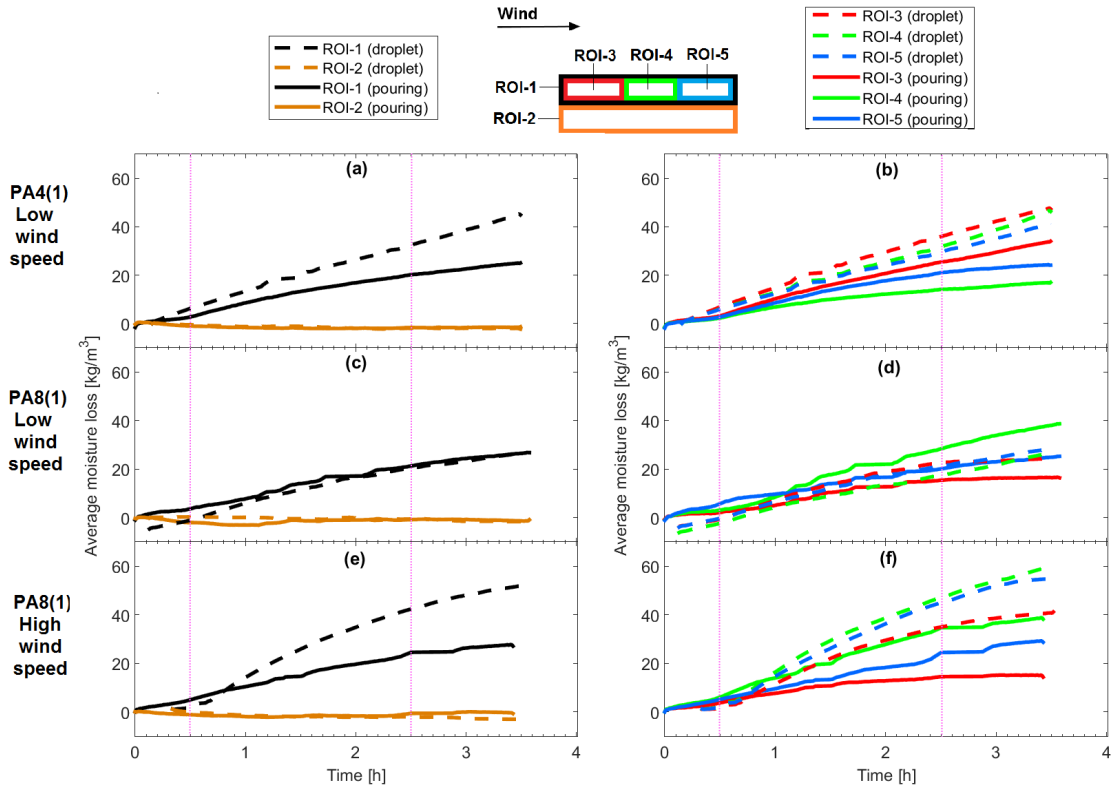


Figure 4.14.: Influence of the initial moisture content (type of wetting) on the drying process of specimens. The temporal evolution of average moisture loss from different regions of interest (ROIs) in the specimens are plotted for (a,b) PA4(1)–low wind speed case, (c,d) PA8(1)–low wind speed case and (e,f) PA8(1)–high wind speed case. The schematic of the selected ROIs is given at the top. The vertical lines represent the times at which the fan and the lamp are switched on.

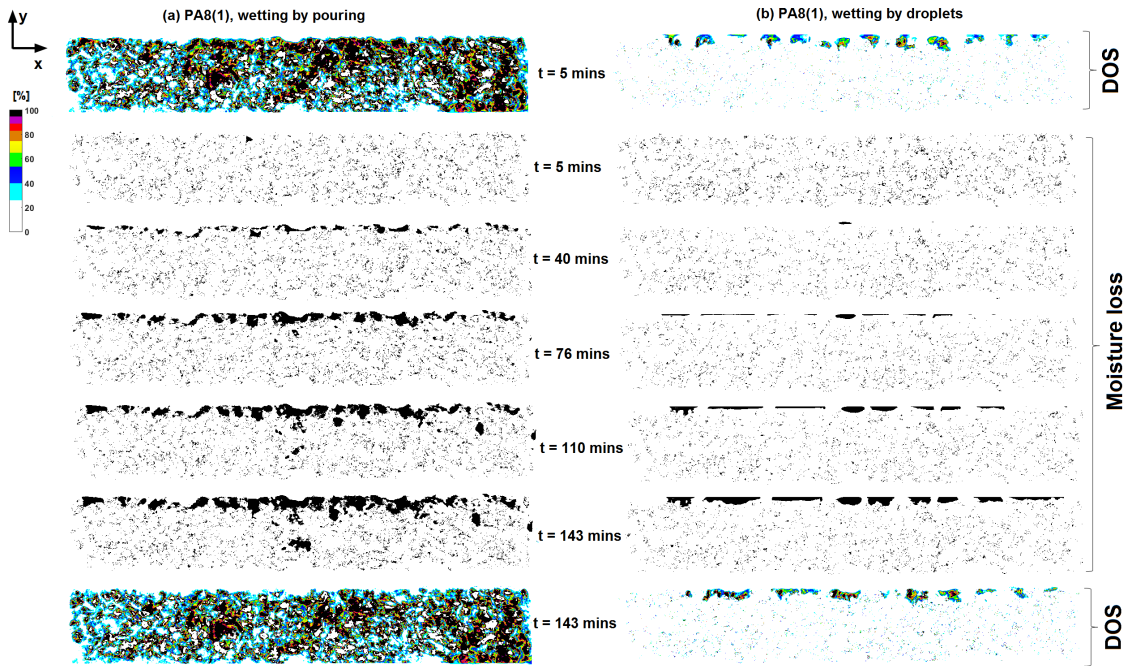


Figure 4.15.: Degree of saturation (DOS) during drying of (a) PA8(1)-wetting by pouring and (b) PA8(1)-wetting by droplet in the high wind-speed case (i.e. Figs. 4.14(e-f)). The first and last images of each column show the DOS distribution at the beginning and end of the drying process while the plots in between are thresholded images at different time steps including and in between the first and last time steps, where the black pixels represent a reduction of more than 20% moisture loss as compared to the reference wet image. The legend is applicable only for the top and bottom images of both columns.

In Fig. 4.15, the temporal evolution of moisture distribution in PA8(1), which is graphically shown in Figs. 4.14(e-f), is visualized in terms of the degree of saturation. Figure 4.15(a) shows the drying process of PA8(1) after it was wetted by pouring while Fig. 4.15(b) shows the same for wetting by droplets. The first and last images of each column show the degree of saturation (DOS) distribution at the beginning and end of the drying process while the other plots are thresholded images at different time steps between the first and last time steps, where the black pixels represent a reduction of more than 20% moisture loss compared to the reference wet image. The reference image represents the initial condition with the highest average moisture content. The initial moisture configuration in the poured and droplet-wetted specimens is significantly different as evident from the DOS distributions at  $t = 5 \text{ mins}$ . In Fig. 4.15(a), water is spread

throughout the specimen while in Fig. 4.15(b), water only accumulates close to the top surface. In Fig. 4.15(a), most of the drying is confined to the top part of the specimen, although at  $t = 143 \text{ mins}$ , there is a small patch in the center which loses considerable moisture. In Fig. 4.15(b), moisture remains accumulated near the top surface even at  $t = 143 \text{ mins}$ . This could be due to the cohesive droplet behavior where the rather smaller sizes of the droplet, the surface tension of the droplet, the high hydrophobicity of the surface and the high roughness of the materials work together in maintaining the droplet at the top even after coalescence, in the absence of capillary action.

#### 4.4.3.3 *Influence of pore sizes on drying*

The pore space characteristics of the types of specimens used in this study, PA4, PA8 and PA11, discussed in detail in Section 3.3.1.2, indicate that pore sizes increase with the maximum aggregate size i.e. PA4 has the smallest pores, PA11 has the largest pores and the pore sizes of PA8 are in between that of PA4 and PA11. The effect of increasing pore sizes on the drying rate is investigated in this section. Figure 4.16 shows a comparison of the drying processes of PA4(1), PA8(1) and PA11(2) after they are wetted by pouring. The wind speed conditions are also given in the figure. In Fig. 4.17, the spatial distribution of moisture content corresponding to the graphs shown in Fig. 4.16 is given, with a threshold level equal to a reduction of  $20 \text{ kg/m}^3$  of moisture content. It is to be noted that different threshold parameters are used in Figs. 4.15 and 4.17 in order to better interpret the drying process while qualitatively conveying the same picture.

From Figs. 4.16 and 4.17, it can be seen that the three types of PA display a similar drying behavior although their droplet wetting behavior was found to be quite different in fig. 3.16. During drying, the top 10 mm of the specimen undergoes significant moisture loss while the bottom 20 mm hardly displays any, except for a few small isolated patches as seen in Figs. 4.17(a) and 4.17(b). Furthermore, as can be observed in Fig. 4.17(c), patches of significant moisture loss are surrounded by large aggregates (white area). From the observed drying patterns, the influence of airflow above the surface on the drying process within PA seems to be the enhancement of vapor transfer at the air-material interface by thinning of the vapor concentration boundary layer. If turbulent momentum exchange resulting from air entrainment into the specimen played a major role in the drying process at wind speeds of 3 m/s, then the drying of PA11(2) might have been much faster than that of PA4(1) and PA8(1) since PA11(2) has large pores opening to the surface. The limited air entrainment is explained by the tortuous nature of PA's pore space that hinders air entrainment into the specimen's internal structure, at least for mean wind speeds of up to 3 m/s. Air entrainment into PA at higher wind speeds is a possibility that is investigated in detail in Chapter 6. For modeling purposes, this implies that up to wind speeds of 3 m/s, it is more important to accurately model the water vapor diffusion

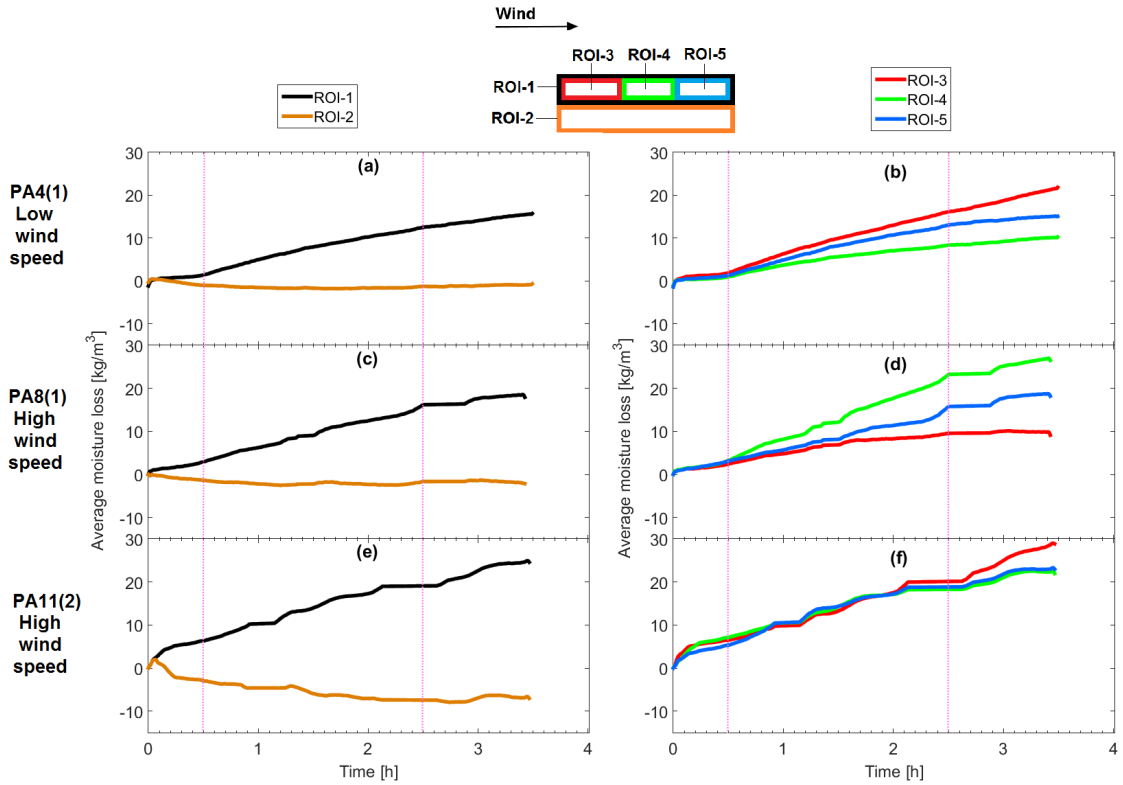


Figure 4.16.: Influence of pore sizes (type of PA) on the drying process of specimens wetted by pouring. The temporal evolution of average moisture loss from different regions of interest (ROIs) in the specimens are plotted for (a,b) PA4(1)–low wind speed case, (c,d) PA8(1)–high wind speed case and (e,f) PA11(2)–high wind speed case. The schematic of the selected ROIs is given at the top. The vertical lines represent the times at which the fan and the lamp are switched on.

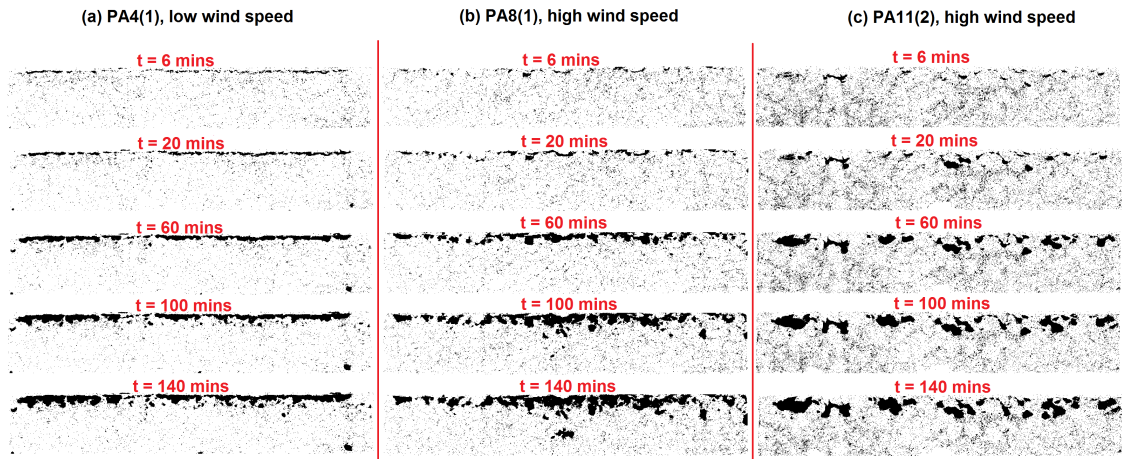


Figure 4.17.: Thresholded images of moisture content distribution during the drying of (a) PA4(1)–low wind speed case, (b) PA8(1)–high wind speed case and (c) PA11(2)–high wind speed case. Black pixels represent a moisture loss of more than  $20 \text{ kg/m}^3$  as compared to the reference wet image.

and, possibly, liquid transport within the material rather than focusing on air entrainment in the material.

#### 4.4.3.4 Influence of wind speed on drying

In the previous section, it was assumed that air entrainment in PA is less significant at the tested wind speeds. This means that the influence of wind speed on drying in PA is not expected to be a significant factor since the vapor diffusion resistance of the material is expected to be the decisive factor influencing drying rather than air entrainment and convective vapor transport within the pore system. Nevertheless, air speed can affect the boundary layer resistance above the air-material interface. This aspect is further investigated in this section through Fig. 4.18, where a comparison of the drying processes under low and high wind speeds is shown. The specimens and type of wetting used for the comparison are given in the figure. As expected, wind speed has mainly an influence on the drying process when the specimen is wetted by droplets, as can be seen in Figs. 4.18(e) and 4.18(g), since moisture is concentrated at or near the upper surface of the specimens in these cases and hence the vapor diffusion resistance of the material does not come into play.

The most interesting case is the drying of PA8(1), shown in Figs. 4.18(c-d), as it is wetted by pouring and therefore moisture is distributed throughout the specimen when drying begins. Significantly, in this case, the effect of wind speed is found to be less

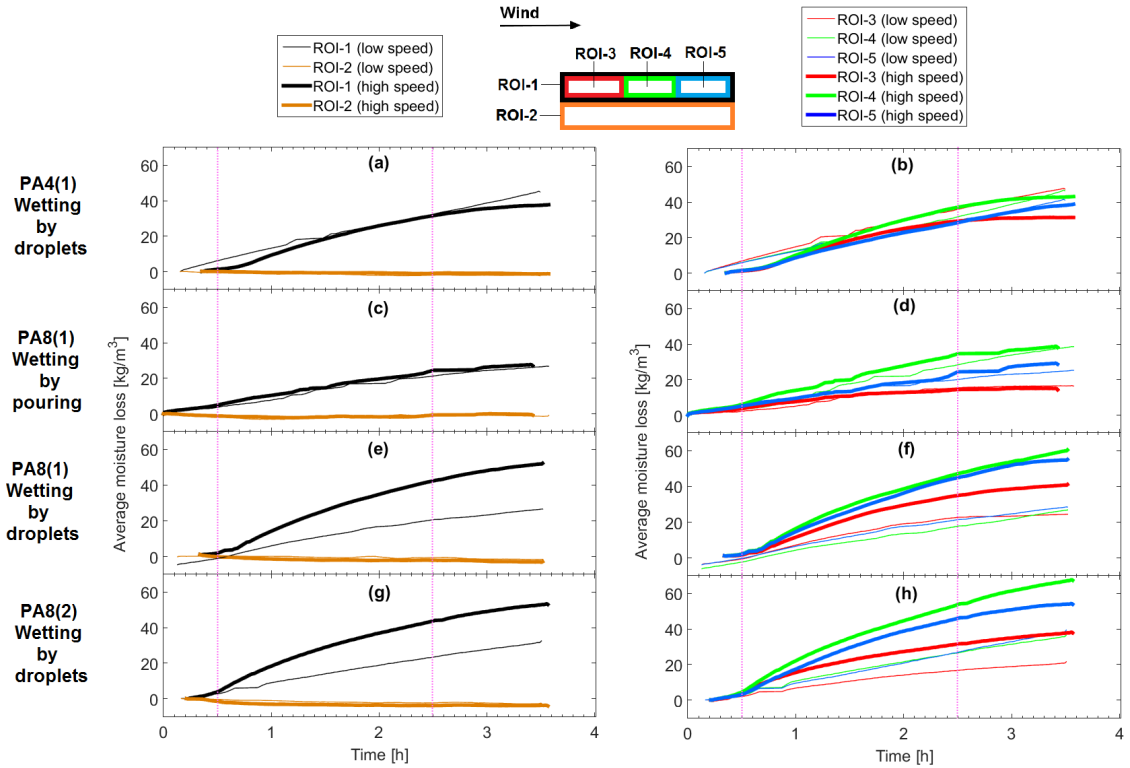


Figure 4.18.: Influence of wind speed on the drying process of specimens. The temporal evolution of average moisture loss from different regions of interest (ROIs) in the specimens are plotted for (a,b) PA4(1)–wetting by droplets, (c,d) PA8(1)–wetting by pouring, (e,f) PA8(1)–wetting by droplets and (g,h) PA8(2)–wetting by droplets. The schematic of the selected ROIs is given at the top. The magenta lines represent the times at which the fan and the lamp are switched on.



significant as both the low and high wind speed drying curves almost overlap. In essence, our observations are similar to those of Reis et al. (2006) wherein it was seen that the higher the wind speed, the slower a DEM droplet that was embedded in 120  $\mu\text{m}$  glass beads dried when compared to a saturated pool of DEM subjected to the same wind speed, thereby indicating the role of vapor diffusion resistance of the material to drying. Additionally, Babalis and Belessiotis (2004) observed that beyond a threshold wind speed of 2 m/s, a higher wind speed did not have any effect on the drying rate of a microporous material like figs, which pointed to the predominance of internal mass transfer resistance over the external one. Considering that the pore structure of PA is larger, more complex and more hydrophobic than that of the materials used in these studies, the vapor diffusion resistance of PA presents a complex picture. On the one hand, the hydrophobic nature of the solid matrix will prohibit capillary liquid transport while on the other, the larger pore sizes may contribute to a lower vapor diffusion resistance. However, the high tortuosity of the PA pore space is likely to result in a strong vapor diffusion resistance. Therefore, the influence of the overall vapor diffusion resistance of PA on the drying process at high wind speeds ( $\approx 10$  m/s) is a topic that requires a more detailed investigation and is consequently analyzed in Chapter 6.

#### 4.4.4 *Conclusions*

Drying of porous asphalt (PA) is analyzed under various conditions such as low and high wind speeds, different initial moisture distributions and heat from solar radiation. Three types of porous asphalt, PA4, PA8 and PA11, are used in this study. The specimens are sealed on all sides except the top surface so that gravity-driven drainage is completely blocked. The following important observations and conclusions are made from the experiments:

1. Even though the wetting patterns in the three types of PA are seen to be completely different, i.e. only PA11 shows a significant penetration of water droplets into the internal structure, their drying patterns are similar i.e. even after 3.5 hours of forced convective thermal drying, water evaporates mainly near the top surface.
2. A temperature increase of 6  $^{\circ}\text{C}$  due to heat from the solar radiation simulator did not influence the drying process significantly. This could be because by the time the heat source was turned on and increases the temperature at the upper region of the specimen, most of the pores near the surface already dried out, while the temperature increase is not high enough to influence drying in the deeper pores.
3. The dominant drying mechanism in PA appears to be evaporation of water at the surface of the material, followed by the diffusion of vapor from within the material to

the top surface and its subsequent convective removal by airflow above the surface. The contributions of air entrainment into the specimen and capillary transport of water to the surface appeared to be less significant during the drying process, which could be due to the roughness and tortuosity of the pore system of PA as well as the hydrophobicity of the solid matrix. However, in this chapter, wind speed was limited to 3 m/s, and therefore air entrainment into specimens at larger wind speeds needs to be investigated further.

4. Because of the high vapor diffusion resistance and the limited liquid water transport in hydrophobic PA, a higher wind speed leads to faster drying only if moisture is concentrated near the top surface of the PA specimen, due to convective vapor removal.

#### 4.5 INFLUENCE OF GRAVITY-DRIVEN DRAINAGE ON TOTAL MOISTURE LOSS

In terms of the boundary conditions of the specimens during the two set of experiments presented in this chapter, the most important difference is that while the specimens are uncovered on all sides in the first set of experiments, only the top surface is uncovered in the second set. This feature makes it possible to clearly isolate the influence of gravity drainage on the total moisture loss by comparing the two sets of experiments.

In Fig. 4.19, the temporal evolution of the average moisture loss from the entire specimen is plotted for PA8 and PA11 specimens from the first set of experiments (Section 4.3) and the second set of experiments (Section 4.4). They are denoted as 'uncovered' and 'covered' respectively. It is to be recalled that in the uncovered experiments, all the specimens are wetted by immersing them in water till they are fully saturated. Additionally, there is no thermal drying in the uncovered experiments and the duration of the experiments are longer. Although the uncovered specimens are not the same as the ones in this study, both set of specimens were prepared following the same standards and hence their pore space characteristics are expected to be similar. The most remarkable feature in Fig. 4.19 is the high moisture loss in the uncovered specimens in the initial stages, which is due to gravity-driven drainage. In the later stages, the covered specimens, due to their significantly higher moisture retention, lose moisture at a faster rate as compared to the uncovered specimens. However, despite the occurrence of gravity-driven drainage, the uncovered specimens show a high moisture content even after 6 hours of forced convective drying at low wind speed, thereby again indicating the strong influence of the high vapor diffusion resistance of PA.

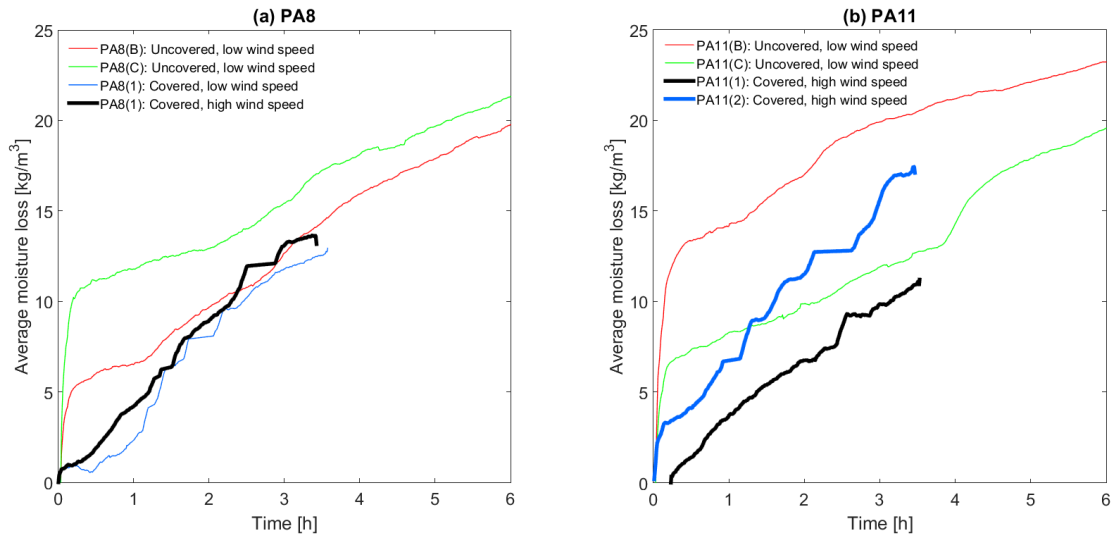


Figure 4.19.: Comparison of the temporal evolution of average moisture loss during the two sets of experiments presented in this chapter for (a) PA8 and (b) PA11 specimens. While the specimens in Section 4.3 are open on all sides (and hence called 'uncovered'), the specimens in Section 4.4 are covered at all sides except the top (and hence called 'covered').

## 4.6 SYNTHESIS

The experiments presented in the current and previous chapter involved the application of neutron radiography to analyze various liquid transport mechanisms in PA such as gravity drainage, capillary uptake, capillary redistribution and evaporation. Although the influence of airflow on the drying process in PA is studied in this chapter, the airflow itself is neither visualized nor analyzed in detail. This aspect is investigated in the next chapter.

## EXPERIMENTAL INVESTIGATION OF AIRFLOW ABOVE POROUS ASPHALT

---

*This chapter is based on the paper Lal et al. (2016).*

### 5.1 INTRODUCTION

In microporous materials like bricks, rocks and concrete, convective drying is enhanced by the turbulence induced by the porosity and/or roughness near the air-material interface. Turbulence increases the air-water vapor mixing at the interface, resulting in the reduction of the vapor pressure at the interface. In a macroporous material such as porous asphalt, drying can be further accelerated by air penetration into the large pores connected to the surface. Therefore, in this chapter, airflow near the surface of porous asphalt is studied in detail through wind tunnel experiments. The flow field is visualized by means of Particle Image Velocimetry (PIV). The specific objectives of this study are to characterize the turbulent air boundary layer in the near-wall region of PA pavements and to compare it to the boundary layer on a quasi-smooth surface, as well as to use conditional sampling techniques to assess the contribution of organized flow structures to the overall turbulence in the near-wall region. The turbulence statistics employed in this study are based mainly on previous studies on turbulent boundary layers over (impermeable) rough walls (Adrian et al. 1989; Raupach et al. 1991; Adrian 1996). To the author's best knowledge, this study is the first application of these statistics to characterize the flow over a macroporous surface.

### 5.2 MATERIAL CHARACTERIZATION

Three types of surfaces are used for the wind tunnel experiments in this study: PA8, PA11 and extruded polystyrene (henceforth referred to as foam). In Table 5.1, the results from a sieve analysis of the aggregates are shown for both types of asphalt. Each number corresponds to the relative contribution of the mass of aggregates in the corresponding size range to the total mass of all aggregates. It can be observed that, in PA8, most aggregates are in the 4-8 mm size range, while in PA11 most aggregates are in the 8-11.2 mm size range. Due to the larger aggregate sizes of PA11, the pore sizes are larger in PA11, as was shown in Section 3.3.1.2. Therefore, PA11 is characterized by larger pores

Table 5.1.: Aggregate size distributions of the PA8 and PA11 specimens used in wind tunnel experiments

Sieve size (mm)	Mass-%	
	PA8	PA11
0 - 0.063	4	4
0.063 - 0.125	1	1
0.125 - 0.25	2	1
0.25 - 0.5	2	1
0.5 - 1	2	2.5
1.0 - 2.0	4	2
2.0 - 4.0	6	4.5
4.0 - 5.6	38	7
5.6 - 8.0	38	7
8.0 - 11.2	3	60
11.2 - 16.0	0	10

at the air-material interface. This can be appreciated from the photographs of the top and side surfaces of PA8 and PA11, shown in Fig. 5.1. Figure 5.1(e) depicts the evolution of porosity (ratio of pore area to aggregate area) as a function of depth from the surface. The porosity profiles are determined from X-ray microcomputer tomography (X-ray  $\mu$ -CT) scans with a spatial resolution of 200  $\mu\text{m}$  for two PA8 and PA11 specimens of dimensions  $80 \times 80 \times 30 \text{ mm}^3$ . These specimens were compacted in a similar way as those used for these wind tunnel tests and hence their pore structures are expected to be similar. From Fig. 5.1(e), shows that, near the surface, larger pore sizes in PA11 do not lead to larger overall porosity.

The large pores near the surface of a typical PA specimen are interconnected as shown in a previous study (Poulikakos et al. 2013b). Unlike in the case of nonporous rough surfaces, a roughness height, which is commonly defined as the distance between the average peak height and the average valley depth of the surface roughness profile, cannot be estimated since the peaks and valleys are not clearly defined at the PA surface due to the interconnected nature of pores. The PA slabs used in this experiment are of dimensions  $2400 \times 400 \times 30 \text{ mm}^3$ , the same depth as actual PA pavements. The slabs were freshly prepared specifically for these experiments. The measurements over foam boards are used as a baseline case since foam is airtight and has a much lower roughness than that of PA, thereby making it a quasi-smooth surface. For the measurements over foam boards, the PA slab is simply replaced by a slab of foam of similar dimensions.

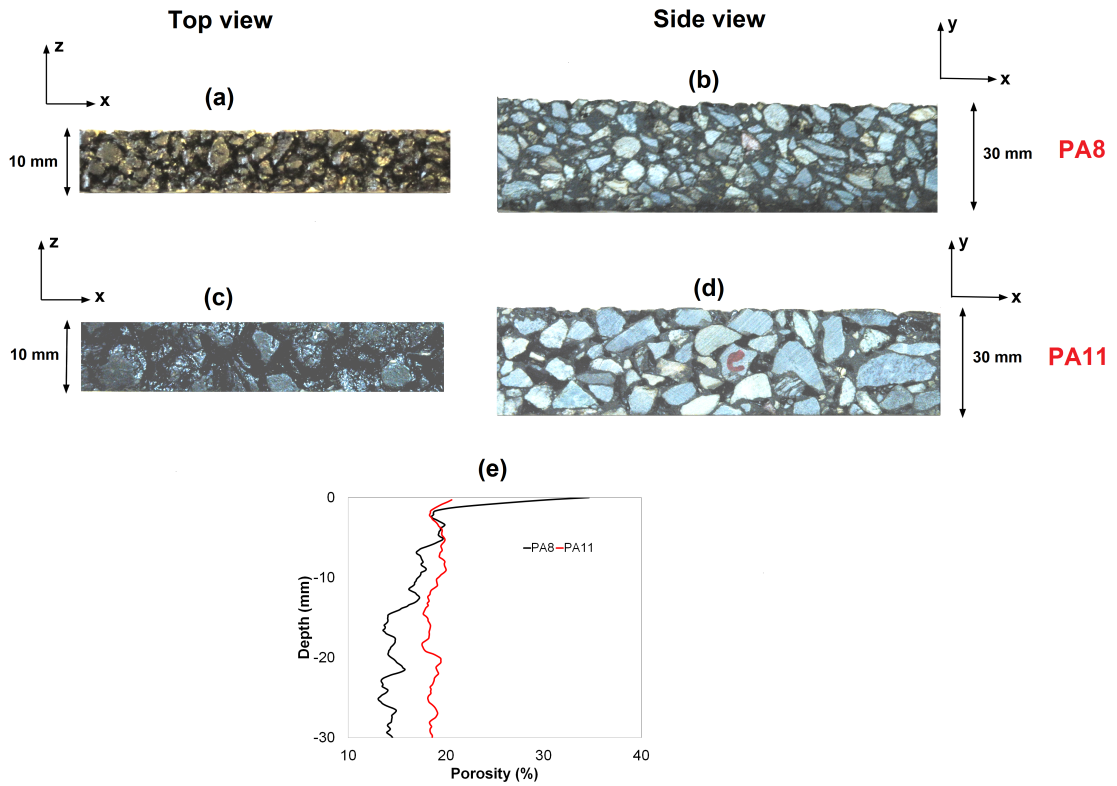


Figure 5.1.: Photographs of a section of the PA specimens: (a) top view and (b) side view of a section of the PA8 specimen, (c) top view and (d) side view of a section of the PA11 specimen and (e) porosity as a function of material height.

### 5.3 EXPERIMENTAL SETUP AND PROCEDURE

The experiments are performed at the ETH-EMPA wind tunnel in a closed-loop configuration. A photograph and schematic layout of the experimental setup is shown in Fig. 5.2. A large slab of porous asphalt ( $2400 \times 400 \times 30 \text{ mm}^3$ ) is placed in the wind tunnel. The slab is flush-mounted by adding an extruded polystyrene board around it and a smooth fairing upstream to avoid boundary layer separation. After the installation of the model, the test section has a free cross-section of  $1900 \times 1050 \text{ mm}^2$ . Special care is taken during the installation so that no damage is experienced by the samples.

The PIV system consists of two CMOS cameras (LaVision GmbH, 12-bit dynamic range,  $2016 \times 2016$  pixels), mounted side-by-side to obtain a total field of view (FOV) of  $280 \times 140 \text{ mm}^2$ . The airflow is seeded by means of spherical Di-Ethyl-Hexyl-Sebacat (DEHS) particles with a narrow size distribution around an average diameter of  $1 \mu\text{m}$ . The seeding is done with a 5-nozzle particle generator placed before the honeycombs and screens. After the seeding process, a sufficient time is allowed for the particles to be uniformly distributed in the entire wind tunnel and this is verified through preliminary images. A Nd:YLF laser with a power of 30 mJ/pulse is used to illuminate the DEHS particles within the field of view. The vertical plane of the laser sheet is parallel to the airflow direction and is centered along the asphalt slab (Fig. 5.2(c)). For each experimental run, 3155 statistically independent image pairs are acquired at a frequency of 10 Hz, which is estimated from the integral time-scale (the characteristic time-scale for the turbulence dynamics) of preliminary measurements. Best practice guidelines for PIV (Bolinder 1999; Keane and Adrian 1990) are taken into account to minimize the errors of the measurements. 3155 image pairs corresponds to a full camera memory and allows the calculation of the mean properties of the flow. The acquired images are first pre-processed by subtracting the background light intensity. Both images of each pair are cross-correlated following a three-level multi-pass approach, starting from a coarse interrogation window of  $48 \times 48$  pixels up to a fine interrogation window of  $24 \times 24$  pixels, with an overlap of 50% for all the passes. Between the passes, a median filter is applied to remove or replace vectors whose difference from the root mean square (rms) value of the neighbor signal is more than 10 times the standard deviation of the neighboring rms values. The final vector resolution achieved is 0.9 mm. Due to considerable reflection of the laser from the asphalt surface, the lowest location at which velocity could be measured is 5 mm above the surface. Measurements are conducted at three different free-stream air velocities i.e. 1, 2.85 and 4.75 m/s to allow verification of Reynolds independency of the observed quantities. The measurement window is at a distance of 1540 mm from the leading edge of the specimen. This distance is found to be sufficient to obtain fully developed velocity profiles in the measurement window.



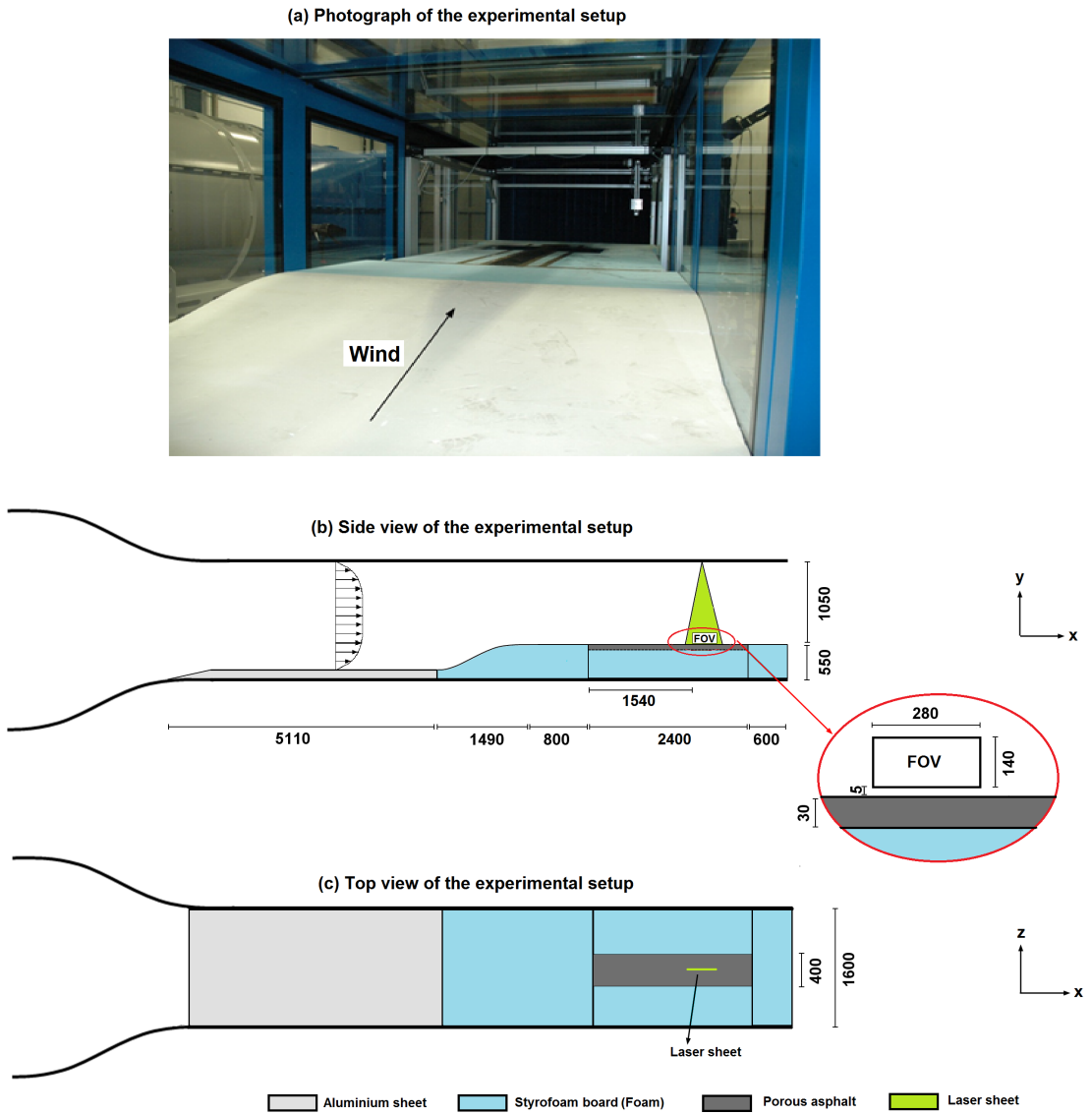


Figure 5.2.: Description of the wind tunnel experimental setup; (a) Photograph of the setup, and schematics of the (b) side view and (c) top view. All measurements are in mm. FOV = field of view.

## 5.4 RESULTS AND DISCUSSION

### 5.4.1 *Uncertainty in the estimation of statistical quantities*

The relative error in the estimation of mean air speed from  $N$  statistically independent images can be estimated as:

$$\varepsilon_{\mu} = \frac{Z_c \cdot TI}{\sqrt{N}}, \quad (5.1)$$

where  $Z_c$  is the confidence coefficient, which is equal to 1.96 for a confidence level of 95%, and  $TI$  is the turbulence intensity, defined as:

$$TI = \frac{\sqrt{rms(u')^2 + rms(v')^2}}{\langle U \rangle}, \quad (5.2)$$

where  $u'$  and  $v'$  are velocity fluctuations in the streamwise and wall-normal directions respectively and  $\langle U \rangle$  is the mean air speed defined as:

$$\langle U \rangle = \frac{1}{N} \sum_{i=1}^N U_i, \quad (5.3)$$

where  $U_i$  is the instantaneous streamwise velocity magnitude. The relative error in the standard deviation is estimated as:

$$\varepsilon_{\sigma} = \frac{Z_c}{\sqrt{N}}. \quad (5.4)$$

The maximum uncertainty of the mean and standard deviations within each experiment in this study is given in Table 5.2. As expected, the maximum uncertainty in mean air speed is at the near-wall location for all experiments i.e. at  $y = 5 \text{ mm}$ . However, due to the high number of sampling images used in this study, it can be seen that even the maximum uncertainties are below 2% and 2.5% for the mean and standard deviations respectively.

### 5.4.2 *Mean and turbulent statistics*

In this section, the airflow measurements over the three different surfaces i.e. foam board (smooth), PA8 and PA11, at three different speeds i.e. 1 m/s (low speed,  $Re_{\theta} = 700$ ), 2.85 m/s (moderate speed,  $Re_{\theta} = 2900$ ) and 4.75 m/s (high speed,  $Re_{\theta} = 4200$ ) are studied. It should be noted that air speeds are classified into low, moderate and high in this study solely for better readability and this does not imply a strict classification for scaling.

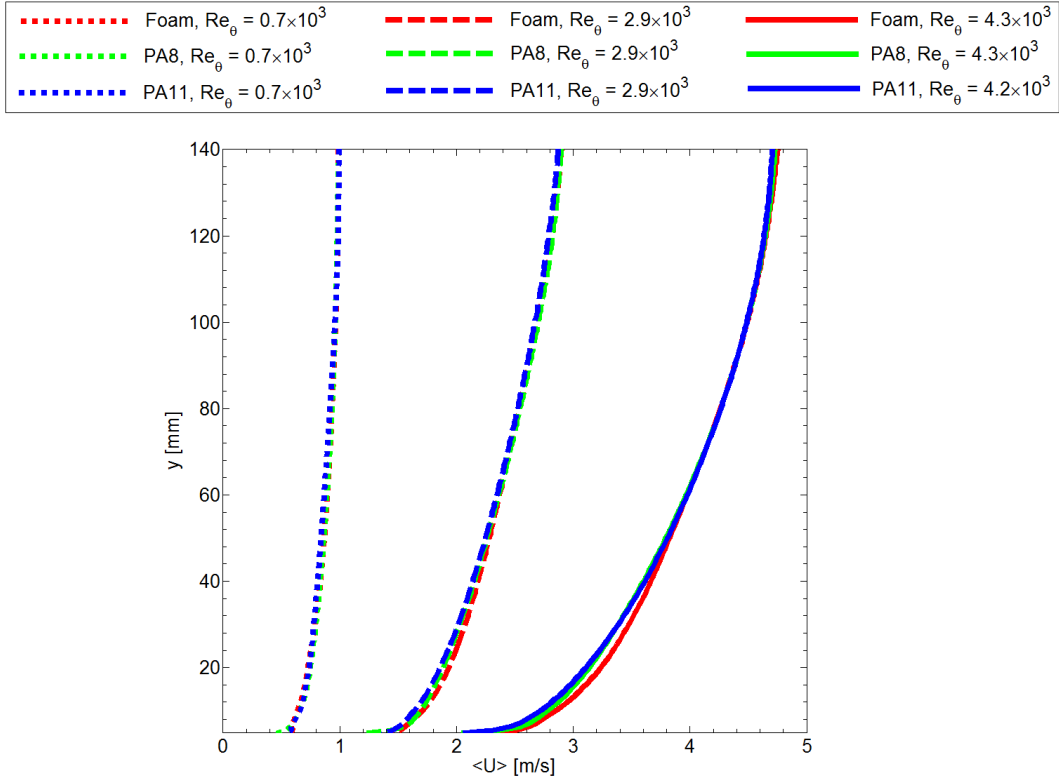


Figure 5.3.: Vertical profiles of mean streamwise velocity

Further details about the calculation of  $Re_\theta$ , the Reynolds number based on momentum thickness, are found below. Figure 5.3 shows the mean air speed,  $\langle U \rangle$ , as a function of the normal distance from the wall,  $y$ , for the different cases. As expected, at each tested air speed, a boundary layer develops due to the interaction with the surface. The boundary layer is more clearly distinguishable at high air speeds. At low speed, the effect of surface pores on the velocity profiles is less pronounced. At moderate and high speeds, the effect can be seen up to  $y = 60 \text{ mm}$ . At high speed, a small effect of the size difference of the surface pores between the two types of PAs is visible in the airflow velocity profiles. This aspect will be investigated in more detail in the subsequent sections.

Figure 5.4 shows the same profiles as Fig. 5.3 after normalization. In this figure, the mean air speed is replaced by the non-dimensional mean air speed  $U^+ = \langle U \rangle / u_*$ , and the vertical coordinate by the non-dimensional height above the surface  $y^+ = y \cdot u_* / \nu$ , where  $u_*$  is the friction velocity and  $\nu$  is the kinematic viscosity of air. The normalized profiles

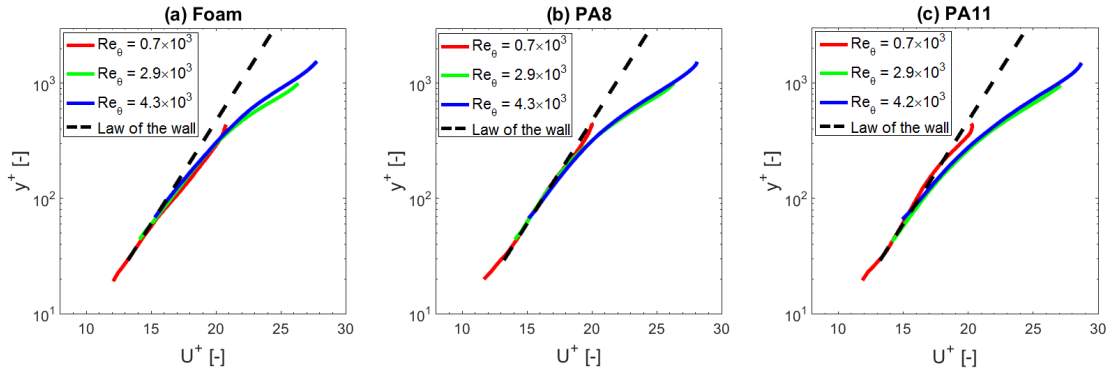


Figure 5.4.: Vertical profiles of mean streamwise velocity, scaled by friction velocity for (a) Foam, (b) PA8 and (c) PA11.

theoretically follow the so-called roughness-modified law-of-the-wall within the logarithmic layer (i.e.  $y^+ < 30$ ), which is given by:

$$U^+ = \frac{1}{\kappa} \log y^+ + B - \Delta U^+, \quad (5.5)$$

where  $\kappa$  is the Von Karman constant,  $B = 5.2$  and is the roughness function (Clauser 1954). The friction velocity  $u_*$  can then be estimated by minimizing the difference between the law-of-the-wall and the measured mean velocity profiles in the logarithmic layer. Since the velocity profiles of the same surface are collapsed over each other,  $u_*$  becomes independent of the roughness function. The calculated friction velocities for all the cases are listed in Table 5.2 and are used later in this study to scale the turbulence parameters.

In Table 5.2, various other boundary layer parameters are listed. The first parameter of interest is the boundary layer height,  $\delta$ , which is the height at which 99% of the free-stream velocity,  $U_\infty$ , is reached (see Fig. 5.5). Above the boundary layer height, the mean air speed remains approximately constant and, below, a boundary layer profile is found. Based on Fig. 5.3, the boundary layer height seems to exceed the field of view for the moderate and high-speed measurements. However, as the velocity observed at the top of the field of view (i.e. at  $y = 140 \text{ mm}$ ) is close to the free-stream velocity, measured by a pitot-tube positioned in the free stream, we make the assumption that  $U_\infty = U|_{y=140\text{mm}}$  for these cases. The impact of this assumption on all derived parameters was evaluated by a sensitivity study (see Appendix A). Although Schlichting and Gersten (2000) observed a decrease in the boundary layer height with increasing air speed as  $\delta \propto U_\infty^{-1/5}$ , the results from this study indicate the existence of a critical Reynolds number below which this inverse proportionality breaks down. This is similar to the results of Paterna (2015), who found an unexpectedly low boundary layer height at low speed ( $Re_\theta = 1500$ ) and attributed

Table 5.2.: Boundary layer parameters calculated in the wind tunnel experiments

Surface	Free-stream velocity $U_\infty$ (m/s)	Boundary layer height $\bar{\delta}$ (mm)	Displacement thickness $\bar{\delta}^*$ (mm)	Momentum thickness $\theta$ (mm)	Shape factor SF (-)	Friction velocity u. (m/s)	Reynolds number $Re_\theta$ (-)	$\varepsilon_{\mu,\max}$ (%)	$\varepsilon_{\sigma,\max}$ (%)
Foam	1.00	107.8	13.9	11.0	1.3	0.048	$0.7 \times 10^3$	1.92	2.47
	2.85	115.1	22.0	16.5	1.3	0.110	$2.9 \times 10^3$	0.85	2.47
	4.75	112.4	19.9	15.2	1.3	0.171	$4.3 \times 10^3$	0.70	2.47
PA8	1.00	125.1	14.4	11.7	1.2	0.050	$0.7 \times 10^3$	1.59	2.47
	2.85	131.4	22.3	16.6	1.3	0.110	$2.9 \times 10^3$	0.63	2.47
	4.75	126.9	20.1	15.0	1.3	0.168	$4.3 \times 10^3$	0.48	2.47
PA11	1.00	115.1	15.2	12.1	1.3	0.049	$0.7 \times 10^3$	1.76	2.47
	2.85	132.3	22.6	16.7	1.4	0.106	$2.9 \times 10^3$	0.59	2.49
	4.75	125.1	19.7	14.7	1.3	0.164	$4.2 \times 10^3$	0.56	2.47

this to a high degree of organization in the flow. Prior to investigating this hypothesis, we ensure that the obtained trend is not a product of the method used to determine the boundary layer thickness. Therefore, in Table 5.2, two related yet more robust quantities are calculated, namely the displacement thickness,  $\delta^*$ , and the momentum thickness,  $\theta$  (Coles 1956; Schlichting and Gersten 2000). These parameters are defined as:

$$\delta^* = \int_0^\infty \left(1 - \frac{U}{U_\infty}\right) dy, \quad (5.6)$$

$$\theta = \int_0^\infty \frac{U}{U_\infty} \left(1 - \frac{U}{U_\infty}\right) dy. \quad (5.7)$$

The displacement thickness can be interpreted as the distance by which an inviscid flow has to be displaced in wall-normal direction to account for the drop in velocity within the boundary layer in a real fluid. Similarly, the momentum thickness can be thought of as the distance by which an inviscid outer flow has to be displaced in a wall-normal direction to give the same lower momentum that exists in the boundary layer in a real fluid. These two parameters are illustrated in Fig. 5.5. The ratio of the displacement thickness to the momentum thickness is called the shape factor,  $SF = \delta^*/\theta$ , which is also given in Table 5.2. The final parameter in the table is the Reynolds number based on the momentum thickness,  $Re_\theta = U_\infty\theta/\nu$ , which is used to characterize the different air speed regimes.

Analogous to the boundary layer height,  $\delta^*$  and  $\theta$  are expected to decrease with increasing Reynolds number. However, from Table 5.2, it can be observed that this is not the case for any of the surfaces. In other words, the low-speed measurements have an unusually low boundary layer thickness. This anomaly is reflected in the shape factor  $SF$  as well and

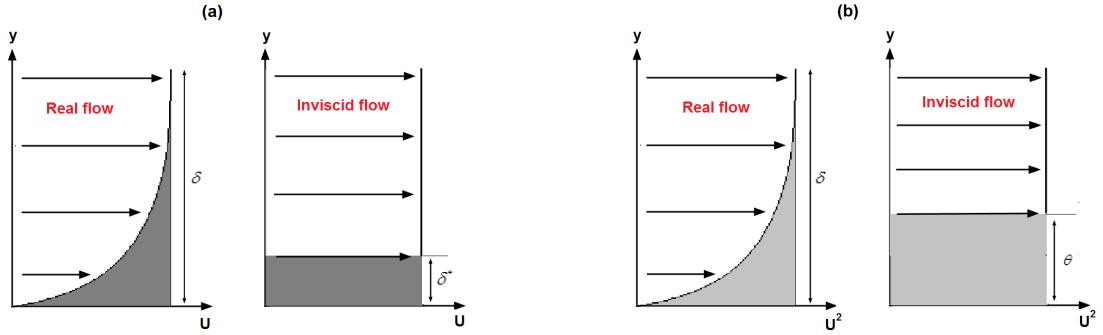


Figure 5.5.: Analogous representation of boundary layer parameters in a real flow to a hypothetical inviscid flow to obtain robust parameters such as (a) displacement thickness and (b) momentum thickness.

could be due to the occurrence of organized turbulent structures at low air speeds (Adrian et al. 2000; Paterna 2015). This hypothesis is analyzed in more detail in the subsequent paragraphs.

Figure 5.6 shows the skewness profiles,  $\langle S_q \rangle$ , of the streamwise velocity component,  $u$ , and the wall-normal velocity component,  $v$ . Skewness is the time-averaged third-order moment defined as:

$$\langle S_q \rangle = \frac{1/N \sum_{n=1}^N [q_n(r, t) - \langle q(r, t) \rangle]^3}{\left\{ \sqrt{1/N \sum_{n=1}^N [q_n(r, t) - \langle q(r, t) \rangle]^2} \right\}^3}, \quad (5.8)$$

where  $q_n(r, t)$  is a spatially ( $r$ ) and temporally ( $t$ ) instantaneous quantity,  $\langle q_n(r, t) \rangle$  is the time-averaged quantity and  $N$  is the total number of time steps. The skewness of a Gaussian distribution is zero. A positive skewness points to a large number of excursions with higher values than the mean while a negative skewness points to a large number of excursions with lower values than the mean. Unlike the velocity profiles in Fig. 5.3, the third order moments reveal small surface pores-induced differences for all considered air speeds. An important observation from Fig. 5.6 is that in the near-wall region, only the low-speed measurements show positive skewness of  $u$  and  $v$ . A positive skewness near the wall reflects the presence of high shear events imposed on a background of lower turbulence (Fernholz 1994; Johansson and Alfredsson 1982). This could explain the low values found for the displacement and momentum thickness in the low speed (and low turbulence) measurements (see Table 5.2). In the near-wall region, high positive values of the skewness of streamwise velocity,  $\langle S_u \rangle$ , are found only in the low-speed measurements, indicating

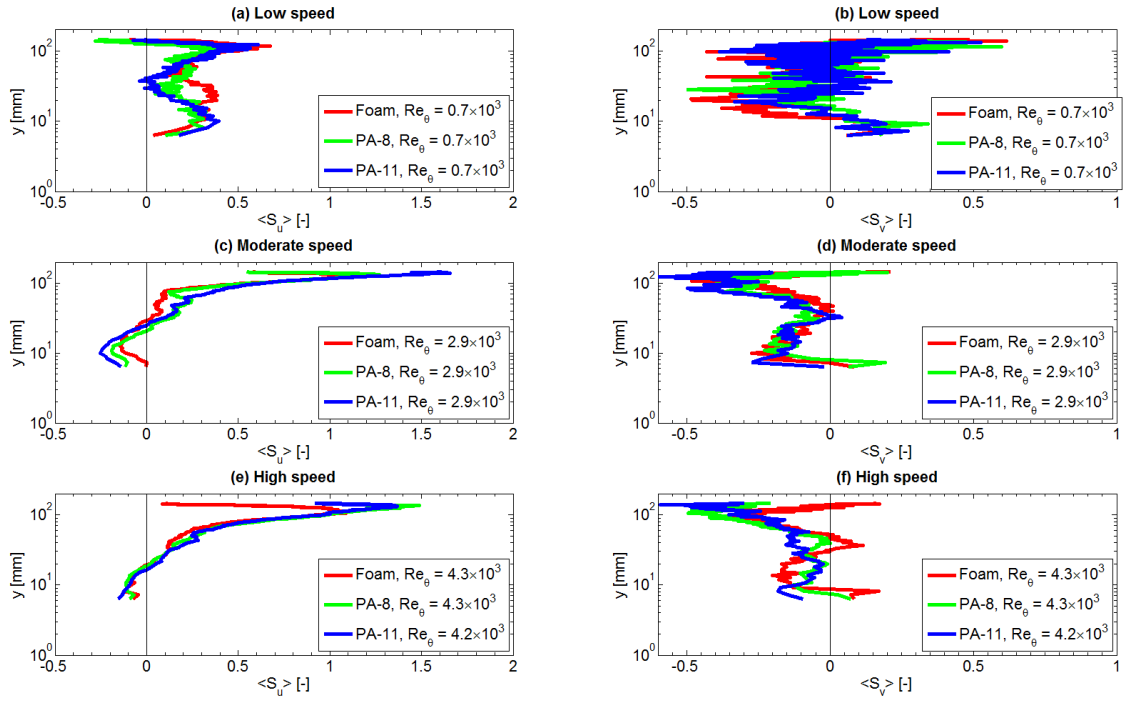


Figure 5.6.: Skewness profiles of  $u$  (left) and  $v$  (right) at the three air speeds.

the dominance of sweep events at this speed. This observation is further strengthened from the results of the Q-H analysis (see Section 5.4.3). Due to the higher magnitude of  $u$  compared to  $v$ ,  $\langle S_u \rangle$  gives more insight into the dynamics of turbulent flows than  $\langle S_v \rangle$ . For the moderate and high-speed measurements, the general trend is that  $\langle S_u \rangle$  changes from negative to positive along the wall-normal direction. This points to the dominance of events with velocities lower than the average velocity, near the surface. This is expected due to the low airflow velocity in the inner layer of the boundary layer. However, this is not the case with the low-speed measurements, where the dominance of events with velocities higher than the average velocity can be observed, near the surface. This is yet another indication of a small boundary layer thickness, which was already observed from Table 5.2. It can also be observed that, with increasing velocity, the skewness profiles of the different surfaces overlap more. Reading this together with Fig. 5.3, it can be observed that, while the differences in the velocity profiles of the three surfaces increase with increasing air speed, the skewness profiles increasingly converge with increasing air speed. This could be due to the fact that the relative magnitude of the increase in velocity fluctuations is small compared to the increase in mean air speed.

Figure 5.7 presents the three measured time-averaged Reynolds stress components i.e. the shear stress  $\langle u'v' \rangle$ , streamwise turbulence  $\langle u'u' \rangle$  and wall-normal turbulence  $\langle v'v' \rangle$ , as a function of the distance from the wall. No scaling is applied in this figure. For the low speed flow, the Reynolds stresses are low and the profiles above all the surfaces share a similar shape except very close to the wall. At the moderate speed, the profiles above the two PA surfaces are similar, though they are slightly different from those above foam. At the highest speed, a clear dependency of the profiles on the surface pore size can be observed, especially close to the surface. Furthermore, at high air speed, the maximum Reynolds stress is found at a different height for the three surfaces. The peaks in shear stress and streamwise turbulence for the two PA surfaces are vertically separated at the highest speed by at least 10 mm, as can be seen in Figs. 5.7(a) and 5.7(b). Finally, high-speed flow generates significantly more turbulence over the surface of PA11 than over PA8. In the low and moderate-speed measurements, though a difference in the turbulence plots can be observed between the smooth surface and the PA surface, there is no appreciable difference between the two PA surfaces.

Figures 5.8 and 5.9 present the Reynolds stress components in inner velocity scaling (normalized with  $u_*$ ) and outer velocity scaling (normalized with  $U_\infty$ ), respectively. In inner scaling, Reynolds independence of both shear and streamwise Reynolds stress components (Figs. 5.8(a) and 5.8(b)) can be observed for the moderate and high speed cases for  $y > 80 \text{ mm}$  and for the wall-normal component (Fig. 5.8(c)) at all heights. The same observations hold in outer scaling, but from  $y > 50 \text{ mm}$  onwards (Fig. 5.9). However, as already observed, the lowest speed is a rather abnormal case and does not follow the Reynolds scaling.



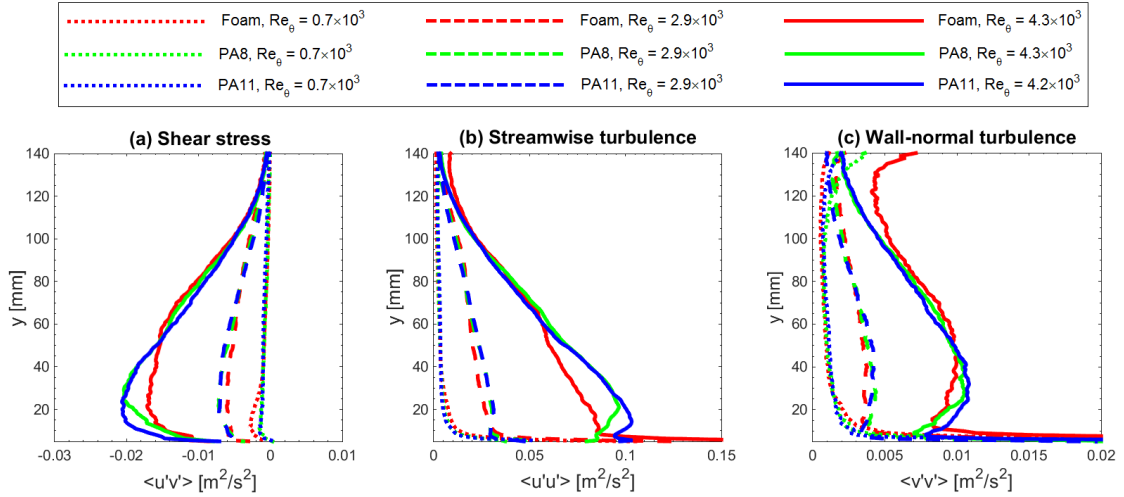


Figure 5.7.: Profiles of Reynolds stress components without scaling: (a) Shear stress, (b) Streamwise turbulence and (c) Wall-normal turbulence.

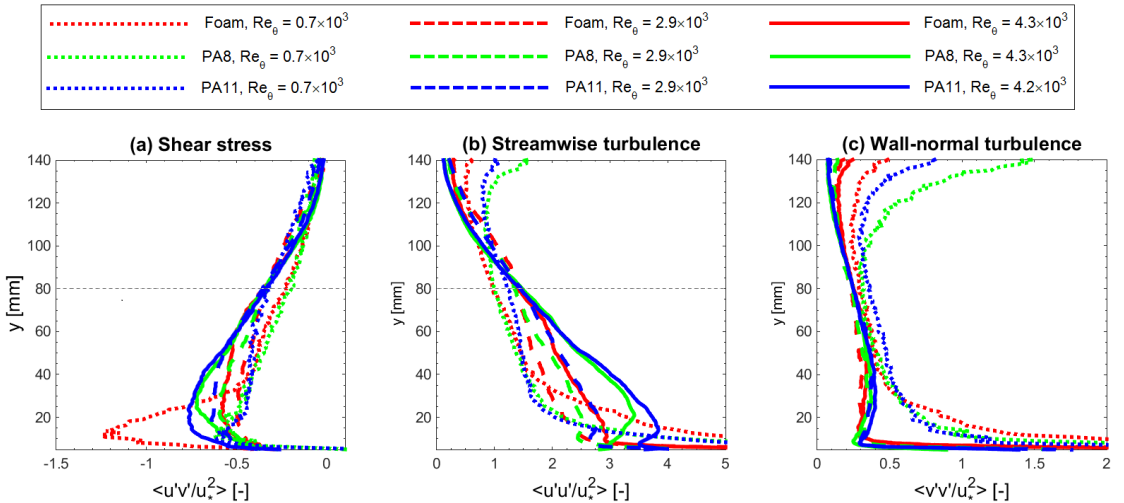


Figure 5.8.: Profiles of Reynolds stress components in inner scaling: (a) Shear stress, (b) Streamwise turbulence and (c) Wall-normal turbulence.

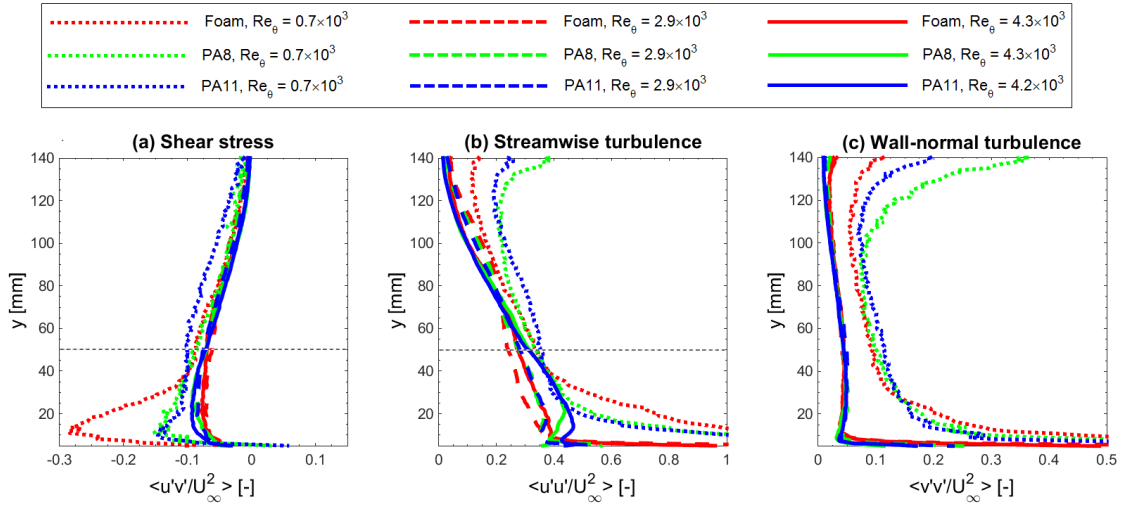


Figure 5.9.: Profiles of Reynolds stress components in outer scaling: (a) Shear stress, (b) Streamwise turbulence and (c) Wall-normal turbulence.

The fact that no generally valid scaling is found has important practical implications for future experiments that would study forced convective drying of wet porous asphalt. The presence of strong, organized turbulent structures near the wall during the low-speed measurements could be the reason why the boundary layer velocity profiles at the low speed do not show similarity with the moderate and high-speed profiles after scaling. This aspect is examined in further detail in the next section. Scaling laws are found to be valid for the moderate and high speed flows, but only above a certain height. This is not surprising. The scaling of turbulence parameters has always been a challenge for researchers and has led to a variety of inner-outer mixed scalings, especially in and around the near-wall region. Energy balance of the boundary layer indicates that the total power dissipated by the boundary layer scales with free-stream velocity and shear stress, while shear stress in turn scales with friction velocity (De Graaff and Eaton 2000). Thus, the total rate of energy dissipated by the turbulence depends on both free-stream velocity (used for outer scaling) and friction velocity (used for inner scaling).

To sum up, for all the air speeds considered in this study, no generally valid scaling was found close to the surface, where drying occurs. Hence, studies of drying would require performing experiments at full-scale and for the entire range of velocities, similar to the experiments reported in this paper. This is all the more important since low speed flows ( $<2.85$  m/s) are a common occurrence over land surfaces (Archer and Jacobson 2005) and we observed distinctive turbulence profiles at the lowest speed. In this context, it should be noted that a generally valid velocity scaling, even if it were observed, would not imply

a scalable drying behavior in a macro-porous material like PA since air penetration into the material should also be taken into account, especially at high wind speeds, as is shown in Chapter 6.

### 5.4.3 Conditional sampling of turbulence parameters

It is now widely accepted that downdraft motion (sweeps) and updraft motion (ejections) of air are the most important constitutive events occurring in turbulent airflow near a rough surface. These events are the most important contributors to the Reynolds stresses and momentum transfer near the air-material interface. Conditional statistics, such as Quadrant-Hole (Q-H) analysis as developed by e.g. Raupach (1981) and Willmarth and Lu (1972), are often used to study such turbulent structures in the flow near a fluid-solid interface (Longo et al. 2015; Paterna 2015; Wang et al. 2010). In this section, Q-H analysis is used to investigate the contribution of coherent motions such as sweeps and ejections in the turbulent flow. The shear stresses are conditionally-averaged to distinguish between the contributions of 'organized' and 'unorganized' events to the total turbulence. Based on the signs of the instantaneous velocity fluctuations of the streamwise and wall-normal velocity components,  $u'$  and  $v'$  respectively, the events can be classified as Q1 events ( $u' > 0$ ,  $v' > 0$ ), Q2 events ( $u' < 0$ ,  $v' > 0$ ), Q3 events ( $u' < 0$ ,  $v' < 0$ ) and Q4 events ( $u' > 0$ ,  $v' < 0$ ), according to the quadrants in which these points fall in a  $u' - v'$  diagram, as shown in Fig. 5.10(b). The Q2 events are ejections while the Q4 events are sweeps. The most important events fall in quadrants 2 and 4 since these events give positive instantaneous contributions ( $-u'v'$ ) to the Reynolds stress (Guo et al. 2010). Ejections and sweeps (Fig. 5.10(a)) are assumed to be associated with organized structures, responsible for significant transfer of momentum between the surface and the air (Willmarth and Lu 1972). Despite the possible importance of such coherent motions for forced convective drying of soil or porous asphalt surfaces, no study has been reported so far on this relationship, to the best of our knowledge.

In order to introduce a notion of scale, the time-averaged contribution of each quadrant  $i$ ,  $\langle u'v' \rangle_{i,H}$ , can be filtered to exclude fluctuations with a magnitude smaller than the size of the hyperbolic hole  $H$ , which is indicated by the shaded region in Fig. 5.10(b):

$$\langle u'v' \rangle_{i,H} = \lim_{T \rightarrow \infty} \frac{1}{T} \int_0^T u'(t)v'(t) I_{i,H} [u'(t)v'(t)] dt, \quad (5.9)$$

where  $I_{i,H}$  is a binary variable that is used to select the events to include, and which implicitly accounts for the minimum shear stress that should be considered:

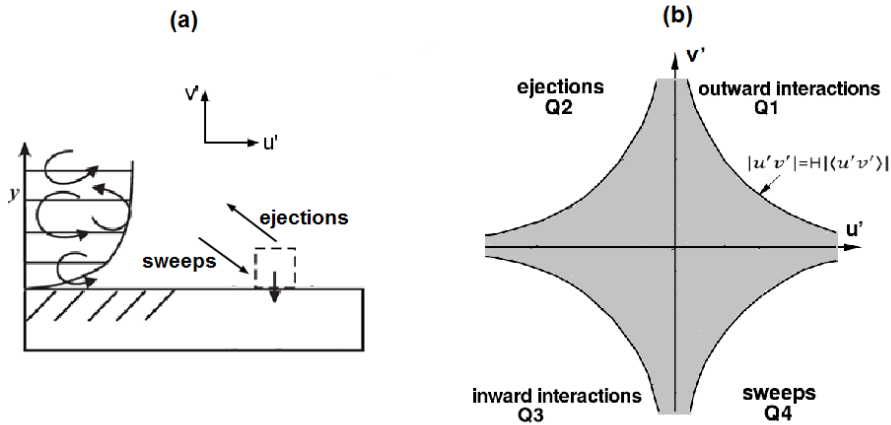


Figure 5.10.: (a) Schematic representation and (b) graphical representation of sweeps and ejections, where the shaded region indicates the hyperbolic hole region which is used to filter out fluctuations of small magnitudes.

$$I_{i,H} [u'(t) v'(t)] = \begin{cases} 1 & \forall (u', v') \in Q_i; |u'v'|_{i,H} \geq H \sqrt{\langle u'^2 \rangle} \sqrt{\langle v'^2 \rangle} \\ 0 & otherwise \end{cases} \quad (5.10)$$

By varying  $H$ , the contributions of eddies with different scales can be analyzed and their impact on the relative importance of the individual quadrants can be recognized.

Figures 5.11, 5.12 and 5.13 present the results of the Q-H analysis on foam, PA8 and PA11 respectively, scaled by friction velocity i.e. inner velocity scaling. Subplots 'a', 'd', 'g' concern the low-speed measurements, subplots 'b', 'e', 'h' the moderate-speed measurements and subplots 'c', 'f', 'i' the high-speed measurements. Three different values of the hyperbolic hole are considered for the analysis i.e.  $H = 0, 2$  and  $4$ . It can be observed that generally, ejections (Q2) and sweeps (Q4) dominate over the Q1 and Q3 events. Among ejections and sweeps, sweeps are more dominant, especially at the low-speed measurements. Above all surfaces, at  $H = 2$ , the contributions from Q1 and Q3 events fall to almost zero. The high intensity of Q2 and Q4 events close to the wall in the low-speed measurements confirms the hypothesized presence of organized structures based on the low displacement and momentum thicknesses in Table 5.2 and the positive skewness near the surface in Fig. 5.6(a) and 5.6(b).

As the value of  $H$  increases, the overall dominance of sweeps over ejections increases. Specifically, for the moderate and high-speed plots of both PAs, the location of the Q2 and Q4 peaks shifts further from the wall with increasing value of  $H$ , and also the peaks

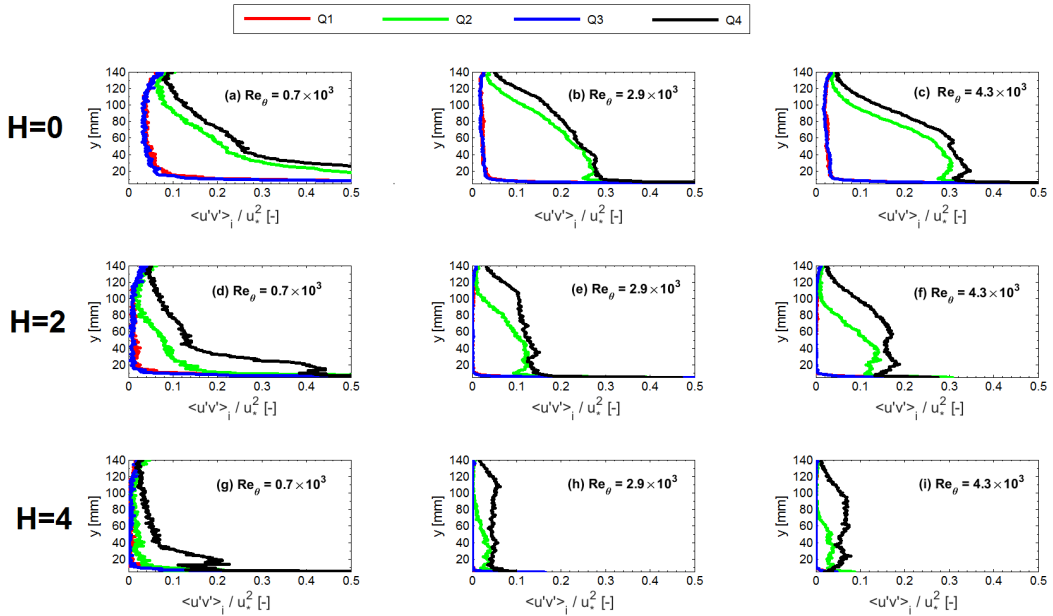


Figure 5.11.: Q-H analysis on foam board with inner velocity scaling, where Q2: ejections and Q4: sweeps.

widen. This shows that the effect of sweep and ejection events is felt across a much larger distance from the wall along the wall-normal direction compared to that of the weak ones. In other words, the stronger the intensity of the sweeps and ejections, the lesser the probability that the momentum transfer from these organized structures will be restricted to the surface region. On the two PA surfaces, at the moderate and high velocities, the intensities of sweeps and ejections are similar in the near-wall region. Along the wall-normal direction, the gap between them widens in favor of sweeps. This clear trend can also be seen in the measurements on foam, but to a lesser extent. Near a perfectly smooth surface, ejections are the dominant events while sweeps are the dominant events near a rough surface (Keirsbulck et al. 2002). This can be the reason why sweeps are still dominant near the smoother foam surface, but not as dominant as they are near the rougher PA surfaces.

Figure 5.14 presents the comparison between the three surfaces in terms of the sweeps and ejection events for the three considered air speeds. Only the results for  $H = 4$  are compared. The wall similarity hypothesis states that, outside the roughness sublayer, the turbulent motions are independent from the wall roughness, as confirmed by Perry et al. (1969), Raupach (1981) and Raupach et al. (1991). The effect of surface roughness on the sweep and ejection events can indeed be observed only up to a certain wall-normal distance.

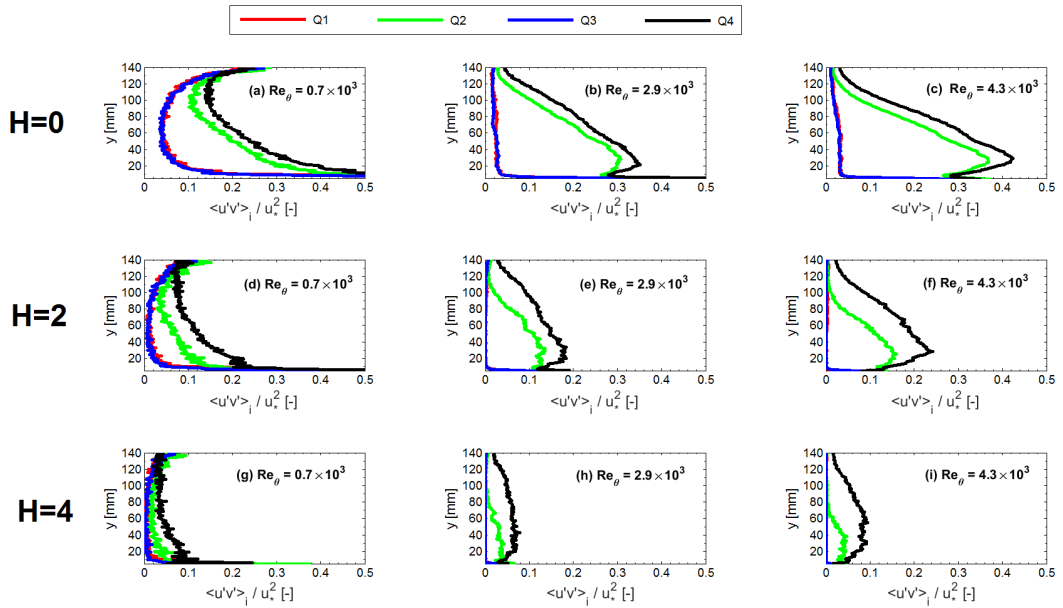


Figure 5.12.: Q-H analysis on PA8 with inner velocity scaling, where Q2: ejections and Q4: sweeps.

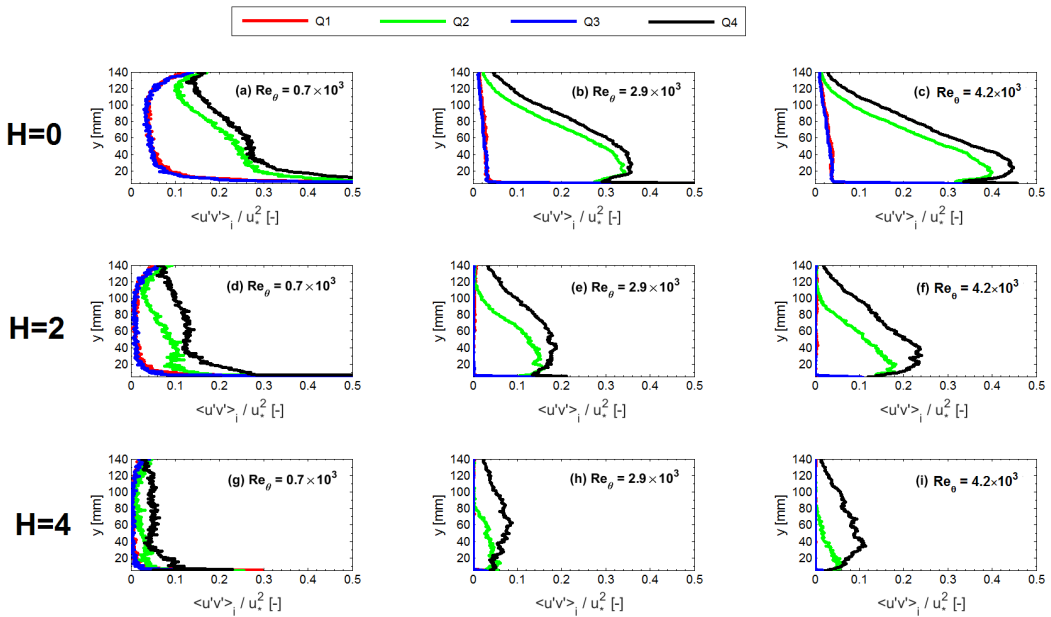


Figure 5.13.: Q-H analysis on PA11 with inner velocity scaling, where Q2: ejections and Q4: sweeps.

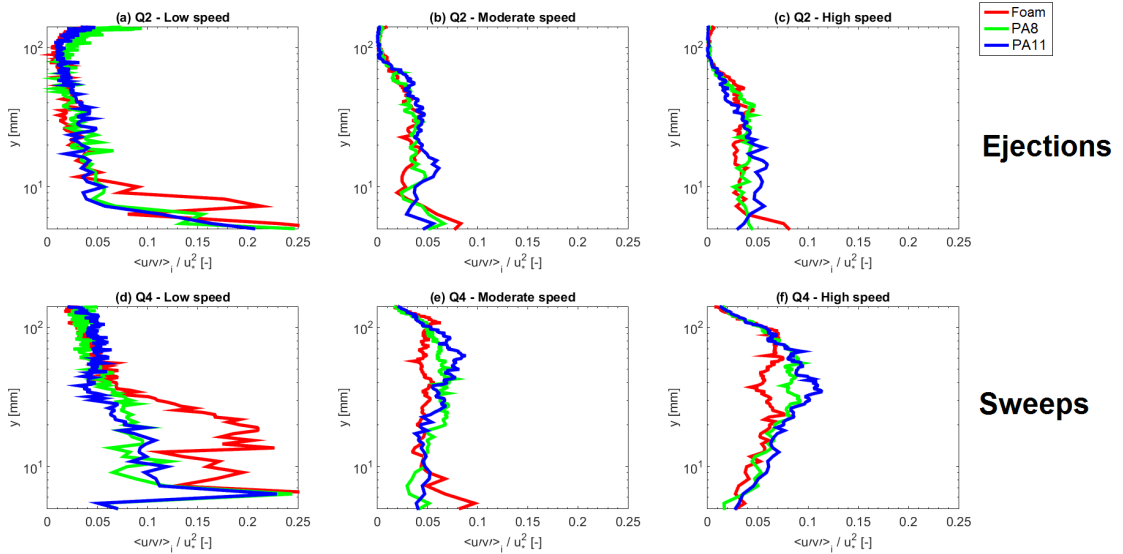


Figure 5.14.: Comparison of Q2 (ejection) and Q4 (sweep) events between foam, PA8 and PA11 at  $H = 4$ .

From the moderate and high-speed measurements, it can be observed that this distance is approximately  $y = 70 \text{ mm}$  and  $y = 100 \text{ mm}$  for the ejections and sweeps respectively. Significantly, close to the surface, a large difference in the sweeps or ejection profiles of PA8 and PA11 can be seen only in Fig. 5.14(c). This is consistent with the inferences made from Figs. 5.7-5.9, i.e. a difference in drying behavior of the two PAs, as a consequence of their different surface pore sizes, is expected to be prominent only at air speeds equal to or higher than 4.75 m/s. This has an important implication for future studies to model convective drying of PAs with different surface pore sizes. If the air speed is equal to or lower than 3 m/s, a uniform turbulent boundary layer can be assumed near all the PA surfaces, as long as their surface pore sizes and the pore profiles on the surface are not very different from those of PA8 and PA11. In this context, a detailed analysis of surface pore sizes of the different types of PAs would be an ideal complement to the present study.

In Fig. 5.14(d)-(f), the surface with the largest pores i.e. PA11, is not always the one displaying the strongest sweeps. This contradicts the observations of Keirsbulck et al. (2002) who noted strong sweeps on rough surfaces. In fact, for the low-speed measurements, the sweep events are even the strongest on the smooth surface (foam), as seen in Fig. 5.14(d). However, as the speed increases, the sweep events on the rougher surfaces gain strength and at high speed (Fig. 5.14(f)), the roughest surface (PA11) has the strongest sweep events. A high fluctuation in the  $v$ -component of velocity facilitates stronger sweep events (Krogstad et al. 1992). Therefore, higher air speeds, producing higher turbulence,

and rougher surfaces, which lead to a reduced damping of the  $v$ -component by the cavities, should lead to more dominant sweep events. While the measurements in Keirsbulck et al. (2002) were done at  $Re_\theta=8500$ , the high-speed measurements in this study are at  $Re_\theta=4300$  only. This could explain why the observations of Keirsbulck et al. (2002) are not applicable to the low and moderate velocity measurements in this study, since the wall-normal turbulence is too low at these speeds. Additionally, these results also point to the existence of a critical Reynolds number above which the difference in the surface pore sizes of PA pavements influences the presence of organized structures in the near-wall region.

## 5.5 CONCLUSIONS

The mean and turbulent flow characteristics of airflow above macroporous PA surfaces are analyzed in this chapter. Airflow over two types of porous asphalt (PA) pavements, PA8 and PA11, is studied at three air speeds at constant temperature. Measurements over foam boards (quasi-smooth surface) are used as a reference to which the measurements over the rougher PA pavements are compared. The most important conclusions are:

1. At low air speed, the small values of the displacement and momentum boundary layer thicknesses indicate the presence of organized turbulent structures, which is confirmed by the positive skewness of the streamwise velocity component in the near-wall region. Moreover, in the Q-H analysis, a high intensity of ejection (Q2) and sweep (Q4) events is also observed in the near-wall region in the low-speed measurements.
2. The effect of sweeps and ejections is observed across a significant distance along the wall-normal direction above the macroporous PA-surfaces. As the distance from the wall increases, the difference between the intensities of sweep and ejection events also increases, with sweeps dominating ejections. This implies that, as the distance from the wall increases, the occurrence of high-speed air from regions far from the wall dominates the arrival of low-speed air from the wall.
3. For the moderate and high-speed measurements, a sensitivity of sweep and ejection events to surface pore sizes is observed but only within the first 80 and 100 mm respectively above the surface. Within these heights and at these velocities, the sensitivity of sweeps to surface pore sizes is more pronounced than that of ejections. However, no clear dominance of either sweeps or ejections on any particular surface is observed, although sweep events over more porous surfaces gained strength with increasing air speeds.



4. The turbulence statistics plots exhibit significant Reynolds dependency under low speed conditions. As no generally valid scaling law could be found, realistic drying experiments on macroporous materials like porous asphalt need to be performed at full-scale and for the entire range of velocities of interest.
5. Close to the PA surface, the air turbulence profiles are found to be sensitive to surface pore sizes/roughness only at high air speed, mainly due to higher ejections on the porous surface at this speed. This has an important practical implication. At low air speeds (less than 3 m/s), the contribution of surface pores-induced turbulence to convective drying will be similar for different PAs, provided their porosity profile is similar to that of the specimens used in this study. In such cases, from a macro-scale modelling perspective, this means that a simplified assumption of the roughness induced by surface pores can be made for PA specimens while performing convective drying simulations on them.

## 5.6 SYNTHESIS

This chapter presented an in-depth analysis of the turbulent air boundary layer in the near-wall region of porous asphalt. However, another important factor that can influence drying is the momentum transfer from air infiltration in PA. At the wind speeds considered in this study, sweeps and ejections are found to occur near the surface. But it cannot be concluded at this stage if these sweeps and ejections are as a result of air infiltration into the pores or as a result of the surface roughness. This implies that the air velocity fields in the pores, especially in the ones close to the air-material interface, should be investigated in more detail and for higher mean wind speeds. This aspect is studied through computational fluid dynamics simulations in the next chapter.



## COMPUTATIONAL FLUID DYNAMICS MODELING OF AIRFLOW AND WATER VAPOR TRANSPORT IN POROUS ASPHALT

---

### 6.1 INTRODUCTION

The previous chapters provided experimental insights into air and water flow within porous asphalt. While the combination of neutron radiography and X-ray  $\mu$ -CT imaging allowed the visualization of water flow within PA specimens, PIV imaging provided a clear visualization of the air velocity field above PA specimens. However, for a complete understanding of multiphase flow within PA, what is missing at this stage is the visualization of airflow within PA and its influence on the transport of water vapor from the specimen. Therefore, in this chapter, computational fluid dynamics (CFD) simulations are used to study airflow and vapor transport within PA. The PA domain used in the simulations is extracted from a three-dimensional X-ray  $\mu$ -CT scan without applying any geometric simplification. The influence of two parameters on vapor transport from PA are investigated in this chapter: wind speed and the depth of the vapor source within the material.

### 6.2 MATERIALS AND METHODS

#### 6.2.1 *Numerical model and computational domain*

Two sets of CFD simulations are carried out in this study. The first set of simulations (precursor simulations) are two-dimensional simulations performed to select the appropriate near-wall air turbulence model and grid sizes for the second set of simulations. The second set of simulations (PA simulations) are three-dimensional simulations performed to carry out the objectives of this study i.e. analyze air and vapor (i.e. scalar) flow in an actual PA geometry. The computational domains of both sets of simulations along with the respective boundary conditions are presented in Fig. 6.1. The overall domains of both sets of simulations consist of two domains merged together: the upper domain that consists of the air inlet and outlets of both air and vapor, and the lower domain that consists of the vapor source. The upper and lower domains of the 3D PA simulations are marked in Fig. 6.1(b). For the 2D precursor simulations, the upper domain is a 2D channel with height,  $H_c = 50 \text{ mm}$  and length,  $L_c = 380 \text{ mm}$ . For the 3D PA simulations, the upper domain is a 3D channel with the same height and length as the 2D channel and width,

$W_c = 50 \text{ mm}$ . Thus, with an equal height and width of 50 mm, the aspect ratio of the upper domain of the PA simulations is 1. For the precursor simulations, the lower domain is a linear source ( $L_s = 180 \text{ mm}$ ) that is placed flush at the bottom of the upper domain while in the PA simulations, the linear source is replaced by the X-ray  $\mu$ -CT scan of an actual PA11 specimen ( $180 \times 10 \times 30 \text{ mm}^3$ ), and is attached to the upper domain at its top surface, as shown in Fig. 6.1(b). The PA11 specimen used in this study is the PA11(A) specimen used and described in Section 4.3 and its material characteristics are detailed in Section 4.3.1. During the merging process of the PA scan with the upper channel domain, all pores in the scan that are not connected to the upper domain are removed since these pores will not have any air entry. Thus, the domain of the PA simulations is designed to reproduce real world conditions i.e. wind flow above PA pavements and possible air entrainment into the pores. The domain dimensions and computational grid are based on best practice guidelines (Casey and Wintergerste 2000). Upstream (50 mm long) and downstream (150 mm long) channel sections are given in the domain to prevent any impact of the imposed inlet and outlet boundary conditions on the air momentum and scalar transport near the PA geometry. The grid of the precursor simulations is composed of  $76 \times 103$  hexahedral cells while the grid of the PA simulations is a hybrid grid of more than  $9 \times 106$  cells composed of multiple types of polyhedral cells. From the grid sensitivity analysis in the precursor simulations, the spatial discretization error is determined to be below  $10^{-4}$  using Richardson extrapolation (Roache 1994). The parameter used for the Richardson extrapolation analysis is the shear stress at the flat plate,  $\tau_w = \rho\nu(du/dz)_w$ , where  $(du/dz)_w$  is the wall-normal velocity gradient at the plate,  $\rho$  is the air density ( $1.2 \text{ kg/m}^3$  in this study) and  $\nu$  is the kinematic viscosity of air ( $1.5 \times 10^{-5} \text{ m}^2/\text{s}$  in this study). Wall shear stress is chosen for the grid sensitivity analysis since it is the parameter that determines the convection in the vicinity of the flat plate, which is also where the scalar is released (source).

The computational grid in the near-wall region of the PA simulations is presented in Fig. 6.2 for the breadthwise centerplane i.e.  $z = 25 \text{ mm}$ . As can be seen in Fig. 6.2, the grid resolution in the near-wall region is very high. Such a high resolution is necessary since the air flow in the near-wall region is modeled with Low Reynolds Number Modeling (LRNM) in this study, which explicitly solves the flow in the boundary layer, unlike wall functions which represent the flow in the near-wall region with semi-empirical functions. In the near-wall region, where sharp gradients in the flow-field are expected, LRNM requires a high grid resolution i.e.  $y_w^+ \approx 1$ , where  $y_w^+$  is the  $y^+$  value at the wall-adjacent cell center and is defined as  $y_w^+ = (\tau_w/\rho)^{1/2}y_w/\nu$  and  $y_w$  is the wall-normal distance from the cell center of the wall-adjacent cell to the wall. In the precursor simulations, the  $y_w^+$  values for all the wind speeds in this study was determined to be around 1, thereby justifying the selection of LRNM.

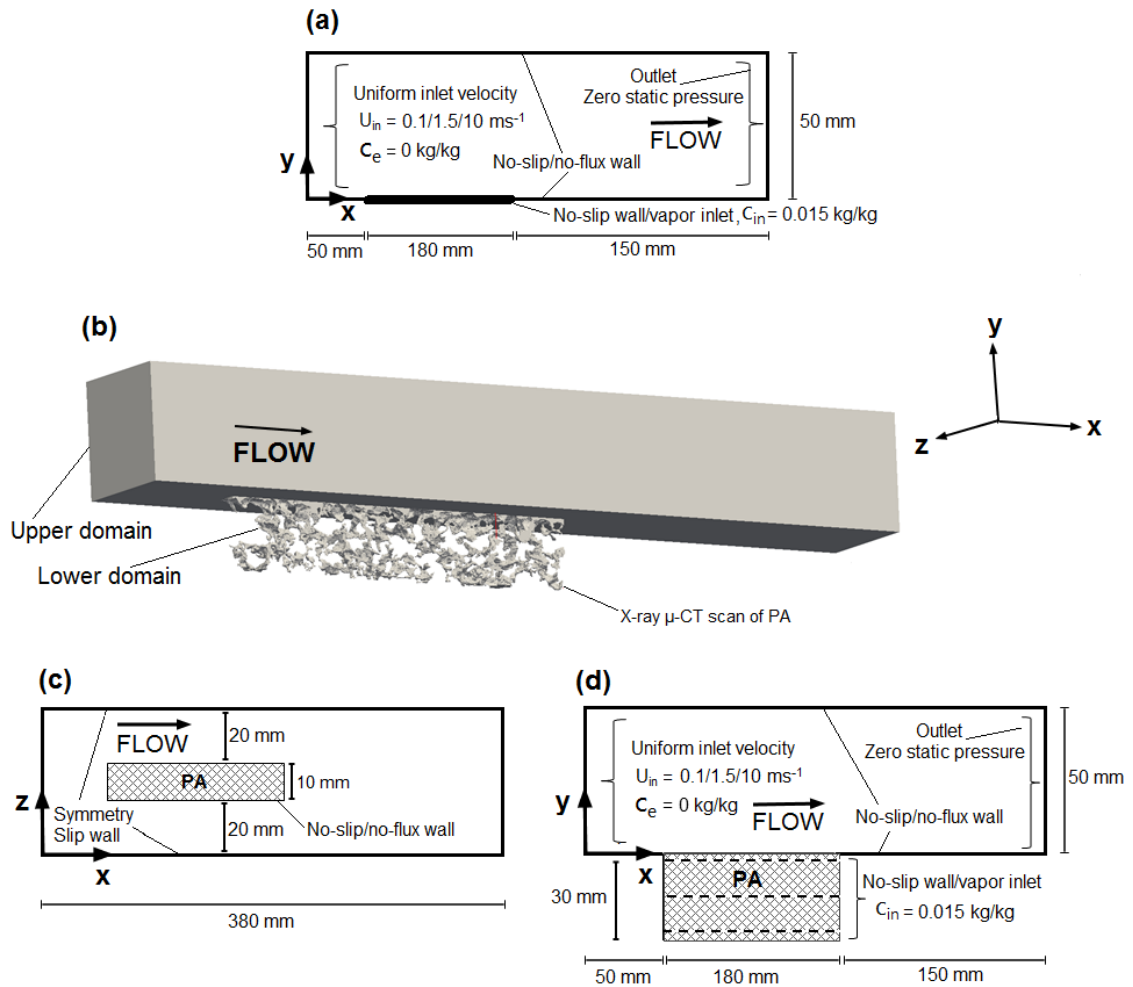


Figure 6.1.: The computational domains (not to scale) and boundary conditions used for (a) the two-dimensional precursor simulations and (b-d) the three-dimensional PA simulations. The three-dimensional view of the PA simulations domain is given in (b) while the top and side views of (b) are given in (c) and (d) respectively. The PA scan in (b) is represented by the hatched region in (c) and (d).

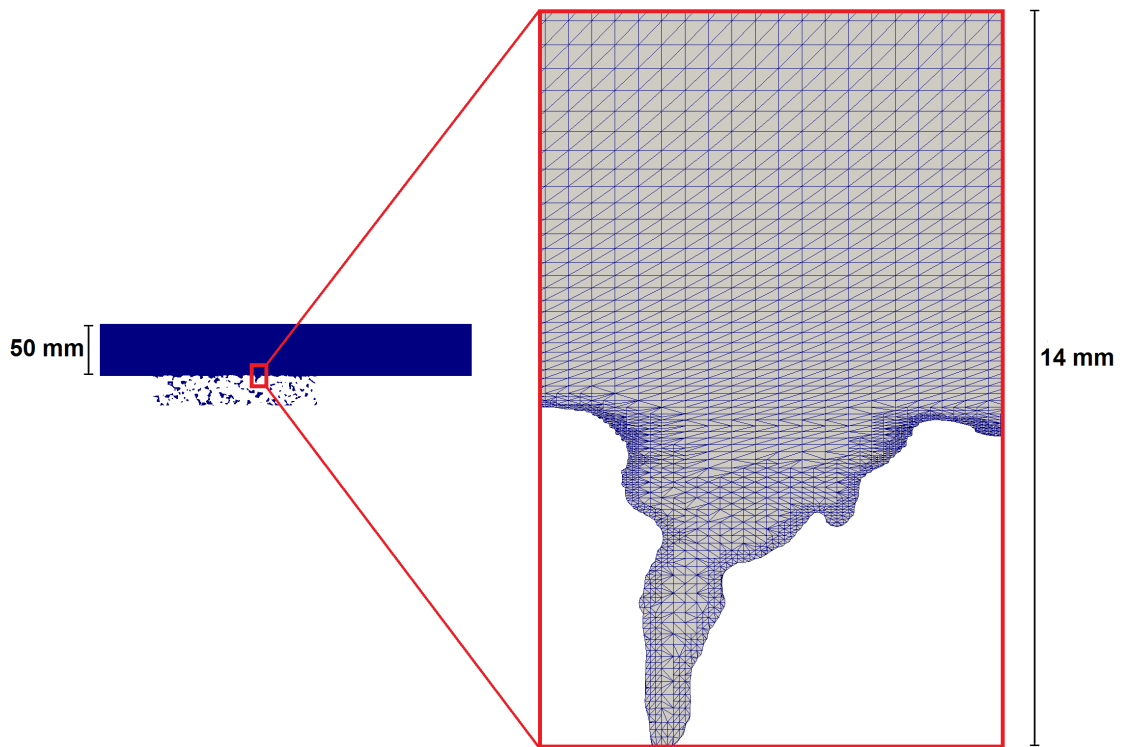


Figure 6.2.: Computational grid of the near-wall region, shown at the plane  $z = 25 \text{ mm}$  (breadthwise centerplane of PA).

At  $x = 0$  (see Fig. 6.1), a uniform inlet velocity is imposed. This leads to a flow with strong boundary layer development at the region of interest i.e. the vapor source domain, similar to real world conditions. Free stream air speeds ( $U_{in}$ ) of 0.1, 1.5 and 10 m/s are used in this study. These speeds correspond to bulk Reynolds numbers ( $Re_b = U_{in}L_s/\nu$ ) of  $1.2 \times 10^3$ ,  $1.8 \times 10^4$  and  $1.2 \times 10^5$  respectively. The corresponding channel Reynolds numbers ( $Re_c = U_{in}H_c/\nu$ ) are  $3.3 \times 10^2$ ,  $5 \times 10^3$  and  $3.3 \times 10^4$ . Zero static pressure is imposed at the outlet. At the upper and lower boundaries, no-slip (for airflow) and no-flux (for scalar transport) conditions are imposed, which implies that the air velocity is zero at these boundaries and that these boundaries are impermeable to scalar transfer. In the 2D precursor simulations, the flat plate is also imposed with a no-slip condition for airflow whereas for the scalar transport, the plate is the scalar source. Similarly, in the 3D PA simulations, a no-slip condition is imposed at the PA domain and it also acts as the scalar source. Furthermore, in the 3D PA simulations, symmetric boundary conditions (slip walls) are imposed at the lateral faces which implies that the normal velocity component and normal scalar gradients at these boundaries are zero. It should be noted that the walls are modeled with zero surface roughness in this study.

The difference between the precursor and PA simulations is that the level of the scalar source in PA is a variable input parameter in the latter case, as shown schematically in Fig. 6.1(d). The different levels of scalar source essentially represent the different free water surfaces in a PA filled with water. In this study, the scalar source levels are  $y = -0.13 \text{ mm}$ ,  $y = -15 \text{ mm}$  and  $y = -29 \text{ mm}$ . In a physical sense, these levels represent the states, respectively, that PA is almost fully saturated with water, PA is half-full with water (in terms of the free water height) and PA is almost dry. In this study, water vapor transport is modeled as a passive scalar transport, which implies that airflow influences scalar transport but not vice versa. The scalar parameter that is used in this study is the mass fraction of water vapor in dry air,  $c$  [kg/kg]. As the scalar source represents the free water surface, all cells at the scalar source have a uniform value of  $c_{in} = 0.015 \text{ kg/kg}$ , which is the saturated water vapor mass fraction at 20 °C and atmospheric pressure. At the upper domain, the incoming air is assumed to be dry i.e.  $c_e = 0 \text{ kg/kg}$  at the inlet of the upper domain.

### 6.2.2 Governing equations

The air flow field is solved with the single-phase, steady state, incompressible Reynolds-averaged Navier-Stokes equation:

$$U_j \frac{\partial U_i}{\partial x_j} = -\frac{1}{\rho} \frac{\partial P}{\partial x_i} + \frac{\partial}{\partial x_j} \left( \frac{\mu}{\rho} \frac{\partial U_i}{\partial x_j} \right) + \frac{\partial \left( \overline{-u'_i u'_j} \right)}{\partial x_j}, \quad (6.1)$$

with the mass continuity equation:

$$\frac{\partial U_i}{\partial x_j} = 0, \quad (6.2)$$

where  $U$  [m/s] is the air velocity,  $P$  [Pa] is the static pressure and  $\rho$  [kg/m<sup>3</sup>] is the air density. The last term in eq. (6.1) is the Reynolds stress term, which is often defined in terms of known (averaged) quantities. One such approach is to define the Reynolds stresses in terms of the Boussinesq hypothesis which yields a simple relationship between Reynolds stresses and velocity gradients through the eddy viscosity. Although there are many eddy viscosity models used in turbulence modeling, the most common approach, and the one adopted in this study, is the two-equation  $k$ - $\varepsilon$  model, in which turbulence is described by means of two partial differential equations (PDEs). The first transported variable determines the energy in the turbulence and is called turbulent kinetic energy,  $k$ . The second transported variable is the turbulent dissipation,  $\varepsilon$ , which determines the rate of dissipation of the turbulent kinetic energy. The equations for the two terms can be written as:

$$\frac{\partial k}{\partial t} + U_j \frac{\partial k}{\partial x_j} = \frac{\mu_t}{\rho} S^2 - \varepsilon + \frac{\partial}{\partial x_j} \left[ \frac{1}{\rho} \left( \mu + \frac{\mu_t}{\sigma_k} \right) \frac{\partial k}{\partial x_j} \right], \quad (6.3)$$

$$\frac{\partial \varepsilon}{\partial t} + U_j \frac{\partial \varepsilon}{\partial x_j} = \frac{\varepsilon}{k} \left( C_{1\varepsilon} \frac{\mu_t}{\rho} S^2 - C_{2\varepsilon} \varepsilon \right) + \frac{\partial}{\partial x_j} \left[ \frac{1}{\rho} \left( \mu + \frac{\mu_t}{\sigma_\varepsilon} \right) \frac{\partial \varepsilon}{\partial x_j} \right], \quad (6.4)$$

where the eddy viscosity  $\mu_t$  and the term  $S$  are defined as:

$$\mu_t = \rho C_\mu \frac{k^2}{\varepsilon}, \quad (6.5)$$

$$S = \frac{1}{\sqrt{2}} \left( \frac{\partial U_i}{\partial x_j} + \frac{\partial U_j}{\partial x_i} \right). \quad (6.6)$$

In this study, the Launder-Sharma constants (Launder and Sharma 1974) are used in the above equations i.e.  $\sigma_k = 1.00$ ,  $\sigma_\varepsilon = 1.3$ ,  $C_{1\varepsilon} = 1.44$ ,  $C_{2\varepsilon} = 1.92$  and  $C_\mu = 0.09$ .

Once the air flow field is obtained, the turbulent water vapor transport is solved with the convection-diffusion equation:

$$\nabla \cdot (Uc) - \nabla \cdot ((D_M + \nu_t / Sc_t) \nabla c) = 0, \quad (6.7)$$

where  $c$  is the transported scalar,  $D_M$  ( $2.5 \times 10^{-5}$  m<sup>2</sup>/s in this study) is the molecular diffusion coefficient of water vapor in dry air,  $\nu_t$  [m<sup>2</sup>/s] is the turbulent air viscosity and  $Sc_t$  (0.7 in this study) is the turbulent Schmidt number. From eq. (6.7), it can be seen that the enhanced diffusion of vapor in air due to turbulence is taken into account using



the parameter  $\nu_t/Sc_t$ . Vapor absorption in PA is known to be negligible and is therefore not taken into account.

### 6.2.3 Numerical simulation

The simulations are performed with the open source CFD package OpenFOAM (Weller et al. 1998). The numerics are implemented in OpenFOAM with the Finite Volume Method on an unstructured grid. The computational grid is generated with the unstructured grid generator 'SnappyHexMesh' which is pre-installed in OpenFOAM. The SnappyHexMesh code is able to import the STL format of the three-dimensional X-ray  $\mu$ -CT scan of PA. The air flow field is solved with the solver 'simpleFoam' while scalar transport is solved with the solver "simpleScalarFoam", which takes into account turbulent diffusion. As already stated, steady Reynolds-averaged Navier-Stokes (RANS) k- $\epsilon$  model with LRNM for the near-wall region is used for turbulence modeling. Specifically, the Launder-Sharma LRNM model (Launder and Sharma 1974) is used in this study. The accuracy of the used turbulence model is verified with precursor simulations (see Section 6.3.1). The SIMPLE algorithm is used for pressure-velocity coupling. Second-order discretization schemes are used at all stages.

## 6.3 RESULTS AND DISCUSSION

### 6.3.1 CFD validation with convective scalar transfer from a flat plate

The accuracy of the turbulence model used in this study i.e. RANS k- $\epsilon$  with LRNM for the boundary layer, is assessed by comparing the simulation results of convective scalar transport from a linear scalar source placed flushed in a 2D channel (Fig. 6.1(a)) with analytical functions. Since there is no analytical correlation for convective mass transfer from a flat plate placed in a developing, rectangular channel (internal) flow, the nearest case is considered i.e. a developing, external flow on a flat plate. For a flat plate subjected to a developing external flow, the convective mass transfer coefficient (CMTC),  $h_m$  [m/s], can be expressed as a function of the distance from the leading edge ( $x = 50$  mm),  $x_L$ , as (Kothandaraman 2004):

$$h_m(x_L) = \frac{Sh_x D_M}{x_L} = \begin{cases} \frac{0.332 Re_{x_L}^{1/2} Sc^{1/3} D_M}{x_L}, & Re_b < 5 \times 10^5 \\ \frac{0.0296 Re_{x_L}^{4/5} Sc^{1/3} D_M}{x_L}, & 5 \times 10^5 < Re_b < 10^8 \end{cases} \quad (6.8)$$

where  $Re_{x_L} = U_{in} x_L / \nu$  and  $Sh_x$  is the Sherwood number. From the CFD simulations, CMTC is calculated at a wall-normal distance of  $y = 0.5$  mm from the wall with the following equation (Bergman et al. 2011):

$$h_m(x_L) = \frac{D_M(c_{in} - c_{x_L})}{(c_{in} - c_e)y}. \quad (6.9)$$

The comparison of the analytical functions with the results from the CFD simulations is shown in Fig. 6.3 for three wind speeds. The local CMTC is normalized with the average CMTC at that wind speed while the distance from the leading edge of the flat plate is normalized with the total length of the flat plate. It can be seen that the CMTC calculated from simulations at the two lower wind speeds, 0.1 and 1.5 m/s, agree well with the laminar CMTC correlation while the CMTC calculated from the simulation at the highest wind speed, 10 m/s, agrees well with the turbulent CMTC correlation. For the 10 m/s wind speed case, the simulated CMTC shows some divergence from the correlation near the leading edge. However, the divergence lasts only over a very short distance and there is excellent agreement thereafter. While the two  $Re_b$  at the two lower wind speeds ( $1.2 \times 10^3$  and  $1.8 \times 10^4$ ) clearly fall in the laminar region according to eq. (6.8),  $Re_b = 1.2 \times 10^5$  at the highest wind speed is much closer to the transition region. Indeed, previous studies (Ghalichi et al. 1998) have shown that LRNM is an efficient method to model flows where both laminar and transitional/turbulent flows coexist. Furthermore, the good agreements also attest to the quality of the grid near the wall since LRNM, as mentioned earlier, is a grid-intensive method as compared to wall functions.

### 6.3.2 CFD simulation of convective scalar transport from PA

#### 6.3.2.1 Integrated scalar flux at the air-material interface

Convective mass transport from PA at the air-material interface at different wind speeds and scalar source levels is analyzed in this section. Simulations are performed for three wind speeds and for three different levels of scalar source, as shown in Table 6.1. Additionally, pure diffusion simulations are also performed in which there are no wind flows, and thereby no forced convection. The pure diffusion simulations are discussed in detail in Section 6.3.2.5. In Table 6.1, the integrated total scalar flux,  $J_y$  [m/s], along the  $y$  (interface-normal) direction, as measured close to the PA surface at  $y = -0.05$  mm, is also given and is calculated as:

$$J_y = J_{D,y} + J_{C,y} = -\nabla c_y \left( D_M + \frac{\nu_t}{Sc_t} \right) + U_y c, \quad (6.10)$$

where the total scalar flux is the sum of the diffusive scalar flux,  $J_{D,y}$  [m/s], and the convective scalar flux,  $J_{C,y}$  [m/s]. From the CFD simulations, the integrated total scalar flux is calculated as the area-integrated flux at all the cells in the plane  $y = -0.05$  mm:

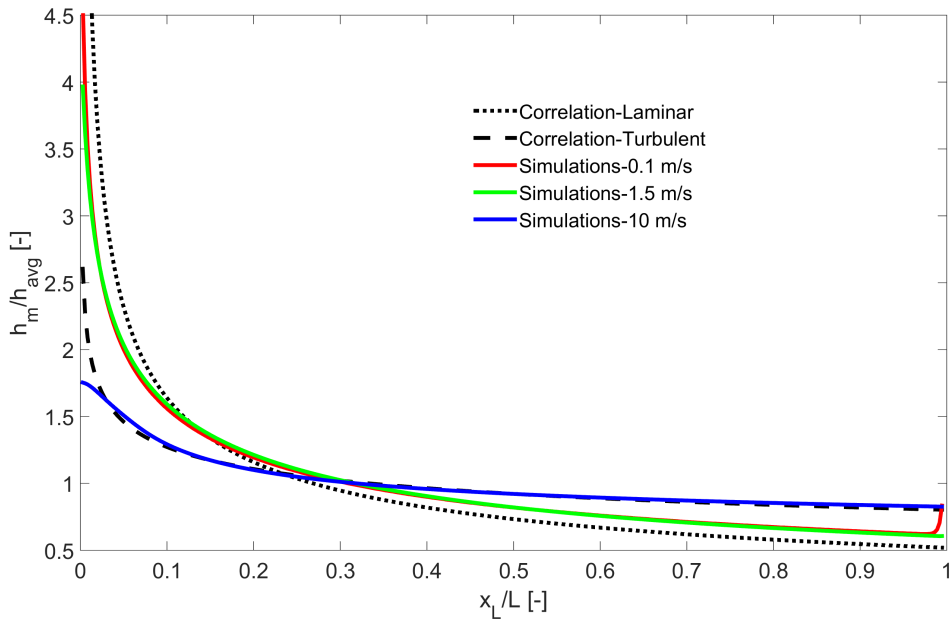


Figure 6.3.: Comparison of CFD simulations of convective scalar transfer from a flat plate in a rectangular channel (RANS  $k-\varepsilon$  and LRNM model) with the analytical expression, computed for three wind speeds. The CMTC is normalized with the average CMTC at that wind speed while the distance from the leading edge of the flat plate is normalized with the total length of the flat plate.

Table 6.1.: Total interface-normal scalar flux measured at the air-PA interface during pure diffusion (no wind), forced convection at different wind speeds and different scalar source levels

Wind speed	Reynolds number	Scalar source level	Integrated total flux
$U_{in}$ [m/s]	$Re_b$ [-]	$y$ [mm]	$J$ [m/s]
0	0	-0.13	-
		-15	7.85E-10
		-29	1.82E-10
0.1	$1.2 \times 10^3$	-0.13	8.57E-08
		-15	8.07E-10
		-29	1.81E-10
1.5	$1.8 \times 10^4$	-0.13	2.55E-07
		-15	1.04E-09
		-29	1.80E-10
10	$1.2 \times 10^5$	-0.13	2.67E-06
		-15	8.08E-09
		-29	7.89E-10

$$J_y = \frac{\sum_{i=1}^n J_{y,i} A_i}{\sum_{i=1}^n A_i}, \quad (6.11)$$

where  $n$  is the total number of cells in the plane and  $A$  is the cell area.

It can be seen from Table 6.1 that the total flux for a given wind speed decreases with increasing depth of the scalar source level. This decrease becomes sharper as the wind speed increases. In other words, while convective transport at the upper part of the specimen becomes stronger at higher wind speeds, convective transport within the lower part is not affected significantly by an increase in the wind speed. This is confirmed by the fact that the order of magnitude of the total flux remains the same for all three wind speeds when the scalar source is at  $y = -29$  mm. These observations give a first indication of an important trend that will be analyzed in detail below i.e. the low influence of wind speed on scalar transport below a certain specimen depth. In Fig. 6.4, the integrated total scalar flux is split into integrated convective and diffusive fluxes for all the simulations listed in Table 6.1. The integrated convective and diffusive fluxes are also calculated based on eq. (6.11). Isolating the diffusive and convective components of the total flux provides an insight into the individual roles of the two major mechanisms of vapor transport i.e. diffusion of vapor from the bottom of the specimen to the air-material interface purely due to concentration gradients, and the transport of vapor due to momentum exchange

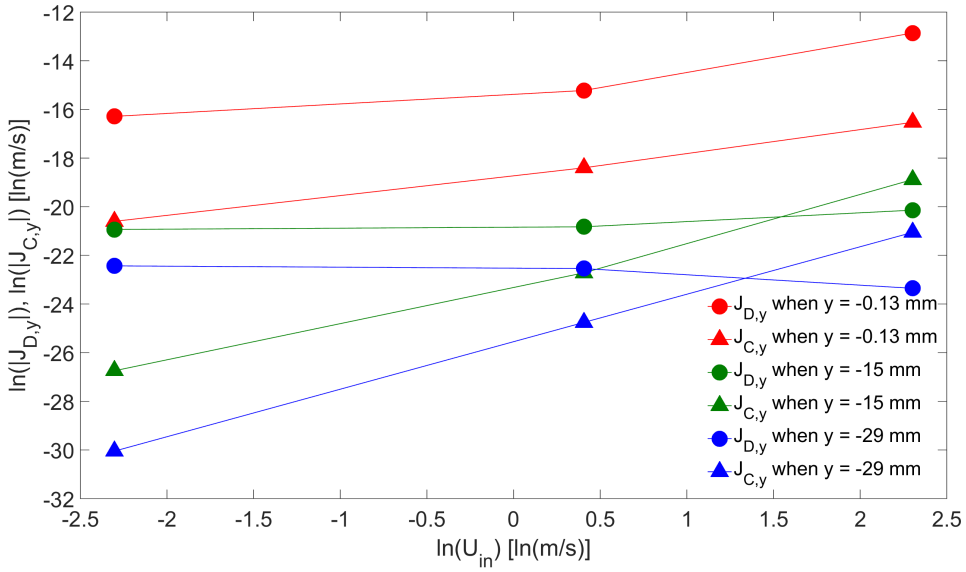


Figure 6.4.: Integrated convective scalar flux ( $J_{C,y}$ ) and diffusive scalar flux ( $J_{D,y}$ ) at the surface of the specimen, along the interface-normal direction, for different wind speeds and scalar source levels.

from the wind. In reality, these two components are not completely uncoupled, an aspect that is investigated in more detail in Section 6.3.2.5.

A few key observations can be made from Fig. 6.4. While the convective flux increases with wind speed at all scalar source levels, the diffusive flux does not show a clear trend. At all wind speeds, the strongest flux at the specimen surface is the diffusive flux when the scalar source is at  $y = -0.13 \text{ mm}$ . This is because of the proximity of the measurement plane i.e.  $y = -0.05 \text{ mm}$ , to the scalar source plane and the resulting strong scalar concentration gradients near the measurement plane. The most important observation, however, is that for a given wind speed and scalar source level, the convective flux is stronger than the diffusive flux only when the wind speed is 10 m/s, and the scalar source levels are  $y = -15 \text{ mm}$  and  $y = -29 \text{ mm}$ . This implies that at normal environmental wind speeds, which are considerably less than 10 m/s, vapor diffusion through the PA layer will be the most important factor influencing the drying of a wet layer. In general, due to the large pore sizes in PA, vapor transport to the surface is expected to be more dominant than capillary transport of water to the surface, and the observations from Fig. 6.4 indicate that this vapor transport is driven by diffusion for wind speeds much lower than 10 m/s.

### 6.3.2.2 Air flow-field and scalar distribution in PA

In this section, the main conclusions drawn from Table 6.1 and Fig. 6.4 are visualized with scalar distribution plots at the scalar source levels  $y = -15 \text{ mm}$  and  $y = -29 \text{ mm}$ . Figure 6.5 shows the scalar distribution at  $y = -15 \text{ mm}$  and Fig. 6.6 shows the scalar distribution at  $y = -29 \text{ mm}$  for the three wind speeds. A comparison of Figs. 6.5 and 6.6 gives the reader an idea of how the scalar source levels are specified in the simulations. Essentially, the lower (PA) domain is cut at the desired scalar source level and the cells in the resulting intersection of the cut plane and the PA cross-section are specified as the scalar source cells. Therefore, the depth of PA given in Fig. 6.5 is half of that given in Fig. 6.6 i.e. when the scalar source level is  $y = -29 \text{ mm}$ , scalar distribution in the entire specimen, whose total height is 30 mm, is solved, whereas when the scalar source level is  $y = -14 \text{ mm}$ , scalar distribution in only half of the specimen (in the vertical direction) is solved since bulk water is assumed to occupy the other half.

In Figs. 6.5 and 6.6, strong gradients in scalar distribution from the source plane to the top surface of the specimen can be seen, which attests to the high material resistance to vapor diffusion. Although it is seen from Table 6.1 that the overall effect of a higher wind speed is to enhance vapor diffusion, from Figs. 6.5 and 6.6, it can also be observed that a higher wind speed also enhances the spatial distribution of vapor within the specimen. This can be seen for instance in pores A, C and D in Fig. 6.5 and pores B and C in Fig. 6.6, where the scalar concentration increases with increasing wind speed. However,

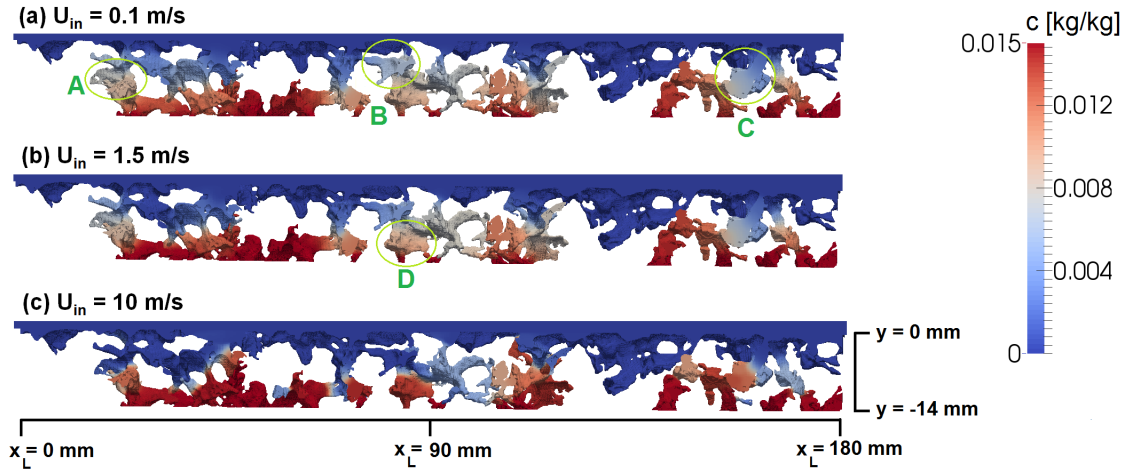


Figure 6.5.: Scalar distribution in PA at different wind speeds ( $U_{in}$ ) when scalar source level is  $y = -14$  mm.

in pores such as pore B in Fig. 6.5 and pore A in Fig. 6.6, the reverse phenomenon is observed i.e. decreasing scalar concentration with increasing wind speed.

### 6.3.2.3 Convective and diffusive fluxes along the air-material interface

In this section, the convective and diffusive fluxes along the air-material interface are investigated. The fluxes are plotted as a function of the (normalized) distance from the leading edge of the specimen, as shown in Fig. 6.7. Similar to Fig. 6.4, the fluxes in Fig. 6.7 are also measured at  $y = -0.05$  mm, but with the important distinction that these are not fluxes integrated over the entire plane. Instead, each point in Fig. 6.7 represents the average convective or diffusive flux at all the cells at a particular  $x_L/L$  value. This makes it possible to analyze not only the magnitude but also the sign of the fluxes in the interface-normal direction. In Fig. 6.7, graphs are presented in rows arranged per scalar source levels and in columns per wind speeds. The decrease in fluxes with decreasing wind speeds and increasing scalar source depth is also reflected in the  $y$ -axis range of the figures. While the diffusive flux is always positive as  $-\partial c_y/\partial y$  is always positive, the convective flux is negative at quite a few positions along the interface, especially at the two higher wind speeds. This indicates air penetration into the specimen even at a wind speed of 1.5 m/s. However, as already observed from Fig. 6.4, the convective fluxes become stronger than the diffusive fluxes only when the wind speed is 10 m/s and the scalar source levels are  $y = -15$  mm and  $y = -29$  mm. In all other cases, the clear dominance of diffusive fluxes can be observed.

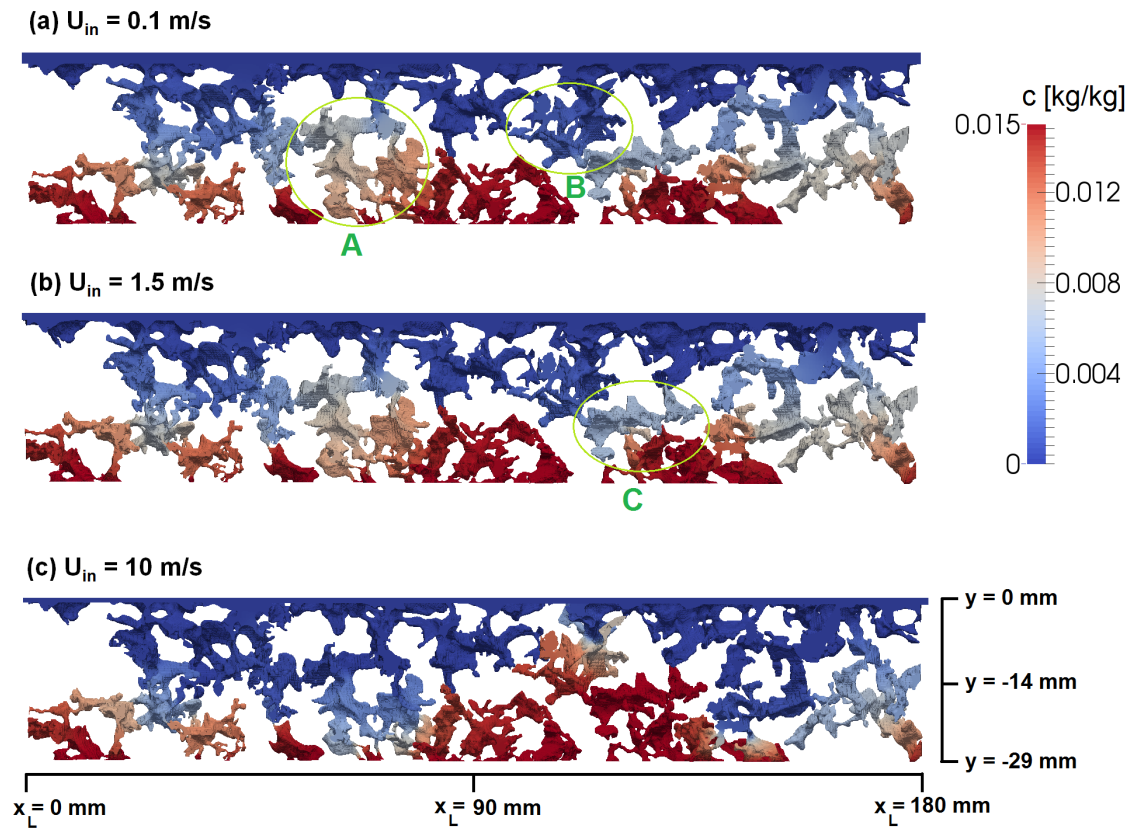


Figure 6.6.: Scalar distribution in PA at different wind speeds ( $U_{in}$ ) when scalar source level is  $y = -29 \text{ mm}$ .



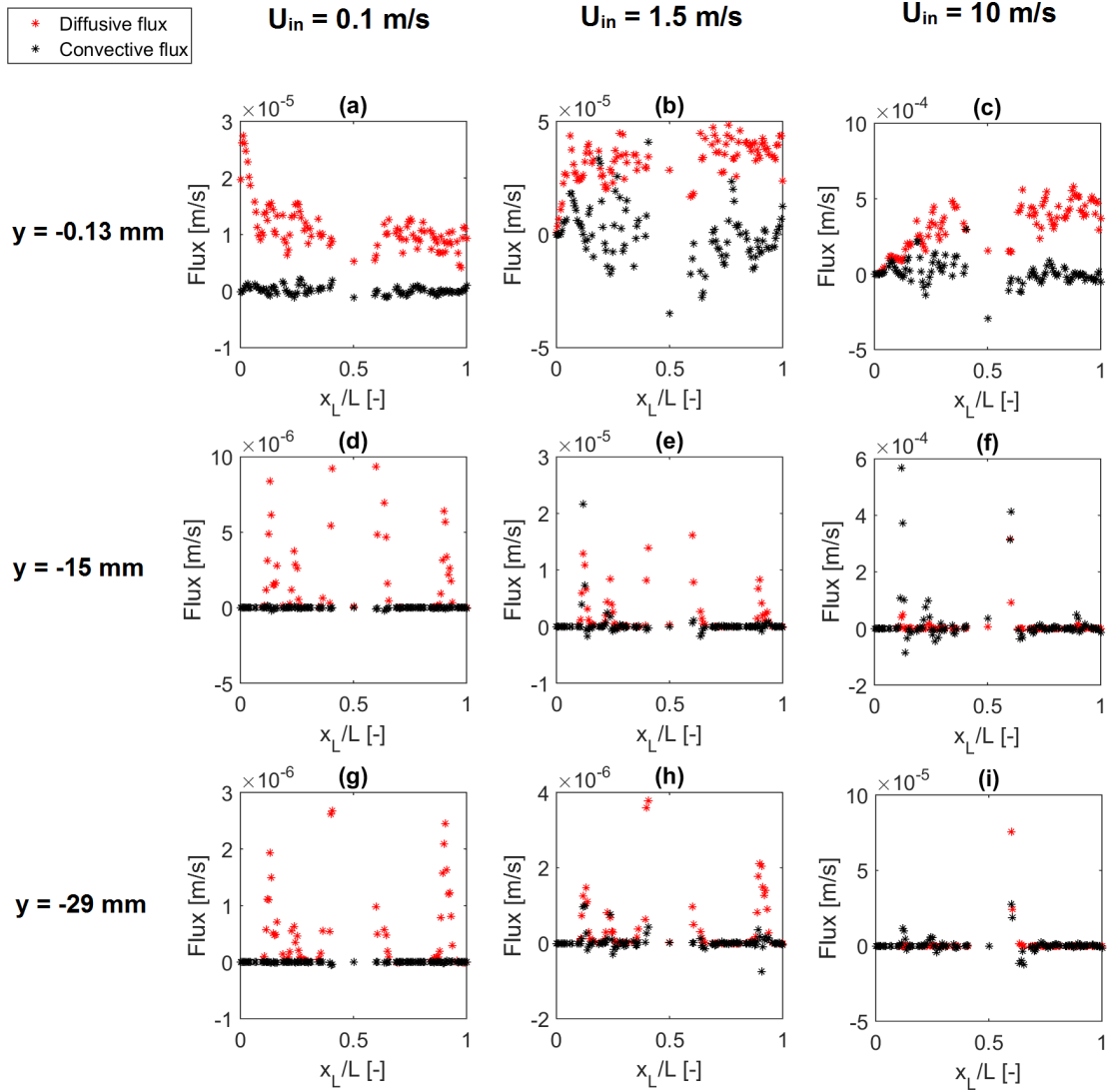


Figure 6.7.: Convective and diffusive interface-normal fluxes at the air-material interface as a function of the distance from the leading edge. Rows represent the three scalar source levels while columns represent the three wind speeds. Note the different scales of the  $y$ -axis.

#### 6.3.2.4 *Visualization of air flow-field and scalar distribution in pores near the air-material interface*

Porous asphalt is a material that has large pores throughout its structure, including large, connected pores near the surface. In the event of low air entrainment in the specimen, the air flow-field in these surface pores can influence the convection and diffusion of vapor in the entire specimen since the vapor pressure at pores across the specimen is influenced by the rate at which vapor is convected from these pores. Therefore, in this section, the air flow-field and scalar distribution in two types of pores at the air-material interface are analyzed. The first type of pore, called here a 'cavity' pore, resembles a cavity while the second type of pore, called here a 'connected' pore, is actually a pore system in which two pores near the surface are connected to each other through a throat underneath the surface, forming somewhat of a U-shape. The air flow-field and scalar distributions in one chosen cavity pore and one connected pore are shown in Figs. 6.8 and 6.9 respectively, for the three wind speeds tested in this study. While the left column of the figures show the scalar distribution in the concerned pore, the right column of figures show the streamlines of the air flow-field within the same pore. The scalar source is at  $y = -15 \text{ mm}$  in both the plots since this configuration shows a direct dependency of scalar transport on the wind speed, according to Table 6.1. The maximum legend value for the velocity field is chosen to be an order of magnitude lesser than the respective bulk wind speed to optimally visualize the full range of velocities inside the pore.

The complex roughness of the air-material interface is clearly evident from Figs. 6.8 and 6.9. Sharp gradients in scalar concentration within the same pore can be observed. Air entrainment can be observed in both pore types at all three wind speeds. In Fig. 6.8, vortices can be seen in the cavity pore at all the three wind speeds. However, a surprising result from Fig. 6.8 is the comparatively lower scalar removal from the cavity pore at  $U_{in} = 10 \text{ m/s}$  as compared to that at the two lower wind speeds. This is because at this wind speed, the clockwise vortex occupies the entire pore space by which it actually closes the entire pore, and not a part of it like in the two lower speeds, and thereby blocks the scalar exchange at the air-material interface.

In contrast, in case of a connected pore, the removal of scalar steadily increases with increasing wind speed, as shown in Fig. 6.9. The connecting pore under investigation, its inlet and its outlet are marked in Fig. 6.9. Air entrainment at the inlet of the connected pore as well as air exit from the outlet can be clearly seen in Fig. 6.9. Unlike in the cavity pore, large vortices are not observed in the connected pore at any wind speed. At the highest wind speed, momentum transfer from air entrainment into the pore appears to be the driving force for removal of the scalar. This could be an important reason why the integrated total flux increases with increasing wind speed when the scalar source is at

$y = -15 \text{ mm}$ , as shown in Table 6.1. The effect of air entrainment into the pore space on scalar removal is quantitatively investigated in the next section.

### 6.3.2.5 *Effect of air entrainment into the pore space on scalar convection*

The important question of air entrainment into PA and its effect on scalar transport was touched upon briefly in the previous sections. In this section, this phenomenon is investigated in more detail with six additional simulations. These additional simulations are similar to the simulations presented so far except for one condition: scalar transport within the specimen is governed solely by diffusion. This is ensured by specifying zero velocity field within the specimen, although there is still airflow above the specimen. This implies that although diffusion within the specimen is enhanced by the airflow above, there is no enhancement of scalar transport within the specimen from the additional momentum transfer provided by air entrainment into the specimen, a phenomenon which was clearly seen in Fig. 6.9. Figure 6.10 presents the interface-normal fluxes measured at the air-material interface for three bulk wind speeds (0.1, 1.5 and 10 m/s) and two scalar source levels (-15 and -29 mm), with and without air entrainment into the specimen. Similar to Figs. 6.4 and 6.7, the fluxes are measured at  $y = -0.05 \text{ mm}$ .

From Fig. 6.10(a), it can be observed that when the scalar source level is  $y = -15 \text{ mm}$ , air entrainment into the specimen does not have any significant influence on the total flux at the lowest wind speed i.e.  $U_{in} = 0.1 \text{ m/s}$ , as the magnitude of fluxes in both cases (with and without air entrainment) are similar, an observation which can also be made from Table 6.1. For the same scalar source level, at  $U_{in} = 1.5 \text{ m/s}$ , the total scalar flux is considerably higher when air entrainment is considered, as seen in Fig. 6.10(b), and at  $U_{in} = 10 \text{ m/s}$ , air entrainment makes an even higher impact on the total flux, as seen in Fig. 6.10(c) and Table 6.1. When the scalar source level is  $y = -29 \text{ mm}$ , the fluxes at the two lower wind speeds and the no entrainment case are similar, as can be seen in Fig. 6.10(d-f) and Table 6.1. At the highest wind speed, flux values are higher for both scalar source levels when compared to the simulations with no air entrainment, as can be seen from Table 6.1. Additionally, from Fig. 6.10(f), it can be seen that at  $x_L/L = 0.6$ , air entrainment has a large influence on scalar transport. However, as seen from Table 6.1 and Fig. 6.10(f), the influence of air entrainment on scalar transport at the highest wind speed is clearly much lower when the scalar source level is  $y = -29 \text{ mm}$ , compared to its influence when the scalar source level is  $y = -15 \text{ mm}$ . This is because the positive influence of air entrainment on scalar transport is restricted to the upper region of the specimen, and therefore, the larger the depth of the scalar source level within the specimen, the smaller is the contribution of air entrainment to the total scalar transport from the specimen. In other words, at larger depths of the scalar source level, the scalar has to

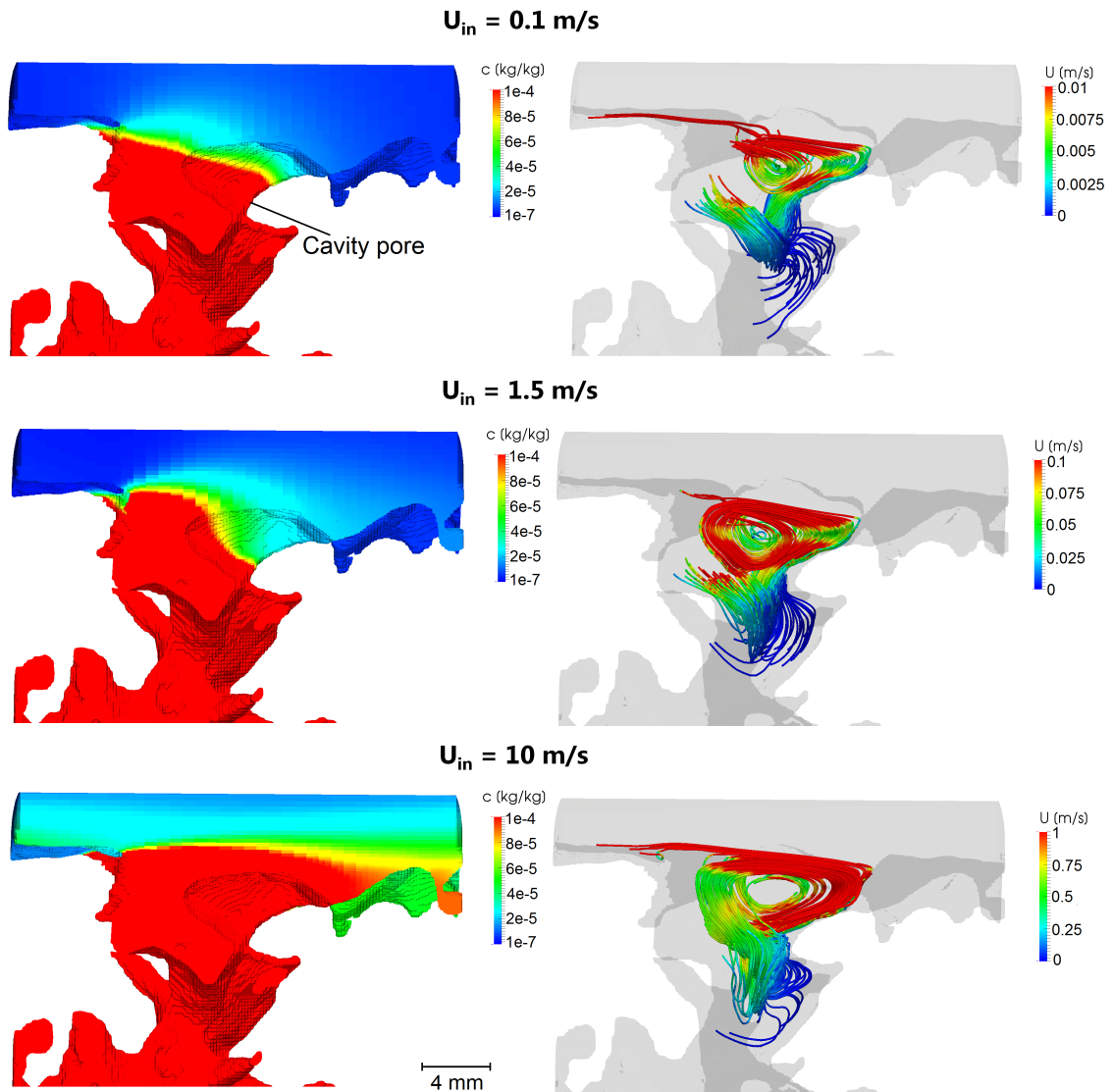


Figure 6.8.: Scalar distribution (left) and streamlines of the air flow-field (right) in a cavity pore at the air-material interface for bulk wind speeds 0.1 m/s, 1.5 m/s and 10 m/s. The scalar source (not shown) is at  $y = -15 \text{ mm}$ .

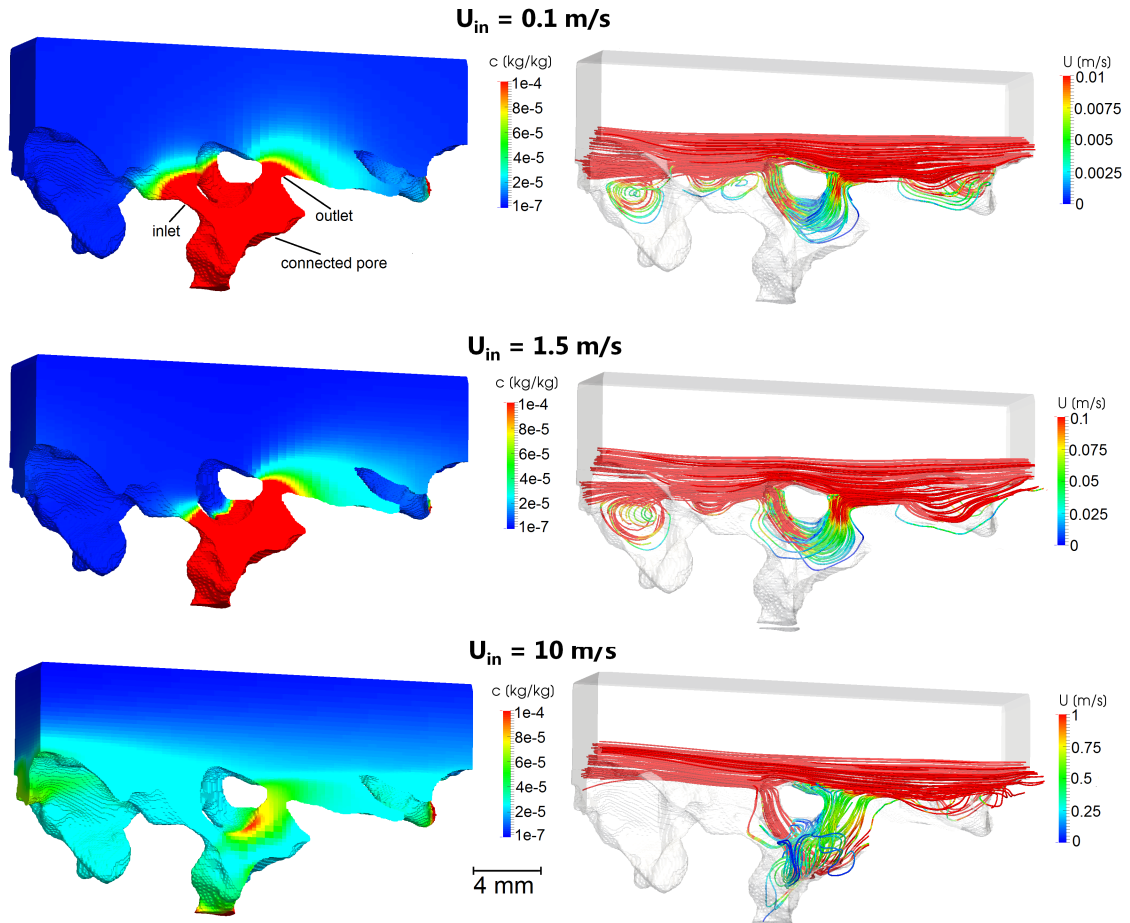


Figure 6.9.: Scalar distribution (left) and streamlines of the air flow-field (right) in a connected pore at the air-material interface for bulk wind speeds 0.1 m/s, 1.5 m/s and 10 m/s. The scalar source (not shown) is at  $y = -15 \text{ mm}$ .

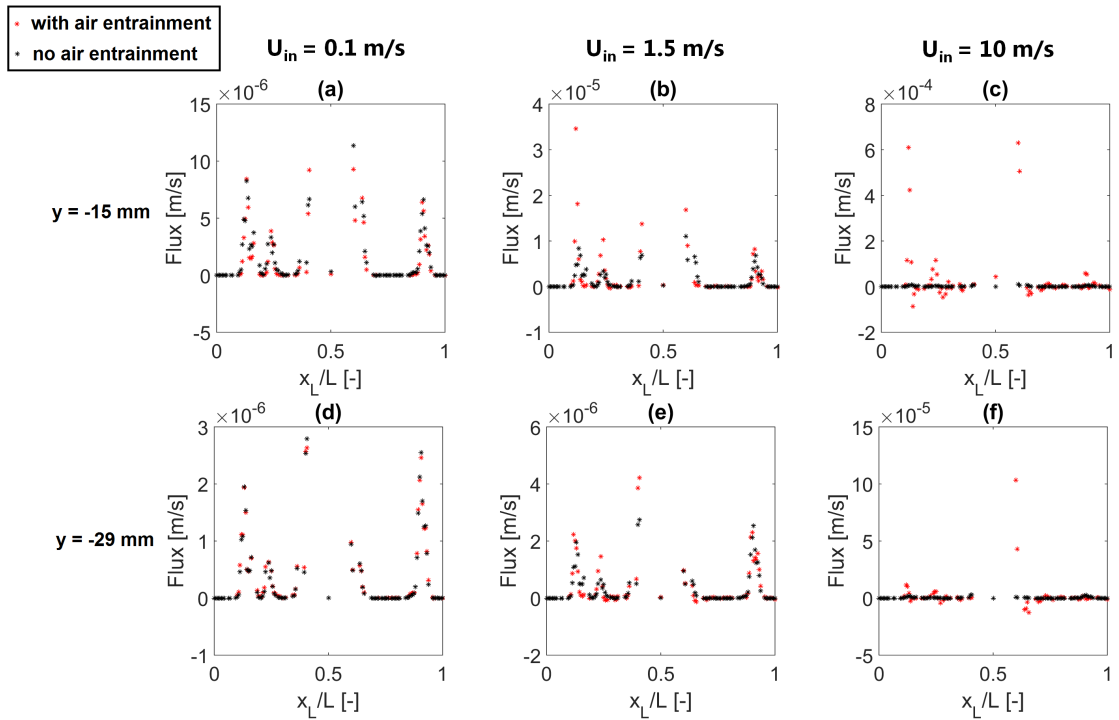


Figure 6.10.: Interface-normal fluxes at the air-material interface as a function of the distance from the leading edge, with and without air entrainment into the specimen. Rows represent the two scalar source levels while columns represent the three wind speeds. Note the different scales of the  $y$ -axis.

travel a longer distance within the specimen and therefore, due to high material resistance, the flux near the top surface becomes lower, as was already observed in Fig. 6.4.

## 6.4 CONCLUSIONS

In this chapter, convective passive scalar transport in an actual porous asphalt (PA) specimen, reconstructed from a three-dimensional X-ray  $\mu$ -CT, is simulated using CFD. The motivation behind this study is to analyze the influence of airflow on water vapor removal from a wet PA material. Two-dimensional precursor simulations, in which the PA specimen is substituted with a flat plate, are performed to select the appropriate turbulence model. The precursor simulations yield a good agreement between the analytical and simulated convective mass transfer coefficients for a flat plate subjected to channel flow, by using the  $k$ - $\varepsilon$  turbulence model with low Reynolds number modeling (LRNM) for

the boundary layer. Three-dimensional simulations are used to study convective scalar transport in PA at three wind speeds, 0.1, 1.5 and 10 m/s, and three depths of scalar source, -0.13, -15 and -29 mm, within the specimen.

The most important results from the simulations are:

1. Only the highest wind speed has some influence on the total vapor flux measured at the interface. This is because small increases in wind speed only enhances scalar transport within the upper region of the specimen. At the highest wind speed, air entrainment in pores near the air-material interface plays an important role in scalar removal. At lower speeds, diffusion is the dominant transport mechanism and hence, the contribution of air entrainment to the overall convection rate is not significant.
2. At a wind speed of 1.5 m/s, which is close to normal environmental wind speeds, the diffusive vapor flux at the air-material interface is always higher than the convective flux, irrespective of the vapor source level within the specimen.
3. At a wind speed of 10 m/s, the formation of strong vortices in a cavity-type pore at the air-material interface may inhibit vapor removal from that pore by recirculating the scalar within the pore. However, at the same wind speed, vapor transport in a connected-pore (a pore system that has both inlet and outlet connected to the interface) is found to be very strong due to strong air convection.
4. Although higher wind speeds and consequently stronger convection generally lead to lower vapor concentration within PA, it is observed that higher wind speeds increase vapor concentration in some pores. This is due to the stronger distribution of vapor within the specimen at higher wind speeds.
5. The scalar source level within PA is assumed to be constant in this study. In reality, liquid distribution within the specimen is will have a more complex configuration. Nevertheless, this study shows the trends to be expected in real conditions.

## 6.5 SYNTHESIS

The chapters presented so far have provided elaborate insights into fluid flow in porous asphalt. While Chapters 3 and 4 provided a comprehensive understand of liquid flow in PA under different environmental loads, Chapters 5 and 6 focused on airflow and vapor transport within and above a PA layer. In the next chapter, the observations made so far on liquid and vapor transport in PA are used to model gravity-drainage and drying in PA using pore network modeling and continuum modeling.





## PORE NETWORK MODELING OF DRAINAGE AND DRYING OF WATER IN POROUS ASPHALT

---

### 7.1 INTRODUCTION

The experiments and simulations presented in the previous chapters have provided a comprehensive understanding of the drainage and drying processes in porous asphalt. While gravity-driven drainage is observed to be the most important contributor to liquid water loss, significant moisture loss also takes place due to drying. Therefore, in this chapter, the insights gained from previous chapters are used to develop pore network models of drainage and drying in PA. In essence, the three-dimensional pore space of PA is represented as a simplified, while equivalent, network of large pores connected by narrow throats and two-phase flow simulations are performed on this three-dimensional network. In this chapter, first, the fundamentals of modeling two-phase flow in pore networks are presented, followed by a description of the governing equations of the drainage and drying algorithms used in this study. Thereafter, the extraction of pore networks from X-ray  $\mu$ -CT scans of PA specimens is described. The results of the pore network simulations on PA are then presented, followed by an upscaling to continuum modeling. The pore network simulations in this study are performed with self-written modules developed within the framework of the open source pore network modeling code OpenPNM (Gostick et al. 2016), which is written in Python with Scipy.

### 7.2 FUNDAMENTALS OF PORE NETWORK MODELING WITH CORNER FILMS

A pore network consists of representing the larger pores in the medium as a set of nodes, and the smaller pores connecting these larger pores as a set of links or throats. Typically, a pore network is extracted from three-dimensional scans of materials after the segmentation of the pore space using techniques such as skeletonization (Al-Raoush and Willson 2005) and watershed method (Beucher and Meyer 1992). Physical properties such as volume, conductance etc. are then applied to these elements i.e. pores and throats. A pore network model can either be a structured network, where the elements are arranged along a regular grid e.g. a cubic lattice, or an unstructured network, where they are arranged in a highly irregular manner. Various cross-section shapes such as circle, square, triangle and even irregular polygons have been used for pores and throats. In Fig. 7.1, the representation of

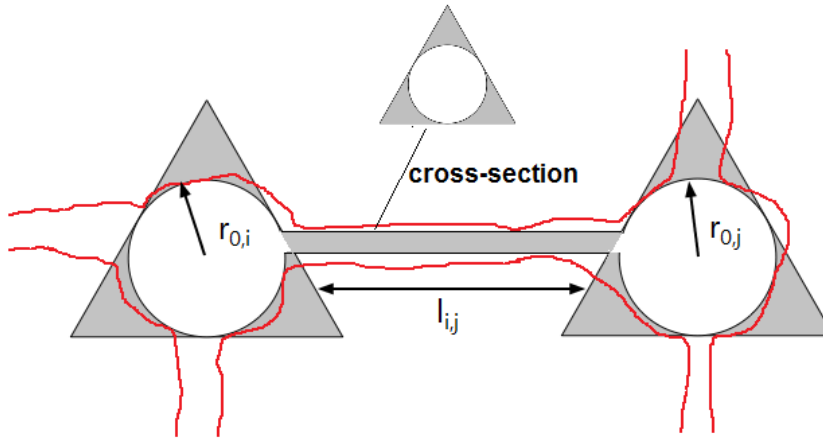


Figure 7.1.: Schematic representation of part of an irregular pore space (in red). First, the pores and throat are represented with the largest circle that can be fitted inside them. A circumscribed equilateral triangle is then fitted around the circle. Pores are connected with a throat having triangular (not shown) cross-section. The radius of the inscribed circle is considered as the pore/throat radius while the distance between the two triangular pores is the throat length.

an irregular pore space with a triangular pore and throat cross-sections is shown, since triangular pores and throats are used for the simulations in this study. The pores are characterized by the inscribed radius  $r_0$ , the radius of the largest inscribed sphere within the triangular cross-section, while the throats are characterized by the inscribed radius and its length,  $l$ .

Many studies have shown that the pore shapes of real porous media are highly irregular and non-circular, and that during two-phase flow, the wetting phase occupies the pore corners while the non-wetting phase occupies the pore center, as shown schematically in Fig. 7.2 for a triangular pore. The films of wetting fluid formed at pore corners are referred to as arc menisci (AMs). The radius of curvature of an arc meniscus,  $r_{nw}$ , is also shown in Fig. 7.2.

Once the pore space is defined and phase areas within each element are calculated at a given stage of drainage/drying, fluid flow rates through the network are computed by defining a conductance for each phase at all throats. The conductance of a phase within a throat is dependent on the throat's shape, dimensions and the phase area within it. Conductances can be defined using various methods such as assuming Poiseuille's flow for specific geometric configurations, volume averaging (Darcy's law), analytical solutions (Mason and Morrow 1991) and computation with direct numerical simulations (Marcke

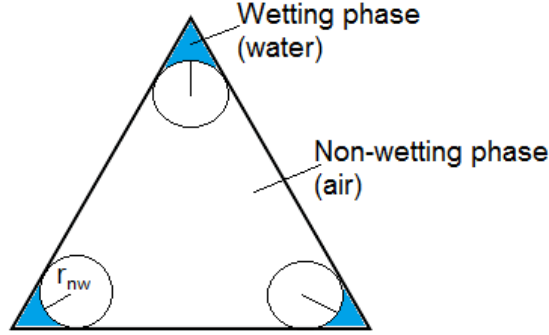


Figure 7.2.: Schematic representation of arc menisci in an equilateral triangle during two-phase flow. The radius of curvature of an arc meniscus  $r_{nw}$  is also given.

et al. 2010). The conductance of a throat is often defined as the harmonic mean of the local conductances of the throat itself and of the two pores connected to it. For instance, for the configuration shown in Fig. 7.1, the total conductance of a phase  $p$  is defined as:

$$g_{throat,p} = \frac{1}{\frac{1}{g_{i,p}} + \frac{1}{g_{j,p}} + \frac{1}{g_{ij,p}}}, \quad (7.1)$$

where  $g_{i,p}$ ,  $g_{j,p}$  and  $g_{ij,p}$  are the local conductances of the phase  $p$  in the two pores and the throat connecting them, and are defined in eqns. (7.10) and (7.11). Thereafter, the local pressures of each phase at all pores in the network are calculated by solving a linear system of equations resulting from the imposition of mass conservation condition at all pores i.e. the fluxes entering a pore are equal to the fluxes leaving the pore. For a pore system with a notation of the configuration as in Fig. 7.1, the flux of the phase  $p$  between the two pores,  $q_{ij,p}$ , is calculated as:

$$q_{ij,p} = g_{throat,p} (P_{i,p} - P_{j,p}), \quad (7.2)$$

where  $P_{i,p}$  and  $P_{j,p}$  are the local pressures of the phase at the pores and  $\mu_p$  is the dynamic viscosity of the phase. When the local pressure of the phase at each pore is known, the fluxes entering and leaving the entire network can be determined as:

$$q_{network,p} = - \sum_{i \in inlet} g_{in-i,p} (P_{i,p} - P_{in,p}) = - \sum_{i \in outlet} g_{in-i,p} (P_{out,p} - P_{i,p}). \quad (7.3)$$

Macroscopic properties such as fluid permeability,  $K_p[s]$ , can now be calculated for a certain direction as:

$$K_p = \frac{\mu_p q_{network,p} L}{A (P_{out,p} - P_{in,p})}, \quad (7.4)$$

where  $A$  is the normal cross-section area of the network and  $L$  is the network length. Additionally, various parameters such as relative permeability, drainage rate, drying rate, capillary pressure curves etc. can also be calculated from pore networks once the pressures and fluxes are known. These parameters are often calculated as a function of the total moisture content in the network. At a given liquid configuration, there is a mixture of saturated and unsaturated pores and throats in the network. Since eqns. (7.1) - (7.5) are defined for each phase, the aforementioned parameters can be calculated for each phase as a function of the total moisture content.

### 7.3 DRAINAGE AND DRYING ALGORITHMS WITH GOVERNING EQUATIONS

#### 7.3.1 *Modeling gravity-driven drainage with invasion percolation*

In this study, gravity-driven drainage is modeled as an invasion percolation (IP) process in the pore network (Wilkinson and Willemsen 1983). While the standard percolation theory (Broadbent and Hammersley 1957) is used to represent fluid flow as a result of the randomness in both the fluid motion as well as the medium through which it is flowing, invasion percolation theory describes the invasion of one fluid through the displacement of another, along the path of least resistance. Although IP was originally introduced as an algorithm for low capillary number, capillary-fingering dominated flow, IP has also been used to simulate gravity-destabilized flows (Meakin et al. 1992) by accounting for the decrease in air entry pressure due to gravity. IP is a quasi-static process in which microscopic fluid distributions are frozen at each capillary pressure or saturation level. Viscous and buoyancy effects are neglected. Initially, the network is fully saturated with water. Air then displaces water from pores and throats along the path of least resistance. In other words, during drainage, air is the invading phase and water is the defending phase.

The classic IP algorithm is already implemented in the standard version of OpenPNM. However, in the classic version, unsaturated flow and the effect of gravity are not considered. Therefore, in this study, the classic IP algorithm is modified to take into account unsaturated flow and the effect of gravity, and proceeds as follows:

1. At each step, a list of pores and throats is made such that both types of element are accessible to the invading phase and belong to a water cluster that is connected to the outlet. Water clusters not connected to the outlet cannot drain and remain as

water islands at the end of the drainage process and form part of the initial liquid configuration at the beginning of drying.

2. The list is sorted in ascending order of the threshold or entry capillary pressure (Eq. 7.5),  $p_c^t$ , of the pores and throats.
3. The element or elements with the lowest  $p_c^t$  is then invaded with air.
4. The invaded elements have two-phase flow i.e. air at the pore or throat center and water at the corners. The surface areas of air at the center and water at the corners depends on the system capillary pressure, as explained next in Eqs. (7.6) and (7.7). The conductances of air and water phases (below in Eqs. (7.10) and (7.11)) are then computed.
5. The IP algorithm proceeds until all accessible throats are invaded by air with increasing capillary pressure. At the end of drainage, the connected films have the same film radius and the possibility of snap-off (below as per Eq. (7.13)) in the pores and throats is examined. Subsequently, the pores and throats fulfilling the criteria for snap-off are refilled with water.

The threshold or entry capillary pressures are calculated using the Mayer and Stowe (Mayer and Stowe 1965) and Princen (Princen 1969) (MS-P) method, which relates the radius of arc meniscus to the capillary pressure. At the threshold capillary pressure, air invades the throat with a fixed curvature and displaces water from the center of the pore or throat, leaving some water as arc menisci in the corners. The MS-P method equates the radius of curvature of AMs to the curvature of the invading air-water interface. The MS-P method is extended here to include the effect of gravity as a second term of pressure. The values of all parameters in the equations below are given in Sections 7.4 and 7.5. The threshold pressure,  $p_c^t$ , according to the MS-P method, with the addition of the effect of the gravity, is:

$$p_c^t = \left( \frac{\gamma}{r_0} \cos \theta_r \left( 1 + 2\sqrt{\pi G} \right) F_d(\theta_r, G) \right) - \rho g \Delta h, \quad (7.5a)$$

$$F_d(\theta_r, G) = \frac{1 + \sqrt{1 + 4GY/\cos^2 \theta_r}}{1 + 2\sqrt{\pi G}}, \quad (7.5b)$$

$$Y = \pi \left( 1 - \frac{\theta_r}{60} \right) + 3 \sin \theta_r \cos \theta_r - \frac{\cos^2 \theta_r}{4G}. \quad (7.5c)$$

Here,  $\gamma$  is the air-water surface tension,  $\theta_r$  is the receding contact angle,  $G$  is the shape factor of the pore and  $\Delta h$  is the position of the pore or throat with respect to the lowest

point in the cluster to which it belongs. If AMs are assumed to be present at all corners, the function  $F_d(\theta_r, G)$  is universal for a given  $G$  and  $Y$  is only dependent on  $\theta_r$ . The equations given above are based on the principle that if AMs are displaced by a small distance, the work for the displacement is balanced by the change in surface free energy. A detailed derivation of the expressions in eq. (7.5) is given by Oren et al. (1998).

Fluid conductances are calculated by assuming Poiseuille flow in each element. For this to be determined, first the cross-sectional area of the wetting phase (water) in each element is given by:

$$A_w = N_c r_{nw}^2 \left[ \frac{\cos \theta}{\sin \alpha_c} \cos(\alpha_c + \theta) - \frac{\pi}{2} + \alpha_c + \theta \right], \quad (7.6)$$

where  $N_c$  is the number of corners,  $r_{nw} = \gamma/p_c^t$  is the radius of the AMs in the corner,  $\theta$  is the receding contact angle and  $\alpha_c$  is the corner half-angle. The cross-sectional area occupied by the non-wetting phase (air) in this case is:

$$A_{nw} = A_{tot} - A_w = 3\sqrt{3}r_0^2 - A_w, \quad (7.7)$$

where  $A_{tot}$  is the total cross-section area of the element. In the simulations in this study, an upper limit for the AM radius,  $r_{nw}^t$ , is imposed according to Wong et al. (1992):

$$r_{nw}^t = \frac{r_0}{\chi}. \quad (7.8)$$

According to Mason and Morrow (1984), the dimensionless curvature,  $\chi$ , can be expressed as a function of the static contact angle,  $\theta$ , and the critical contact angle,  $\theta_c = \pi/N_c$ , as:

$$\chi = \cos \theta + [(\theta_c - \theta + \sin \theta \cos \theta)/\tan \theta_c]^{1/2}. \quad (7.9)$$

From the wetting and non-wetting phase areas, phase conductances are then calculated according to Hughes and Blunt (2000). For the non-wetting phase, the diffusive conductance,  $g_{nw}$  [ $\text{m}^3/(\text{Pa}\cdot\text{s})$ ], of an element is given by:

$$g_{nw} = \frac{\pi r_{eff}^4}{8\mu_{nw}l}, \quad (7.10)$$

where  $r_{eff} = \sqrt{A_{nw}/\pi + r_0^2}/2$ ,  $l$  is the element length and  $\mu_{nw}$  is the non-wetting phase viscosity. For the wetting phase, the hydraulic conductance,  $g_w$  [ $\text{m}^3/(\text{Pa}\cdot\text{s})$ ], of an element is given by:

$$g_w = \frac{A_w r_{nw}^2}{\mu_w R_c l}, \quad (7.11)$$

where  $\mu_w$  is the wetting phase viscosity. The term is the crevice resistance factor (Hughes and Blunt 2000; Ransohoff and Radke 1988), which accounts for the effect of corner geometry and contact angle on the change in the cross-sectional area available for flow, and therefore the effect of surface shear viscosity on the boundary condition at the gas-liquid interface.  $R_c$  is defined as:

$$R_c = \frac{12\sin^2\alpha_c(1-B)^2(\psi_1 - B\psi_2)[\psi_3 + fB\psi_2]^2}{(1 - \sin\alpha_c)^2 B^2 [\psi_1 - B\psi_2]^3}, \quad (7.12a)$$

$$\psi_1 = \cos^2(\alpha_c + \theta) + \cos(\alpha_c + \theta) \sin(\alpha_c + \theta) \tan\alpha_c, \quad (7.12b)$$

$$\psi_2 = 1 - \frac{\theta}{\pi/2 - \alpha_c}, \quad (7.12c)$$

$$\psi_3 = \frac{\cos(\alpha_c + \theta)}{\cos\alpha_c}, \quad (7.12d)$$

$$B = \left(\frac{\pi}{2} - \alpha_c\right) \tan\alpha_c. \quad (7.12e)$$

The term  $f$  is a factor ranging between 0 and 1 depending on the boundary condition at the fluid interface. In this study,  $f = 0$  as a free boundary is assumed.

Snap-off is a phenomenon that occurs when the arc menisci at the corners of an element become unstable at a certain threshold capillary pressure, and as a result, they fuse together and collapse, resulting in the element cross-section becoming filled with the wetting phase. For a system like PA in which the pore to throat size ratio at certain points at the network are expected to be large, the phenomenon of snap-off should be considered. The threshold pressure for snap-off,  $p_c^s$ , is given as:

$$p_c^s = \frac{\gamma}{r_0} \left( \frac{\cos\theta/\tan(\frac{\pi}{2} - 2\alpha_c) - \sin\theta}{1/\tan(\frac{\pi}{2} - 2\alpha_c)} \right). \quad (7.13)$$

### 7.3.2 Modeling drying of residual liquid after drainage with a cluster-based algorithm

After the completion of gravity drainage, two types of liquid configurations can be seen in the elements of the network. If an element is invaded by air, liquid is present at its corners as arc menisci, and such an element is referred to as a 'film' element. If snap-off occurred in the element, water occupies the entire cross-section area, although the element may or may not be liquid saturated depending on the height of the liquid region, and such an element is referred to as 'bulk' element. Note that the term 'bulk' element applies only to liquid-filled elements and not air-filled elements. Therefore, the volume of liquid in a wet element can be defined as:

$$V_{lt} = \begin{cases} V_{lb} + V_{lf}, & \text{for bulk elements} \\ V_{lf}, & \text{for film elements} \end{cases} \quad (7.14)$$

where  $V_{lb}$  is the volume of liquid in the center (bulk) of the element and  $V_{lf}$  is the volume of liquid in the corner films (AMs). Drying is assumed to take place only at the top surface of the network, where a convective mass transfer boundary condition is applied by specifying the evaporation flux density,  $e$ :

$$e = \rho_g D_M \frac{(c_i - c_\infty)}{\delta}, \quad (7.15)$$

where  $\rho_g$  is the gas phase density,  $c_i$  and  $c_\infty$  are the water vapor mass fractions at the top surface and the environment respectively, and  $\delta$  is the air boundary layer thickness across which the transfer of vapor from the open surface of the porous medium to the environment takes place.

In a highly complex pore space such as that of PA, the formation of clusters of liquid and gas regions is expected during the drying process. Therefore, the next step is to model the drying of this residual liquid content with a cluster-based drying algorithm, in which the following assumptions are made:

1. The vapor mass fraction in a pore adjacent to a throat containing liquid is the equilibrium vapor mass fraction,  $c_e$ . This also implies that there is no vapor diffusion within a wet throat.
2. Liquid transport due to capillary forces is neglected. This assumption is based on the neutron radiography experiments presented in Chapter 4.
3. Since liquid regions are assumed to be hydraulically connected, capillary equilibrium is assumed. This means that the corner film radius is the same in all the elements that are part of the same cluster.
4. An element is assumed to be dry when the corner film radius becomes lower than a threshold value,  $r_{nw,\min} = \eta r_0$ , where  $\eta$  is a number less than 1.
5. Viscous effects are neglected.

The drying algorithm developed in this study is in principle similar to the works of Prat (1993) and Prat (2007). In these works, the liquid stored in films is not explicitly tracked as the liquid mass in films is considered negligible compared to the overall initial liquid mass. However, in the drying model developed in this study, the liquid mass in the films is explicitly tracked. In essence, drying proceeds by first drying the central area of bulk elements and then proceeds to dry the film elements by decreasing their liquid film



thickness in a step-by-step manner. Since viscous effects in saturated pores and throats are neglected, invasion percolation rules can be applied to determine the element that should be invaded in each cluster (Prat 1993). Although liquid redistribution may occur, as observed during the neutron radiography experiments described in Chapter 4, such redistribution is not expected to significantly influence the drying process. Moreover, fresh PA specimens are considered for the simulations in this chapter, in which liquid redistribution is expected to be negligible due to a combination of large pores and a hydrophobic solid matrix. The drying algorithm used in this study was fully implemented by the author in OpenPNM, although several pre-installed modules are also used e.g. to calculate macroscopic properties such as relative permeability.

The flowchart of the drying algorithm developed in this study is given in Fig. 7.3 while the detailed algorithm is as follows:

1. Determine liquid clusters  $cl$  present in the network.
2. Determine the radius of the largest element in each cluster  $i$ ,  $r_{0\max,cl}^i$ . If the cluster contains bulk elements,  $r_{0\max,cl}^i$  is determined considering only the bulk elements. In other words, the film elements are not considered for determining  $r_{0\max,cl}^i$  in this case.
3. Compute the vapor mass fraction field in all the pores in the network.
4. Compute evaporation rate  $F_{cl}^i$  [kg/s] at the boundary of each liquid cluster present in network by computing the vapor flow through the elements adjacent to the cluster boundary elements.
5. Determine the evaporation time to either fully dry or dry the center of the element with the maximum size in each cluster as follows. If a cluster  $i$  contains one or more bulk elements, then  $t_{cl}^i = \rho_l V_{lb} / F_{cl}^i$ , where  $V_{lb}$  is the volume of the liquid at the center of the element determined in step 2. Note that a bulk throat becomes a film throat when the liquid goes from occupying the entire cross-section to becoming films with a radius of  $r_t / \chi$ . If a cluster  $i$  contains only film elements, the procedure is as follows. Suppose the corner film radius of curvature is  $r_{nw,cl}^i(t)$  in the considered cluster at time  $t$ . Then the volume of liquid  $V_{lf}^k$  in each element  $k$  of this cluster can be computed from  $r_{nw,cl}^i(t)$ . From this, the mass of liquid present in this cluster can be computed as  $m_{cl}^i = \rho_l \sum_{k=1}^{n_k} V_{lf}^k$ . The evaporation time to fully dry the largest element in the cluster will therefore be  $t_{cl}^i = \left( m_{cl}^i \left( r_{nw,cl}^i(t) \right) - m_{cl}^i \left( \eta r_{0\max,cl}^i \right) \right) / F_{cl}^i$ , where  $\eta r_{0\max,cl}^i$  is the radius at which the largest element in the cluster is assumed to be fully dry.

6. Set time step as  $\delta t = \min(t_{cl}^i)$ .
7. In the cluster that has the element which corresponds to  $\min(t_{cl}^i)$ , set to zero the volume of liquid ( $V_{lt} = 0$ ) in the element if it is a film element. Set the volume of liquid in the element to film volume ( $V_{lt} = V_{lf}$ ) if it is a bulk element. Note that for simplicity, the modification of the capillary equilibrium in the cluster due to this status change is not taken into account in this study.
8. In all other clusters, update the liquid content as follows. If it is a cluster with only film elements, decrease the film thickness of all elements in the cluster, according to the mass conservation condition  $m_{cl}^i(r_{nw,cl}^i(t + \delta t)) = m_{cl}^i(r_{nw,cl}^i(t)) - F_{cl}^i(\delta t)$ . If it is a cluster whose largest element is a bulk element, decrease the liquid volume in that element by decreasing the height of the liquid free surface while ensuring mass conservation.
9. Determine the new total liquid mass in the network,  $m(t + \delta t) = \sum m_{cl}^i$ .
10. Update time,  $t = t + \delta t$ .
11. Go back to step 1 until  $m(t + \delta t) = 0$ . The new iteration proceeds with possibly a different cluster configuration and a new mass fraction distribution field.

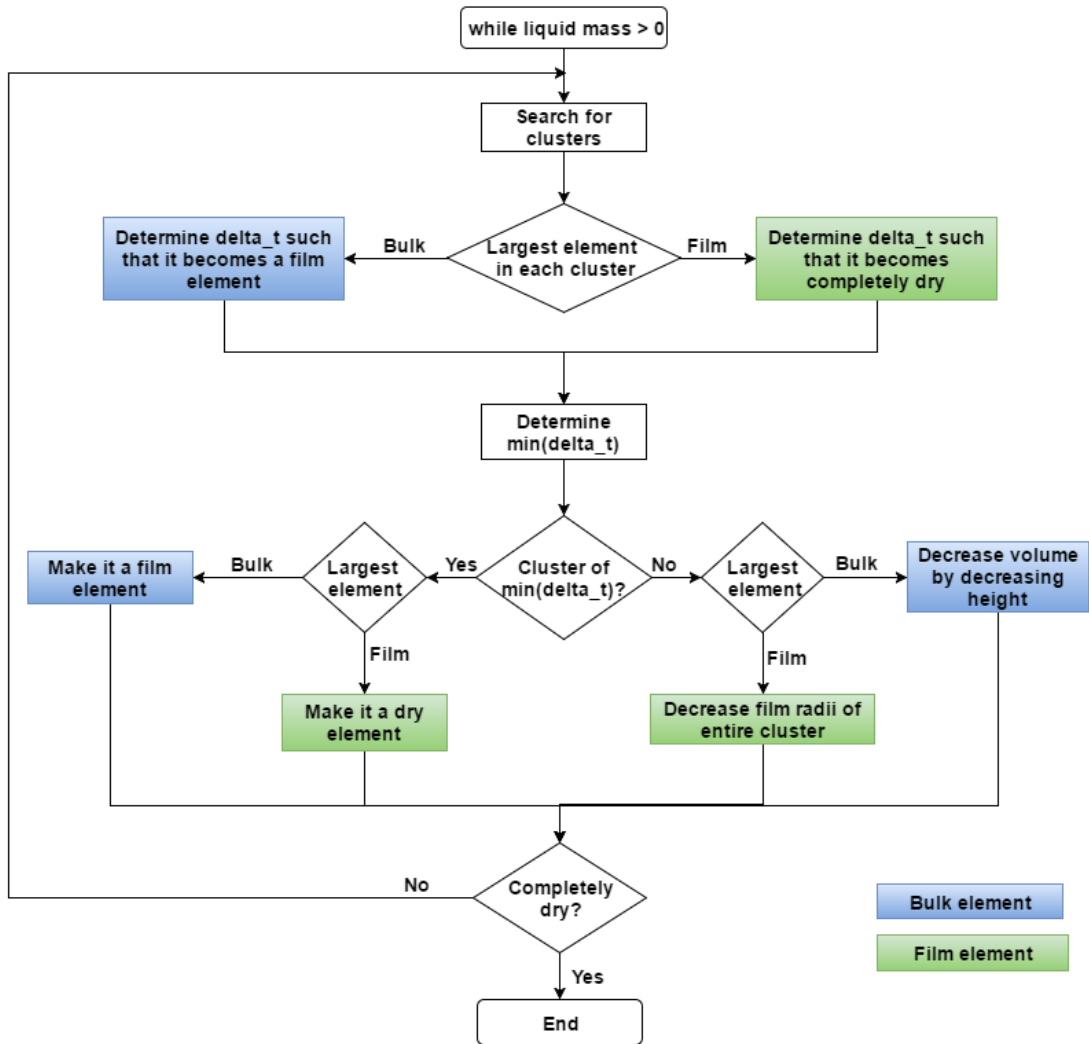


Figure 7.3.: Flowchart of the drying algorithm developed in this study.

#### 7.4 PORE NETWORK EXTRACTION FROM POROUS ASPHALT SPECIMENS

Pore network simulations in this study are based on PA11 specimens of dimensions  $100 \times 100 \times 100 \text{ mm}^3$ . The three specimens are named PA11(1), PA11(2) and PA11(3). The PA specimens are imaged in 3D with an X-ray microcomputed tomography (X-ray  $\mu$ -CT) setup ( $\mu$ DETECT). In this instrument, the X-ray radiation is generated by a micro-focus X-ray tube from Finetec (model FOMR 300.03Y RT) operating at an acceleration voltage of 300 kV and a tube current of 100  $\mu$ A. A 1 mm thick filtration plate made of copper is placed in front of the source for hardening the beam. The projection images are acquired by a flat panel detector from Perkin Elmer (model XRD 1611-CP3) used in its  $2 \times 2$  binning mode, corresponding to pixels of 200  $\mu\text{m}$ . An acquisition time of 2.5 s is employed and a total of 4 frames are averaged per orientation of the sample. The sample is rotated in 1600 steps around a fixed axis in steps of  $0.225^\circ$ . The radiographs are corrected for ring artefacts with adequate image processing techniques. A median filter of radius 3 is applied to the images, which are then reconstructed using an in house implementation of the Feldkamp-Davis-Kress algorithm (Feldkamp et al. 1984). The resulting volumes with a voxel size of approximately  $72 \times 72 \times 72 \text{ }\mu\text{m}^3$ .

The X-ray  $\mu$ -CT images of the specimens are then thresholded to extract the pore space of PA. The pore networks are extracted from the thresholded X-ray  $\mu$ -CT images using the modified maximal ball algorithm of Dong and Blunt (2009), which is an extension of the work of Silin and Patzek (2006). The maximal ball (MB) algorithm works by fitting the largest possible spheres, centered on each air voxel, such that they just touch the solid boundary. Spheres that are completely inscribed within other spheres are removed and the remaining spheres are called maximal balls, where the largest maximal balls are considered as pores and the smaller balls between them are considered as throats. In Fig. 7.4, the irregular pore network generated from a small region of interest of  $30 \times 30 \times 30 \text{ mm}^3$  from PA11(1) is visualized. In Fig. 7.5, the pore size distributions (PSD) and throat size distributions (TSD) of the 100 mm cubes of PA11(1), PA11(2) and PA11(3) are given, as estimated with the MB algorithm. The MB algorithm showed instabilities for datasets larger than  $85 \times 85 \times 85 \text{ mm}^3$  and therefore, the actual pore networks are generated from a volume of  $85 \times 85 \times 85 \text{ mm}^3$  from the center of the specimens. Additionally, extracting the pore network from the center of the specimens prevents the presence of unrealistically large pores in the generated pore network and also helps to avoid the edge effect issues that are commonly encountered in pore network extraction. Although the MB algorithm generates an unstructured pore network, structured pore networks (cubic lattices) generated using the Weibull fit parameters estimated from Fig. 7.5 are used for the simulations in this study.

Weibull probability distribution function is often used to model the pore space characteristics of porous media (Kuttanikkad et al. 2011; Neithalath et al. 2010). The histograms in

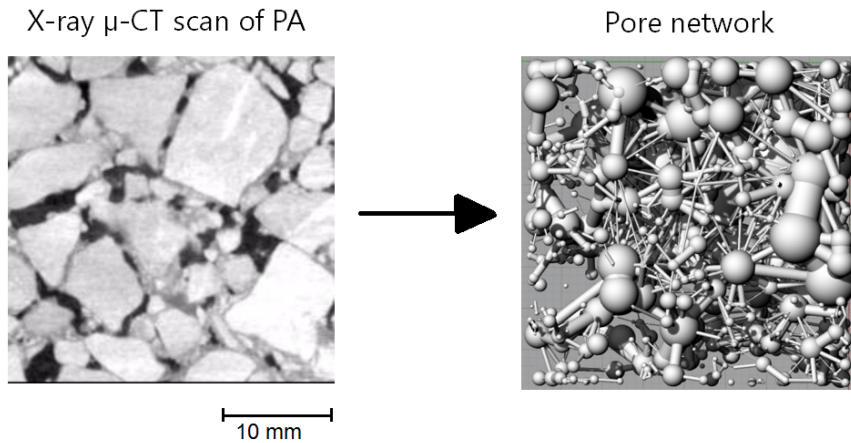


Figure 7.4.: Extraction of pore network, using the Maximal Ball algorithm (Dong and Blunt 2009), from an X-ray  $\mu$ -CT scan (a slice of the scan is shown on the left) of a region of interest of  $30 \times 30 \times 30 \text{ mm}^3$  of the specimen PA11(1).

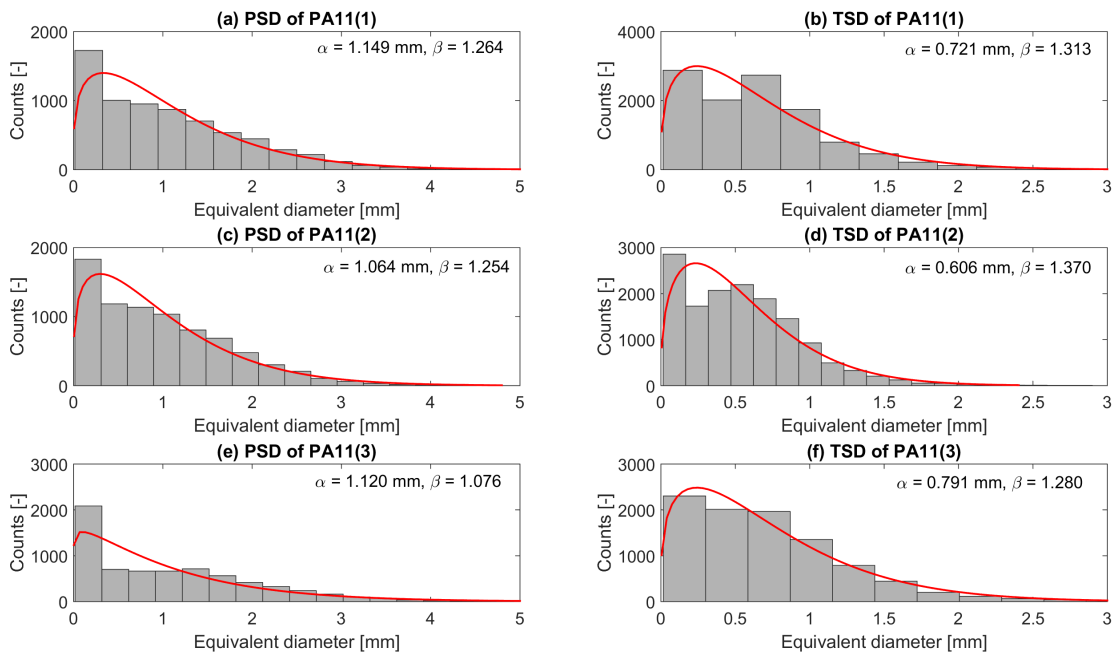


Figure 7.5.: Histograms of pore size distribution (PSD) and throat size distribution (TSD) of specimens PA11(1), PA11(2) and PA11(3) fitted with a two-parameter Weibull distribution (red curve). The scale ( $\alpha$ ) and shape ( $\beta$ ) parameters of the fit are given in the respective figures.

Fig. 7.5 are fitted with a two-parameter Weibull probability distribution function (PDF), which is given by the red curve in the figure. The two-parameter Weibull PDF is defined as:

$$f(d_0; \alpha, \beta) = \begin{cases} \beta \left( \frac{d_0^{\beta-1}}{\alpha^\beta} \right) \exp \left( -(d_0/\alpha)^\beta \right), & d_0 \geq 0 \\ 0 & , \quad d_0 < 0 \end{cases} \quad (7.16)$$

In Eq. (7.16),  $d_0$  is the pore diameter while  $\alpha$  and  $\beta$  are the scale and shape parameters, respectively, of the Weibull distribution. The scale parameter defines the width of the distribution while the shape parameter, as the name implies, defines the shape of the distribution. The values of the shape and scale parameters of the Weibull curves in Fig. 7.5 are also given in the respective figures. The next step is to quantitatively assess whether the data is adequately captured by the Weibull distribution. This is done by means of a probability plot, in which the cumulative distribution function (CDF) of the distribution, whose scale and shape parameters are determined from the histogram fits, is plotted against the data points in a log-log plot. If the data points are predicted well by the distribution, then these points should overlap with the straight line in the probability plot, as shown in Fig. 7.6. The ordinate of the probability plots is a rearranged form of the Weibull CDF, defined by the following equation:

$$\log \left[ \ln \left( \frac{1}{1 - F(d_0)} \right) \right] = \beta \log(d_0) - \beta \log(\alpha). \quad (7.17)$$

If  $y = \ln(1/1 - F(d_0))$ , then  $\log(y)$  is linear to  $\log(d_0)$  with slope  $\beta$  and intercept  $\beta \log(\alpha)$ . This linear relationship is indicated by the red line in Fig. 7.6, along with the original data (points) from the histograms in Fig. 7.5.

The values of  $\alpha$  and  $\beta$  give physical insights into the pore and throat sizes of PA. In a two-parameter Weibull distribution,  $\alpha$  can be interpreted as the value below which 63.2% of all observations fall, irrespective of the value of  $\beta$ . From Fig. 7.5, it can be seen that values of  $\alpha$  for PSD ( $\approx 1.1$  mm) and TSD ( $\approx 0.7$  mm) are similar between the specimens. However, a significant number of pores with 2-4 mm diameters and throats with 1-3 mm diameters are also seen in the specimens. These large pores and throats are primarily responsible for the excellent drainage properties of PA. From Fig. 7.6, it can be seen that Weibull distributions accurately predict PSD and TSD of all the three specimens as most of the data points fall on the straight line of the probability plots. It should be noted that in a probability plot, data points at low probability values will never fall on a straight line since the number of data points is finite.

Using the PSD and TSD distribution parameters estimated from Fig. 7.5, a  $17 \times 17 \times 17$  structured, cubic lattice pore network is generated for all the three specimens. A constant connectivity of 6 is assumed for all pores. The throats are given a constant length of 5 mm

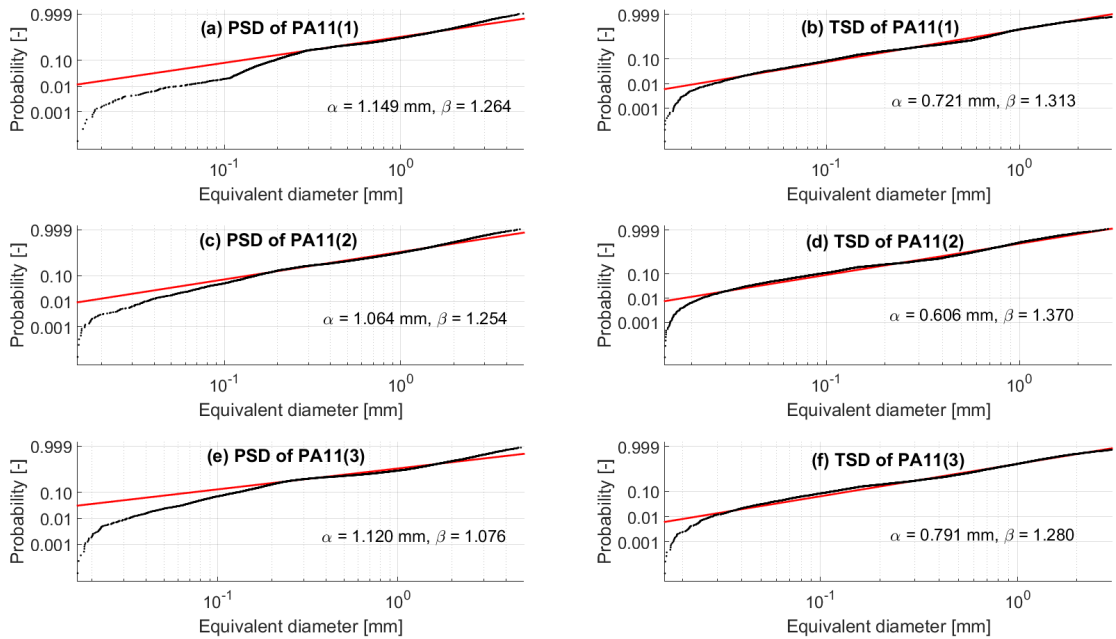


Figure 7.6.: Cumulative probability plots of pore size distribution (PSD) and throat size distribution (TSD) of specimens PA11(1), PA11(2) and PA11(3), which are fitted with a two-parameter Weibull distribution in Fig. 7.5. The red line indicates the predicted distribution while the points represent the original data. The scale ( $\alpha$ ) and shape ( $\beta$ ) parameters of the fit are also shown in the respective figures.

while the pore length is assumed to be equal to its inscribed circle diameter. The constant throat length of 5 mm is a realistic assumption since the throat length distribution of all the three specimens as calculated by the MB algorithm peaks around 5 mm. The final network has 6647 pores and 15,606 throats, which is roughly similar to the number of pores and throats calculated by the MB algorithm. Considering that PA has a porosity of approximately 20%, an  $85 \times 85 \times 85 \text{ mm}^3$  specimen will have a pore space volume of  $123 \times 10^{-6} \text{ m}^3$ . This means that the pore space of the generated pore network captures only 40% of the pore space of a real specimen of similar dimensions. However, it is to be noted that while the real specimen has many enclosed pores that can never be invaded by water, all the elements in the pore network can be potentially invaded by water. In other words, the porosity of PA that is relevant for fluid transport will be much lower than 20% of the total specimen volume, and therefore the fraction of pore space captured by the pore network that is actually relevant for fluid transport is much higher than 40%.

Triangular pores and throats are used in the pore network, which implies that  $\alpha_c = 30^\circ$  and  $N_c = 3$ . A triangular cross-section is used since arc menisci can exist in an angular geometry only if  $\theta < \pi/N_c$  (Prat 2007). Considering that the solid matrix of a fresh PA specimen is mainly a hydrophobic structure ( $\theta > 90^\circ$ ), it is impossible to simulate corner flow with this contact angle as no angular geometry would satisfy the condition for corner flow. Therefore,  $\theta = 55^\circ$  is assumed for the simulations as this is the approximate contact angle between water and the aggregates used in PA (Poulikakos 2011). Given  $\theta = 55^\circ$ , only a triangular geometry satisfies the condition for corner flow. Moreover, the use of pore shapes such as squares and hexagons will result in a drastic reduction of the pore network volume as compared to the real specimen. For simplicity, equilateral triangles are used which implies that the shape factor  $G = 0.048$ . The impact of assuming a hydrophilic contact angle on the simulation results is studied in detail in Section 7.5.3. Furthermore, it is also assumed that the pore networks do not have a preferential direction, which may not be the case for real PA layers. A pore network is built for each of the three PA specimens analyzed above.



## 7.5 RESULTS AND DISCUSSION

In this section, the results from the simulations of gravity-driven drainage and snap-off, followed by the results of drying simulations are presented for the three PA11 specimens described above. An important parameter that acts as a control variable in the simulations is the proportion of hydrophobic, hydrophilic and dead-end elements in the pore network. As stated earlier, the contact angle cannot be given a value larger than  $60^\circ$ , which implies that all pores are hydrophilic by default. Water existing as films in these hydrophilic pores are represented as film elements. Hydrophobic pores that are already dry and dead-end elements that are liquid saturated at the beginning of drying are indirectly introduced into the network by specifying a certain number of elements as dry and bulk elements respectively. Ultimately, the proportions of dry, bulk and film elements in the network determine the residual liquid content and its distribution in the network at the beginning of drying. Since the real proportion of these element types in PA is not known, for the drying simulations in this study, the proportions are chosen in such a way that the residual liquid contents in the pore networks after drainage matches those measured during the validation experiments which are described in Section 7.5.2.

### 7.5.1 Gravity-driven drainage and snap-off

Gravity-driven drainage from a fully saturated specimen is simulated using the algorithm described in Section 7.3.1. Air invades from the top surface of the cubic lattice network while water exits the network from the bottom surface. Dirichlet boundary conditions of atmospheric pressure (101325 Pa) are applied at both these surfaces. The four lateral surfaces are impermeable to both air and water. For simplicity of the invasion percolation algorithm, the possibility of snap-off is checked only after the entire drainage process is completed, and all elements satisfying the snap-off criteria (Eq. (7.13)) are refilled with water. The choice to check for snap-off after drainage is further justified by the fact that drainage in PA is an extremely fast process, in the order of seconds, while snap-off is a comparatively slower phenomenon.

The fluid properties used for the simulations, and introduced in Section 7.3, are:  $\gamma = 0.027$  N/m,  $D_M = 2.068 \times 10^{-5}$  m<sup>2</sup>/s,  $\mu_w = 8.9 \times 10^{-4}$  Pa · s,  $\mu_a = 1.84 \times 10^{-5}$  Pa · s,  $\rho_w = 997$  kg/m<sup>3</sup> and  $\rho_a = 1.184$  kg/m<sup>3</sup>, which are standard air and water properties at 23 °C. In the drainage results presented in this section, 40% of all throats are randomly specified to be always saturated. As stated earlier, these elements represent the dead end and hydrophobic pores in PA that do not drain. The main aim of the drainage simulations is to study the evolution of capillary pressure as a function of saturation in three macroporous specimens and to see if they show a similar trend. Therefore, at this

stage, the exact residual liquid content in the specimens after drainage is not a parameter of concern, unlike for the drying simulations.

The drainage pattern in the network is visualized in Section 7.6 in which the evolutions of liquid distribution in the network during drainage with gravity (considered in this section) and without gravity are compared. In Fig. 7.7, the air and water relative permeabilities of the three specimens as function of water saturation,  $S_w$ , is given. The relative permeability of a phase at a certain liquid saturation level is defined as the ratio of the effective permeability of the phase at that saturation level to the absolute permeability of the material, i.e.:

$$k_{r,p} = \frac{k_{eff,p}}{K}. \quad (7.18)$$

While the absolute permeability  $K$  is an intrinsic material property that is independent of the fluid type as long as the material is fully saturated with any fluid, relative permeability depends on both the material structure, the type of fluid and configuration of the liquid inside the porous medium. From the pore network simulations, the relative permeability is estimated from the mean pore pressure at the network boundary as:

$$k_{r,p} = \frac{\bar{P}_{i-1}^p - \bar{P}_i^p}{\bar{P}_{i-1} - \bar{P}_i}, \quad (7.19)$$

where the subscript  $i$  denotes the top or bottom network boundary while  $i - 1$  denotes the adjacent layer of pores.

The permeability behavior of all the three specimens is found to be similar from Fig. 7.7. While the liquid permeability expectedly decreases sharply with decreasing liquid saturation, a noteworthy feature is that air permeability does not show an equally sharp rise. This could be due to the phenomena described as 'compact cluster growth' by Hughes and Blunt (2000) and described in detail by Lenormand and Zarcone (1984). Essentially, the low air permeability even at a low liquid content can be attributed to the phenomena of trapping. Air entering the network is trapped between clusters of pores that are fully liquid saturated due to snap-off. As a result, although the air content is high, the network has a low air permeability as there are few low resistance, continuous air pathways from inlet to outlet.

Water saturation,  $S_w$ , as a function of the capillary pressure,  $p_c$ , during drainage in the three specimens is presented in Fig. 7.8. Several models are used in literature to fit  $p_c - S_w$  curves, one of which is the van Genuchten (VG) model (Genuchten 1980), and a modified version of the VG model is used in this study to fit the  $p_c - S_w$  data:

$$S_w = (1 + (\alpha_{VG} p_c)^n)^{\left(\frac{1-n}{n}\right)} + f_{VG}, \quad (7.20)$$

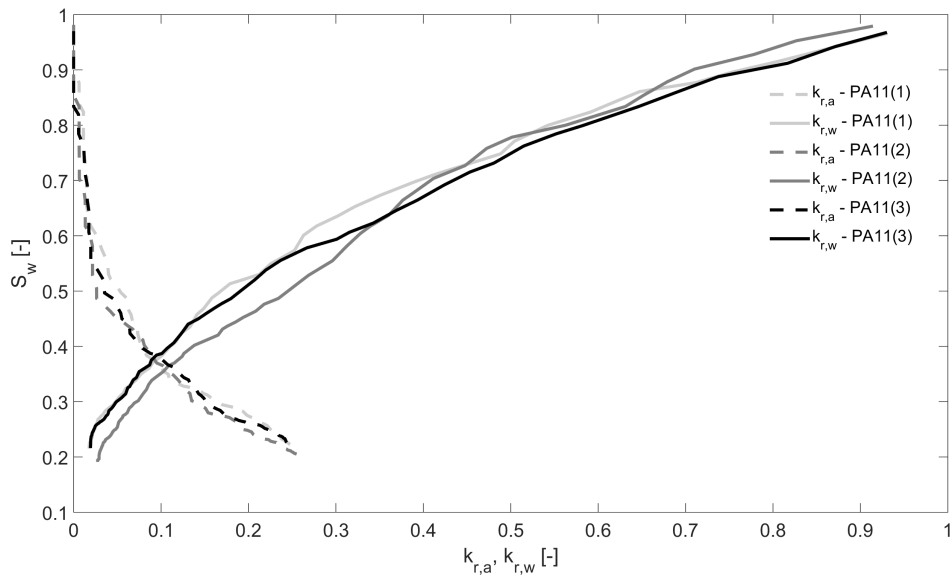


Figure 7.7.: Relative permeability of air,  $k_{r,a}$ , and water,  $k_{r,w}$ , as a function of water saturation,  $S_w$ , for specimens PA11(1), PA11(2) and PA11(3), during drainage from  $S_w = 1$  to  $S_w = 0.2$ .

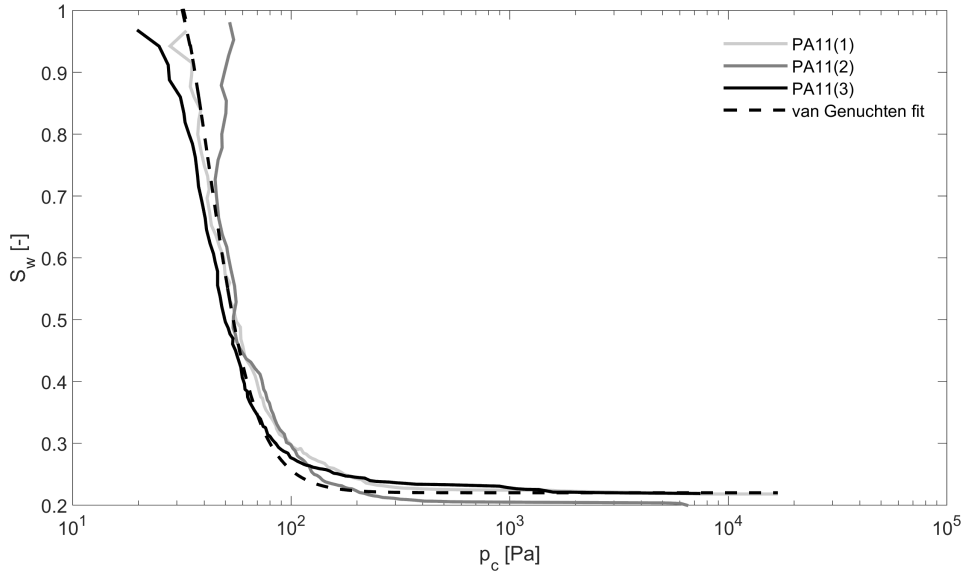


Figure 7.8.: Capillary pressure,  $p_c$ , as a function of water saturation,  $S_w$ , for specimens PA11(1), PA11(2) and PA11(3), during drainage from  $S_w = 1$  to  $S_w = 0.2$ .

where  $\alpha_{VG} = 0.025$ ,  $f_{VG} = 0.22$  and  $n = 4.6$  are the fitting parameters used in this study. The fit is valid only for  $p_c > 0$ . The VG fitted curve is also given in Fig. 7.8. It can be seen that the VG model is able to accurately capture the  $p_c - S_w$  relation in PA during drainage, especially the sharp rise in  $p_c$  towards the end of the drainage process.

From Figs. 7.7 and 7.8, a residual moisture content of around 20% can be seen in all the three specimens, which is the sum of water in the 40% of throats that are saturated and the corner films in all other elements. The overall  $p_c - S_w$  behavior of the three specimens are largely similar, although PA11(2) exhibits a small divergence at the beginning and at the end of the drainage process. The shape of the capillary pressure curve is along expected lines i.e. there is a smooth rise in  $p_c$  initially, followed by a sharp rise towards the end of the drainage process as air progressively enters pores that are more difficult to invade. The smooth rise in  $p_c$  is usually ignored for simulations of large porous media like rock beds, as this part is not representative of an infinite medium (Gostick et al. 2006). However, for a material like PA, whose layer thickness is in the order of centimeters, this part is an intrinsic aspect of the material behavior, and therefore cannot be ignored. Finally, compared to the magnitudes of  $p_c$  towards the end of drainage in microporous materials (e.g.  $\approx 10^6$  Pa for sandstone), the corresponding value for PA is seen to be much lower, which is due to the large pores in PA and the strong influence of gravity.

### 7.5.2 *Drying of residual liquid and experimental validation*

The residual water after gravity-driven drainage in PA is subjected to evaporation using the drying algorithm described in Section 7.3.2. All the lateral surfaces as well as the bottom surface of the network is assumed to be impervious. Vapor transfer occurs only at the top surface of the network, where the effect of the air boundary layer is applied using Eq. (7.15) i.e. the transfer of vapor from the top surface to the environment is assumed to take place through a diffusive layer of uniform thickness  $\delta$ . At temperatures close to 20 °C,  $\delta \approx 10^{-4} - 10^{-3}$ m (Prat 2007). In the simulations in this study,  $\delta \approx 10^{-3}$ m is assumed, the implications of which are discussed in detail. Furthermore, the environmental vapor mass fraction is taken as  $c_\infty = 0.011$ , which is the vapor mass fraction at a temperature of 23 °C and relative humidity of 65%, the equilibrium vapor mass fraction  $c_e = 0.018$ , and the film thickness cut-off factor  $\eta = 0.01$ . The value for  $\eta$  is chosen arbitrarily with the only criteria that elements are considered dry only if film thickness are small enough to not influence the drying process in the last stages. The fluid properties are the same as the ones used for the gravity drainage simulations. Preliminary laboratory experiments performed at 23 °C showed that temperature gradients within PA during the drying process is negligible ( $< 0.2$  °C). In this experiment, the evolution of temperature at the lateral edges and at the center of a PA11 specimen was recorded with eleven thermocouples, two each at the four lateral edges and three at the center. Therefore, the assumption of isothermal drying is found to be valid, at least for the simulations and validation experiments performed in this study. At the beginning of the PNM simulations of drying, all pores and throats that are directly connected to the six boundary faces of the cubic lattice are assumed to be completely dry. This assumption is justified as all sides of the PA11 cubic specimens are open during drainage in both the experiments and the PNM simulations. Due to a high static pressure head, the elements near the top surface are especially conducive to air entry. Moreover, this step also introduces a certain degree of hydrophobicity into the network by not retaining any water in certain pores.

The PNM simulations are validated with gravimetric experiments of drying of PA11(1), PA11(2) and PA11(3). The same  $100 \times 100 \times 100$  mm<sup>3</sup> from which the pore networks for the simulations are extracted are also used for the experiments. It is noted that even though real PA layers are not more than 30-50 mm long in the direction of gravity, larger specimens are chosen for this study to get a representative pore network. The specimens are first submerged in water for at least 24 hours. Thereafter, they are taken out of water and water is allowed to drain from all sides for 2 hours. Then the specimens are placed in a Styrofoam box (thermal insulator) which is closed on all sides except the top, thereby reproducing the simulation conditions. The moisture loss from the specimens is then monitored until they become completely dry. The drying experiments are carried out in a controlled environment of 23 °C and 65% relative humidity. In Fig. 7.9, the moisture loss

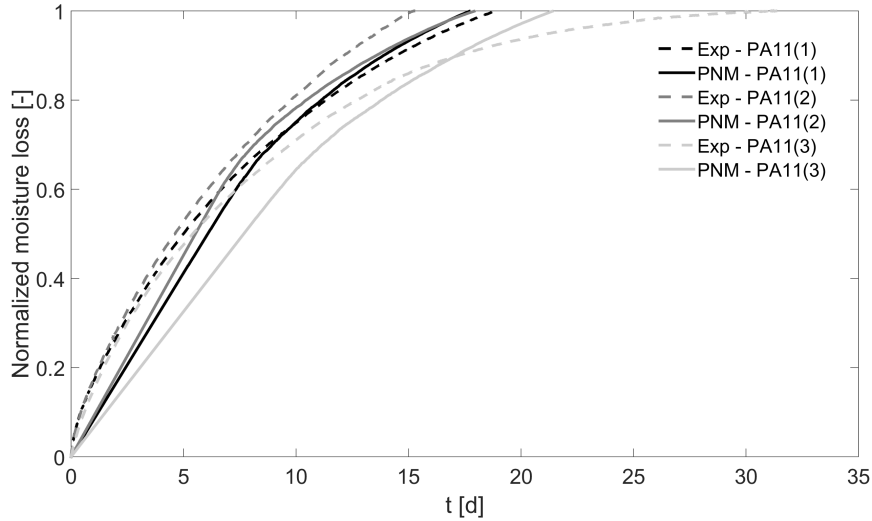


Figure 7.9.: Experimental results and pore network modeling (PNM) results of normalized moisture loss as a function of time during drying for specimens PA11(1), PA11(2) and PA11(3).

normalized by the initial moisture mass in the specimens,  $m_{loss} = (m(t_0) - m(t))/m(t_0)$ , as a function of time, is presented for the experiments and PNM simulations performed on the three specimens. As stated before, since PA is a mostly hydrophobic material, most of the residual liquid content after drainage is expected to be in the dead-end pores or trapped in hydrophilic pores, rather than exist as corner films in hydrophobic pores. Therefore, a majority of the elements, i.e. around 60-70% of the total number of elements, depending on the specimen, are specified to be fully saturated throughout the drainage process. The remaining elements can retain water in their corners. This allowed the residual liquid content in the pore networks after drainage to be approximately equal to the observed liquid mass during the experiments. Laboratory measurements showed that PA specimens retained a residual liquid content of 25-28 kg/m<sup>3</sup> after drainage from an average fully saturated mass of 125 kg/m<sup>3</sup>, which translates to a liquid saturation of approximately 0.2 at the beginning of the drying process. However, as stated earlier, due to the lower absolute volume of the pore network as compared to that of the actual PA pore space volume, the same liquid mass translates to a saturation of at least 0.5 in the pore networks. Therefore, the aim of the results presented in this section is to compare the drying rate of the residual liquid as a function of time, and not as a function of saturation. The drying experiment of PA11(3) is run for an extended duration since it is observed to dry slower than the other two specimens.

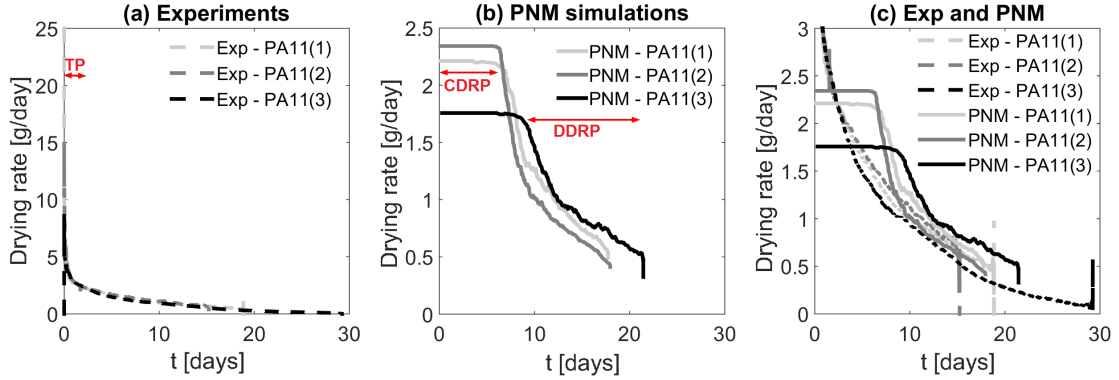


Figure 7.10.: First derivative of the moisture loss (drying rate) as a function of time of (a) experimental observations, (b) pore network modeling simulations and (c) both experiments and PNM simulations, with the drying rate curve of the experiments starting from  $t = 1.5$  d, plotted for specimens PA11(1), PA11(2) and PA11(3). The transition period (TP) of the experiments is indicated in (a), while the constant drying rate period (CDRP) of PA11(1) and PA11(2) and the decreasing drying rate period (DDRP) of PA11(3) are indicated in (b).

From Fig. 7.9, a good overall agreement can be seen between the simulations and the experiments for PA11(1) and PA11(2). For PA11(3), the agreement is not good because the material resistance to drying is very high. This aspect is discussed in detail later. From Fig. 7.9, the drying curves of the PNM simulations are seen to have two distinct slopes while the curves of the experiments are not. This observation requires further analysis of the drying rates. Therefore, in Fig. 7.10, the drying rate,  $\dot{m}_{dry} = d(m(t_0) - m(t))/dt$ , which is the first derivative of the curves in Fig. 7.9, is plotted as a function of time. In Fig. 7.10(b), two drying rate periods can be clearly distinguished in the PNM simulations and they are marked in the figure for the respective specimens. For specimens PA11(1) and PA11(2), until  $t = 7$  d, the drying rate is constant, and this period is known as the constant drying rate period (CDRP). For PA11(3), CDRP is seen until  $t = 10$  d. After that period, the drying rate constantly decreases until the material is almost dry, and this period is known as the decreasing drying rate period (DDRP). However, the drying phase during all the experiments is always DDRP, as seen in Fig. 7.10(a).

At the beginning of the experiments, there is a transition period (TP) during which there is a sharp drop in the drying rate, as can be seen in Fig. 7.10(a). This period is mainly characterized by the drying of water at the top of the solid surface, which dries at a very fast rate. Additionally, water at the top pores also dries very quickly, first in the large pores and then in the smaller pores. At the end of TP, there are only a few liquid

paths in the material that are connected to the environment. During the evaporation of most porous materials, TP is followed by the constant drying rate period (CDRP), during which liquid continuity is ensured through corner films, even if the percolation front i.e. the bulk air infiltration front, does not have a macroscopic connectivity to the surface. These liquid films ensure a constant supply of liquid to the surface during CDRP, and therefore the drying rate remains constant during this period as, at the surface, the moisture content lost by evaporation is replaced by liquid flow arriving from the material. During CDRP, the drying rate is therefore determined by  $\delta$ , the external mass transfer coefficient. Once the surface starts to become dry, the hydraulic connectivity from corner films starts to break down as the tips of the films recede deeper into the material. The drying rate at this stage starts to progressively decrease and is therefore called DDRP. During DDRP, the drying rate is determined by the effective diffusivity of water vapor within the material. As seen in Fig. 7.10(a), in reality, the drying process in PA completely skips the CDRP and goes from TP to DDRP. This is because there is negligible capillary transport of water within the material, which implies that there is no continuous transport of water to the evaporating surface to balance the rate of evaporation from the surface. This is yet another indication that fluid transport in PA cannot be modelled akin to that in conventional porous media, where the presence of CDRP during the initial stages is quite common even in materials where gravity effects are significant (Yiotis et al. 2015). Also absent during drying in PA is a second CDRP, which is observed when liquid flow in film regions is primarily driven by gravity instead of capillary pressure gradients, and the evaporation front remains stationary leading to a constant evaporation rate (Yiotis et al. 2015).

In Fig. 7.10(c), the drying rates of the experiments and simulations are compared after excluding the TP seen in the experiments. While the drying rates of the experiments and simulations are largely similar after  $t = 7$  d for PA11(1) and PA11(2), those of PA11(3) are always different, as expected. The large difference in the drying rates of the experiments and simulations in the first 24 h of drying can be attributed to the difference in the initial liquid configuration at the beginning of drying. While the hydraulic connectivity within the specimens seem to be very low at the beginning of the experiments, leading to the onset of DDRP, the initial drying in the simulations is concentrated at the top region of the specimen, thereby making the strong material resistance to vapor diffusion, which was already observed in the CFD simulations in Chapter 6, completely irrelevant to the drying process. This leads to CDRP in the simulations as observed in Fig. 7.10(b). However, as pointed out earlier, the latter half of the drying process in the PNM simulations from  $t = 7$  d onwards shows good agreement with the experiments as by this time the influence of vapor diffusion resistance of the material is reflected on the drying process.

The drying algorithm developed in this study is not expected to result in a top-down drying gradient in the network as the algorithm is based on a cluster-based invasion process.



In other words, the proximity of a wet element to the open surface is not the only factor influencing its drying rate. To check if drying gradients develop during the simulations, additional simulations are performed on a smaller domain, which is divided into a  $12 \times 12$  checkerboard grid, and the liquid saturation  $S_w$  in each of them is monitored throughout the drying process, as shown in Fig. 7.11. The specifications of this smaller grid are given in the next section. To enable a comparison between this smaller grid and the larger grid of the real PA simulations, time is normalized with the total drying time,  $t_{tot}$ . In the figure, no significant drying gradient can be seen in the network at any stage of the drying process. The absence of a drying front is also observed in the neutron radiography experiments presented in Chapter 4. At the beginning of drying, there is just one large liquid cluster spanning the entire volume of the network. According to the algorithm, the elements near the open surface have to dry first since there is only one cluster and these are the elements that happen to be at the edge of the cluster. However, as drying progresses, the number of liquid clusters in the network also starts to increase. In such a scenario, the proximity of an element to the open surface starts to matter less, the drying ceases to be top-down, and as a result there is no definite pattern of drying, as seen in Fig. 7.11. Therefore, the drying behavior seen in the simulations i.e. CDRP until  $t = 7$  d (for PA11(1) and PA11(2)) and  $t = 10$  d (for PA11(3)), and DDRP thereafter, cannot be attributed to a receding drying front that goes from top to bottom of the network.

Rather, the observed drying behavior can be attributed to the assumption of film flow in the drying model. An underlying principle of the drying algorithm is the two-step drying process i.e. in a cluster with both bulk and film elements, bulk elements lose moisture first and in the process become film elements. Therefore, during CDRP, most of the moisture loss occurs as a result of bulk elements becoming film elements. An important assumption in the drying algorithm is that the mass fraction in a pore adjacent to a throat containing liquid is the equilibrium vapor mass fraction,  $c_e$ . Due to this assumption, during CDRP, most of the drying occurs from the transformation of bulk elements to film elements. As a result, most of the pores until this time are adjacent to wet throats and therefore  $c = c_e$  at all these pores. Consequently, the drying process is confined to the top region of the network as only the pores and throats near the surface are capable of transporting vapor to the environment. At this stage, vapor diffusion within the network is totally controlled by the diffusion happening across the external transfer length,  $\delta$ . As a result, the drying rate remains constant as  $\delta$  is assumed to be constant throughout the simulations. After CDRP, the film elements begin to dry, resulting in vapor transport within the network, which implies that the vapor diffusion resistance of the material begins to influence the drying process, which is why the drying rate starts to decrease as more pores and throats start to become dry and thereby increase the material resistance to vapor diffusion continuously. This explanation is analyzed in more detail in the next section. As the drying resistance of PA11(3) is much higher compared to those of the other two specimens, the simulation of

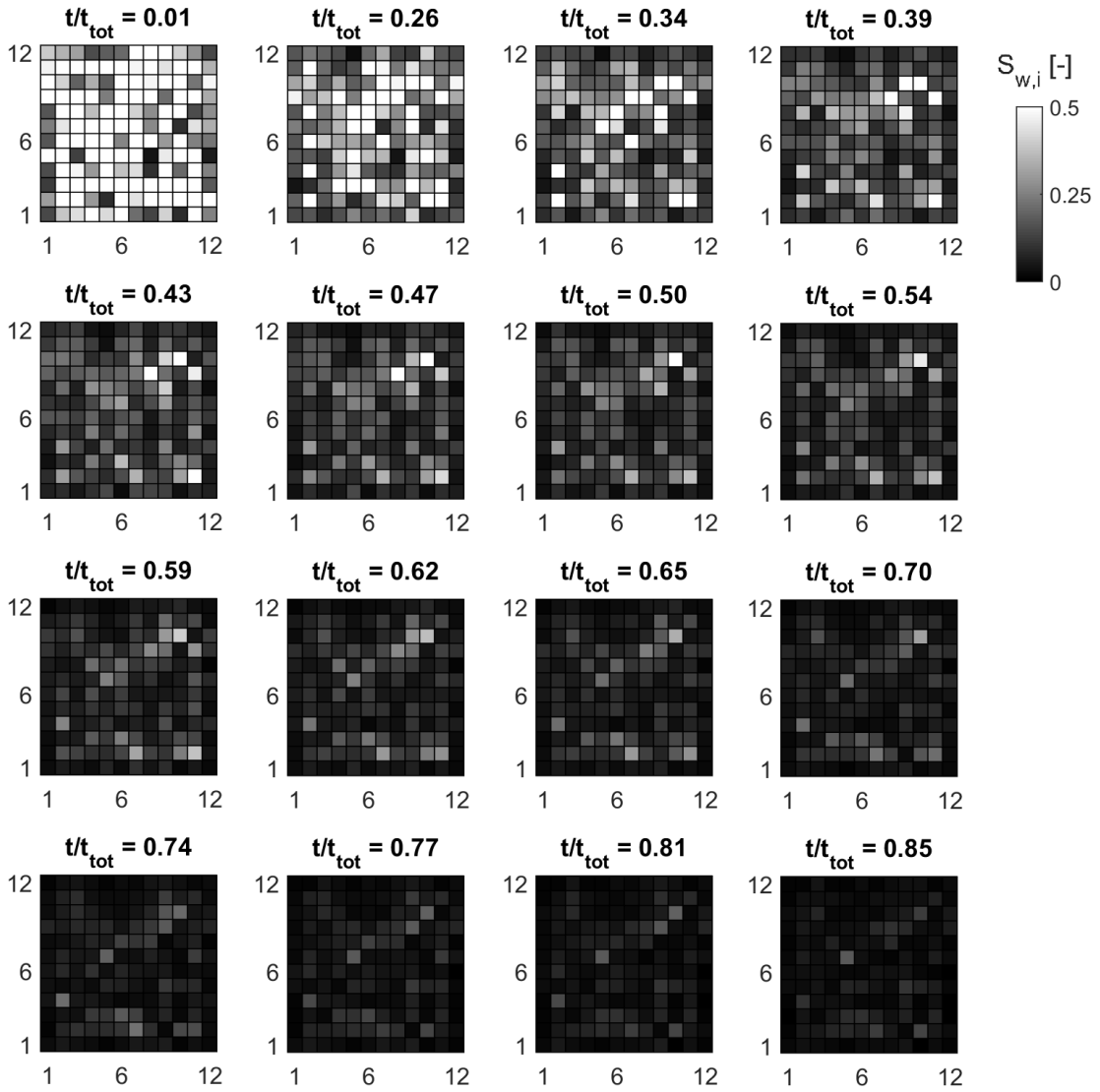


Figure 7.11.: Checkerboard pattern of drying as simulated by the pore network model with time steps indicated above each figure. The domain is divided into 144 equi-sized grids and the grid color indicates the water saturation  $S_{w,i}$  at the grid along the entire thickness (out of plane direction) of the network.

drying in PA11(3) does not show a good agreement with the experiments since the drying model does not account for material resistance at the beginning of the drying process. The observed drying rate in the simulations also implies that the drying at the beginning is sensitive to the value of  $\delta$ . An exact quantification of  $\delta$  for a very rough and permeable surface like that of PA is a challenging task. However, it is noted that the determination of  $\delta$  for PA is a promising avenue for future studies. Moreover, an important aim of the pore network simulations is also to understand its coupling with continuum modeling for a macroscopic material and the sensitivity of the inputs to pore network modeling on the results from continuum modeling.

## 7.6 SENSITIVITY ANALYSIS OF RANDOMNESS IN THE PORE NETWORK, GRAVITY AND CORNER FILMS

In this section, the results from additional simulations to check the sensitivity of various parameters on the simulation results are presented. On the one hand, this analysis helps to identify the strengths and weaknesses of the developed pore network in terms of the flow physics modeled in the network, while on the other, it helps to analyze the influence of various parameters on flow in macroporous media. Due to significantly higher computational speed, all the simulations in this section are presented for a  $12 \times 12 \times 12$  network with the same pore diameters, throat diameters and throat lengths of the PA11(1) network. Although the magnitudes of the outputs extracted from this smaller network is different from those of the  $17 \times 17 \times 17$  specimens, the influence of the parameters considered in this section are similar in both the network sizes.

The randomness in pore network generation can often influence the properties extracted from simulations. In a medium such as PA with a wide range of pore sizes, an important factor to be considered is the neighborhood of large pores. For instance, a large flow path in the real specimen may be represented as a series of large and small pores in the pore network, leading to drastically different flow behaviors in these two configurations. Additionally, with the same set of pore and throat size distributions, the flow behavior in two large pores connected to each other will be very different compared to that in one large and one small pore connected to each other. Therefore, the influence of randomness in the pore network is investigated in Fig. 7.12, where the capillary pressure curve during drainage and the drying curve are presented for four realizations with the same input parameters. It can be seen that the realizations display similar flow behavior during both drainage and drying and therefore the randomness in pore network generation has little influence on the macroscopic properties extracted from the simulations. The negligible influence of randomness is mainly due to the structured grid and equal throat lengths used in this study. If an unstructured grid was used instead of a simple structured grid, the number of parameters influencing the generated pore network would have increased,

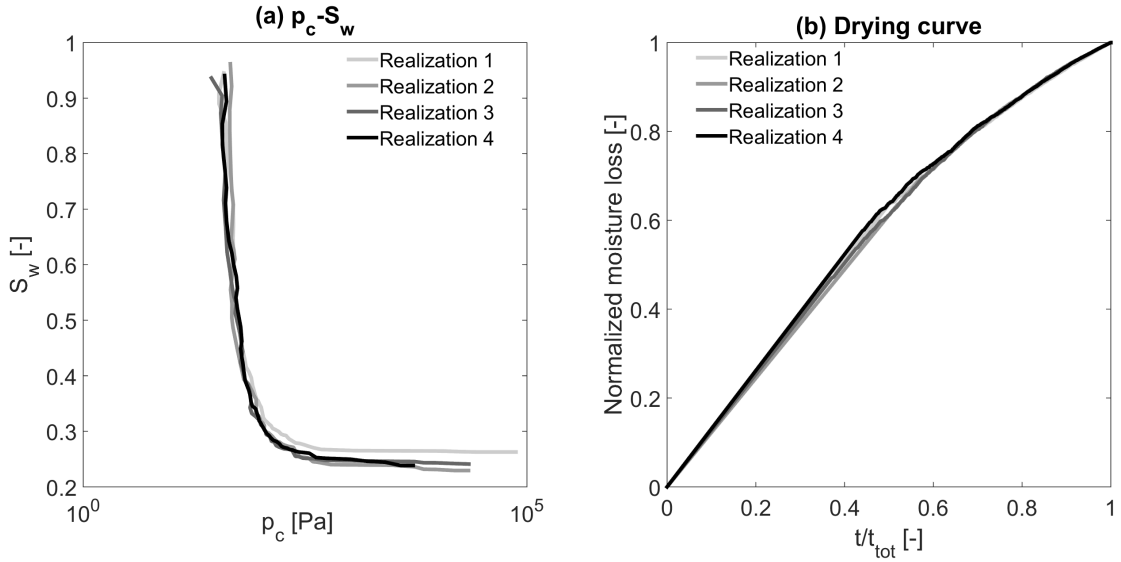


Figure 7.12.: Influence of randomness in the pore network on (a) capillary pressure curve and (b) drying curve, investigated for four realizations.

thereby increasing also the influence of randomness in the network. In an unstructured grid, a particularly significant factor would be the pore connectivity, especially the connectivity of the large pores.

In Fig. 7.13, the checkerboard pattern of drainage in the network is analyzed for two cases: without and with gravity respectively. Similar to Fig. 7.11, the degree of saturation in each of the grids is analyzed for the initial stages of the drainage process. The degree of saturation in the entire network is also given for each considered step. In Fig. 7.13, in both cases, initially the elements at the top start to drain since the invasion percolation algorithm begins with the invasion of elements connected to the top surface. However, in the absence of gravity, air invasion depends only on the liquid capillary pressure. Therefore, for the case without gravity, at  $S_w = 0.79$ , air percolation from the top to bottom surface can be seen with a clear preferential path. The width of the percolation front is very narrow in the bottom half of the network. On the contrary, when the effect of gravity is considered, the air percolation front is much wider, as can be seen from  $S_w = 0.94$  to  $S_w = 0.72$ , since gravity assists air invasion, especially in the upper region of the network. Thus, the impact of gravity as modeled in the invasion percolation algorithm is reflected in the results.

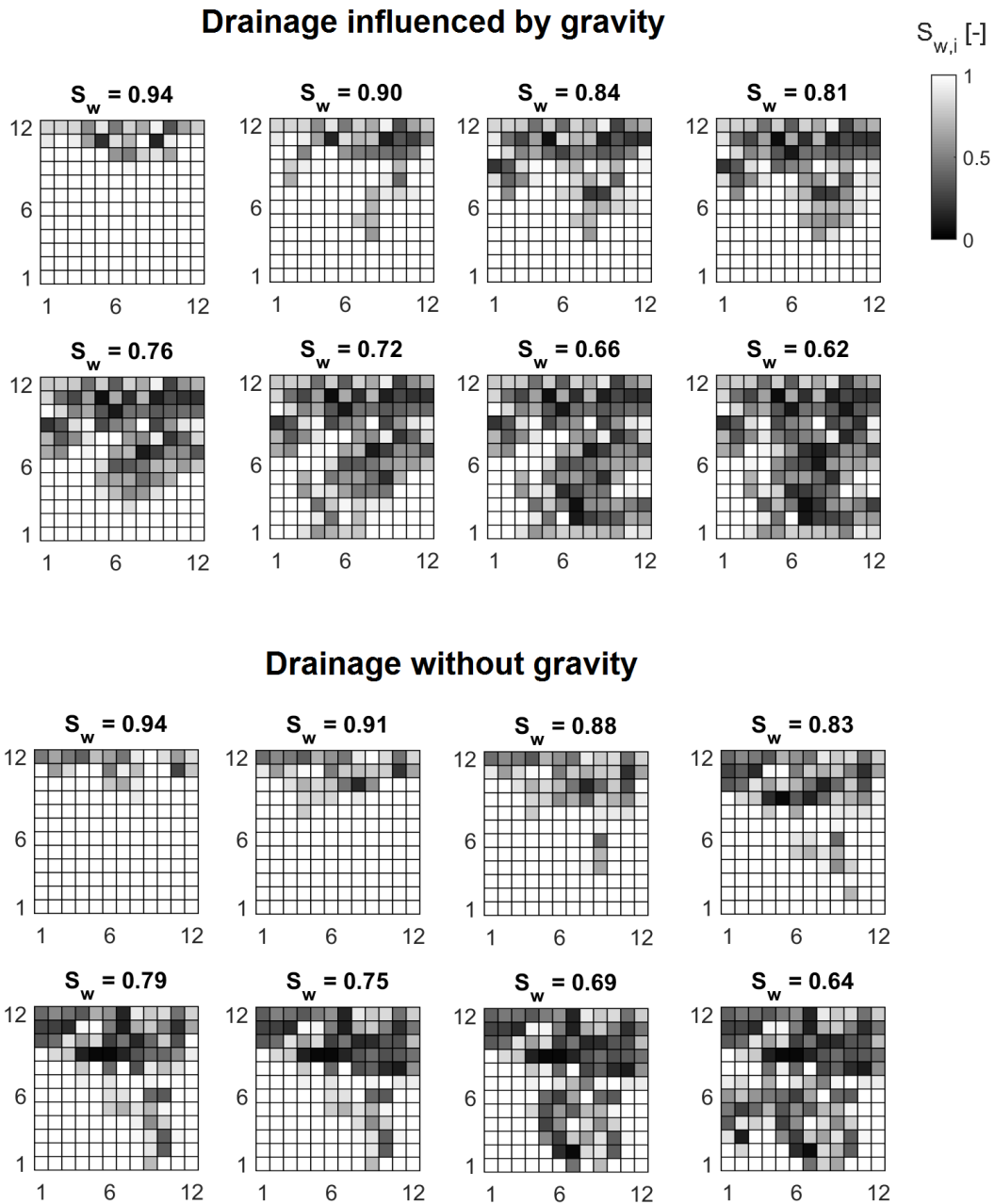


Figure 7.13.: Checkerboard pattern of drainage in the pore network with and without the effect of gravity, with the total saturation level indicated above each figure. The domain is divided into 144 equi-sized grids and the grid color indicates the water saturation  $S_{w,i}$  at the grid along the entire thickness (out of plane direction) of the network.

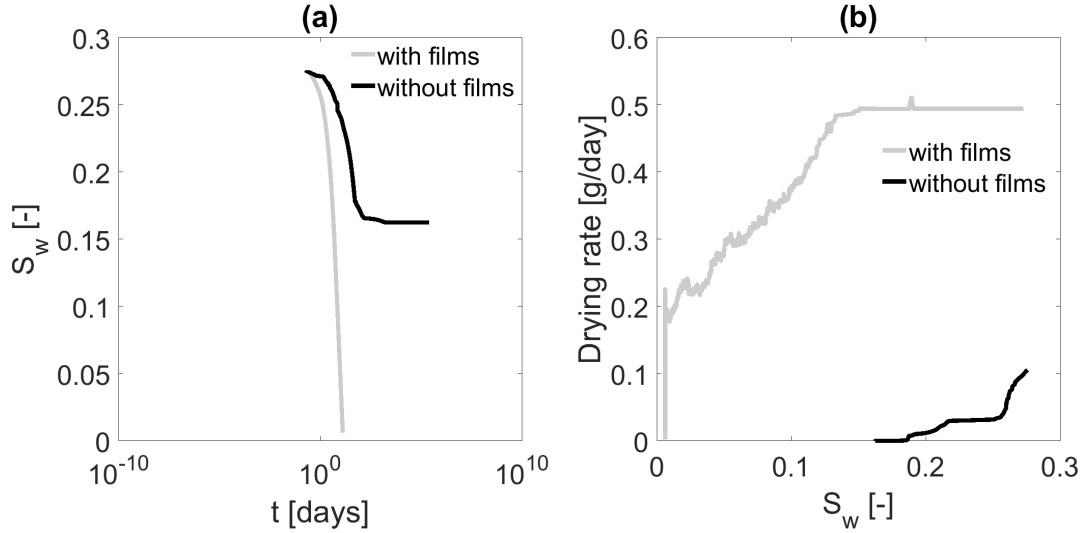


Figure 7.14.: Effect of corner films on the simulated drying process using pore network modeling; (a) temporal evolution of saturation and (b) drying rate as a function of saturation

The influence of considering corner films on the drying rate in the developed model is investigated in Fig. 7.14. In Fig. 7.14(a), the temporal evolution of the network saturation during drying is given for two cases: with and without corner films in the network. The simulation with corner films has 40% saturated elements and 60% film elements at the beginning of drying while the simulation without corner films has 40% saturated elements and 60% dry elements at the beginning of drying. The initial moisture content at the beginning of drying is only slightly higher for the latter case. In the absence of films in the network, the drying algorithm is slightly modified. The initial steps of the algorithm are essentially the same i.e. identifying clusters, determining the vapor flux from each cluster, identifying the largest element in each cluster and then choosing the element among them that will dry the fastest. The difference is in the fact that now this chosen element is completely dried in the given time step (instead of becoming a film element), and the largest elements in all other clusters dry partially such that mass conservation is ensured. The influence of such an approach on the drying rate is strikingly visible in Fig. 7.14. While the network with film flow completely dries out in 13 days, the network without film flows starts to dry at a lower rate. At  $S_w = 0.17$ , the drying rate in the absence of films becomes negligible and the material practically stops drying. Nevertheless, in Fig. 7.14(b), it can be seen that drying without films begins with DDRP, similar to what is observed in the experiments but at a much lower rate. This proves that the CDRP at the beginning of the simulations with film flow is due to the over prediction of film elements in

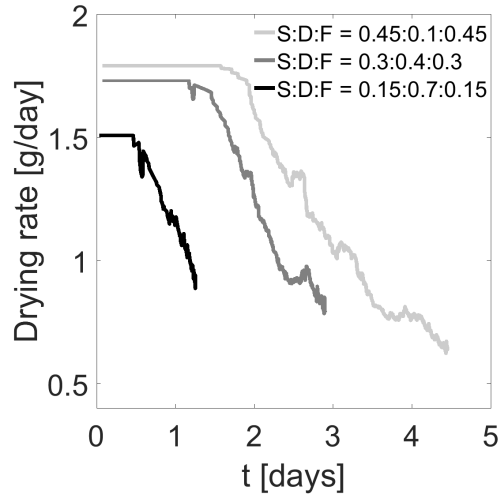


Figure 7.15.: Influence of increasing the number of dry elements on the drying rate. The initial ratio of saturated (S) to dry (D) to film (F) elements in each simulation is given.

the PA pore network. However, simulating drying without considering any film elements will lead to a large under prediction of the drying rate, as seen in Fig. 7.14.

To assess if increasing number of the dry pores in the network at the beginning of drying influences the drying rate in the simulations with film flow, in Fig. 7.15, the drying rates of three simulations with different ratios of saturated (S) to dry (D) to film (F) elements are presented. As the number of dry elements at the beginning of drying increases, the magnitude of the constant drying rate decreases, which is due to lower initial liquid saturation in the network. More importantly, it can be seen that the duration of the CDRP decreases sharply with increasing proportion of dry elements. A further increase in the proportion of dry elements did not change the drying behavior. However, with such a high proportion of dry elements in the pore network, the pore network extracted in this study from the PA specimens will not be able to reproduce the quantity of residual liquid observed in PA after drainage. Therefore, the best approach to simulate drying in PA would be to combine the strengths and weaknesses of the two approaches discussed above i.e. with and without film flow, since clearly, there will be a number of elements in PA that are fully liquid saturated or dry and at the same time have also pores which enhances the hydraulic connectivity in the medium. As a result, it is essential to know the exact wettability distribution of the solid matrix in PA as well as the initial liquid configuration at the beginning of drying. Nevertheless, the drying algorithm developed in this study captures part of the drying behavior of PA and is a promising first step towards developing robust pore network models of drying in highly complex, macroporous media.

The model also stands to gain with a more realistic pore network which, in particular, captures accurately the connectivity of the large pores in PA, since large pores that are highly connected will have a significant impact on the drainage and drying processes in PA.

## 7.7 UPSCALING TO CONTINUUM MODELING

### 7.7.1 *Introduction*

In the continuum approach of transport in porous materials, the porous material is considered as a continuum where transport properties are defined at the macroscale. Heat and mass conservation laws are combined with adequate transport laws, resulting in partial differential equations (PDEs), which are solved by appropriate computational models. As an example, Janssen et al. (2007) implemented a three-dimensional heat and moisture transport model into finite elements to simulate the coupled heat and moisture transport in porous media. Their approach coupled atmospheric boundary conditions to mass and energy transfer within the porous medium in a conservative manner. In this section, the results of such a coupled heat-air-moisture (HAM) model to simulate drying in PA are presented. Since the pore structure of PA is macroporous and hydrophobic, and very different from that of conventional porous materials, the application of continuum modeling for drying of PA is not straightforward, and questions remain on the applicability of such an approach for drying of macroporous media.

For the continuum modeling of drying, two moisture transport properties are required, which can be obtained from the pore network simulations: the drying capillary pressure curve and vapor permeability as a function of saturation. To understand the applicability of the proposed PNM drying model for an upscaling to continuum model, two sets of continuum simulations are performed. In both sets, the capillary pressure (moisture capacity) curve as a function of saturation as determined from the PNM simulations is used. The difference between the two sets of simulations is in the vapor permeability curve. In the first set of simulations, the vapor permeability curve of PA as determined from the PNM simulations is used. In the second set of simulations, a common description of the vapor permeability curve for porous materials is used. The exact permeability curve is indirectly determined from the measurements by minimizing the difference between experimental and simulated moisture loss versus time.



### 7.7.2 Governing equations

The wet porous medium consists of three phases: a solid phase (solid matrix), a liquid phase (liquid water) and gas phase (mixture of dry air and water vapor). The following are the most important assumptions in the model:

- The residual liquid phase at the beginning of the drying process is mainly entrapped and discontinuous. It is assumed that these liquid islands do not move and dry out mainly by vapor diffusion. This allows to assume that liquid transport is negligible with respect to vapor transport.
- No heat and mass source terms are present apart from the evaporation of water.
- Thermal equilibrium exists between all phases.
- Pressure variations are small enough to not affect thermodynamic properties.
- The pressure of the gaseous phase is constant and equal to atmospheric pressure and the gaseous phase does not contribute to heat or mass storage.

Under these assumptions, the equation for conservation of mass can be expressed as:

$$\frac{\partial w_{PM}}{\partial t} = \frac{\partial w_{PM}}{\partial p_c} \cdot \frac{\partial p_c}{\partial t} = -\nabla \cdot (\mathbf{q}_v), \quad (7.21)$$

where  $w_{PM}$  [kg/m<sup>3</sup>] is the moisture content in the porous material and  $p_c$  is the capillary pressure. The definition of all variables and their values in the simulations are given in Table 7.1. It is noted that capillary pressure is used as driving potential, although vapor transport by diffusion is governed by concentration (or vapor pressure) gradients. The reason for the use of capillary pressure is that capillary pressure is determined from PNM simulations as a function of moisture content.

The water vapor flux  $\mathbf{q}_v$  [kg/(m<sup>2</sup>s)] in Eq. (7.21) is defined as:

$$\mathbf{q}_v = -K_v(w_{PM}) \nabla p_c - \frac{K_v(w_{PM})}{T} (\rho_l L_v + p_c (T\psi - 1)) \nabla T, \quad (7.22)$$

where  $K_v(w)$  [s] is the water vapor permeability as a function of moisture content and is calculated from the pore network simulations. In Eq. (7.22), vapor diffusion through the material is driven by capillary pressure as well as temperature gradients. The vapor transport due to a temperature gradient accounts for effects of latent heat  $L_v$  and dependence of surface tension on temperature through  $\psi$ . The relation  $w_{PM}(p_c)$  during drying, which determines the moisture capacity in the LHS of Eq. (7.21) is obtained from the pore network simulations. The equation for conservation of energy can be expressed as:

$$\begin{aligned} & \left( c_{p,l} (T - T_{ref}) \frac{\partial w_{PM}}{\partial p_c} \right) \frac{\partial p_c}{\partial t} + (c_{p,s} w_s + c_{p,l} w_{PM}) \frac{\partial T}{\partial t} \\ & + \nabla \cdot \left( (c_{p,v} (T - T_{ref}) + L_v^{ref}) \mathbf{q}_v \right) = -\nabla \cdot \mathbf{q}_h, \end{aligned} \quad (7.23)$$

$$\mathbf{q}_h = -\lambda \nabla T, \quad (7.24)$$

where  $\mathbf{q}_h$  [J/(sm<sup>2</sup>)] is the heat flux. The first two terms in the LHS accounts for heat storage due to changes in moisture (capillary pressure) and heat, respectively. The third term accounts for the change in enthalpy due to vapor transport and phase changes.

At the boundary of the material where convective exchange takes place with the environment, the following boundary conditions apply for heat and mass transfer:

$$\mathbf{q}_{v,w} = \text{CMTC} (p_{v,\infty} - p_{v,w}), \quad (7.25)$$

$$\mathbf{q}_{h,w} = \text{CHTC} (T_w - T_\infty), \quad (7.26)$$

where the subscript  $w$  indicates the wall conditions at the surface exposed to the environment,  $p_v$  is the vapor pressure, CMTC is the convective mass transfer coefficient and CHTC is the convective heat transfer coefficient. The external environment conditions are represented by the subscript/superscript  $\infty$ .

### 7.7.3 Numerical model and input parameters

The heat and mass conservation equations are solved in COMSOL Multiphysics, a commercial finite-element software. The conservation equations, expressed in terms of dependent variables  $p_c$  and  $T$ , are implemented as user-defined PDEs in COMSOL. The experimental conditions of drying of PA11(1) (Fig. 7.9) is reproduced in the HAM simulations. The computational domain is given in Fig. 7.16. The values for thermal conductivity and specific heat capacity of PA are taken from Hassn et al. (2016). The convective mass transfer coefficient (CMTC) is the same as the one used in the PNM simulations of PA11(1). The convective heat transfer coefficient (CHTC) is also accordingly determined from the Lewis analogy. All other values are standard thermodynamic parameters.

In Fig. 7.17(a), the moisture capacity curve that is used for both continuum simulations are given. Note that the saturation is defined as  $S_w = w_{PM}/w_{cap}$  where  $w_{cap}$  is assumed to be the moisture content such that  $S - w$  at the beginning of drying of PA11(1) is the same in both PNM and continuum models. The discrete  $p_c - S_w$  points as calculated from the PNM simulation of drying of PA11(1) is first averaged and the average values are then modeled with a Van Genuchten fit (Eq. (7.20)), with parameters  $\alpha_{VG} = 0.00283$  and  $n = 8.6$ . In Fig. 7.17(b), the vapor permeability from the PNM simulations of PA11(1) is fitted with a 6th order polynomial fit i.e.:

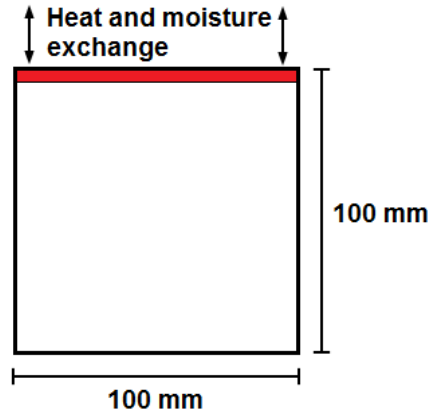


Figure 7.16.: Computational domain of the continuum simulations. Only the top surface has heat and moisture exchange with the environment. The other surfaces are impermeable to both heat and moisture transport.

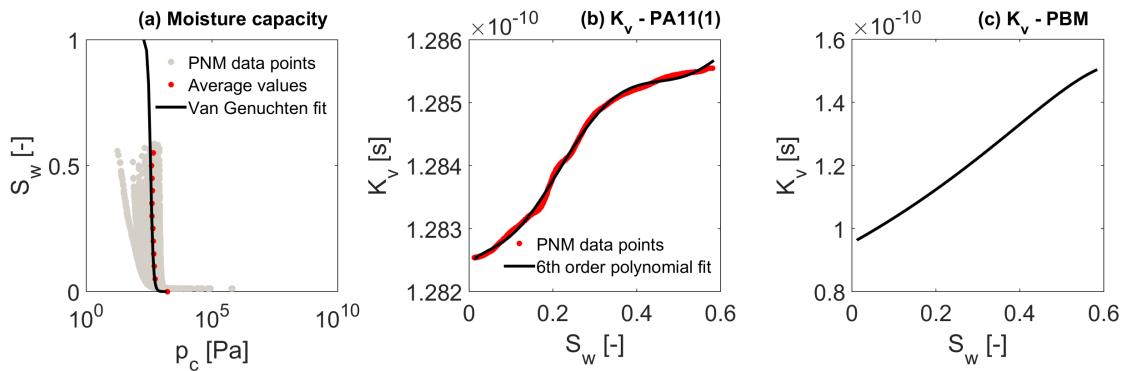


Figure 7.17.: Input parameters to the continuum model; (a) moisture capacity curve calculated from pore network model (PNM) simulations of PA11(1) and fitted with van Genuchten parameters, (b) vapor permeability  $K_v$  as a function of saturation  $S_w$  determined by fitting the data from PNM simulations of PA11(1) and (c) an alternate  $K_v - S_w$  relationship for a porous building material (PBM). Note the different y axes scales in (b) and (c).

Table 7.1.: Material and thermodynamic properties used in the continuum modeling simulations.

<b>Parameter</b>	<b>Symbol</b>	<b>Units</b>	<b>Value</b>
Thermal conductivity of solid	$\lambda_s$	W/(mK)	0.9
Solid matrix content	$w_s$	kg/m <sup>3</sup>	1950
Capillary moisture content	$w_{cap}$	kg/m <sup>3</sup>	48.8
Water vapor resistance	$\mu_{dry}$	-	2
Liquid density	$\rho_w$	kg/m <sup>3</sup>	1000
Specific heat liquid	$c_{p,l}$	J/(kgK)	4182
Specific heat vapor	$c_{p,v}$	J/(kgK)	1880
Specific heat solid	$c_{p,s}$	J/(kgK)	1050
Universal gas constant	$R$	J/(molK)	8.3145
Specific gas constant of water vapor	$R_v$	J/(kgK)	461.524
Molar mass of water vapor	$M_v$	g/mol	18.01534
Molar mass of dry air	$M_a$	g/mol	28.966
Atmospheric pressure	$P_{atm}$	Pa	101325
Normalized thermal derivative of surface tension	$\psi$	1/K	0
Reference temperature	$T_{ref}$	K	273.15
External temperature	$T_\infty$	K	296
External relative humidity	$\phi_e$	%	65
Convective heat transfer coefficient	$CHTC$	W/(m <sup>2</sup> K)	16
Convective mass transfer coefficient	$CMTC$	s/m	$1.17 \times 10^{-7}$
Vaporization heat of water	$L_v^{ref}$	J/(kg)	$2.5 \times 10^6$

$$K_v = p_1 S_w^6 + p_2 S_w^5 + p_3 S_w^4 + p_4 S_w^3 + p_5 S_w^2 + p_6 S_w + p_7, \quad (7.27)$$

where  $p_1 = -1.958e - 10$ ,  $p_2 = 3.849e - 10$ ,  $p_3 = -2.712e - 10$ ,  $p_4 = 7.9e - 11$ ,  $p_5 = -7.729e - 12$ ,  $p_6 = 6.639e - 13$  and  $p_7 = 1.282e - 10$ . The vapor permeability curve of a porous building material (PBM) is given in Fig. 7.17(c) and is defined as:

$$K_v = \frac{D_M}{\mu_{dry} R_v T} \cdot \frac{1 - S_w}{0.89(1 - S_w)^2 + 0.11}. \quad (7.28)$$

Equation (7.28) is similar to the vapor permeability curves of several porous building materials such as brick, concrete etc. and is therefore used for a realistic vapor permeability input. The factor  $\mu_{dry}$  is the vapor resistance factor of the dry material, and is determined by adjusting its value to simulate properly the experimental drying curve.

Two-dimensional continuum simulations are performed for a  $100 \times 100 \text{ mm}^2$  domain and the results are extrapolated to the third dimension. The grid sizes are chosen after a mesh sensitivity analysis. As stated earlier, the simulations are carried out for two cases with one case using the  $K_v - S_w$  curve from the pore network simulations of PA11(1), as given in Fig. 7.17(b), and the other using the  $K_v - S_w$  curve given in Fig. 7.17(c).

#### 7.7.4 Results and discussion

In hygroscopic materials, vapor permeability increases with saturation, taking into account the enhancement of moisture transport by the presence of microscopic liquid zones in the pore space due to capillary condensation. Indeed, the vapor permeability of the porous building material shows a steady decrease with decreasing saturation and that of PA11(1) as determined from the PNM simulations shows a very small decrease (note the different  $y$  axes scales of Figs. 7.17(b) and 7.17(c)). The near constant values of vapor permeability throughout the PNM simulation of drying of PA11(1) can be attributed to the simplified pore network geometry and high pore connectivity. Additionally, two assumptions in the drying PNM algorithm i.e.  $p_v = p_{v,sat}$  at pores near a liquid element and that a bulk element becomes a film element at the first step of drying, lead to a network with many pores having the condition  $p_v = p_{v,sat}$ , especially in the absence of any dry pores in the network at the beginning of drying. This results in many throats in which vapor transport is blocked and therefore the additional resistance to vapor diffusion contributed by these throats when they dry out with time is not reflected in the evolution of vapor permeability. These observations show that there is a need to improve the current pore network geometry to reflect better the pore scale processes to capture the high vapor diffusion resistance of PA.

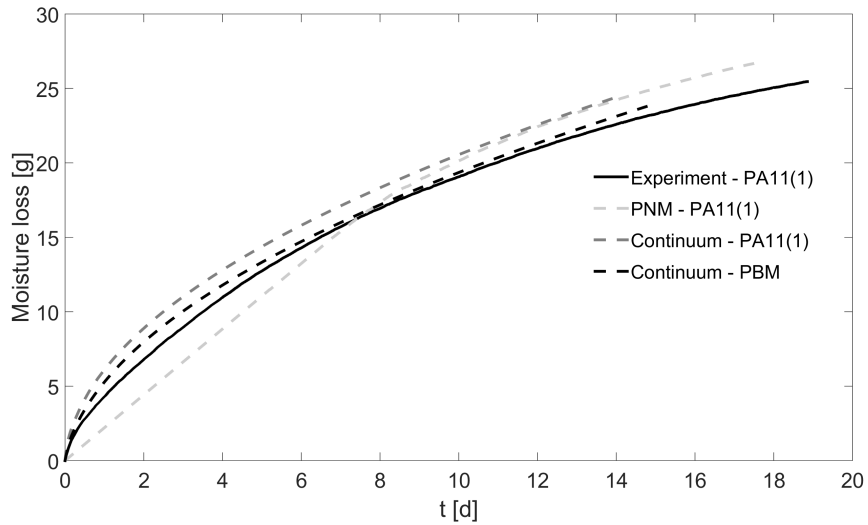


Figure 7.18.: Moisture loss as a function of time calculated with continuum modeling for two different inputs of vapor permeability  $K_v$  curves, from pore network model (PNM) simulations of PA11(1) and from a porous building material (PBM), and its comparison with the experimental drying curve of PA11(1). The drying curve of the PNM simulation of drying of PA11(1) is also given.

In Fig. 7.18, the drying curves of the two continuum simulations are presented along with the experimental drying curve of PA11(1). Additionally, the drying curve of PA11(1) as calculated by the PNM simulations is also given in Fig. 7.18. The drying is represented in terms of moisture loss as the liquid mass at the beginning of the drying is similar across the three presented results. It is recalled that the moisture capacity curve for both the continuum simulations is taken from the PNM simulations of PA11(1). From Fig. 7.18, it is seen that the continuum simulation with the vapor permeability of the porous building material compares more favorably to the experimental drying behavior of PA11(1) than that with the vapor permeability determined from PNM simulations of PA11(1). This is because the vapor permeability of the porous building material captures the higher resistance in the material to vapor diffusion as the material dries, whereas the vapor permeability determined from PNM simulations of PA11(1) does not capture this phenomenon. Nevertheless, the continuum simulation of drying in PA11(1) shows a good agreement with the experimental observation, especially with respect to the curvature of the drying curve, thereby indicating that the coupling between PNM and continuum approaches for modeling drying in macroporous media, as attempted in this thesis, is a promising step.

## 7.8 CONCLUSIONS

Pore network model (PNM) simulations of gravity-driven drainage from a fully saturated porous asphalt specimen and subsequent drying of the residual liquid are presented in this chapter, along with the application of the results determined from pore networks to continuum modeling. The pore networks for the simulations are extracted from X-ray  $\mu$ -CT scans of PA. Pore and throat size distributions of PA specimens are accurately modeled with two-parameter Weibull distributions. Gravity-driven drainage is simulated using a modified invasion percolation algorithm that includes the effect of gravity. Drying of residual liquid after drainage is simulated using a cluster-based approach with a two-step drying process i.e. elements transform from being fully saturated to having liquid only in pore and throat corners to becoming completely dry. Gravimetric experiments on PA are performed to validate the drying simulations.

The most important results from this chapter are:

1. At the end of drainage simulations, air permeability is very low as a result of trapping of air between liquid clusters. This results in only a small number of low resistance, continuous air pathways from inlet to outlet.
2. Capillary pressure as a function of saturation during drainage is approximated by a modified van Genuchten approximation. In general, air entry pressures in pores

and throats of PA are very low due to the presence of large pores and the effect of gravity.

3. From experiments, it is seen that drying in PA completely skips the first drying phase, the constant drying rate period (CDRP), and instead begins with the second drying phase, the decreasing drying rate period (DDRP). This can be explained as a consequence of the large pores drying out fast and a low hydraulic connectivity of the other pores in PA. The drying rate in the experiments show a steep drop within the first 24 h of drying.
4. The drying experiments and PNM simulations show a good overall agreement for two of the three specimens investigated. The third specimen has a very high resistance to drying and this is not captured by the PNM model. The PNM simulations exhibits CDRP initially and transitions to DDRP thereafter. In the second half of the drying period, the drying rates of experiments and simulations show good agreement for the two specimens with lower drying resistance. A detailed analysis showed that the CDRP at the beginning of the PNM simulations is due to the simplified liquid configuration assumed in the network, and its duration can be minimized to an extent by increasing the number of dry elements in the network after drainage.
5. The need to represent the pore space of PA more accurately using pore networks is identified in the results. Specifically, the knowledge of wettability distribution of the solid matrix of PA, the pore connectivity especially of the large pores and an exact understanding of the liquid distribution at the beginning of the drying in PA will help to make the drying model developed in this study more representative of the drying behavior in real specimens.
6. Continuum modeling of drying in PA using vapor permeability and capillary pressure curves determined from PNM simulations showed that although the use of capillary pressure data determined by the model for continuum modeling looks promising, the increasing resistance to vapor diffusion in the pore network with decreasing water saturation is not captured adequately. This again underscores the need to improve the pore network geometry to reflect the high vapor diffusion resistance of PA.



## CONCLUSIONS AND PERSPECTIVES

---

The goal of this research was to develop an integrated multiscale methodology to accurately capture the wetting and drying processes of a macroporous material exposed to environmental loadings. Towards this end, the research presented in this dissertation involved multiscale experimental investigations and numerical modeling of fluid transport in a highly complex, macroporous material, namely, porous asphalt (PA), with the aim to determine the most important environmental conditions and material characteristics that determine the residence time of water in PA. This chapter presents the main conclusions of this research: pore space characterization of PA with computed tomography, neutron radiography investigations of water transport in PA, wind tunnel study of airflow near the air-PA interface, computational fluid dynamics (CFD) simulations of air entrainment in PA and its effect on vapor diffusion, pore network model (PNM) simulations of gravity-driven drainage and drying of PA and the implications of modeling drying in PA with a continuum approach. The scientific contributions of this study to the porous media and road engineering communities are also highlighted. This chapter, and the dissertation, concludes by exploring future work that could be done in order to better understand and model the wetting and drying of a macroporous material in general and PA in particular.

### 8.1 MAIN CONCLUSIONS

The three-dimensional pore space of PA is visualized by high-resolution X-ray microcomputed tomography (X-ray  $\mu$ -CT). The wide range of pore sizes and pore connectivity as well as the tortuous nature of the pore space in PA became evident from a detailed investigation of these X-ray  $\mu$ -CT scans. The pore and throat size distributions of representative elementary volumes of PA are fitted with two-parameter Weibull distributions. Moreover, the difference in pore space characteristics across different types of PA is also examined. A large, well-connected pore space is observed even in very thin specimens of PA11, a type of PA in which the largest aggregate size is 11 mm. Furthermore, the segmented pore space from X-ray  $\mu$ -CT scans of PA is used as the computational domain in CFD and PNM simulations.

The mechanisms of water flow in PA are identified with neutron radiography (NR) imaging. The experiments are carried out in a custom-built mini wind tunnel that reproduces the effects of wind, solar radiation and rain. Gravity drainage, capillary uptake, moisture redistribution, and droplet imbibition phenomena are investigated. The effect of

combined wind and solar radiation on drying and droplet accumulation and drainage is also studied. By combining NR images, X-ray  $\mu$ -CT scans and three-dimensional pore space reconstruction in a novel way, saturated and unsaturated flows in specific areas of the specimens are distinctly identified.

Gravity-driven drainage is found to be the most important contributor to moisture loss in PA. Within seconds, gravity drainage of water significantly reduces the water saturation level in PA. The co-occurrence of gravity drainage and forced convective drying in PA is also studied. Airflow and heat from a solar radiation simulator did not significantly increase the drying rate of PA. Even after 8-10 hours of forced convective drying, water islands are observed in PA specimens. The liquid configuration within PA seemed to be affected little by the external conditions, even for PA11 specimens with the largest pores. These observations give a first indication of the high resistance of PA to drying, resulting from the complex, tortuous pore space of PA. Furthermore, a slow liquid redistribution through saturated flow between adjacent pores is observed. However, due to large pore sizes and the hydrophobicity of the solid matrix, capillary transport of water all the way to the open surface, which could have accelerated the drying process, is found to be negligible.

In addition, wetting by capillary take and droplet deposition is also investigated. It is found that capillary uptake of water, which begins as saturated flow but changes into a combination of saturated flow and unsaturated flow along the pore corners, is occurring only in aged PA specimens due to the exposure of hydrophilic aggregates to water. Saturated-flow finite volume simulations show that regions where faster uptake are seen during the experiments are the ones with relatively less tortuous and more connected flow paths. In case of droplet wetting, water droplets rest and coalesce on the top surface of PAs with finer pore sizes and strong moisture penetration is observed only in PA11 specimens in which, as in capillary uptake, a combination of saturated and unsaturated flows along a well-connected pore space enabled faster penetration of water.

The interaction of airflow with PA is studied using two techniques. To investigate the first phenomenon i.e. the development of air boundary layer above the air-PA interface, wind tunnel experiments are carried out on large slabs of PA. Particle imaging velocimetry (PIV) is used to visualize the air boundary layer as well as the turbulent structures that are active just above the air-PA interface at different wind speeds. Above a certain interface-normal distance, turbulence profiles can be scaled to make them independent of the flow speed. However, at low wind speed (1 m/s), the scaling breaks down due to a combination of organized turbulent structures of high-intensity and a low turbulence background. To investigate another phenomenon i.e. air entrainment into PA and its effect on convective vapor removal, single-phase CFD simulations with an actual PA geometry are performed. The  $k$ - $\epsilon$  turbulence model with low Reynolds number modeling is used for modeling the boundary layer. By varying the wind speed and the depth of the vapor source plane within the specimen, the influence of air entrainment and vapor diffusion

resistance of PA on the drying process is studied in detail. Air entrainment in pores near the air-material interface played an important role in scalar transport only at high wind speeds ( $\approx 10$  m/s) and when the vapor source is not far from the open surface. At lower wind speeds and deeper scalar source depths, diffusion is the dominant vapor transport mechanism in PA and hence, the drying rate at these speeds is not likely to be influenced significantly by airflow. This reinforces the observations from the neutron radiography experiments.

Since gravity-driven drainage and drying are found to be the two most important factors determining the residence time of water in PA, pore network model (PNM) simulations of drainage in PA and subsequent drying of the residual liquid are performed. As intermediate wind speeds and heat did not accelerate the drying rate in any of the previous experiments, natural convective drying is simulated. Gravity-driven drainage is simulated using a modified invasion percolation algorithm that includes the effect of gravity while drying is simulated using a cluster-based approach. Capillary pressure as a function of saturation during drainage is modeled with the Van Genuchten fit. In general, air entry pressures in pores and throats of PA are very low due to the presence of large pores and the effect of gravity. From experiments, it is seen that drying in PA completely skips the first drying phase, the constant drying rate period (CDRP), and instead begins with the second drying phase, the decreasing drying rate period (DDRP), due to the poor hydraulic connectivity in PA because of its large and hydrophobic pores. The PNM simulations exhibit CDRP initially and transitions to DDRP after a third of the total drying time. The CDRP at the beginning of the PNM simulations is due to the assumption of film flow in the network, and its duration can be minimized by increasing the number of hydrophobic pores in the network that does not retain any liquid after drainage. The temporal evolution of capillary pressure and vapor permeability during drying, as determined from PNM simulations, is used to model drying of PA with a continuum approach. A continuum approach to drying in PA could be valid provided the pore networks, and therefore the macroscopic parameters determined from them, capture more accurately the connectivity, tortuosity and hydrophobicity of the real PA structure.

Finally, as a result of this spatially multiscale investigation, the residence time of water in PA is found to have different time scales. Drainage by gravity is in the order of seconds in specimens that are 30 mm and 100 mm high. Drainage is followed by a long, decreasing drying rate period, which can last more than 8 hours for a  $180 \times 30 \times 10$  mm<sup>3</sup> specimen subjected to airflow up to 3 m/s and solar radiation, and as long as 25 days for a 100 mm cubic specimen subjected to natural convection. Wind and solar radiation can influence the drying process only under extreme weather conditions i.e. wind speeds much above 3 m/s and temperatures much higher than 35 °C. Under normal conditions, the hydrophobic solid matrix and the large pores of PA hinder liquid water redistribution within the specimen,

and therefore, drying is determined largely by the vapor diffusion resistance of PA, which is confirmed by both experiments and simulations.

## 8.2 CONTRIBUTIONS TO RESEARCH FIELDS

The research presented in this dissertation involved novel applications of existing experimental, modeling and analytical techniques, on both stand-alone and synergic bases. The contributions from this research extend to the fields of porous media (experimental and theoretical), image analysis, boundary layer characterization over rough surfaces and road engineering. The scientific contributions can be summarized as:

- Development of a multiscale, integrated methodology for identifying the factors influencing the residence time of water in porous media exposed to environment, by starting with laboratory-scale experimental and numerical investigations of fluid transport, followed by determination of the most influential environmental loadings and finally, the modeling of drainage and drying using simplified models with assumptions validated by the aforementioned steps. The methodology also incorporates an upscaling of the detailed information towards a continuum characterization of the macroporous material transport behavior.
- Development of an image analysis technique to predict the exact type of flow (saturated or unsaturated) at well-defined pore spaces, even with two-dimensional neutron radiography. This is achieved by first computing the degree of liquid saturation in pores by combining neutron radiography and X-ray  $\mu$ -CT images, and thereafter reading together the saturation degree images with three-dimensional visualization of pore spaces. The images are obtained using a self-designed multifunctional neutron radiography setup incorporating a self-designed mini wind tunnel, a multi-droplet injector and radiation lamps.
- Application of turbulence statistics that are originally developed for impermeable and rough surfaces to characterize flow over macroporous, permeable surfaces. This methodology can be applied to other research areas such as wind-induced erosion of coarse soil.
- Development of a pore network model of drying that accounts for gravity-driven drainage and evaporation of complex configurations of water in porous materials, especially in materials in which a large number of pores with corner films are expected. With some additional work, the proposed model, which is computationally less expensive than its peers, can also be applied to model evaporation in hydrophobic media where liquid redistribution is negligible e.g. gas diffusion layer in fuel cells.

The contributions towards material design of porous asphalt can be summarized as:

- No generally valid scaling law of wind speed to air turbulence behavior near the air-material interface is found. Hence, the need for performing drying experiments on PA at full-scale and for the entire range of velocities of interest is identified, especially if average wind speeds at the planned road location are below 3 m/s.
- At wind speeds below 10 m/s, air entrainment in PA is found to be insignificant. Consequently, in terms of modeling forced convective drying, PA can be considered as a conventional porous material in which vapor-air mixing occurs above the air-material interface.
- Liquid redistribution in fresh PA can be neglected. However, as the material ages, there can be some liquid redistribution within the material due to capillary pressure gradients induced by an increasingly heterogeneous distribution of surface roughness and wettability.
- After a large rain event, at temperatures close to the dew point, thermal gradients within PA is likely to be negligible, even in the presence of solar radiation, and consequently isothermal drying can be assumed.
- The strong positive influence of percolation paths, created by large pores, on the overall drainage and drying process of PA specimens is observed in the experiments and simulations in this study. In this context, techniques such as gap grading can be used to control the final pore structure in PA pavements to increase liquid permeability.

### 8.3 FUTURE PERSPECTIVES

The conducted research has answered many important questions related to fluid transport in macroporous media. However, it has also opened up a few interesting research questions that should be addressed in the future:

- There is a need to better understand the air boundary layer in the near-wall region of a macroporous material, especially momentum transfer at high wind speeds. Rapidly developing techniques such as refractive index matching methods can be utilized for the same.
- The PA microstructure needs to be better characterized better for providing more accurate input and boundary conditions for drainage and drying simulations. For instance, the heterogeneity in the wettability of the solid matrix of aged PA specimens

can be analyzed with techniques such as low-field Nuclear Magnetic Resonance (NMR) spectroscopy.

- The proposed pore network model of drying has scope for further improvements. Foremost among them is to consider the effect of viscous forces on the liquid distribution pattern, since liquid configuration is found to have an important influence on the drying process in PA. However, although PNM algorithms of drying that includes viscous effects are present in literature, they remain computationally expensive. So there is a need to find a balance. Additionally, an unstructured network, more complicated pore shapes and fractal-type models of pore wall roughness will make the pore network more reflective of the real PA microstructure. Although the proposed drying model underestimated the resistance of the pore network to drying, the sensitivity of the model to increasing complexity of the pore space will throw more light to the efficiency of the model.
- Complementarily, the three-dimensional visualization and quantification of water inside PA is an area that requires more attention. A promising technique is to visualize iodine-doped water with conventional X-ray  $\mu$ -CT scanning after drainage is completed. However, the segmentation of thin liquid films and the sensitivity of wettability of water to iodine content are areas of concern.
- The presented research did not investigate the contribution of the pumping effect of vehicular loads towards air and water flow in PA. This calls for more complex airflow conditions at the surface and the load of the car itself for a poromechanical approach that couples stress distribution in the solid matrix to local pressure build-up of air and water.
- Finally, in the general scope of understanding the time of residence of water in porous media, metrics should be developed to better convey such results, not only in terms of the time of drying but also of the distribution of water within the macrostructure and the contact time with different materials making up a composite structure.

## APPENDIX A

In Chapter 5, the boundary layer height for the moderate and high-speed measurements was located outside the field of view. For the analyses presented in that chapter, it was assumed that the velocity observed at the top of the field of view equals the free-stream air speed. This assumption was supported by the fact that the differences between the velocities observed at this point and those recorded by the Pitot tube located inside the wind tunnel in the free stream were small. The sensitivity analysis presented in this appendix aims to verify the impact of that assumption on the values of the boundary layer parameters calculated in Table 5.2. We define the boundary layer thickness,  $\delta$ , as the height at which a velocity reaches a fraction  $h$  of the free stream air speed  $U_\infty$ :

$$\delta = y|_{U=hU_\infty}, \quad (\text{A.1})$$

where  $h = 0.7, 0.75, 0.8, 0.85, 0.88, 0.9, 0.92, 0.94, 0.96, 0.98$ . It is to be noted that  $h = 0.99$  in the generally accepted definition of boundary layer thickness. Using this criterion, the more robust parameters calculated earlier in Chapter 5 are re-evaluated i.e. displacement thickness (Eq. 5.6), the momentum thickness (Eq. 5.7) and the shape factor, for each value of  $h$ . The results are presented in Figs. A.1 - A.3. The sensitivity study focuses on PA8 and PA11.

In Figs. A.1 - A.3, the step-wise increase in the boundary layer parameters at the low speed measurements is due to the spatial resolution of the PIV images. It can be observed that irrespective of the definition of the boundary layer thickness (Eq. A1), the three considered boundary layer parameters are abnormally low at the low air speed, as compared those at the moderate and high air speeds. This is true for both types of PA. The conclusions of our study therefore do not depend on the assumption for the boundary layer height. On the contrary, the sensitivity study further reinforces the conclusion that there exists a critical air speed,  $U_{crit}$ , where  $1 < U_{crit} < 2.85 \text{ m/s}$ , below which the flow over PA becomes Reynolds number dependent and scaling laws therefore lose validity.

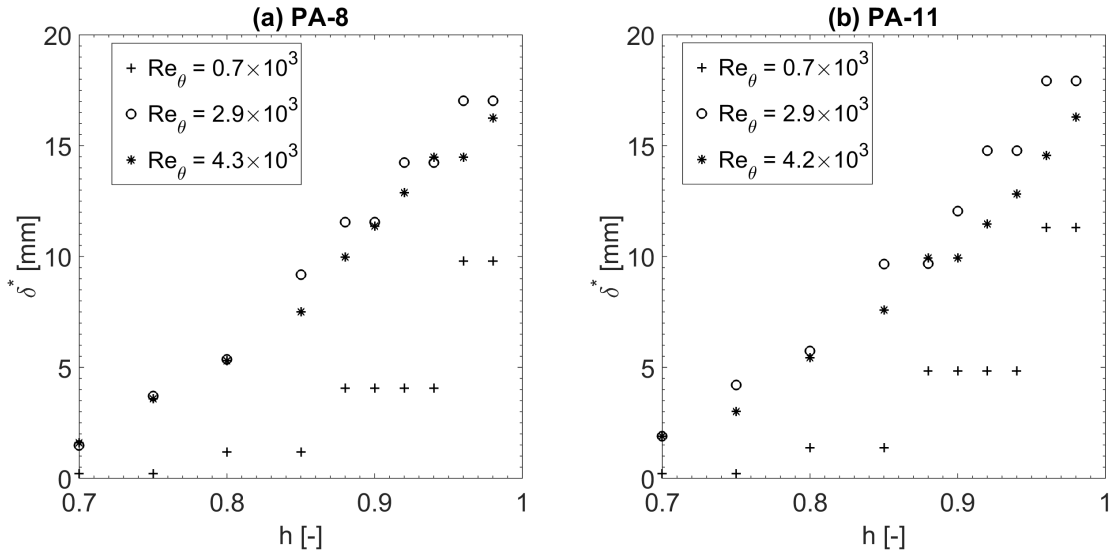


Figure A.1.: Sensitivity study of displacement thickness for (a) PA8 and (b) PA11.

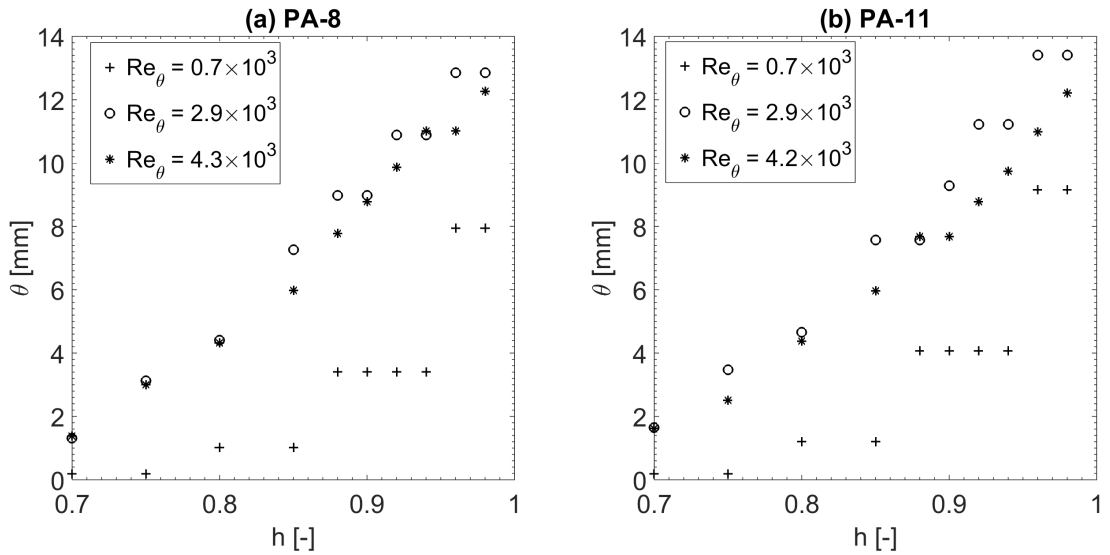


Figure A.2.: Sensitivity study of momentum thickness for (a) PA8 and (b) PA11.



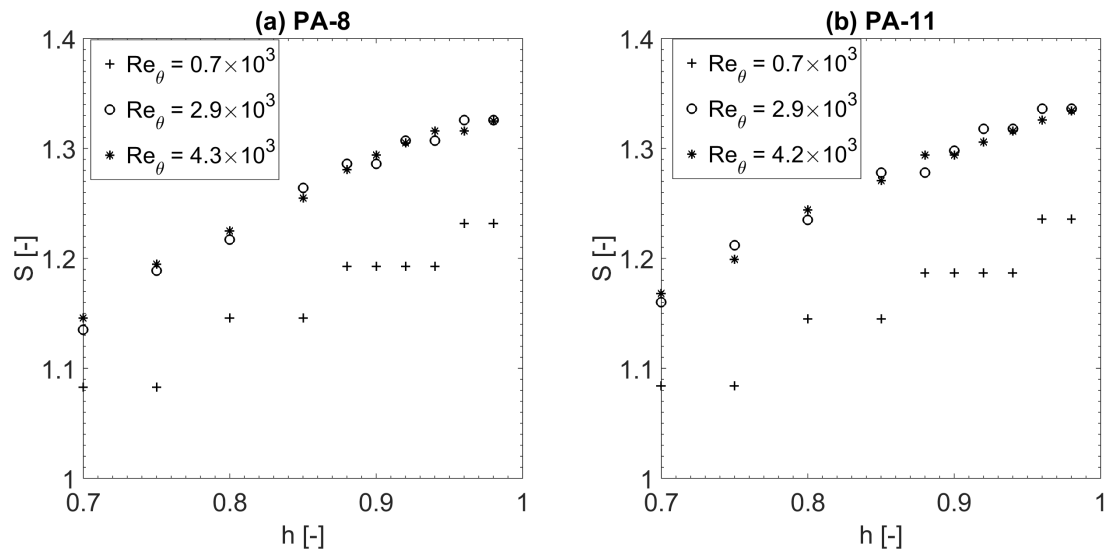


Figure A.3.: Sensitivity study of shape factor for (a) PA8 and (b) PA11.



## BIBLIOGRAPHY

---

- Adler, PM and H Brenner (1988). "Multiphase flow in porous media." In: *Annual review of fluid mechanics*.
- Adrian, R. J., B. G. Jones, M. K. Chung, Yassin Hassan, C. K. Nithianandan, and a. T.-C. Tung (1989). "Approximation of turbulent conditional averages by stochastic estimation." In: *Physics of Fluids A: Fluid Dynamics* 1.6, p. 992.
- Adrian, R. J., C. D. Meinhart, and C. D. Tomkins (2000). "Vortex organization in the outer region of the turbulent boundary layer." In: *Journal of Fluid Mechanics* 422, pp. 1–54.
- Adrian, R.J. (1996). "Stochastic estimation of the structure of turbulent fields." In: *Eddy Structure Identification*. Ed. by J. P. Bonnet. Wien: Springer-Verlag, pp. 145–195.
- Agelinchab, M., M. F. Tachie, and D. W. Ruth (2006). "Velocity measurement of flow through a model three-dimensional porous medium." In: *Physics of Fluids* 18.1, p. 017105.
- Al-Raoush, R.I. and C.S. Willson (2005). "Extraction of physically realistic pore network properties from three-dimensional synchrotron X-ray microtomography images of unconsolidated porous media systems." In: *Journal of Hydrology* 300.1-4, pp. 44–64.
- Amiri, A., K. Vafai, and T. M. Kuzay (1995). "Effects of Boundary Conditions on Non-Darcian Heat Transfer Through Porous Media and Experimental Comparisons." In: *Numerical Heat Transfer, Part A: Applications* 27.6, pp. 651–664.
- Arambula, Edith, Silvia Caro, and Eyad Masad (2010). "Experimental Measurement and Numerical Simulation of Water Vapor Diffusion through Asphalt Pavement Materials." en. In: *Journal of Materials in Civil Engineering* 22.6, pp. 588–598.
- Archer, Cristina L. and Mark Z. Jacobson (2005). "Evaluation of global wind power." In: *Journal of Geophysical Research* 110.D12, p. D12110.
- Arthur, J. K., D. W. Ruth, and M. F. Tachie (2009). "PIV measurements of flow through a model porous medium with varying boundary conditions." In: *Journal of Fluid Mechanics* 629, p. 343.
- Asaeda, Takashi and Vu Thanh Ca (2000). "Characteristics of permeable pavement during hot summer weather and impact on the thermal environment." In: *Building and Environment* 35.4, pp. 363–375.
- Babalís, Stamatios J. and Vassilios G. Belessiotis (2004). "Influence of the drying conditions on the drying constants and moisture diffusivity during the thin-layer drying of figs." In: *Journal of Food Engineering* 65.3, pp. 449–458.
- Bäckström, M and A Bergström (2000). "Draining function of porous asphalt during snowmelt and temporary freezing." en. In: *Canadian Journal of Civil Engineering* 27.3, pp. 594–598.

- Bauters, Tim W. J., Tammo S. Steenhuis, Jean-Yves Parlange, and David A. DiCarlo (1998). "Preferential Flow in Water-Repellent Sands." en. In: *Soil Science Society of America Journal* 62.5, p. 1185.
- Bauters, T.W.J, D.A DiCarlo, T.S Steenhuis, and J.-Y Parlange (2000). "Soil water content dependent wetting front characteristics in sands." In: *Journal of Hydrology* 231-232, pp. 244–254.
- Bech, Niels, Ole K. Jensen, and Birger Nielsen (1991). "Modeling of Gravity-Imbibition and Gravity-Drainage Processes: Analytic and Numerical Solutions." In: *SPE Reservoir Engineering* 6.01, pp. 129–136.
- Belessiotis, V. and E. Delyannis (2011). "Solar drying." In: *Solar Energy* 85.8, pp. 1665–1691.
- Bell, J. M. and F. K. Cameron (1906). "The flow of liquids through capillary spaces." In: *The Journal of Physical Chemistry* 50.30, pp. 658–674.
- Bell, James H. and Rabindra D. Mehta (1989). *Design and calibration of the mixing layer and wind tunnel*. en. Tech. rep. Stanford University, Dept. of Aeronautics and Astronautics.
- Bergman, T.L., a.S. Lavine, F.P. Incropera, and P. Dewitt (2011). *La*. Vol. 86. 3.
- Best, A. C. (1950). "The size distribution of raindrops." In: *Quarterly Journal of the Royal Meterological Society* 76, pp. 16–36.
- Beucher, S and F Meyer (1992). "The morphological approach to segmentation: the watershed transformation." In: *Optical Engineering*. Vol. 34. New York: Marcel Dekker.
- Blunt, Martin, Michael King, and Harvey Scher (1992). "Simulation and theory of two-phase flow in porous media." In: *Physical Review A* 46.12, pp. 7680–7699.
- Blunt, Martin J., Matthew D. Jackson, Mohammad Piri, and Per H. Valvatne (2002). "Detailed physics, predictive capabilities and macroscopic consequences for pore-network models of multiphase flow." In: *Advances in Water Resources* 25.8-12, pp. 1069–1089.
- Bolinder, J. (1999). *On the accuracy of a digital particle image velocimetry system*. Tech. rep. Sweden: Lund Institute of Technology.
- Braudeau, E., J. M. Costantini, G. Bellier, and H. Colleuille (1999). "New Device and Method for Soil Shrinkage Curve Measurement and Characterization." In: *Soil Science Society of America Journal* 63, pp. 525–535.
- Brinkman, H. C. (1949). "A calculation of the viscous force exerted by a flowing fluid on a dense swarm of particles." In: *Applied Scientific Research* 1.1, pp. 27–34.
- Broadbent, SR and JM Hammersley (1957). "Percolation processes." In: ... *Proceedings of the ...*
- Bundt, Maya, Achim Albrecht, Pascal Froidevaux, Peter Blaser, and Hannes Flühler (2000). "Impact of Preferential Flow on Radionuclide Distribution in Soil." In: *Environmental Science & Technology* 34.18, pp. 3895–3899.

- Cahill, T H, M Adams, and C Marm (2004). "ASPHALT - THE RIGHT CHOICE FOR POROUS PAVEMENTS." In: *Better Roads* 74.11.
- Cai, Jianchao and Boming Yu (2011). "A Discussion of the Effect of Tortuosity on the Capillary Imbibition in Porous Media." In: *Transport in Porous Media* 89.2, pp. 251–263.
- Cai, Jianchao, Edmund Perfect, Chu-Lin Cheng, and Xiangyun Hu (2014). "Generalized modeling of spontaneous imbibition based on Hagen-Poiseuille flow in tortuous capillaries with variably shaped apertures." In: *Langmuir : the ACS journal of surfaces and colloids* 30.18, pp. 5142–51.
- Calmidi, V. V. and R. L. Mahajan (2000). "Forced Convection in High Porosity Metal Foams." In: *Journal of Heat Transfer* 122, pp. 557–565.
- Carmeliet, J, F Descamps, and G Houvenaghel (1999). "A multiscale network model for simulating moisture transfer properties of porous media." In: *Transport in Porous Media* 35, pp. 67–88.
- Casey, M. and T. Wintergerste (2000). *ERCOfTAC special interest group on "Quality and Trust in Industrial CFD": best practice guidelines*. Tech. rep. ERCOfTAC.
- Chandler, R and J Koplík (1982). "Capillary displacement and percolation in porous media." In: *Journal of Fluid ...*
- Chau, JF and D Or (2006). "Linking drainage front morphology with gaseous diffusion in unsaturated porous media: A lattice Boltzmann study." In: *PHYSICAL REVIEW-SERIES E*.
- Clarke, A., T. D. Blake, K. Carruthers, and A. Woodward (2002). "Spreading and imbibition of liquid droplets on porous surfaces." In: *Langmuir* 18.8, pp. 2980–2984.
- Clauser, F. H. (1954). "Turbulent Boundary Layer in Adverse Pressure Gradients." In: *Journal of Fluid Mechanics* 1.2, pp. 191–226.
- Coles, D. (1956). "The law of the wake in the turbulent boundary layer." In: *Journal of Fluid Mechanics* 1.2, pp. 191–226.
- Daian, JF and J Saliba (1991). "Détermination d'un réseau aléatoire de pores pour modéliser la sorption et la migration d'humidité dans un mortier de ciment." In: *International journal of heat and mass transfer*.
- Day, Paul R. and James N. Luthin (1956). "A Numerical Solution of the Differential Equation of Flow for a Vertical Drainage Problem." en. In: *Soil Science Society of America Journal* 20.4, p. 443.
- De Gennes, P. G., F. Brochard-Wyart, and D Quéré (2013). *Capillarity and wetting phenomena: drops, bubbles, pearls, waves*. Springer Science & Business Media.
- De Graaff, David B. and John K. Eaton (2000). "Reynolds-number scaling of the flat-plate turbulent boundary layer." In: *Journal of Fluid Mechanics* 422, pp. 319–346.
- Defraeye, Thijs, Bert Blocken, and Jan Carmeliet (2012). "Analysis of convective heat and mass transfer coefficients for convective drying of a porous flat plate by conjugate modelling." In: *International Journal of Heat and Mass Transfer* 55, pp. 112–124.

- Dehghanpour, Hassan, David A. DiCarlo, Behdad Aminzadeh, and Mohammad Mirzaei Galeh-Kalaei (2010). “Two-Phase and Three-Phase Saturation Routes and Relative Permeability During Fast Drainage.” In: *SPE Improved Oil Recovery Symposium*. Society of Petroleum Engineers.
- Denesuk, M, G L Smith, B J J Zelinski, N J Kreidl, and D R Uhlmann (1993). “Capillary penetration of liquid droplets into porous materials.” In: *Journal of Colloid and Interface Science* 158, pp. 114–120.
- DiCarlo, D. A. (2013). “Stability of gravity-driven multiphase flow in porous media: 40 Years of advancements.” In: *Water Resources Research* 49.8, pp. 4531–4544.
- DiCarlo, D.A., Sahni Akshay, and M.J. Blunt (2000). “Three-Phase Relative Permeability of Water-Wet, Oil-Wet, and Mixed-Wet Sandpacks.” In: *SPE Journal* 5.01, pp. 82–91.
- DiCarlo, David A. (2010). “Can Continuum Extensions to Multiphase Flow Models Describe Preferential Flow?” en. In: *Vadose Zone Journal* 9.2, p. 268.
- Diment, G. A. and K. K. Watson (1985). “Stability Analysis of Water Movement in Unsaturated Porous Materials: 3. Experimental Studies.” In: *Water Resources Research* 21.7, pp. 979–984.
- Dong, Hu and Martin Blunt (2009). “Pore-network extraction from micro-computerized-tomography images.” In: *Physical Review E* 80.3, p. 036307.
- D’Onofrio, Terrence G., Homayun K. Navaz, Bojan Markicevic, Brent a. Mantooth, and Kenneth B. Sumpter (2010). “Experimental and Numerical Study of Spread and Sorption of VX Sessile Droplets into Medium Grain-Size Sand.” In: *Langmuir* 26.5, pp. 3317–3322.
- Doube, Michael, Michał M. Kłosowski, Ignacio Arganda-Carreras, Fabrice P. Cordelières, Robert P. Dougherty, Jonathan S. Jackson, Benjamin Schmid, John R. Hutchinson, and Sandra J. Shefelbine (2010). “BoneJ: Free and extensible bone image analysis in ImageJ.” In: *Bone* 47.6, pp. 1076–1079.
- Du Prey, E. Lefebvre (1978). “Gravity and Capillarity Effects on Imbibition in Porous Media.” In: *Society of Petroleum Engineers Journal* 18.03, pp. 195–206.
- Fatt, I. (1956). “The Network Model of Porous Media I. Capillary Pressure Characteristics.” In: *Petroleum Transactions, AIME* 207, pp. 144–181.
- Feldkamp, L. A., L. C. Davis, and J. W. Kress (1984). “Practical cone-beam algorithm.” In: *Journal of the Optical Society of America A* 1.6, pp. 612–619.
- Fernholz, H H (1994). “Near-wall phenomena in turbulent separated flows.” In: *Acta Mechanica* 4, pp. 57–67.
- Fredrich, JT, KH Greaves, and JW Martin (1993). “Pore geometry and transport properties of Fontainebleau sandstone.” In: . . . *journal of rock mechanics and mining* . . .
- Gabriels, D., W. Cornelis, I. Pollet, T. Van Coillie, and M. Ouessar (1997). “The I.C.E. wind tunnel for wind and water erosion studies.” In: *Soil Technology* 10.1, pp. 1–8.
- Geistlinger, Helmut, Iman Ataei-Dadavi, Sadjad Mohammadian, and Hans-Jörg Vogel (2015). “The impact of pore structure and surface roughness on capillary trapping for

- 2-D and 3-D porous media: Comparison with percolation theory.” In: *Water Resources Research* 51.11, pp. 9094–9111.
- Geller, J. T. and J. R. Hunt (1993). “Mass transfer from nonaqueous phase organic liquids in water-saturated porous media.” In: *Water Resources Research* 29.4, pp. 833–845.
- Genuchten, M. Th. van (1980). “A Closed-form Equation for Predicting the Hydraulic Conductivity of Unsaturated Soils<sup>1</sup>.” en. In: *Soil Science Society of America Journal* 44.5, p. 892.
- Genuchten, M. Th. van and P. J. Wierenga (1977). “Mass Transfer Studies in Sorbing Porous Media: II. Experimental Evaluation with Tritium ( $^3\text{H}_2\text{O}$ )<sup>1</sup>.” In: *Soil Science Society of America Journal* 41, pp. 272–278.
- Ghalichi, F, X Deng, A De Champlain, Y Douville, M King, and R Guidoin (1998). “Low Reynolds number turbulence modeling of blood flow in arterial stenoses.” In: *Biorheology* 35.4-5, pp. 281–94.
- Gillette, D. (1978). “A wind tunnel simulation of the erosion of soil: Effect of soil texture, sandblasting, wind speed, and soil consolidation on dust production.” In: *Atmospheric Environment (1967)* 12.8, pp. 1735–1743.
- Glass, R.J., T.S. Steenhuis, and J.-Y. Parlange (1988). “Wetting front instability as a rapid and far-reaching hydrologic process in the vadose zone.” In: *Journal of Contaminant Hydrology* 3.2-4, pp. 207–226.
- Gostick, Jeff, Mahmoudreza Aghighi, James Hinebaugh, Tom Tranter, Michael A. Hoeh, Harold Day, Brennan Spellacy, Mostafa H. Sharqawy, Aimy Bazylak, Alan Burns, Werner Lehnert, and Andreas Putz (2016). “OpenPNM: A Pore Network Modeling Package.” In: *Computing in Science & Engineering* 18.4, pp. 60–74.
- Gostick, Jeff T., Marios a. Ioannidis, Michael W. Fowler, and Mark D. Pritzker (2007). “Pore network modeling of fibrous gas diffusion layers for polymer electrolyte membrane fuel cells.” In: *Journal of Power Sources* 173.1, pp. 277–290.
- Gostick, Jeff T., Marios A. Ioannidis, Michael W. Fowler, and Mark D. Pritzker (2009). “Wettability and capillary behavior of fibrous gas diffusion media for polymer electrolyte membrane fuel cells.” In: *Journal of Power Sources* 194.1, pp. 433–444.
- Gostick, Jeffrey T., Michael W. Fowler, Marios a. Ioannidis, Mark D. Pritzker, Y. M. Volfkovich, and a. Sakars (2006). “Capillary pressure and hydrophilic porosity in gas diffusion layers for polymer electrolyte fuel cells.” In: *Journal of Power Sources* 156.2, pp. 375–387.
- Grattoni, C. A., X. D. Jing, and R. A. Dawe (2001). “Dimensionless groups for three-phase gravity drainage flow in porous media.” In: *Journal of Petroleum Science and Engineering* 29, pp. 53–65.
- Grifoll, Jordi, Josep Ma Gastó, and Yoram Cohen (2005). “Non-isothermal soil water transport and evaporation.” In: *Advances in Water Resources* 28, pp. 1254–1266.

- Gruber, I., I. Zinovik, L. Holzer, a. Flisch, and L. D. Poulikakos (2012). “A computational study of the effect of structural anisotropy of porous asphalt on hydraulic conductivity.” In: *Construction and Building Materials* 36, pp. 66–77.
- Gunstensen, Andrew K. and Daniel H. Rothman (1993). “Lattice-Boltzmann studies of immiscible two-phase flow through porous media.” In: *Journal of Geophysical Research* 98.B4, p. 6431.
- Guo, H., V. I. Borodulin, Y. S. Kachanov, C. Pan, J. J. Wang, Q. X. Lian, and S. F. Wang (2010). “Nature of sweep and ejection events in transitional and turbulent boundary layers.” In: *Journal of Turbulence* 11.November, N34.
- Haghighi, E., E. Shahraeeni, P. Lehmann, and D. Or (2013). “Evaporation rates across a convective air boundary layer are dominated by diffusion.” In: *Water Resources Research* 49.3, pp. 1602–1610.
- Haines, W. B. (1930). “Studies in the physical properties of soil. V. The hysteresis effect in capillary properties, and the modes of moisture distribution associated therewith.” In: *The Journal of Agricultural Science* 20.1, pp. 97–116.
- Hapgood, Karen P, James D Litster, Simon R Biggs, and Tony Howes (2002). “Drop Penetration into Porous Powder Beds.” In: 253, pp. 353–366.
- Happel, J. and H. Brenner (1983). *Low Reynolds number hydrodynamics: with special applications to particulate media*. Springer Science & Business Media, p. 553.
- Hassanein, René, Eberhard Lehmann, and Peter Vontobel (2005). “Methods of scattering corrections for quantitative neutron radiography.” In: *Nuclear Instruments and Methods in Physics Research, Section A: Accelerators, Spectrometers, Detectors and Associated Equipment* 542, pp. 353–360.
- Hassn, Abdushaf, Andrea Chiarelli, Andrew Dawson, and Alvaro Garcia (2016). “Thermal properties of asphalt pavements under dry and wet conditions.” In: 91, pp. 432–439.
- Hendrickx, Jan M.H. and Tzung-mow Yao (1996). “Prediction of wetting front stability in dry field soils using soil and precipitation data.” In: *Geoderma* 70.2-4, pp. 265–280.
- Hilpert, Markus and Cass T Miller (2001). “Pore-morphology-based simulation of drainage in totally wetting porous media.” In: *Advances in Water Resources* 24, pp. 243–255.
- Huang, Liang Kai and Mao Jiun J Wang (1995). “Image thresholding by minimizing the measures of fuzziness.” In: *Pattern Recognition* 28.1, pp. 41–51.
- Hughes, R.G. and M.J. Blunt (2000). “Pore Scale Modeling of Rate Effects in Imbibition.” In: *Transport in Porous Media* 40, pp. 295–322.
- Huinink, H.P., L. Pel, M.A.J. Michels, and M. Prat (2002). “Drying processes in the presence of temperature gradients –Pore-scale modelling.” In: *The European Physical Journal E* 9, pp. 487–498.
- Hyvaluoma, J, P Raiskinmaki, A Jasberg, A Koponen, M Kataja, and J Timonen (2006). “Simulation of liquid penetration in paper.” In: October 2005, pp. 1–8.



- Iida, T., A. Taneo, M. Kaneda, and K. Suga (2014). “PIV measurements of interface turbulence over hetero-porous media.” In: *Journal of Physics: Conference Series* 530, p. 012058.
- James, Chris, Carey J. Simonson, Prabal Talukdar, and Staf Roels (2010). “Numerical and experimental data set for benchmarking hygroscopic buffering models.” In: *International Journal of Heat and Mass Transfer* 53.19-20, pp. 3638–3654.
- Janssen, Hans, Bert Blocken, and Jan Carmeliet (2007). “Conservative modelling of the moisture and heat transfer in building components under atmospheric excitation.” In: *International Journal of Heat and Mass Transfer* 50.5-6, pp. 1128–1140.
- Jazia, Dorra Ben, Laurent Vonna, Gautier Schrodj, Hugues Bonnet, Yves Holl, and Hamidou Haidara (2011). “Imbibing drops of ethanol / water mixtures in model nanoporous networks with tunable pore structure: Deviation from square root to linear time regime imbibition kinetics.” In: *Colloids and Surfaces A: Physicochemical and Engineering Aspects* 384.1-3, pp. 643–652.
- Jerjen, I., L.D. Poulikakos, M. Plamondon, Ph. Schuetz, Th. Luethi, and A. Flisch (2015). “Drying of Porous Asphalt Concrete Investigated by X-Ray Computed Tomography.” In: *Physics Procedia* 69.October 2014, pp. 451–456.
- Joekar Niasar, V., S. M. Hassanizadeh, L. J. Pyrak-Nolte, and C. Berentsen (2009). “Simulating drainage and imbibition experiments in a high-porosity micromodel using an unstructured pore network model.” In: *Water Resources Research* 45.2, n/a–n/a.
- Johansson, Arne V. and P. Henrik Alfredsson (1982). “On the structure of turbulent channel flow.” In: *Journal of Fluid Mechanics* 122, pp. 295–314.
- Keane, R D and R J Adrian (1990). “Optimization of particle image velocimeters. I. Double pulsed systems.” en. In: *Measurement Science and Technology* 1.11, pp. 1202–1215.
- Keirsbulck, L., L. Labraga, A. Mazouz, and C. Tournier (2002). “Surface Roughness Effects on Turbulent Boundary Layer.” In: 124.1, pp. 127–135.
- Kianinejad, A., B. Aminzadeh, X. Chen, and D.A. DiCarlo (2014). “Three-Phase Relative Permeabilities as a Function of Flow History.” In: *SPE Improved Oil Recovery Symposium*. Society of Petroleum Engineers.
- Knackstedt, M.A., C.H. Arns, A. Limaye, A. Sakellariou, T.J. Senden, A.P. Sheppard, R.M. Sok, W.V. Pinczewski, and G.F. Bunn (2013). “Digital Core Laboratory: Properties of reservoir core derived from 3D images.” In: *SPE Asia Pacific Conference on Integrated Modelling for Asset Management*. Society of Petroleum Engineers.
- Kothandaraman, CP (2004). *Heat and mass transfer data book*. New Age International.
- Krogstad, P.-Å., R. A. Antonia, and L. W. B. Browne (1992). “Comparison between rough- and smooth-wall turbulent boundary layers.” In: *Journal of Fluid Mechanics* 245, pp. 599–617.
- Kronlund, Dennis, Andreas Bergbreiter, Axel Meierjohann, Leif Kronberg, Mika Lindén, David Grosso, and Jan-Henrik Smått (2015). “Hydrophobization of marble pore surfaces

- using a total immersion treatment method – Product selection and optimization of concentration and treatment time.” In: *Progress in Organic Coatings* 85, pp. 159–167.
- Kubilay, A., D. Derome, B. Blocken, and J. Carmeliet (2014). “High-resolution field measurements of wind-driven rain on an array of low-rise cubic buildings.” In: *Building and Environment* 78, pp. 1–13.
- Kulkarni, Vinayak, Niranjan Sahoo, and Sandip D. Chavan (2011). “Simulation of honeycomb–screen combinations for turbulence management in a subsonic wind tunnel.” In: *Journal of Wind Engineering and Industrial Aerodynamics* 99.1, pp. 37–45.
- Kuttanikkad, S. Pulloor, M. Prat, and J. Pauchet (2011). “Pore-network simulations of two-phase flow in a thin porous layer of mixed wettability: Application to water transport in gas diffusion layers of proton exchange membrane fuel cells.” In: *Journal of Power Sources* 196.3, pp. 1145–1155.
- Lake, L. (1989). *Enhanced Oil Recovery*. Englewood Cliffs, NJ: Prentice Hall.
- Lal, Sreeyuth, Lily D. Poulikakos, Marjan Sedighi Gilani, Iwan Jerjen, Peter Vontobel, Manfred N. Partl, Jan C. Carmeliet, and Dominique Derome (2014). “Investigation of Water Uptake in Porous Asphalt Concrete Using Neutron Radiography.” In: *Transport in Porous Media*.
- Lal, Sreeyuth, Peter Moonen, Lily D. Poulikakos, Manfred N. Partl, Dominique Derome, and Jan Carmeliet (2016). “Turbulent airflow above a full-scale macroporous material: Boundary layer characterization and conditional statistical analysis.” In: *Experimental Thermal and Fluid Science* 74, pp. 390–403.
- Lauder, B.E. and B.I. Sharma (1974). “Application of the energy-dissipation model of turbulence to the calculation of flow near a spinning disc.” In: *Letters in Heat and Mass Transfer* 1.2, pp. 131–137.
- Laurindo, Joao Borges and Marc Prat (1998). “Numerical and experimental network study of evaporation in capillary porous media. Drying rates.” In: *Chemical Engineering Science* 53.12, pp. 2257–2269.
- Lehmann, E. H., P. Vontobel, and L. Wiesel (2001). “Properties of the Radiography Facility Neutra At Sinq and Its Potential for Use As European Reference Facility.” In: *Nondestructive Testing and Evaluation* 16, pp. 191–202.
- Lenormand, R (1988). “Numerical models and experiments on immiscible displacements in porous media.” In: *Journal of Fluid Mechanics* 189, pp. 165–187.
- Lenormand, Roland and Cesar Zarcone (1984). “Role Of Roughness And Edges During Imbibition In Square Capillaries.” In: *SPE Annual Technical Conference and Exhibition*. Society of Petroleum Engineers.
- Leverett, MC (1941). “Capillary behavior in porous solids.” In: *Transactions of the AIME* 142.01.
- Li, Xiao-Yan and Bruce E. Logan (2001). “Permeability of Fractal Aggregates.” In: *Water Research* 35.14, pp. 3373–3380.

- Liakopoulos, A. C. (1964). “Theoretical Solution Of The Gravity Drainage Problem.” en. In: *Journal of Hydraulic Research* 2.1, pp. 50–74.
- Lindquist, WB and SM Lee (1996). “Medial axis analysis of void structure in three-dimensional tomographic images of porous media.” In: *Journal of ...*
- Liu, Benli, Jianjun Qu, Weimin Zhang, Lihai Tan, and Yanhong Gao (2014). “Numerical evaluation of the scale problem on the wind flow of a windbreak.” In: *Scientific Reports* 4, p. 6619.
- Liu, Fang, Baoming Chen, and Li Wang (2013). “Experimental and numerical estimation of slip coefficient in a partially porous cavity.” In: *Experimental Thermal and Fluid Science* 44, pp. 431–438.
- Longo, Sandro, Francisco M. Domínguez, and Alessandro Valiani (2015). “The turbulent structure of the flow field generated by a hydrofoil in stalling condition beneath a water–air interface.” In: *Experimental Thermal and Fluid Science* 61, pp. 34–47.
- Lucas, R (1918). “Rate of capillary ascension of liquids.” In: *Kolloid Z.*
- Mahadevan, J., M. S. Sharma, and Y. C. Yortsis (2006). “Flow-Through Drying of Porous Media.” In: *AIChE Journal* 52.7, pp. 2367–2380.
- Mahmud, Walid Mohamed and Viet Hoai Nguyen (2006). “Effects of Snap-Off in Imbibition in Porous Media with Different Spatial Correlations.” In: *Transport in Porous Media* 64.3, pp. 279–300.
- Makhanov, K., A. Habibi, H. Dehghanpour, and E. Kuru (2014). “Liquid uptake of gas shales: A workflow to estimate water loss during shut-in periods after fracturing operations.” In: *Journal of Unconventional Oil and Gas Resources* 7, pp. 22–32.
- Marcke, P Van, B Verleye, and J Carmeliet (2010). “An improved pore network model for the computation of the saturated permeability of porous rock.” In: *Transport in porous ...*
- Marmur, Abraham (2003). “Kinetics of Penetration into Uniform Porous Media: Testing the Equivalent-Capillary Concept.” In: *Langmuir* 19.14, pp. 5956–5959.
- Masad, Eyad, Aslam Al Omari, and Hamn-Ching Chen (2007). “Computations of permeability tensor coefficients and anisotropy of asphalt concrete based on microstructure simulation of fluid flow.” In: *Computational Materials Science* 40.4, pp. 449–459.
- Mashayekhizadeh, V., R. Kharrat, M. H. Ghazanfari, and M. Dejam (2012). “An Experimental Investigation of Fracture Tilt Angle Effects on Frequency and Stability of Liquid Bridges in Fractured Porous Media.” en. In: *Petroleum Science and Technology* 30.8, pp. 807–816.
- Mashayekhizadeh, Vahid, Mohammad Hossein Ghazanfari, Riyaz Kharrat, and Morteza Dejam (2011). “Pore-Level Observation of Free Gravity Drainage of Oil in Fractured Porous Media.” In: *Transport in Porous Media* 87.2, pp. 561–584.
- Mason, G and NR Morrow (1991). “Capillary behavior of a perfectly wetting liquid in irregular triangular tubes.” In: *Journal of Colloid and Interface Science*.

- Mason, Geoffrey and Norman R. Morrow (1984). “Meniscus curvatures in capillaries of uniform cross-section.” In: *Journal of the Chemical Society, Faraday Transactions 1* 80.9, p. 2375.
- Mayer, Raymond P and Robert a Stowe (1965). “Mercury porosimetry—breakthrough pressure for penetration between packed spheres.” In: *Journal of Colloid Science* 20.8, pp. 893–911.
- Meakin, P, A Birovljev, and V Frette (1992). “Gradient stabilized and destabilized invasion percolation.” In: *Physica A: Statistical . . .*
- Meakin, Paul, Geri Wagner, Anne Vedvik, Håkon Amundsen, Jens Feder, and Torstein Jøssang (2000). “Invasion percolation and secondary migration: experiments and simulations.” In: *Marine and Petroleum Geology* 17.7, pp. 777–795.
- Méheust, Yves, Grunde Løvoll, Knut Jørgen Måløy, and Jean Schmittbuhl (2002). “Interface scaling in a two-dimensional porous medium under combined viscous, gravity, and capillary effects.” In: *Physical review. E, Statistical, nonlinear, and soft matter physics* 66.5 Pt 1, p. 051603.
- Meiarashi, S., M. Ishida, T. Fujiwara, M. Hasebe, and T. Nakatsuji (1996). “Noise reduction characteristics of porous elastic road surfaces.” In: *Applied Acoustics* 47.3, pp. 239–250.
- Mirzaei-Paiaman, Abouzar, Mohsen Masihi, and Dag Chun Standnes (2011). “Study on Non-equilibrium Effects during Spontaneous Imbibition.” In: *Energy & Fuels* 25.7, pp. 3053–3059.
- Moghaddam, Mehdi Bahari and Mohammad Reza Rasaei (2015). “Experimental Study of the Fracture and Matrix Effects on Free-Fall Gravity Drainage With Micromodels.” In: *SPE Journal* 20.02, pp. 324–336.
- Montoto, M (1995). “Microfractography of granitic rocks under confocal scanning laser microscopy.” In: *Journal of . . .*
- Narasimhan, Arunn, K. S. Raju, and S. R. Chakravarthy (2014). “Experimental and Numerical Determination of Interface Slip Coefficient of Fluid Stream Exiting a Partially Filled Porous Medium Channel.” In: *Journal of Fluids Engineering* 136.4, 041201–1 : 041201–9.
- Neithalath, Narayanan, Milani S Sumanasooriya, and Omkar Deo (2010). “Characterizing pore volume , sizes , and connectivity in pervious concretes for permeability prediction.” In: *Materials Characterization* 61.8, pp. 802–813.
- Northrup, M. A., T. J. Kulp, and S. M. Angel (1991). “Fluorescent particle image velocimetry: application to flow measurement in refractive index-matched porous media.” In: *Applied optics* 30.21, pp. 3034–40.
- Nowicki, S C, H T Davis, L E Scriven, H T Davis, and L E Scriven Microscopic (1992). “Microscopic determination of transport parameters in drying porous media.” In: *Drying Technology* 10.4.

- Olson, John F. and Daniel H. Rothman (1997). “Two-fluid flow in sedimentary rock: simulation, transport and complexity.” English. In: *Journal of Fluid Mechanics* 341, pp. 343–370.
- Or, Dani (2008). “Scaling of capillary, gravity and viscous forces affecting flow morphology in unsaturated porous media.” In: *Advances in Water Resources* 31.9, pp. 1129–1136.
- Oren, P.-E., Stig Bakke, and O.J. Arntzen (1998). “Extending Predictive Capabilities to Network Models.” In: *SPE Journal* 3.04, pp. 324–336.
- Pack, Min, Han Hu, Dong-ook Kim, Xin Yang, and Ying Sun (2015). “Colloidal Drop Deposition on Porous Substrates : Competition among Particle Motion , Evaporation , and In fi ltration.” In: 31, pp. 7953–7961.
- Parlange, J.-Y. and D. E. Hill (1976). “Theoretical analysis of wetting front instability in soils.” In: *Soil Science* 122.4, pp. 236–239.
- Paterna, E. (2015). “Wind tunnel investigation of turbulent flow in urban configurations: a time-resolved PIV analysis.” PhD thesis. Dissertation 22609, ETH Zurich.
- Patzek, Tad W (2001). “Verification of a Complete Pore Network Simulator of Drainage and Imbibition.” In: *SPE Journal* 6.02, pp. 144–156.
- Perraton, D and A Carter (2005). “In-Situ Permeability of the Outermost Layer of Asphalt and Cement Concrete Road Materials: Water Permeability Evaluated with Gas Flow.” In: *Road materials and pavement design*.
- Perry, A. E., W. H. Schofield, and P. N. Joubert (1969). “Rough wall turbulent boundary layers.” In: *Journal of Fluid Mechanics* 37.02, pp. 383–413.
- Philip, J R and D A De Vries (1957). “Moisture movement in porous materials under temperature gradients.” In: *Transactions, American Geophysical Union* 38.2, pp. 222–232.
- Plourde, F. and M. Prat (2003). “Pore network simulations of drying of capillary porous media. Influence of thermal gradients.” In: *International Journal of Heat and Mass Transfer* 46.7, pp. 1293–1307.
- Poulikakos, L. D. (2011). “A multi-scale fundamental investigation of moisture induced deterioration of porous asphalt concrete.” PhD thesis. ETH Zurich.
- Poulikakos, L. D. and M. N. Partl (2010). “Investigation of porous asphalt microstructure using optical and electron microscopy.” In: *Journal of Microscopy* 240.March, pp. 145–154.
- Poulikakos, L. D., R. Gubler, M. Partl, M. Pittet, L. Arnaud, A. Junod, A. Dumont, and E. Simond (2006). *Mechanical properties of porous asphalt, recommendations for standardization*. Tech. rep. UVEK, Switzerland.
- Poulikakos, L D, M Sedighi Gilani, D Derome, I Jerjen, and P Vontobel (2013a). “Time resolved analysis of water drainage in porous asphalt concrete using neutron radiography.” In: *Applied radiation and isotopes : including data, instrumentation and methods for use in agriculture, industry and medicine* 77, pp. 5–13.

- Poulikakos, L.D. and M.N. Partl (2012). "A multi-scale fundamental investigation of moisture induced deterioration of porous asphalt concrete." In: *Construction and Building Materials* 36, pp. 1025–1035.
- Poulikakos, Lily D., Saba Saneinejad, Marjan Sedighi Gilani, Iwan Jerjen, Eberhard Lehmann, and Dominique Derome (2013b). "Forced Convective Drying of Wet Porous Asphalt Imaged with Neutron Radiography." In: *Advanced Engineering Materials* 15.11, pp. 1136–1145.
- Prat, M (1993). "Percolation model of drying under isothermal conditions in porous media." In: *International Journal of Multiphase Flow* 19.4, pp. 691–704.
- Prat, M (1995). "Isothermal drying on non-hygroscopic capillary-porous materials as an invasion percolation process." In: *International journal of multiphase flow* 21.5, pp. 875–892.
- Prat, M (2002). "Recent advances in pore-scale models for drying of porous media." In: 86.5502, pp. 153–164.
- Prat, M. (2007). "On the influence of pore shape, contact angle and film flows on drying of capillary porous media." In: *International Journal of Heat and Mass Transfer* 50.7-8, pp. 1455–1468.
- Prat, M and F Bouleux (1999). "Drying of capillary porous media with a stabilized front in two dimensions." In: *Physical Review E*.
- Praticò, Filippo Giammaria and Antonino Moro (2007). "Permeability and Volumetrics of Porous Asphalt Concrete." en. In: *Road Materials and Pavement Design* 8.4, pp. 799–817.
- Prazak, J., M. Sir, F. Kubik, J. Tywoniak, and C. Zarcone (1992). "Oscillation Phenomena in Gravity-Driven Drainage in Coarse Porous Media." In: 28.7, pp. 1849–1855.
- Prill, Robert C., A.I. Johnson, and Donald Arthur Morris (1965). "Specific yield - laboratory experiments showing the effect of time on column drainage." In: *U.S. Geological Survey Water-Supply Paper 1662-B*.
- Princen, H.M (1969). "Capillary phenomena in assemblies of parallel cylinders." In: *Journal of Colloid and Interface Science* 30.1, pp. 69–75.
- Prinos, Panayotis, Dimitrios Sofialidis, and Evangelos Keramaris (2003). "Turbulent Flow Over and Within a Porous Bed." In: *Journal of Hydraulic Engineering* 129.9, pp. 720–733.
- Ransohoff, TC and CJ Radke (1988). "Laminar flow of a wetting liquid along the corners of a predominantly gas-occupied noncircular pore." In: *Journal of Colloid and Interface Science*.
- Raupach, M. R. (1981). "Conditional statistics of Reynolds stress in rough-wall and smooth-wall turbulent boundary layers." In: *Journal of Fluid Mechanics* 108, pp. 363–382.
- Raupach, M. R., R. A. Antonia, and S. Rajagopalan (1991). "Rough-wall turbulent boundary layers." In: *Applied Mechanics Review* 44, pp. 1–25.

- Reis, N. C., R. F. Griffiths, M. D. Mantle, and L. F. Gladden (2003). “Investigation of the evaporation of embedded liquid droplets from porous surfaces using magnetic resonance imaging.” In: *International Journal of Heat and Mass Transfer* 46.7, pp. 1279–1292.
- Reis, N.C., R.F. Griffiths, M.D. Mantle, L.F. Gladden, and J.M. Santos (2006). “MRI investigation of the evaporation of embedded liquid droplets from porous surfaces under different drying regimes.” In: *International Journal of Heat and Mass Transfer* 49.5-6, pp. 951–961.
- Reis Jr, Neyval C, Richard F Griffiths, and Jane M Santos (2004). “Numerical simulation of the impact of liquid droplets on porous surfaces.” In: 198, pp. 747–770.
- Ritsema, Coen J., Tammo S. Steenhuis, J.-Yves Parlange, and Louis W. Dekker (1996). “Predicted and observed finger diameters in field soils.” In: *Geoderma* 70.2-4, pp. 185–196.
- Roache, P. J. (1994). “Perspective: A Method for Uniform Reporting of Grid Refinement Studies.” In: *Journal of Fluids Engineering* 116.3, p. 405.
- Rogak, Steven N and Richard C Flagan (1990). “Stokes drag on self-similar clusters of spheres.” In: *Journal of Colloid and Interface Science* 134.1, pp. 206–218.
- Rossen, William R (2000). “Snap-off in constricted tubes and porous media.” In: *Colloids and Surfaces A: Physicochemical and Engineering Aspects* 166.1-3, pp. 101–107.
- Saffman, P. G. and G. Taylor (1958). “The Penetration of a Fluid into a Porous Medium or Hele-Shaw Cell Containing a More Viscous Liquid.” In: *Proceedings of the Royal Society A: Mathematical, Physical and Engineering Sciences* 245.1242, pp. 312–329.
- Sahni, Akshay, Jon Burger, and Martin Blunt (1998). “Measurement of Three Phase Relative Permeability during Gravity Drainage using CT.” In: *SPE/DOE Improved Oil Recovery Symposium*. Society of Petroleum Engineers.
- Saleh, S., J.F. Thovert, and P.M. Adler (1992). “Measurement of two-dimensional velocity fields in porous media by particle image displacement velocimetry.” In: *Experiments in Fluids* 12, pp. 210–212.
- Schindelin, Johannes, Ignacio Arganda-Carreras, Erwin Frise, Verena Kaynig, Mark Longair, Tobias Pietzsch, Stephan Preibisch, Curtis Rueden, Stephan Saalfeld, Benjamin Schmid, Jean-Yves Tinevez, Daniel James White, Volker Hartenstein, Kevin Eliceiri, Pavel Tomancak, and Albert Cardona (2012). “Fiji: an open-source platform for biological-image analysis.” en. In: *Nature methods* 9.7, pp. 676–82.
- Schlichting, H. and K. Gersten (2000). *Boundary-layer theory*. Springer.
- Schmid, K. S. and S. Geiger (2012). “Universal scaling of spontaneous imbibition for water-wet systems.” In: *Water Resources Research* 48.3, n/a–n/a.
- Shahidzadeh-Bonn, Noushine, Salima Rafai, Aza Azouni, and Daniel Bonn (2006). “Evaporating droplets.” In: *Journal of Fluid Mechanics* 549, pp. 307–313.
- Shaw, TM (1987). “Drying as an immiscible displacement process with fluid counterflow.” In: *Physical Review Letters*.

- Silin, Dmitriy and Tad Patzek (2006). "Pore space morphology analysis using maximal inscribed spheres." In: *Physica A: Statistical Mechanics and its Applications* 371.2, pp. 336–360.
- Starr, J. L., H. C. DeRoo, C. R. Frink, and J.-Y. Parlange (1978). "Leaching Characteristics of a Layered Field Soil." en. In: *Soil Science Society of America Journal* 42.3, p. 386.
- Stauffer, D. and A. Aharaony (1992). *Introduction to Percolation Theory*. London: Taylor & Francis.
- Stempihar, Jeffrey, Tina Pourshams-Manzouri, Kamil Kaloush, and Maria Rodezno (2012). "Porous Asphalt Pavement Temperature Effects for Urban Heat Island Analysis." en. In: *Transportation Research Record: Journal of the Transportation Research Board* 2293, pp. 123–130.
- Suga, K. and Y. Kuwata (2014). "Turbulence over/inside porous surfaces and challenges to its modelling." In: *Journal of Physics: Conference Series* 530, p. 012004.
- Suga, K., S. Tominaga, M. Mori, and M. Kaneda (2013). "Turbulence Characteristics in Flows Over Solid and Porous Square Ribs Mounted on Porous Walls." In: *Flow, Turbulence and Combustion* 91.1, pp. 19–40.
- Surasani, V. K., T. Metzger, and E. Tsotsas (2008). "Consideration of heat transfer in pore network modelling of convective drying." In: *International Journal of Heat and Mass Transfer* 51.9-10, pp. 2506–2518.
- Taghilou, Mohammad and Mohammad Hassan Rahimian (2014). "Investigation of two-phase flow in porous media using lattice Boltzmann method." In: *Computers and Mathematics with Applications* 67, pp. 424–436.
- Tan, S., T. Fwa, and K. Chai (2004). "Drainage Considerations for Porous Asphalt Surface Course Design." en. In: *Transportation Research Record: Journal of the Transportation Research Board* 1868, pp. 142–149.
- Terwilliger, P.L., L.E. Wilsey, Howard N. Hall, P.M. Bridges, and R.A. Morse (1951). "An Experimental and Theoretical Investigation of Gravity Drainage Performance." In: *Journal of Petroleum Technology* 192.11, pp. 285–296.
- Tokunaga, Tetsu K. and Jiamin Wan (1997). "Water film flow along fracture surfaces of porous rock." In: *Water Resources Research* 33.6, pp. 1287–1295.
- Townsend, A A (1976). *The structure of turbulent shear flow*. 1976th ed. Vol. 41. 01. Cambridge University Press.
- Tsimpanogiannis, IN and YC Yortsos (1999). "Scaling theory of drying in porous media." In: *Physical Review E*.
- Vafai, K., R. L. Alkire, and C. L. Tien (1985). "An experimental investigation of heat transfer in variable porosity media." In: *Transactions of the ASME* 107, pp. 642–647.
- Vafai, Kambiz (1984). "Convective flow and heat transfer in variable-porosity media." In: *Journal of Fluid Mechanics* 147, pp. 233–259.



- Vandersteen, Katrijn, Jan Carmeliet, and Jan Feyen (2003). "A Network Modeling Approach to Derive Unsaturated Hydraulic Properties of a Rough-Walled Fracture." en. In: *Transport in Porous Media* 50.3, pp. 197–221.
- Vogel, H. J. (2000). "A numerical experiment on pore size, pore connectivity, water retention, permeability, and solute transport using network models." In: *European Journal of Soil Science* 51.1, pp. 99–105.
- Vogel, HJ (1997). "Morphological determination of pore connectivity as a function of pore size using serial sections." In: *European Journal of Soil Science*.
- Wang, Lei, Mirko Salewski, and Bengt Sundén (2010). "Turbulent flow in a ribbed channel: Flow structures in the vicinity of a rib." In: *Experimental Thermal and Fluid Science* 34.2, pp. 165–176.
- Wang, Wenqing, Jonny Rutqvist, Uwe-Jens Görke, Jens T. Birkholzer, and Olaf Kolditz (2011). "Non-isothermal flow in low permeable porous media: a comparison of Richards' and two-phase flow approaches." In: *Environmental Earth Sciences* 62.6, pp. 1197–1207.
- Washburn, Edward W. (1921). "The Dynamics of Capillary Flow." In: *Physical Review* 17.3, pp. 273–283.
- Watson, K. K. (1966). "An instantaneous profile method for determining the hydraulic conductivity of unsaturated porous materials." In: *Water Resources Research* 2.4, pp. 709–715.
- Watson, K. K. (1967). "Numerical and experimental study of column drainage." In: *Journal of the Hydraulic Division* 93, 1–15 HY2.
- Weller, H. G., G. Tabor, H. Jasak, and C. Fureby (1998). "A tensorial approach to computational continuum mechanics using object-oriented techniques." In: *Computers in Physics* 12.6, p. 620.
- Wildenschild, D., C.M.P Vaz, M.L. Rivers, D. Rikard, and B.S.B. Christensen (2002). "Using X-ray computed tomography in hydrology: systems, resolutions, and limitations." In: *Journal of Hydrology* 267.3-4, pp. 285–297.
- Wilkinson, D and J F Willemsen (1983). "Invasion percolation: a new form of percolation theory." en. In: *Journal of Physics A: Mathematical and General* 16.14, pp. 3365–3376.
- Willmarth, W. W. and S. S. Lu (1972). "Structure of the Reynolds stress near the wall." In: *Journal of Fluid Mechanics* 55.01, pp. 65–92.
- Wong, Harris, S Morris, and C.J Radke (1992). "Three-dimensional menisci in polygonal capillaries." In: *Journal of Colloid and Interface Science* 148.2, pp. 317–336.
- Yang, Mingdi and Ernest K. Yanful (2002). "Water balance during evaporation and drainage in cover soils under different water table conditions." In: *Advances in Environmental Research* 6.4, pp. 505–521.
- Yiotis, A. G., Andreas. G. Boudouvis, A. K. Stubos, I. N. Tsimpanogiannis, and Y. C. Yortsos (2004). "Effect of liquid films on the drying of porous media." In: *AIChE Journal* 50.11, pp. 2721–2737.

- Yiotis, A G, D Salin, E S Tajer, and Y C Yortsos (2012a). “Analytical solutions of drying in porous media for gravity-stabilized fronts.” In: *Physical review. E, Statistical, nonlinear, and soft matter physics* 85.4 Pt 2, p. 046308.
- Yiotis, A G, D Salin, E S Tajer, and Y C Yortsos (2012b). “Drying in porous media with gravity-stabilized fronts: experimental results.” In: *Physical review. E, Statistical, nonlinear, and soft matter physics* 86.2 Pt 2, p. 026310.
- Yiotis, A G, D Salin, and Y C Yortsos (2015). “Pore Network Modeling of Drying Processes in Macroporous Materials : Effects of Gravity , Mass Boundary Layer and Pore Microstructure.” In: *Transport in Porous Media* 110.1, pp. 1–22.
- Yiotis, A.G, A.K Stubos, A.G Boudouvis, and Y.C Yortsos (2001). “A 2-D pore-network model of the drying of single-component liquids in porous media.” In: *Advances in Water Resources* 24.3-4, pp. 439–460.
- Yiotis, Andreas G., Ioannis N. Tsimpanogiannis, Athanassios K. Stubos, and Yannis C. Yortsos (2007). “Coupling between external and internal mass transfer during drying of a porous medium.” In: *Water Resources Research* 43.6.
- Yoon, Hongkyu, Changyong Zhang, Charles J. Werth, Albert J. Valocchi, and Andrew G. Webb (2008). “Numerical simulation of water flow in three dimensional heterogeneous porous media observed in a magnetic resonance imaging experiment.” In: *Water Resources Research* 44.6, W06405(1–12).
- Zendehboudi, S and I Chatzis (2011). “Laboratory investigation of free fall gravity drainage in fractured porous systems using unconsolidated macromodels.” In: *Energy & Fuels*.
- Zhang, Lei, Ghim Ping Ong, and Fwa Tien Fang (2013). “Evaluating the Influence of Aggregate Size on Permeability Porous Pavements Using Finite Volume Simulation.” In: *International Journal of Pavement Research and Technology* 6.5, pp. 520–526.
- Zippe, H. J. and W. H. Graf (1983). “Turbulent Boundary-Layer Flow Over Permeable and Non-Permeable Rough Surfaces.” In: *Journal of Hydraulic Research* 21.1, pp. 51–65.

## CURRICULUM VITAE

---

SREEYUTH LAL

Date of birth     November 21, 1988  
Place of birth    Thodupuzha, India  
Nationality       Indian  
E-mail address    sreeyuth@gmail.com

### EDUCATION

02.2013 – 07.2016    Doctor of Sciences  
                              D-BAUG  
                              ETH Zurich  
                              Multiscale investigation and numerical modeling of imbibition, drainage and drying of a macroporous medium.

09.2010 – 09.2012    Master of Science  
                              Nuclear Engineering  
                              ETH Zurich | EPF Lausanne  
                              Direct numerical simulation of subcooled and near saturated nucleate boiling.

09.2006 – 09.2010    Bachelor of Engineering (Hons.)  
                              Mechanical Engineering  
                              Birla Institute of Technology and Science, Pilani  
                              Design and Commercialization of a Tesla Turbine.

## ACADEMIC AND INDUSTRIAL RESEARCH EXPERIENCE

- 01.2016 – 02.2016 Visiting Scholar at IMFT (Toulouse, France).
- 08.2011 – 10.2011 Intern at Axpo AG (Baden, Switzerland).
- 07.2009 – 08.2009 Intern at Indian Space Research Organization (Trivandrum, India).

## JOURNAL PUBLICATIONS (EXCLUDING WORKS FROM THIS THESIS)

1. **S. Lal**, Y. Sato and B. Niceno (2015), Direct numerical simulation of bubble dynamics in subcooled and near-saturated convective nucleate boiling. *Int. J. of Heat and Fluid Flow*, 51: 16-28.
2. Y. Sato, **S. Lal**, and B. Niceno (2013), Computational Fluid Dynamics Simulation of Single Bubble Dynamics in Convective Boiling Flows." *Multiphase Science and Technology*, 25.

## CONFERENCE TALKS (EXCLUDING WORKS FROM THIS THESIS)

1. Y. Sato, **S. Lal** and B. Niceno (2013), Development of Mass-Conservative Phase-Change Model for Convective Boiling Simulations, ASME 2013 International Mechanical Engineering Congress and Exposition (IMECE2013), November 15-21, San Diego, California, USA. *Abstract and presentation.*
2. **S. Lal**, Y. Sato and B. Niceno (2012), Highly Resolved Numerical Simulation of Subcooled and Saturated Boiling; a Step Toward Prediction of Critical Heat Flux, 10th Multiphase Flow Conference, June 12-14, Dresden, Germany. *Abstract and presentation.*
3. **S. Lal**, Y. Sato and B. Niceno (2012), Direct Numerical Simulation of Subcooled Nucleate Pool Boiling: Proceedings of International Conference on Nuclear Engineering 2012 – Madrid, World Academy of Science, Engineering and Technology, Issue 63, March 2012. *Abstract and presentation.*

## COLOPHON

This document was typeset in L<sup>A</sup>T<sub>E</sub>X using the typographical look-and-feel `classicthesis`.  
The bibliography is typeset using `biblatex` with `natbib`.